

**Massachusetts Institute of Technology
Woods Hole Oceanographic Institution**



**Joint Program
in Oceanography/
Applied Ocean Science
and Engineering**



DOCTORAL DISSERTATION

*Seismic Scattering of Low-Grazing-Angle Acoustic
Waves Incident on the Seafloor*

by

Robert J. Greaves

June 1998

**19990526 076
910**

MIT/WHOI

98-15

**Seismic Scattering of Low-Grazing-Angle Acoustic Waves Incident on the
Seafloor**

by

Robert J. Greaves

Massachusetts Institute of Technology
Cambridge, Massachusetts 02139

and

Woods Hole Oceanographic Institution
Woods Hole, Massachusetts 02543

June 1998

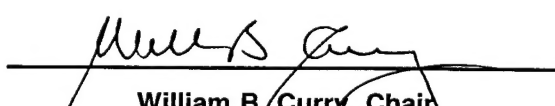
DOCTORAL DISSERTATION

Funding was provided by the Office of Naval Research under grant numbers N00014-93-1-1352,
N00014-90-J-1493, and N00014-95-1-0506 and by a Chevron Fellowship.

Reproduction in whole or in part is permitted for any purpose of the United States Government. This
thesis should be cited as: Robert J. Greaves, 1998. Seismic Scattering of Low-Grazing-Angle Acoustic
Waves Incident on the Seafloor. Ph.D. Thesis. MIT/WHOI, 98-15.

Approved for publication; distribution unlimited.

Approved for Distribution:



William B. Curry, Chair
Department of Geology and Geophysics



Paola Malanotte-Rizzoli

MIT Director of Joint Program



John W. Farrington

WHOI Dean of Graduate Studies

Seismic Scattering of Low-Grazing-Angle Acoustic Waves Incident on the Seafloor

by

Robert John Greaves

B.A., Boston University (1973)
M.S., Stanford University (1977)

Submitted in partial fulfillment of the requirements for the degree of
Doctor of Philosophy
at the
MASSACHUSETTS INSTITUTE OF TECHNOLOGY
and the
WOODS HOLE OCEANOGRAPHIC INSTITUTION

June, 1998

©Robert J. Greaves, 1998. All rights reserved

The author hereby grants to MIT and WHOI permission to reproduce and
distribute publicly paper and electronic copies of this thesis document in whole or in
part, and to grant others the right to do so.

Author *Robert J. Greaves*

Joint Program in Oceanography, Massachusetts Institute of Technology and
Woods Hole Oceanographic Institution, June, 1998

Certified by .. *Ralph A. Stephen*

Dr. Ralph Stephen
Senior Scientist

Accepted by .. *R. K. Smith* for D.Sc.

Deborah K. Smith, Chair, Joint Committee for Marine Geology and Geophysics,
Massachusetts Institute of Technology and Woods Hole Oceanographic Institution

Seismic Scattering of Low-Grazing-Angle Acoustic Waves

Incident on the Seafloor

by

Robert John Greaves

Submitted to the Joint Program in Oceanography, Massachusetts Institute of Technology and Woods Hole Oceanographic Institution, on June, 1998, in partial fulfillment of the requirements for the degree of Doctor of Philosophy

Abstract

The goal of this thesis is to develop a methodology to interpret sound scattered from the seafloor in terms of seafloor structure and subseafloor geological properties. Specifically, this work has been directed towards the interpretation of matched-filtered, beamformed monostatic acoustic reverberation data acquired on the west flank of the Mid-Atlantic Ridge when the seafloor is insonified by a band-limited, low-grazing-angle acoustic pulse. This research is based on the hypothesis that observed backscatter signals are produced by a combination of seafloor (interface) scattering and subseafloor (volume) scattering from structure having variations at scale lengths similar to the wavelength of the insonifying acoustic field. Analysis of monostatic reverberation data acquired during the Site A experiment (Run 1) of the Acoustic Reverberation Special Research Program 1993 Acoustics Cruise suggests that the scattered signals cannot be accounted for quantitatively in terms of large-scale slope, even though a strong correspondence between high intensity backscatter and seafloor ridges is observed. In order to investigate and quantify the actual sources of seafloor scattering, a numerical modeling study of seafloor models is undertaken using a finite-difference solution to the elastic wave equation. Geological data available at Site A and published reports describing geological properties of similar deep ocean crustal regions are used to develop a realistic seafloor model for the study area with realistic constraints on elastic parameters. Wavelength-scale heterogeneity in each model, in the form of seafloor roughness and subseafloor volume heterogeneity is defined using stochastic distributions with Gaussian autocorrelations. These distributions are quantified by their correlation lengths and standard deviation in amplitude. In order to incorporate all seafloor structure in a single parameterization of seafloor scattering, large-scale slope and wavelength-scale seafloor spatial parameters (rms height and correlation length), are included, along with the acoustic beam grazing-angle relative to a horizontal seafloor, in the definition of an 'effective grazing angle'. The Rayleigh roughness parameter, which depends on grazing angle of the insonification, is then

redefined using the effective grazing angle and calculated for a variety of seafloor models. Scattering strengths are shown to vary systematically but nonlinearly with the 'effective Rayleigh roughness parameters' of horizontal rough seafloor models. This leads to an approximate interpretation scheme for backscatter intensity. In general, variation in backscattering is found to be dominated by the scattering from rough seafloor. If the seafloor is smooth or very low velocity (e.g., sediment), then scattering from volume heterogeneity becomes an important factor in the backscattered field. Both wavelength-scale seafloor roughness and volume heterogeneity are shown to be capable of producing the levels of variation in intensity observed in monostatic reverberation experiments. Variations in large-scale seafloor slope and subseafloor average velocity are shown to influence the backscatter response of seafloor models.

Thesis Supervisor: Dr. Ralph Stephen
Title: Senior Scientist

Acknowledgments

This thesis has been made possible by the continued support and encouragement of my advisors, Dr. Ralph Stephen at WHOI and Prof. Nafi Toksöz at MIT. I will be forever grateful to them for providing the opportunity for me to come to MIT and WHOI for this degree program. I wish to thank Nafi for his enduring belief in my ability to carry out this research, and encouragement at critical times. Over the past four years, Ralph has patiently introduced me to many of the more subtle points of wave propagation and scattering, and yet has always had time to remind me that there is life outside the laboratory. His strong support and friendship over this period have carried me over the rough spots.

I also wish to express my sincere gratitude to the other members of my committee, Dr. Brian Tucholke, Prof. Arthur Baggeroer and Dr. George Frisk, who have all taken time to meet with me and provide guidance during my research. I wish to particularly express my appreciation to Brian for his careful review of the writing in this thesis and for taking the time to explain many aspects of seafloor geology to me. I am grateful to my defense committee chairman, Dr. Neal Driscoll, for being such a good chairman and, most important, for being so enthusiastic in his support of my thesis.

Many other people have played important roles in my life at MIT and WHOI. Dr. Jung Mo Lee provided strong friendship and the patience to explain many mysteries of MIT courses and computer programming. Dr. Roger Turpening has consistently provided many interesting research ideas to ponder. Shirley Rieven has been a faithful friend and shared many long hours of coursework since the first day of class. Tom Bolmer has provided humor, friendship and a working computer environment. Matthijs Haartsen and Matthias Imhof provided many interesting discussions about scattering. Dr. Steve Swift answered some very important questions about seafloor properties and showed me the ropes on my first research cruise. My office partner, Dan Lizarralde, was always available for discussion and fun. No one could ask for a better person to share a small space with.

I am also very fortunate to have some very long lasting friends. Dr. Arthur

Weglein has encouraged and supported my interests in science for more than ten years. The enthusiasm he has shown for all wave propagation problems, but particularly scattering problems, has been a strong factor in my decision to focus on scattering in my thesis research. We will also need to find a new topic for discussion during our runs together, since 'going back to school' is completed. Elias Ata has been a strong source of encouragement and friendship for many years, and I wish to express my gratitude for his support and shared wisdom in geophysics and life. Thanks to Frank Filice for also being a good friend and always being available for discussion and moving. John Morell and Richard Stutman have been my friends for almost thirty years. Their support and willingness to discuss life over the past six years has been particularly important. I am looking forward to another thirty years of their friendship.

What makes a life's work valuable is family. I believe that my parents instilled in me the desire to learn and the willingness to work hard to achieve my goals. My father has always been my staunchest supporter and good friend, which has helped me immensely, always, but particularly in the past few years. The memory of my mother has also been strong during this time, and has provided a guiding sense of purpose in carrying out this work. My sisters, Kathy, Nancy and Ginny have, as they always have, taken special care of me in the past few years, and I appreciate their efforts and concern very much. Most importantly, my son, Nick, has matured into a nice, intelligent, fun-loving, and handsome young man, and his presence in my life makes everything worthwhile. I love him very much and am looking forward to watching his life blossom over the coming years.

My first year of study at MIT was supported by a Chevron Fellowship. The work in this thesis was funded by the Office of Naval Research under grant numbers N00014-93-1-1352, N00014-90-J-1493, and N00014-95-1-0506.

Contents

1	Introduction	15
1.1	Background	17
1.2	Thesis Outline	23
1.3	Contributions	25
2	Seafloor acoustic backscattering from different geological provinces in the Atlantic Natural Laboratory	33
2.1	Abstract	33
2.2	Introduction	34
2.3	Geological Setting	37
2.4	Data	40
2.4.1	Acoustic Data	40
2.4.2	Bathymetry Data	41
2.5	Data Processing	42
2.5.1	Transmission Loss	44
2.5.2	Seafloor Locations and Dip Estimation	45
2.5.3	Source and Receiver Range	46
2.5.4	Traveltime and Grazing Angle	47
2.5.5	Beam Averaging and Stacking	48
2.6	Analysis	49
2.6.1	Scattering Strength vs True Grazing Angle	49
2.6.2	Scattering Strength Maps	51
2.6.3	Scattering Strength vs. Seafloor Dip	52

2.7	Discussion and Conclusions	53
3	The Geological Model	95
3.1	2-D vs. 3-D Modeling	98
3.2	Geological Model	100
3.2.1	Seafloor Profile	100
3.2.2	Seafloor Type and Cross-section	101
3.3	Geoacoustic Volume Properties	105
3.3.1	Sediment Properties	105
3.3.2	Sediment Properties: Summary	111
3.3.3	Basaltic Basement and Talus	113
3.3.4	Basaltic Basement and Talus: Summary	120
3.4	Conclusion	121
4	Numerical Elastic Wavefield Modeling of Seabed Scattering	161
4.1	Introduction	161
4.2	The Numerical Scattering Chamber	164
4.2.1	Limitations to the Numerical Modeling	167
4.3	PART 1: Models with Homogeneous Subseafloor	169
4.3.1	Wavelength-Scale Properties of Realistic Seafloor	171
4.3.2	Baseline Model	172
4.3.3	Scattering vs. ka	175
4.3.4	Scattering vs. $k\sigma$	179
4.3.5	Gaussian vs. Self-similar	181
4.4	Large-Scale Seafloor Characteristics	182
4.4.1	Variation in Velocity and Density	182
4.4.2	Variation in Seafloor Slope	184
4.5	Backscatter and Effective Rayleigh Roughness	189
4.5.1	Seafloor Scattering: Models 1-4	192
4.6	PART II: Models with Heterogeneous Subseafloor	196
4.6.1	Scattering from Isotropic Volume Heterogeneity	198

4.6.2	Scattering vs. a_v	198
4.6.3	Scattering vs. σ_v	200
4.6.4	Rough Seafloor and Isotropic Volume Heterogeneity	201
4.6.5	Isotropic Volume Heterogeneity with Sloping Seafloor	202
4.6.6	Variation in Mean Volume Properties: Hard vs. Soft Bottoms	203
4.6.7	Models 1-4 with Isotropic Volume Heterogeneity	205
4.6.8	Scattering from Large-Scale Volume Heterogeneity	207
4.6.9	Realistic Layered Models	209
4.7	Discussion	210
4.8	Conclusion	213
5	Summary and Conclusions	371
5.1	Introduction	371
5.2	Summary	373
5.3	Site A Monostatic Acoustic Reverberation Data	376
5.4	Acoustics Data	377
5.5	Thesis Conclusion	379
A	Transmission Loss Approximation	389
B	Seafloor Photograph Interpretations	399

List of Figures

1-1 ARSRP site locations on the west flank of the Mid-Atlantic Ridge	28
1-2 Monostatic acoustic reverberation travelpath in the deep ocean.	30
2-1 Inside-corner (IC) crust and outside-corner (OC) crust	56
2-2 Site A location and bathymetry map.	58
2-3 Possible characteristics of IC and OC seafloor dip.	60
2-4 Calculating seafloor slope within a grid cell.	62
2-5 Acoustic reverberation beam footprint.	64
2-6 Seafloor dip distribution in IC and OC study areas.	66
2-7 Grazing angles vs. range calculated by ray tracing.	68
2-8 Site A scattering strength vs. true grazing angle.	70
2-9 Syrian Knob scattering strength vs. true grazing angle.	72
2-10 Casa Grande scattering strength vs. true grazing angle.	74
2-11 Site A scattering strength from 'back-looking' seafloor dips vs. true grazing angle	76
2-12 Syrian Knob scattering strength from 'back-looking' seafloor dips vs. true grazing angle	78
2-13 Casa Grande scattering strength from 'back-looking' seafloor dips vs. true grazing angle	80
2-14 Site A stacked scattering strength map	82
2-15 Syrian Knob stacked scattering strength map	84
2-16 Casa Grande stacked scattering strength map	86
2-17 Site A scattering strength vs. seafloor dip.	88

2-18	Syrian Knob scattering strength vs. seafloor dip.	90
2-19	Casa Grande scattering strength vs. seafloor dip.	92
3-1	Site A bathymetry and ARSRP data locations.	122
3-2	Bathymetry around the JASON trackline.	124
3-3	Generating a seafloor profile.	126
3-4	Photographs of seafloor features at Site A.	128
3-5	Surficial seafloor geology based on photographic data.	136
3-6	Site A sediment thickness mapped from seismic and side-scan sonar observations.	138
3-7	Sediment thickness at Site A based on the statistical description of Webb and Jordan (1995).	140
3-8	Profiles of estimated sediment thickness.	142
3-9	The seafloor geological model.	144
3-10	Sediment core and acoustic-lance data.	148
3-11	Geoacoustic parameters of nannofossil ooze.	150
3-12	Geoacoustic parameters of sediment models.	152
3-13	A simple model of fault zones in seafloor basement.	154
3-14	Gaussian vs. self-similar correlation functions.	156
3-15	Geoacoustic parameters of upper-most crustal basalt and talus.	158
4-1	The Numerical Scattering Chamber.	218
4-2	Scattering directions in the NSC.	220
4-3	Gaussian versus Self-similar seafloor models.	222
4-4	Spatial filtering the seafloor profile.	226
4-5	A baseline flat-seafloor model with 'hard-bottom' properties.	230
4-6	Scattering coefficients of the baseline model.	232
4-7	Horizontal rough-seafloor models with different correlation lengths.	234
4-8	Three realizations of a horizontal, rough-seafloor model.	240
4-9	Scattering coefficients for horizontal, rough seafloor with different correlation lengths.	246

4-10	Horizontal, rough-seafloor models with different rms heights.	248
4-11	Scattering coefficients for horizontal rough seafloor with different rms heights.	254
4-12	Gaussian vs. self-similar seafloor scattering.	256
4-13	Schlieren diagrams showing the wavefields at 160 m for rough seafloor ($ka = 6, k\sigma = 4$) with different homogeneous subseafloor velocity.	260
4-14	Schlieren diagrams showing the wavefields at 160 m for rough seafloor ($ka = 6, k\sigma = 0.5$) with different homogeneous subseafloor velocity.	262
4-15	15° scattering coefficients vs. compressional velocity.	264
4-16	Models with sloping smooth seafloor.	266
4-17	Scattering coefficients for sloping smooth seafloor.	270
4-18	Models with sloping rough seafloor.	272
4-19	Scattering coefficients for sloping rough seafloor.	278
4-20	Scattering coefficients vs. the 'effective grazing angle'.	280
4-21	Scattering coefficients of hard vs. soft rough sloping seafloor.	282
4-22	The effective Rayleigh roughness parameter as a function of the 'effective grazing angle' parameters.	284
4-23	Wire diagram of scattering coefficients vs. effective Rayleigh roughness.	286
4-24	Wire diagrams of scattering coefficients vs. effective Rayleigh roughness for different velocities, and a simple interpretation.	290
4-25	Realistic seafloor models with homogeneous subseafloor.	292
4-26	Scattering coefficients for Models 1-4 with sediment, talus, or basalt bottoms.	298
4-27	Estimating roughness parameters (ka and $k\sigma$ from scattering coefficients of realistic seafloor models.	304
4-28	Flat-seafloor models with subseafloor volume heterogeneity having 10% rms perturbation amplitude.	308
4-29	Multiple realizations of a flat basalt seafloor with volume heterogeneity having 10% rms perturbation amplitude.	312

4-30 Scattering functions for flat-seafloor models with 10% rms perturbation amplitude in velocity and density and different correlation lengths.	316
4-31 Flat-seafloor models with subseafloor volume heterogeneity having 50% rms perturbation amplitude.	318
4-32 Scattering functions for flat-seafloor models with different rms perturbation amplitude in velocity and density.	322
4-33 Rough-seafloor models with subseafloor volume heterogeneity.	324
4-34 Scattering functions calculated for rough seafloor with heterogeneous subseafloor.	328
4-35 Seafloor models with 45° large-scale slope, volume heterogeneity and with and without wavelength-scale roughness.	330
4-36 Scattering functions of sloping (45°) basalt seafloor with volume heterogeneity having different correlation lengths.	334
4-37 Comparison of scattering functions for hard (basalt) and soft (sediment) seafloor for different values of σ_v	336
4-38 Realistic seafloor models (Models 1-4) with heterogeneous subseafloor. .	342
4-39 Comparison of scattering functions for Models 1-4 with homogeneous vs. 10% and 50% rms perturbation in velocity and density volume heterogeneity.	348
4-40 Basaltic seafloor models with volume heterogeneity and gradients in the average velocity and density.	350
4-41 Scattering functions for models with gradients in subseafloor velocity and density.	352
4-42 Scattering functions for models with gradients in subseafloor velocity and density for different starting velocities and densities at the seafloor. .	354
4-43 Scattering functions of sloping, rough-seafloor models with homogeneous subseafloor compared to the same models with heterogeneous subseafloor and a gradient.	356
4-44 Models with heterogeneity defined as fault zones.	358
4-45 Scattering functions for Model 3 with and without faults.	362

4-46	Models 1-4 with realistic sediment, talus and basalt layers.	364
4-47	Scattering functions of Models 1-4 with sediment, talus and basalt layers.	368
5-1	Projections of beams from Segments 44 and 76 of the Site A (Run 1) monostatic reverberation experiment that intersect the location of the realistic model.	382
5-2	Site A acoustic reverberation beam data, Segments 44 and 76, intersecting the seafloor model location.	384
5-3	Site A acoustic reverberation beam data, Segments 44 and 76, interpreted as sediment, talus, and basalt.	386
A-1	Deep ocean sound speed profile at Site A.	394
A-2	Transmission loss estimation.	396

List of Tables

4.1	Velocity and density of sediment, talus and basalt.	216
4.2	A comparison of ka and $k\sigma$ calculated from bathymetry to estimates of ka and $k\sigma$ derived from scattering coefficients.	216
4.3	A comparison of $k\sigma$ calculated from bathymetry to estimates of $k\sigma$ derived from scattering coefficients when only large-scale seafloor slope is known.	217

Chapter 1

Introduction

The goal of this thesis is to develop a methodology to interpret sound scattered from the seafloor in terms of seafloor structure and subseafloor geological properties. Specifically, this work has been directed towards the interpretation of matched-filtered, beamformed monostatic (backscattered) acoustic reverberation data acquired on the west flank of the Mid-Atlantic Ridge (Figure 1-1) when the seafloor is insonified by a band-limited, low-grazing-angle acoustic pulse. The geological and acoustic data were acquired during the Acoustic Reverberation Special Research Program (ARSRP) (ARSRP Initial Report, 1993; Tucholke, 1991).

Mapping the structure and geology of the seafloor is an important objective of marine geology and geophysics. There are a variety of geophysical methods that use the analysis of sound waves that have propagated through the earth to interpret the structure and material properties of the earth. These methods use traveltimes, amplitudes and phases of transmitted, refracted, and reflected propagation modes for this interpretation. Interpretations of these data are primarily based on models in which geological properties vary over distances much larger than the sound wavelength. The resolution and depth of penetration of these methods depends on the frequency of the sound as well as the propagation characteristics of the material encountered. In ocean exploration, the reflection of high-frequency (kHz) sound (sonar) from the seafloor is used to map detailed bathymetry but does not penetrate very deeply into the subseafloor due to the rapid attenuation at these high frequencies.

Lower-frequency (<100 Hz) methods, such as seismic reflection and refraction profiling, penetrate much deeper into the subseafloor and are used to map subseafloor structure and velocity, but do not have the resolution to map the seafloor in detail. The interpretation of sonar and seismic data has defined much of what we know about the geological structure and properties of oceanic crust, lithosphere and upper mantle (Fowler, 1990).

However, mapping the seafloor with high resolution sonar and/or seismic methods, requires time and resources that are not usually available in most ocean exploration programs. Multi-beam side-scan systems, which rely on non-specular seafloor scattering, hold some promise of mapping the structure of large areas rapidly and of providing some information about subseafloor properties.

If variation in the structure of the seafloor or in the propagation properties of the subseafloor occurs at scales similar to the wavelength of the sound, a scattered field will be generated (Aki and Richards, 1980). In the analysis of most sound data used in geophysical exploration, sound that is scattered is considered 'noise' and an effort is usually made to eliminate it from the data. Although it is understood that this 'noise' is, in fact, the product of the interaction of the sound waves with geological heterogeneity, the analysis of these scattered signals is usually considered not necessary, or too complex, for adequate interpretation. There are exceptions to this, such as the migration imaging of diffraction scattering in reflection seismic processing, which uses the scattered signal to map abrupt structural changes, such as faults or pinchouts in subsurface layering. Also, all side-scan sonar systems used for mapping seafloor structure rely on sound backscattered from the seafloor. As geophysicists and geologists attempt more detailed interpretations of seismo-acoustic data, the interpretation of scattered energy will take on an increasingly important role.

The physical mechanisms of scattering from fluid-solid boundaries are not well understood. Scattering is a predictable result of the theory of elastodynamics for heterogeneous media, but calculating valid results for realistic (complex) models is a challenging task. Further, it has not been well understood how to define and con-

strain realistic heterogeneous geological models that accurately predict the observed scattered wavefields. If we are to further our understanding of scattering from the seafloor it is important to determine and distinguish the characteristics of geological heterogeneity that cause or strongly influence scattering.

Interpretation requires (1) that a valid acoustic field can be determined from a given model of the earth and (2) that the acoustic field can be quantitatively related, not necessarily uniquely, to variations in the earth model. If the distribution of the heterogeneity in the earth cannot be described by deterministic models then models with random or stochastic parameters must be used. However, when statistical models are used, an infinite number of model realizations can be defined that have the same statistical descriptions. For such models it is then necessary to determine the quantitative relationship between the acoustic field and the geological parameters, and to determine the sensitivity of this quantification to model realizations.

1.1 Background

Everyone has had the experience of listening to their echo. In some places a single shout produces multiple echos, and these echos tend to die off after a period of time. The echo or series of echos that is heard is an example of acoustic reverberation. Ol'shevskii (1967) describes acoustic reverberation in the ocean as "the time variation of the total scattered sound field observed at the point of reception following transmission of a sound signal". Monostatic reverberation is the scattered sound field that is observed when the receiver is co-located with the sound source, i.e., when we listen to our own echo, we are listening to monostatic reverberation. Scattered sound recorded at other locations is referred to as bistatic reverberation.

In the ocean, a significant source of scattering of low-frequency sound is the seafloor. Since the earliest experiments with long-range low-frequency transmissions of sound in the deep ocean basins, backscattering of low-frequency acoustic signals has been correlated with large high-standing bathymetric features (Baggeroer and Dyer, 1986). Long-range propagation occurs because of the upward-refracting sound-speed

profile that is typical of the deep ocean regions (Jensen et al., 1994). An example of a sound-speed profile in the Atlantic is shown in Appendix A. This profile is typical of deep-ocean sound speed profiles; in the first 1000 m or so of water depth the velocity decreases as the temperature of the water decreases, and then begins to increase with increasing pressure and nearly constant temperature. This low-velocity zone (the SOFAR channel) acts an acoustic waveguide, that can 'trap' sound initiated within the zone. Whether the sound becomes and remains trapped depends on its initial downward propagation angle and the depth of the water column. The propagation path can be thought of in terms of a continuous refraction cycle that turns sound upwards at great depth and then as it approaches the sea surface, turns the sound back down. Figure 1-2(a) illustrates this cyclic path. If the sound hits the seafloor anywhere in a cycle, some of the scattered sound will return to the source location along the original refraction path, where it can be recorded as the monostatic reverberation signal. Clearly, in very deep water this propagation path can continue for very great distances unless some high standing seafloor feature is encountered. Since all such features have rising flanks, the acoustic signals will almost always encounter such features near the bottom of a propagation cycle and therefore will interact with the seafloor at very low-grazing-angles. For the ARSRP experiments, the survey was designed such that the seafloor would be encountered within the range of the first few cycles of this propagation path. At Site A, the experiment was designed for scattering from the seafloor within the first turning cycle.

Scattering of low-grazing-angle sound waves from a very rough seafloor has traditionally been estimated by Lambert's Rule which states that the intensity of the backscattered (monostatic) field from a unit seafloor area is proportional to the intensity of the incident wavefield and the square of the sine of the grazing angle (Jensen et al, 1994). Some examples cited by Baggeroer and Dyer (1986) suggest that backscattering is a more complex process than can be explained or predicted by just grazing angle and insonification intensity. In one example they show that a very deep ridge in the Arctic Ocean, assumed to be below the main channel of sound propagation, produces backscatter signal as strong as a much shallower ridge, even though the

deeper ridge is presumably insonified by a much weaker signal. They also point out in this review paper that there are cases of high backscatter intensities that do not correlate with any high standing seafloor features. This suggests that strong scattering is caused by seafloor characteristics that do not require the presence of large-scale structural features.

Such observations raised many questions about backscattering in the deep ocean basins, and led to the initiation of the ARSRP (Acoustics Reverberation Special Research Program) in the early 1990's. A primary goal of this program was to develop an understanding of the mechanisms and characteristics of low-grazing-angle reverberation from the seafloor (Baggeroer and Orcutt, 1993). To a limited extent, a description of the research program and some of the initial results and analysis is published as part of a collection of papers in "Ocean Reverberation" edited by Ellis et al. (1993). Most of the details of the experiments performed, data collected and analysis approaches taken are included in cruise reports and symposia collections prepared for the funding agency, the ONR (Office of Naval Research).

The initial goal of the ARSRP was to collect monostatic and bistatic acoustic reverberation data and high resolution bathymetry data at selected areas within the Atlantic Natural Laboratory, an area of very rough seafloor on the western flank of the Mid-Atlantic Ridge. The system used to collect the reverberation data included a vertical linear array sound source that could be beam-steered to produce sound with a specific downward propagation angle (of the main lobe of the radiation pattern), and a horizontal linear array of receivers that was used to record and beamsteer the received reverberation signal to reduce directional ambiguity. Most of the publications showing analyses of the reverberation data have so far been directed toward solving some of the technical problems associated with the data. There are a number of issues that must be resolved before acoustic reverberation data can be used effectively to interpret seafloor characteristics. The first issue is how to map the acoustic signals to their corresponding seafloor locations, i.e., the locations of the scattering targets must be determined. The range to the seafloor depends on the initial downward propagation angle of the sound source, the sound speed profile of the water column,

and the depth of the seafloor. The azimuthal direction, from the source to the seafloor location, is reduced to a left-right ambiguity after the recorded data is beamsteered. The geometry of the monostatic reverberation experiment is illustrated in Figure 1-2(b). Reducing this left-right ambiguity in the data has been addressed by some researchers (e.g. Preston et al., 1990; Makris, 1993) but it is not yet fully resolved. Much of the published analysis of ARSRP data has been focused on determining the seafloor locations that correspond to the reverberation signals for monostatic and bistatic experiments (e.g. Makris and Berkson, 1994, Makris et al., 1995, and Smith et al., (1996)).

Another issue in the analysis of acoustic reverberation data acquired with beamsteered source and receiver arrays is the size and shape of the seafloor area (the beam footprint) corresponding to individual time series samples. In other words, what is the resolution of the data? Raw reverberation data is omnidirectional, i.e., signals received from all directions are recorded together. In order to constrain the range the acoustic reverberation signal is processed using match-filter processing techniques (Baggeroer et al., 1988). This processing generates a resolved signal but also reduces it to a time series with amplitude proportional to the energy of the scattered signal, rather than amplitude of a propagating acoustic wavefield. The resolution of reverberation data that has undergone match-filter processing can be specified in terms of a time (range) resolution that is dependent on the source frequency bandwidth. Beamforming processing is then used to reduce the directional ambiguity of the data. The azimuthal resolution is dependent on the spatial characteristics of the receiver array. In general, the beam footprint (range resolution \times azimuthal resolution) can be considered a well defined parameter that varies as a function of range and water depth in a predictable way. However, as pointed out by Elisseeff (1995), in an analysis of ARSRP experiments, deviations in the geometry of the receiver array from specifications in the beamforming process produce substantial variations in the size and shape of the insonifying beam footprint. The problem with a variable beam footprint, in particular one that is unpredictable, is that variations in scattered signal intensities associated with variation in the seafloor target area cannot be separated from

variations caused by seafloor characteristics. A system that accounts for variation in beam footprint needs to be included in the processing of the reverberation data before the data are interpreted.

Another important technical issue is whether variation in the intensity of the insonification field is sufficiently accounted for by the sonar equation. All analyses of reverberation data use some form of the sonar equation to correct for transmission loss, initial source intensity levels, variation in the scattering target area (beam footprint), and the directivity of the receiver array (Jensen et al., 1994). An example of the sonar equation correction is described in Chapter 2 of this thesis. The sonar equation, however, may not account for all spatial variations in the intensity within the insonifying beam. In the context of the sonar equation, it can be argued that variation in scattering can only be interpreted if the insonifying wavefield is uniform. Most analysis of acoustic reverberation assumes that the insonification is spatially uniform, at the scale of the beam footprint. Given the long propagation distances involved in acoustic reverberation, it seems unlikely that very strong spatial variation in the wavefront, at the scale of the beam footprint, will be present. However, significant variations in beam intensity that depend on range and azimuth from the source, not fully corrected for by the sonar equation, are possible. If the insonification has spatial variation, this may produce variation in the scattered field that cannot be distinguished from variations caused by seafloor characteristics. Hopefully, future research will yield processing techniques capable of removing any such variability from the reverberation signals.

Very few efforts have been made to explain the variation of low-grazing-angle acoustic reverberation signals in terms of seafloor characteristics. Dyer et al. (1993) proposed that the backscatter is produced by scattering from seafloor facets that are within a few degrees of being normal to the incident wavefield. In this theory, facets that are at least a wavelength in size will be 'self-selected' as the dominant source of backscattered signals. In essence, this is similar to the idea that scattering is dominated by wavelength-scale features, except for the added emphasis on facet orientation. This model seems to be the basis for the suggestion by Makris et al.

(1995) that the strongest reverberation signals are returned from scarps on seafloor ridges that face the source direction.

Most interpretations of reverberation data assume that scattering can be explained by Lambert's Rule. An example of this type of interpretation for ARSRP data is given by Caruthers et al. (1997). Assuming a uniform insonification, Caruthers et al. (1997) attribute all variations in scattering to variations in local grazing angle which can, in turn, be defined as a function of local seafloor slope. However, the scale over which the slope is estimated in such interpretations is usually much larger than the incident wavelength, such that the characteristics of the seafloor that would most strongly effect the scattered field are not accounted for.

In an effort to provide a more theoretically satisfying explanation of the signal variations observed in acoustic reverberation data, a number of researchers associated with the ARSRP project have applied wave equation modeling to demonstrate the scattering of low-grazing-angle incident wavefields from the seafloor. Stephen and Dougherty (1993) compared scattering from rough seafloor defined with elastic versus acoustic properties. They also demonstrated the effects of sediment cover over a rough basalt basement. Their results showed that it is important to treat the seafloor as a fluid/elastic boundary since the existence of shear body-waves and interface-waves, and the re-scattering of these waves back into the water column are an important component of the total scattered field that is not predicted using acoustic models. In particular, secondary scattering of Stoneley waves is shown to be an important source of energy in the backscattered wavefield. They also show that sediment cover significantly decreases the amount of energy that is scattered into the water column, suggesting that the geological properties of the subseafloor may be predicted from the scattered signal. Robertsson and Levander (1995) investigated the effects of sediment velocity, attenuation and thickness on bottom scattering and came to the same conclusion, i.e., that sediment cover, even thin sediment cover on the order of a wavelength in thickness, strongly reduces the backscattered signal. They also re-confirm that Stoneley waves interacting with the rough seafloor are an important source of scattered energy. Stephen and Swift (1994) showed that scattering from

a wavelength-scale facet on the seafloor is dominated by diffraction scattering from the corners of the facet and that 'back-reflection' and transmission are not important components of the scattered field.

In order to thoroughly investigate the origins or mechanisms of scattering from the seafloor, it is also necessary to consider scattering from volume heterogeneity in the subseafloor. Dougherty and Stephen (1988) identify the mechanisms of volume scattering and show that this scattering varies with the spatial scale (quantified as the correlation length of the velocity/density distribution) of the volume heterogeneity. Swift and Stephen (1994) apply the same techniques to investigate and quantify volume scattering, below flat seafloor models, when the incident wavefield has been constrained to a Gaussian pulse beam incident at a low grazing-angle. The Gaussian beam used as the source wavefield approximates the insonification in acoustic reverberation experiments. Their results suggest that volume scattering is an important source of energy in the backscattered signal.

1.2 Thesis Outline

This thesis is directed toward determining what characteristics of the seafloor and subseafloor can be interpreted from the acoustic backscatter reverberation signal, if the incident wavefield is a low-grazing-angle pulse-beam. The primary goal has been to investigate and quantify the sensitivity of the scattered signal to variations in seafloor structure and elastic properties of the subseafloor.

It has not been the object nor intention of this thesis to resolve the technical issues about the corrections and processing necessary to make use of acoustic reverberation data for geological interpretation. The view has been taken that as research on acoustic reverberation continues, these issues will be successfully resolved, i.e., the seafloor locations, resolution, and characteristics of the insonification field will be accurately determined.

The suggestion that the backscattered reverberation signal intensity is a function of seafloor slope and orientation is a common theme in all analyses of reverberation

data. Chapter 2 of this thesis (Greaves and Stephen, 1997) is an attempt to test these ideas quantitatively. Within this context, monostatic reverberation data corresponding to two geologically distinct seafloor areas, inside-corner and outside-corner oceanic crust, is analysed in terms of variations in intensity compared to variations in seafloor slope and slope orientation, measured at the scale of the insonification beam footprint.

In order to establish constraints on seafloor and subseafloor models to be used in developing an interpretation of scattering, an effort was made to determine the parameters of a 'typical' seafloor on the flanks of the Mid-Atlantic Ridge in the area of the ARSRP experiments. A model is developed in Chapter 3 from a combination of high and very high resolution bathymetry data within the Site A experiment region (see Chapter 2 for the location of Site A), from descriptions of seafloor photographs in the same area, and from published descriptions of subseafloor properties of oceanic crust of similar geological age and history. The primary motivation for the development of research in this chapter was the desire to constrain the modeling necessary for the sensitivity study in Chapter 4 to the most realistic structural and elastic parameters expected for seafloor in this area. In the process of developing this model, it became clear that, in reality, very little is known about the details of seafloor structure and particularly about the upper-most subseafloor geology. This suggests that the development of interpretation techniques for acoustic reverberation data in terms of these characteristics will be of great practical value in marine geological mapping.

In any study of scattering, the scale over which wave propagation parameters vary in the propagation medium is very important. In the study of scattering from the seafloor two spatial scales are of primary interest. As described by Goff and Jordan (1988), seafloor structure can be considered a linear combination of features that are either large scale, and usually considered deterministic, or small scale, and adequately described by stochastic distributions. In this thesis, large-scale features are those geological characteristics that vary over distances more than an order of magnitude greater than the wavelength of the insonification. Wavelength-scale features are defined in terms of the characteristic parameters of stochastic spatial distributions.

Chapter 4 of this thesis is a detailed study of the sensitivity of the scattered field intensity, in particular the monostatic backscattered intensity, to variations in both seafloor structure and subseafloor elastic material properties. To make this quantification, the scattered wavefields generated by a wide variety of seafloor models with different seafloor (interface scattering) and subseafloor (volume scattering) characteristics are calculated. The scattered wavefields are calculated using the Numerical Scattering Chamber (Stephen and Swift, 1994) that is a finite-difference numerical wavefield solution to the elastic wave equation. Scattering intensity is quantified in terms of well defined parameters of stochastically defined interface and volume heterogeneity. The effects on scattering caused by variation in deterministic properties, average seafloor slope and subseafloor velocity and density, are also quantified. Much of the stochastic modeling is repeated for multiple realizations to determine the level of signal variation that can be resolved and attributed to variations in the stochastic model parameters. Rough seafloor models with and without subseafloor volume heterogeneity are compared to determine the relative importance of seafloor (interface) scattering and subseafloor (volume) scattering. The results of the sensitivity study are then used to consider the interpretation of scattering from the realistic seafloor model of young outside-corner crust developed in Chapter 3.

1.3 Contributions

The main contributions of this thesis to marine geology and geophysics are as follows:

Chapter 2: The view of scattering embodied in Lambert's Rule, that acoustic reverberation is primarily a function of deterministic seafloor slope, is put to a quantitative test. The results suggest that variations in scattered field intensity are not quantitatively explained by such a simple deterministic model. Therefore, the actual wavefield scattering effects of rough and heterogeneous seafloor must be included in the interpretation of reverberation data.

Chapter 3: A realistic seafloor model, with constraints on structural and elastic properties is defined. This model is considered typical of the very rough seafloor

found on the flanks of slow-spreading ridges, particularly in outside-corner crustal areas. This model could be used in future studies of scattering as a baseline model for further development of interpretation techniques.

Chapter 4: The sensitivity of backscattered acoustic reverberation to seafloor stochastic roughness and subseafloor volume heterogeneity parameters (rms amplitude and correlation length) is quantified. The influence of deterministic seafloor parameters (seafloor slope and average subseafloor velocity and density) on scattering is also quantified. A new 'effective grazing angle' is defined that incorporates both large-scale seafloor slope and the stochastic roughness parameters. This effective grazing angle is found to be useful when included as a parameter in the calculation and interpretation of the Rayleigh roughness parameter. Scattering from subseafloor volume heterogeneity is shown to be much less significant than scattering produced by seafloor roughness. A method of estimating stochastic roughness from the backscatter intensity is described.

Figure 1-1: ARSRP (Acoustic Reverberation Special Research Program) site locations on the west flank of the Mid-Atlantic Ridge are marked on this bathymetry map. Red contours indicate the shallowest seafloor areas and blue the deepest seafloor. A variety of monostatic and bistatic reverberation experiments were carried out at these locations (A-D) in 1993. The research in this thesis has focussed on interpreting monostatic reverberation data acquired at Site A. Site A is located on the south side of the trace of a small-offset discontinuity in the ridge, on outside-corner oceanic crust. This region is about 400 km north of the Kane Fracture Zone.

ARSRP SITE MAP

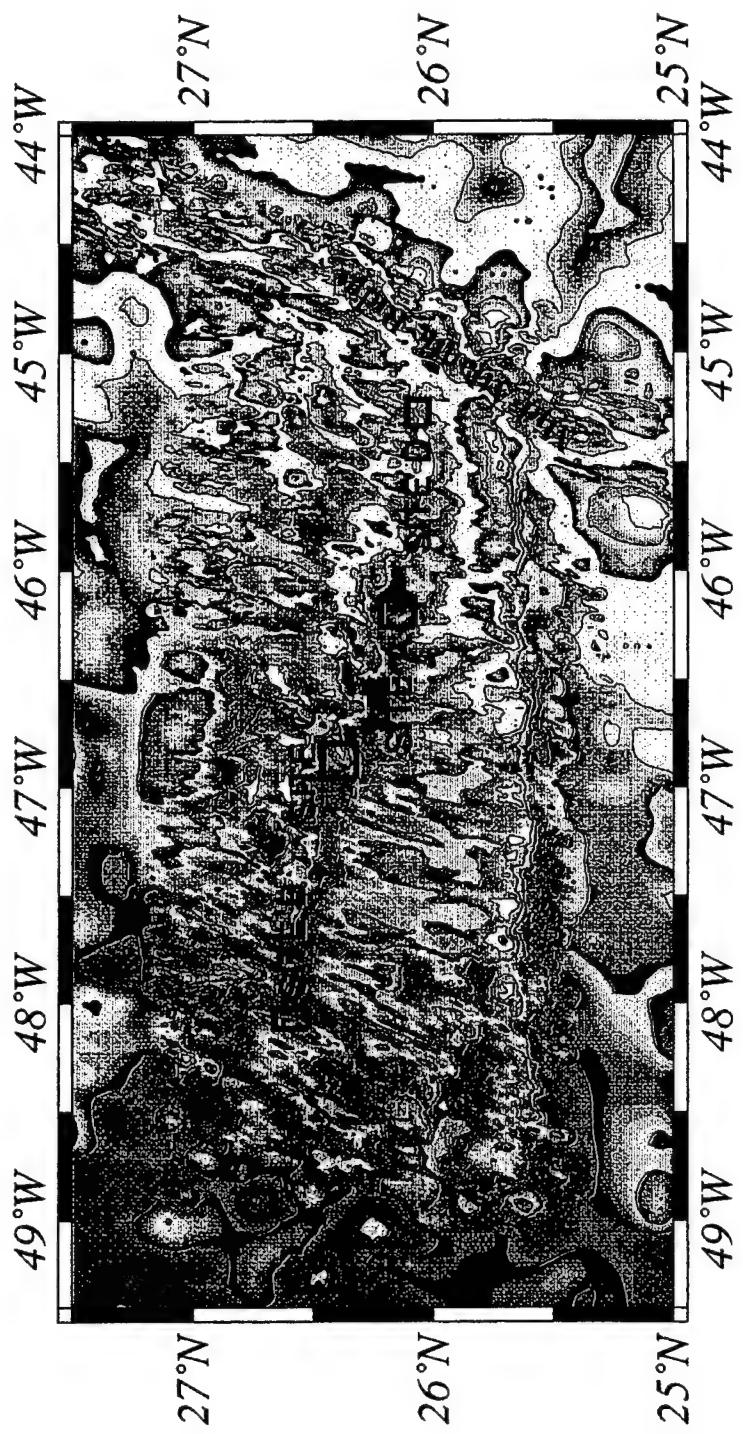
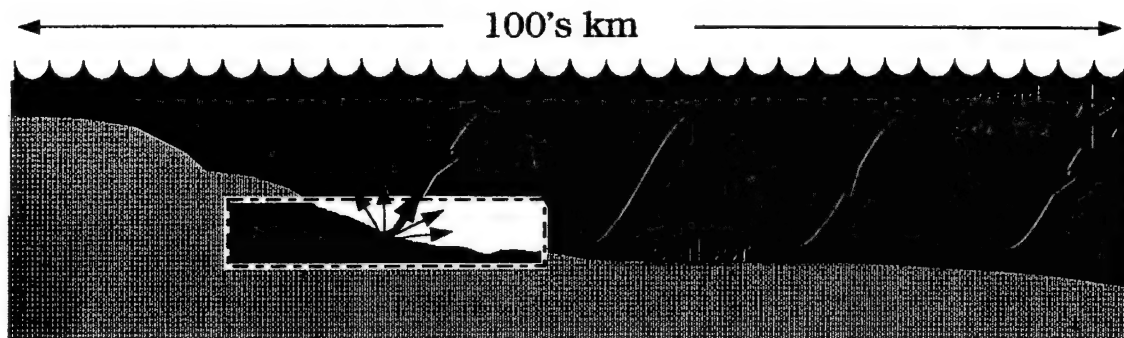


Figure 1-2: (a) The monostatic acoustic reverberation travelpath in the deep ocean. Sound, 'trapped' in the acoustic waveguide formed by the low-velocity zone (SOFAR channel) in the deep ocean sound-velocity profile, follows a cyclic propagation path. Propagation will continue over very long ranges until striking the seafloor. Some of the sound scattered from the seafloor will follow the original travelpath and return to the source location, where it is observed as monostatic acoustic reverberation. For the ARSRP experiments, the survey was designed such that the seafloor would be encountered within the range of the first few cycles of this propagation path. At Site A, the experiment was designed for scattering from the seafloor within the first turning cycle.

(b) In plan view the monostatic reverberation experiment geometry consists of a sound source and a receiver array that are approximately co-located. Matched filtering of the recorded sound provides a range resolution in locating the seafloor origin of the scattering. Data recorded on a linear array of receivers can be beamsteered to reduce the data to specific beam directions, with only a single (left-right) ambiguity in direction referred to as the beam and its opposite-side beam. The intersection of beamwidth and the range resolution defines the beam footprint of the insonifying sound source.

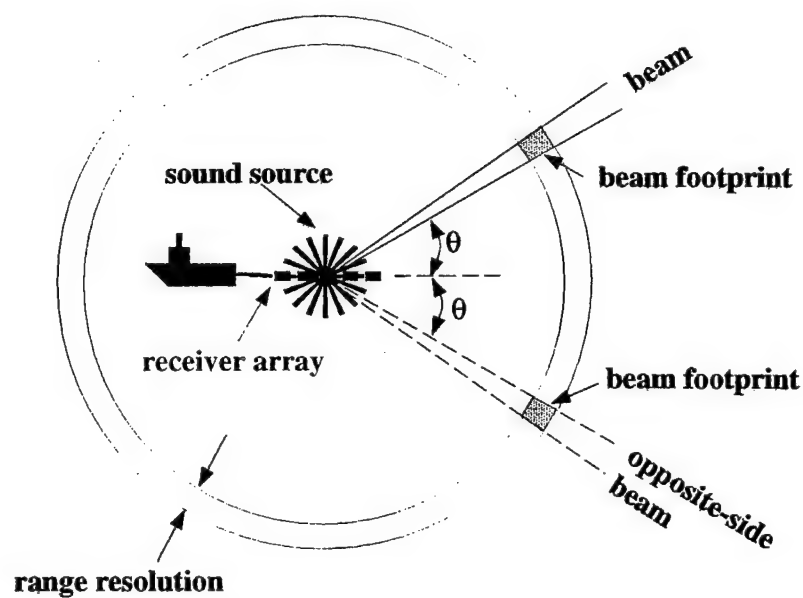
(a)

Long Range Backscatter



(b)

Monostatic Reverberation Geometry



Chapter 2

Seafloor acoustic backscattering from different geological provinces in the Atlantic Natural Laboratory¹

2.1 Abstract

The characteristics of acoustic signals backscattered from inside-corner and outside-corner oceanic crust are investigated using acoustic reverberation data from the 1993 Acoustic Reverberation Special Research Program (ARSRP) Acoustics Cruise. Specifically, we compare the seafloor dip distribution, as measured from Hydrosweep bathymetry data, in areas of each crustal type and look for a correlation between seafloor dip and seafloor scattering strength. Beamformed and matched-filtered acoustic data from the Site A (Run 1) monostatic, wideband, LFM (linear frequency modulated) experiment are used to find the scattering strength corresponding to specific areas of the seafloor. Scattering strength is determined as the average of intersecting

¹Reprinted with permission from, Greaves, Robert J. and Stephen, Ralph A., "Seafloor acoustic backscattering from different geological provinces in the Atlantic Natural Laboratory", *Journal of the Acoustical Society of America* 101(1), 1997, pp 193-208. Copyright 1997 Acoustical Society of America.

beams from different source locations in order to reduce the left-right ambiguity inherent in beamsteering of a linear array. When overlaid on the bathymetry map, high scattering strengths are found to correspond to steep flanks of seafloor features and can be used to determine their shape and orientation. Some of these feature shapes are characteristic of specific crustal regions. Cross-plotting scattering strength with true grazing angle or seafloor dip shows a trend increasing at a rate of about 0.1 dB/degree. This trend is not, however, sufficiently constrained to be a useful predictor. We conclude that the seafloor dip, on the scale of a few hundreds of meters, that can be resolved with Hydrosweep bathymetry data, influences but does not determine, scattering strength. Since the observed variations in scattering strength are larger than can be explained by data error or seafloor dip, we suggest that other characteristics of steeply dipping areas, such as variations in subsurface properties or smaller-scale surface features, (particularly wavelength scales) strongly affect the level of backscattered signals.

2.2 Introduction

In this study we compare acoustic reverberation signals backscattered from inside-corner and outside-corner oceanic crustal regions, which border the trace of a second-order ridge discontinuity on the western flank of the Mid-Atlantic Ridge (MAR). Inside-corner (IC) and outside-corner (OC) refer to the place of origin of oceanic crust relative to the intersection of mid-ocean ridges (MOR) and ridge discontinuities, shown schematically in Figure 2-1. MOR's with slow spreading rates (1-5 cm/yr), such as the MAR, characteristically produce IC and OC crust with distinct, and in some cases, dramatic, differences in seafloor structure and composition (Tucholke and Lin, 1994; Severinghaus and MacDonald, 1988; Karson and Dick, 1983). In particular, large scale features of OC crust produced at slow spreading ridges tend to be strongly lineated and have low relief while IC features tend to be blocky and have higher relief.

The data we use are from the Acoustic Reverberation Special Research Program (ARSRP) 1993 Acoustics Cruise which was funded by the Office of Naval Research.

During this cruise, a variety of acoustic reverberation experiments were conducted over several sites on the western flank of the MAR (ARSRP Initial Report, 1993). All of these sites lie along the trace of a second-order discontinuity and within a region on the west flank of the MAR referred to as the Atlantic Natural Laboratory (Tucholke, 1991). We analyze beamformed and matched-filtered monostatic reverberation data acquired during the Site A (Run 1) experiment. Site A and the locations from which these data were recorded are shown in Figure 2-2. We chose, for comparison, the three seafloor areas labelled as Site A (OC crust), Syrian Knob (IC crust) and Casa Grande (IC crust).

An hypothesis of the ARSRP research community is that backscattered signals from IC crust are characteristically different than those from OC crust. Specifically, it has been suggested that OC crust will produce less monostatic, low-angle backscattering than IC crust. This hypothesis is primarily based on the ideas that, 1) for a fixed incident wavefield grazing angle, the scattering strength increases with increasing seafloor dip (i.e. increasing true grazing angle) and 2) that IC crust has more steeply dipping features than OC crust. The hypothesis presumes that other seafloor properties, such as the thickness of sediment cover or subseafloor rock properties, have less effect than seafloor morphology on backscattered signals.

In our analysis, we look for a quantitative correlation between seafloor scattering strength, determined from low grazing-angle backscattered signals, and the measured seafloor dip as a method for distinguishing IC and OC crustal areas. A preliminary step is to find the correlation between scattering strength and true grazing angle. True grazing angle is defined as the angle between the incident wavefield propagation vector and the plane defining the local seafloor dip. We use Hydrosweep bathymetry data, which has a nominal lateral resolution of 200 m at the water depths in the study area (Kleinrock, 1992), to define seafloor dip. Several studies have shown that there is a general correspondence between strong backscattered signals and large seafloor structural features. Makris et al. (1995) have done detailed analysis of low-angle backscatter data at a site farther to the west and found very good correlation of strong backscatter signals to seafloor ridges in the 1/2 CZ (convergence zone: a full

CZ is the distance at which an acoustic wavefield is refracted and turned at depth by the ocean acoustic velocity gradient, and returned to the sea surface) and 1 1/2 CZ ranges, but they did not determine an explicit relationship between intensity and seafloor dip. Preston et al. (1990) found that seafloor returning high backscattered signals corresponded with the increasing slopes of high-standing seafloor features for CZ's as distant as 400 km from the source and receiver arrays. Stephen et al. (1993) mapped individual beam (the acoustic time series computed for a particular direction by beamsteering the linear receiver array) data sets onto one of our study areas (Site A) and showed a similar correspondence between steep dip and high-intensity backscatter. Using the same acoustic data, but finer-scale bathymetry data, Shaw et al. (1993) found that high-intensity backscatter mapped to areas with the strongest bathymetric gradient. However, they used data from single source locations and did not account for the left-right ambiguity of beamsteered monostatic reverberation data. In our analysis, we combine signals backscattered from each seafloor location from different source locations, before relating them to seafloor dip. This combination of intersecting beams acts to reduce directional ambiguity. Similar techniques have been shown to be effective in reducing left-right ambiguity in the analysis of monostatic reverberation data by Makris et al. (1993) and Preston et al. (1990).

In Figure 2-3 we summarize some of the possible quantitative differences in scattering that could be observed and related to crustal regions. If we take the incident beam grazing angle to be constant, then changes in true grazing angle are due to changes in seafloor dip. If scattering strength increases with increasing dip, and if IC and OC crust have distinct distributions of seafloor dip, then we might expect a result similar to Figure 2-3(a). If the two crustal areas have similar seafloor dip distributions but have different scattering strengths we could see results similar to either Figure 2-3(b) or 2-3(c). If the dip distribution and scattering strength are both similar, then we are not likely to be able to distinguish the crustal types on this basis, as suggested by Figure 2-3(d), however, qualitative characteristics, such as seafloor feature shape determined by simply mapping acoustic backscattering, may still be useful in identifying different crustal regions.

2.3 Geological Setting

Site A lies on outside-corner (OC) crust formed about nine million years ago at a second-order discontinuity on the MAR about 400 km north of the Kane Fracture Zone (Tucholke et al. (1993)). Discontinuities occur frequently along mid-ocean ridges, dividing them into short ridge segments. Displacement of ridge segments occurs between segment ends producing a tectonically active region where crustal plates move in opposite directions. The trace of each discontinuity is marked by a bathymetric low extending into the ridge flanks and generally can be mapped by tracing the axis of maximum depth (AMD). In most cases, these are the deepest features along the ridge system and contain the largest sediment 'ponds'. In general, offset displacement at a discontinuity of more than about 30 km is caused by the strike-slip motion of a transform fault and is referred to as a transform discontinuity. Smaller offsets are indicative of active displacement due to more complex crustal deformation and are referred to as second-order (Tucholke and Lin, 1994) or in cases where no offset is observed, as zero-offset discontinuities (Schouten and White, 1980). Inside-corner (IC) crust refers to the crust found on the side of the ridge where the discontinuity is active (i.e. between the ends of adjacent ridge segments) (see Figure 2-1). Crust on the opposite side of the ridge, where there is no active faulting in the discontinuity, is called outside-corner (OC) crust.

IC crust formed at slow spreading MOR's, is initially significantly higher than the adjacent OC crust. IC and OC crust formed at second-order discontinuities have elevation differences equal to, or greater than, those observed at transform discontinuities (Severinghaus and MacDonald, 1988; Karson and Dick, 1983). As young crust moves away from the spreading center it subsides as thermal cooling of the lithosphere takes place and uplifting forces are reduced. Along transform discontinuities, there will be a substantial elevation difference by the time IC and OC crust become coupled in the fracture zone. Contrary to this, IC crust formed at second-order discontinuities spends relatively little time in the active displacement zone, so that much less subsi-

dence of the original high elevation occurs before it becomes coupled to the OC crust, resulting in a much smaller elevation difference between IC and OC crust away from the ridge. Once the crust moves away from the MOR axis, subsidence lowers both IC and OC regions, but some difference in elevation between them remains locked in place as the plate moves far from the spreading center. This is important in our consideration of seafloor dip as a distinguishable characteristic of crustal type. If we lift a corner of two equal areas of seafloor, but lift one (IC) higher, we can predict that either the average seafloor dip of the region lifted higher will be larger, or that a larger number of faults, or larger faults, will occur on the IC crust. On a regional basis, the OC crust around Site A, which is located about 100 km west of the MAR, is expected to have lower elevations and, on average, fewer or smaller fault scarps than the adjacent IC crust.

A strong morphological distinction between IC and OC crust is that OC crust tends to have highly lineated, large-scale features, while IC crust shows a more blocky structure (Karson and Dick, 1983). The linear features on OC crust are dominated by long ridges that persist for tens of kilometers (equal to at least the half-length of the ridge segment) and trend parallel to the MOR. Over large areas, repetition of the ridges gives OC crust a corrugated appearance. Where they intersect the AMD, they slope downward and end as distinctive 'toes' along the edge of the sediment pond (e.g Alpha Ridge and Blackjack Ridge in Figure 2-2). These ridges are asymmetric in cross-section with the steep side commonly facing the MOR axis. In general, ridges on OC crust are not formed by single faults but are made up of groups of normal faults formed in colinear sequences as blocks of new crust rise from the rift valley. As the blocks rise they tilt away from the spreading center in response to tectonic extension. Individual faults may be quite steep ($70^\circ - 90^\circ$) with short scarp heights, on the order of tens of meters (Tucholke and Lin, 1994). Even though individual faults can be very steep, the dip of the seafloor averaged laterally over hundreds of meters, is much less, on the order of $20^\circ - 45^\circ$.

Long lineations are not characteristic of IC crust. Tucholke and Lin (1994) observe that IC's have one grouping of very steep ($70^\circ - 90^\circ$) and large displacement (> 150 m)

normal faults that face parallel to the rift valley and another grouping of somewhat less steep ($20^\circ - 60^\circ$) faults facing either the rift valley or the ridge-discontinuity intersection. The combination of faulting leads to the blocky structure of IC Crust. The region north of Site A and the sediment pond is dominated by large irregular blocks (with sides extending up to 10 km in length) characteristic of IC crust (Figure 2-2).

In addition, IC and OC crust differ in the type of rock recovered from the seafloor. Tucholke and Lin (1994) summarized rock sample data collected along the MAR. These data suggest that OC crust is almost uniformly covered by volcanic rock (basalt). In contrast, in IC areas, plutonic and ultramafic rocks, in particular gabbro and partially serpentinized peridotites, are frequently recovered in addition to volcanic rocks. They conclude that IC's have anomalously thin oceanic crust and that, to a large extent, the upper (volcanic) layer of normal oceanic crust is missing. Differences in scattering strength from IC and OC crustal regions that could not be associated with large scale seafloor morphology might be related to variations in surface and volume properties between basaltic and gabbroic seafloor.

Sediment thickness has a strong effect on the backscattered field. This has been shown clearly in model studies by Robertsson and Levander (1995) and Stephen and Dougherty (1993), who demonstrated that increasing sediment thickness decreases the backscattered signal. We know of no evidence suggesting that IC and OC (of similar age) have characteristically different sediment thickness. However, we might reason that more steeply dipping areas will hold less sediment and more sediment in local bathymetric lows. On a regional basis, IC crust might be expected to have more steeply dipping areas than OC crust, suggesting that IC crust areas will have a stronger scattering than OC crust regions.

2.4 Data

2.4.1 Acoustic Data

The acoustic reverberation data used in this analysis were collected during the Site A (Run 1) monostatic experiment on board the R/V Cory Chouest. The ARSRP monostatic experiments only approximated the monostatic experiment geometry, because the source and receiver were separated by a horizontal distance of 1.174 km (ARSRP Initial Report, 1993, pg. 106) and the research vessel from which they were deployed was underway (≈ 3 knots) during the data acquisition. Below, we show that accounting for the difference in source and receiver positions is important in analysing 1/2 CZ data, but the correction for the moving ship is small and is neglected.

The acoustic source used for these experiments is a vertical line array (VLA) of ten piezoelectric flexensional acoustic projectors spaced 2.29 m apart. The depth to the center of the VLA for the Site A experiment was 184 meters. Time delays were applied to the ten sound projectors to effectively steer the central beam of the source radiation pattern downward at an angle of 9° from the horizontal. The receiver array consisted of 128 hydrophone groups spaced every 2.5 m in a horizontal line array (HLA). Two of the hydrophones were de-sensitized for source monitoring. The receiver array was towed at depths that varied from 130 to 170 m with the center of the array approximately 1 km from the stern of the ship (ARSRP Initial Report, 1993, p. 278-284). The average depth of the receiver array was 155 m.

To generate a source pulse, the VLA is driven with an LFM (linear frequency modulated) five-second sweep over the frequency band from 200 to 255 Hz. After the backscattered signals are received by the HLA, they are beamformed and matched-filtered on the ship. The beamforming process generates 126 directional beams, each associated with two directions (left-right ambiguity) symmetric about the original receiver array axis. The 0° and 180° beams (endfire) are in-line with the receiver array axis and the 90° beam is the broadside beam. Angular beamwidth varies with beam direction, increasing toward the endfire directions. Beams within 30° of the endfire beams ($0 - 30^\circ$ and $150 - 180^\circ$) were not included in our analysis because they

have much larger beamwidths and are strongly affected by array movement and ship noise.

Time-series data recorded at each source/receiver location were reported, after shipboard processing, in units of the square of the pressure amplitude (μPa^2) observed at two-way traveltimes. These data are corrected in our processing for transmission loss and source beam pattern before they are treated as measurements of seafloor scattering strength. An important acquisition parameter is the consistency of the source strength. The calibrated source level at the time of the Site A (Run 1) experiment is specified as 230 dB (re: $1\mu Pa - 1 m$) (ARSRP Initial Report, 1993, p. 217). Data from the source-monitor hydrophone showed that the source level was very stable with a maximum observed variation of 0.4 dB from the mean but an average deviation of only +/- 0.14 dB.

The HLA has a nominal broadside beamwidth of 1.1° at 250 Hz (ARSRP Initial Report, 1993). This is an important number because it is used to describe the azimuthal resolution of the beamforming system. It has been suggested (A. Baggeroer, personal communication, 1994) that the actual broadside beamwidth may be as large as $2^\circ - 3^\circ$ due to a few inoperative hydrophones and bending of the HLA (Elisseeff, 1995).

The range (time) resolution of the beam data is estimated from the width of the central peak of the autocorrelation of the source function. The width of this peak is inversely proportional to the bandwidth of the source. For the bandwidth of these data (200-255 Hz), the range resolution is estimated to be 13.6 m (ARSRP Initial Report, 1993, p. 145).

2.4.2 Bathymetry Data

The bathymetry data used in the analysis are from a Hydrosweep multi-beam survey conducted as part of the 1992 ARSRP Geology and Geophysics Reconnaissance Cruise (ARSRP, 1992). We use the bathymetry data as a grid of 200 m-spaced samples interpolated from the original swath data.

Kleinrock (1992) describes the horizontal resolution of the Hydrosweep multibeam

bathymetry system as approximately 134 x 134 m in the region nearest the nadir and 187 x 256 m in regions reached by the outermost beams, for a water depth of 3500 m. Depth resolution is considerably better and is estimated to be about 20 m. Lateral variation in seafloor features on the scale of 200 m can be detected but practical feature resolution is on the order of 500 m. Grindlay et al (1992) also review high-resolution multi-beam systems and conclude that multibeam data (such as Hydrosweep) cannot resolve individual seafloor features less than about 200 m and slopes of steep flanks that are greater than 45°. Tucholke and Lin (1994) suggest that steep slope ($> 30^\circ$) areas, determined by multi-beam data, are indicative of average slopes over hundreds of meters, which may include small-scale features with steeper dip. Based on these studies, we consider the nominal resolution of the Hydrosweep data to be 200 m, and treat each bathymetry value as the average depth value within a 200 m diameter circle on the seafloor.

2.5 Data Processing

The objective of the data processing is to transform the 'raw' acoustic data into seafloor (interface) scattering strength. We also calculate the dip of the corresponding seafloor location and the true grazing angle of the incident acoustic wavefield.

An initial review of the scattered signal levels from Site A showed a strong dependence on source azimuth relative to the strike of large-scale features. Therefore, we chose to separate the data into two groups, each having similar source azimuth relative to Site A. One group is to the northeast of Site A (see Figure 2-2) and we call this the North Source Group. The other area is to the east of Site A and we call this the South Source Group.

We make some approximations in our treatment of the backscatter and bathymetry data. First, an approximation is made to account for transmission loss and spatial beam pattern. The exact local beam 'footprint' intensity variation is not accounted for, i.e., we assume that within each beam footprint, the seafloor is uniformly insonified. Second, by stacking intersecting beam signals we reduce the left-right ambiguity

by enhancing repeated scattering. By stacking the data, however, we lose some sensitivity of signal level to seafloor dip and details of signal variability as a function of source azimuth. Third, we do not account for the possibility of multiple scattering between different patches of seafloor. Fourth, we approximate the seafloor dip within a particular beam footprint by a single seafloor dip value extracted from the Hydrosweep data. We also limit analysis to scattering from offset ranges between 10 and 25 km and depths from 3200 to 4500 m and we do not use any beams within 30° of endfire.

The backscattering of CW (monochromatic continuous wave) acoustic signals from a nearly planar surface is described by the active sonar equation (Urick, 1983),

$$RL_s = SL - TL + TS \quad (2.1)$$

where RL_s is the observed signal level; SL is the initial source level; TL is the two-way transmission loss during propagation from source to target and target to receiver and includes the effect of the source beam pattern; and TS is the equivalent target strength of the scattering interface (seafloor). For broad-bandwidth data, equation (1) is descriptively correct, but in application it requires integration over the frequency band. If phase information is retained in the integration, we obtain the 'coherent' broadband result; if phase information is ignored, we obtain the 'incoherent' broadband result (Jensen et al., 1994, p. 158-161).

In this study, the 'raw' data are the matched-filtered beamformed time series which correspond to RL_s . Although there are no actual 'targets' on the seafloor, seafloor scattering appears to be discrete (i.e. some seafloor features backscatter more than others). The equivalent 'target strength', TS , of specific patches of seafloor is defined as

$$TS = S_s + 10 \log_{10} A \quad (2.2)$$

where S_s is the seafloor scattering strength and the approximate beam footprint area, A , is given by

$$A = r \Delta r \Delta \theta \quad (2.3)$$

where r is the range offset, Δr is the range resolution and $\Delta\theta$ is the azimuthal resolution of the beam.

2.5.1 Transmission Loss

We make two corrections for transmission loss. The first is a correction for the source spatial beam pattern and geometric spreading. The second, discussed further in a later section, is the removal of signals that appear to originate from areas shadowed from the incident beams by local bathymetric features.

For calculating the seafloor scattering strength (S_s) from the observed backscattered signal level (RL_s) we use the approximation

$$S_s \approx RL_s - SL + TL_{cyl}^{src} + TL_{cyl}^{rec} + TL_o - 10 \log_{10} A \quad (2.4)$$

where TL_{cyl}^{src} and TL_{cyl}^{rec} are the transmission losses predicted by cylindrical spreading relative to the source and receiver, and TL_o is a static shift that, when combined with TL_{cyl}^{src} and TL_{cyl}^{rec} , accounts for geometric spreading and the source spatial beam pattern. The derivation of this equation is given in Appendix A.

An estimate of the error in scattering-strength values calculated using (4) is made by considering the error associated with each term on the right side of the equation. The background noise level of RL_s (i.e., the reverberation level level due to backscattering within the water column only) is estimated to be more than -10 dB down relative to the average calculated S_s and is negligible. We attribute this background noise level to water column scattering only. As previously stated, the source level, SL , was observed to have a variation of only +/- 0.14 dB. The difference between our approximation and the exact geometric spreading loss combined with the source spatial beam pattern is about +/- 0.5 dB for the majority of the offset ranges used in our analysis (see Appendix A). Thus, the net error in the calculation from the first five terms on the right of equation (4) is about ± 1 dB.

The potential error due to the area correction term is more problematic. For calculating the area in equation (3) we use a beamwidth of 1.1° and range resolution of 13.6 m. At 15 km the area correction ($-10 \log_{10} A$) is then -36 dB. However, the

correction is -40 dB if the beamwidth is 3° . The beamwidth is a function of the receiver array geometry, and if this is continuously changing during the experiment then there could be as much as 4 dB of variation in S_s . If the receiver array is stable but misshaped, then the error reduces to a static shift in the data. We infer that the receiver array was stable during the data collection because there is no evidence in the acquisition logs (ARSRP Initial Report, 1993) suggesting that it was not. Given this assumption, the only 'error' in the area term is an unknown static shift which, in our analysis, does not affect the conclusions. Therefore, we estimate that the total error in the variation of the calculated scattering strength (S_s) is just the +/- 1 dB due to the first five terms on the right of equation (4).

2.5.2 Seafloor Locations and Dip Estimation

Given the nominal 200 m horizontal resolution of the Hydrosweep bathymetry data, we divided each area to be studied into 200 x 200 m grid cells (Figure 2-2) and used each possible set of three cell corners to determine four dip planes in each cell, as shown in Figure 2-4. Each incident beam is associated with a pair of dip planes as defined by two of the triangles, depending on the azimuth of the beam relative to the grid cell. For example, beams incident from the NE or SW quadrants are associated with the dip and dip azimuth determined for dip planes that fit the bathymetry values at the corners of triangle 'dip2' and 'dip4'. Similarly, beams incident from the SE or NW are associated with dip and dip azimuth calculated for values at the corners of triangles 'dip1' and 'dip3'. By defining dip in this way we approximate the directional derivative of the bathymetry while explicitly utilizing every bathymetry value.

In Figure 2-5 we compare approximate beam footprints at 10 km, 20 km and 30 km offset range to the area covered by 200 m diameter circles at the corners of a grid cell. Within the 1/2 CZ, the beam footprint area is on the order of 13 m x 200 m (range resolution x beamwidth) at 10 km, increasing to 13 m x 600 m at 30 km. The three bathymetry values are required to define the dip and dip azimuth can be thought of as estimates of the bathymetry within 200 m diameter circles, as shown in the figure. The net area associated with each estimate of dip is thus quite large and

fully includes the beam footprint up to 25 km in offset, even for beams intersecting the grid cell 100 m from the grid cell center. If beamwidth is on the order of $2^\circ - 3^\circ$, this estimate of dip remains a crude, but reasonable, measure of the dip encountered by the acoustic beam footprint. Note that in final processing we average data from seven consecutive (in range) beam footprints that fit within the 100 m range of each triangle.

Figure 2-6 shows a histogram of seafloor dip as a percentage of total number of dip values calculated separately for each of the three target areas. The mean dip for the IC areas, Casa Grande and Syrian Knob, is a few degrees higher than for the OC area, Site A. This agrees with the hypothesis that IC crust has characteristically steeper dip than OC crust, but is not as large a difference as expected. Also, it is clear from this plot that there is not a distinguishable difference in dip distribution that might have yielded the type of backscattering distinction suggested in Figure 2-3(a). If we considered instead the mode of the dip for each area, it is clear that Site A has a much lower peak value than the other areas. It must also be remembered that the dip distribution determined from Hydrosweep is skewed in that very steep dips (greater than about 45°) are not observed.

2.5.3 Source and Receiver Range

The fact that the source and receiver arrays are not exactly co-located is included in determining range (horizontal offset) and two-way traveltime to each grid cell. Errors in travelttime estimation can be as large as several hundred milliseconds if only the source, receiver, or their midpoint is used in calculating travelttime. We use the ship location recorded on the acquisition logs (ARSRP Initial Report, 1993) as the source location. From this location and the receiver array and ship headings, we calculate the position of the center of the receiver array. The locations shown in Figure 2-2 correspond to the calculated receiver array locations.

Since the ship continues to make way during the time period between source firing and the arrival of the backscattered signals, there is a correction that could be applied to the receiver array position. This correction depends on ship speed, total

signal traveltimes, and the beam direction. For example, the ship speed during the Site A experiment was maintained at about 3 knots ≈ 1.5 m/sec. The largest correction necessary would be for end fire beams, but in our study we exclude all beams within 30° of endfire. In our worst case, beams at 30° , the possible error in range at 10 km is about 17 m and at 20 km about 34 m. For broadside beams, near 90° , there is essentially no error. Since shifting beam footprint locations by such small amounts would not change the grid locations with which they are associated in most cases, we chose to neglect this correction.

2.5.4 Traveltimes and Grazing Angle

A Snell's law ray tracing routine was used to calculate tables of traveltimes and beam grazing angle for depth and range pairs. For this calculation we used the water velocity profile shown in Figure A1. Apparent grazing angle is the angle between the ray (representing the beam or propagation vector) and a horizontal plane at each depth. The distribution of calculated grazing angles for each of the three study areas as a function of range is shown in Figure 2-7. The non-uniqueness of grazing angles for each offset is due to the variation in water depth. Separate traveltimes tables were generated for the source array at 184 m depth and the receiver array at 155 m depth. The offset of each source and receiver to the center of each grid cell and the depth of the grid cell are used to find in the tables the two-way (ray path) traveltimes to the center of each cell and the apparent beam grazing angle. Time windows of 133 ms (horizontal two-way traveltime across a grid cell triangle) on either side of this center time are used to assign beam time series data from each source to the corresponding dip triangle.

We also calculate true grazing angle, which is the angle between the incident beam propagation vector and the plane defining the local seafloor dip. This is calculated as the inverse cosine of the scalar product of the unit vector defined by the grazing angle and azimuth of the incident beams at each grid cell and the dip normal vector of each dip triangle. When the dip normal vector is in the same vertical plane as the beam propagation vector (i.e. the seafloor is 'looking' directly back at or away

from the source location), the true grazing angle is just the sum of the beam grazing angle and seafloor dip (or difference if the seafloor dip faces away from the source direction). For those cases where the seafloor dips away from the incident beam at an angle greater than the beam grazing angle, we treat the area as a shadow zone and exclude the signal corresponding to that dip triangle from any further analysis. This is the second type of transmission loss factor that we account for.

2.5.5 Beam Averaging and Stacking

The next step in our processing is to stack (equal weight average) the time series data from intersecting beams, from the different source locations, at each dip triangle. We do all of the stacking and averaging after the signals have been converted to scattering strength in dB. We found that pre-stack scattering strengths (in dB) are normally distributed, whereas the data in units of squared pressure have a somewhat skewed normal distribution. Averaging the normally distributed signals produces a better estimate of the true signal mean. Once the data are stacked, we find the time average scattering strength over the time window (133 ms) of each triangle. In stacking we have averaged beams with different source azimuths, so we also average the true grazing angles. We find that the range of true grazing angles at any particular grid cell is not large, which is a consequence of the limited variation in range and azimuth of individual sources within each source group. The standard deviation of the mean true grazing angle for each location is about $+/- 2^\circ$.

Figures 2-8 - 2-10 are cross-plots of scattering strength at each dip triangle as a function of the average true grazing angle. This is plotted separately for North and South Source Groups. We also find the linear regression fit to the data, as well as the linear fit to the data when all values below some threshold level are eliminated.

In Figures 2-11 - 2-13 we plot the data after we have constrained the stack such that only those beams with source azimuth and seafloor dip azimuth within 10° of being parallel are included, i.e., beams with source azimuth almost normal to the strike of the dip planes. In effect, this shows the scattering strength of the most directly 'back-looking' seafloor surfaces. We look at this because it has been suggested (Makris et

al., 1995) that 'back-looking' seafloor produce the strongest backscatter signals in monostatic scattering experiments.

We also find the weighted average scattering strength of the four dip triangles within each grid cell, where the weights are the number of beams that make up the stack within each triangle. We reject any stack with less than four beams in the stack. These average scattering strengths, per grid cell, are then overlaid onto the bathymetry contour maps for each of the study areas as shown in Figures 2-14 - 2-16. In these plots we have chosen the threshold of the grey scale range to highlight the locations corresponding to just the highest scattering strengths.

2.6 Analysis

2.6.1 Scattering Strength vs True Grazing Angle

It is clear in Figures 2-8 - 2-10 that there is a trend toward increasing scattering strength with increasing true grazing angle for both IC and OC crustal areas. One exception to this is the case of the South Source Group data in Casa Grande (Figure 2-10(b)). This trend is quantified by the linear regression lines calculated for each data set. The specific slopes and correlation coefficients for each case are given in the figure captions. In general, the slope of this line is on the order of $0.1 =/- 0.01$ dB/degree, but the correlation coefficients are small (< 0.5). This implies that the functional relationship between scattering strength and true grazing angle is poorly described by a linear function. It is also clear that the broad distribution in scattering strength at each grazing angle would not yield a strong correlation for any functional description. We conclude from this that, at the scale of the resolution of Hydrosweep bathymetry data, there is not a simple functional relationship between scattering strength and true grazing angle.

In spite of this we can ask: Is the trend that is observed sufficiently strong to differentiate IC crust from OC crust? The difference in mean seafloor dip of the IC crust area, Site A, compared to mean dips of the IC crust areas (Figure 2-6), is

about 5° , which yields only a 0.5 dB difference in scattering strength between the two crustal areas. Based on our estimates of error in scattering strength calculation ($+/- 1$ dB) and true grazing angle ($+/- 2^\circ$), we conclude that the trend is not steep enough to distinguish between the crustal regions so that the idea expressed in Figure 2-3(c) cannot be applied. We also calculated the averages of scattering strengths in 1° intervals and found that the standard deviation is about $+/- 2.5$ dB. This suggests that there is about $+/- 1.5$ dB of variation in scattering strength not directly correlated to seafloor dip, which again is larger than the difference in strength that can be associated with the average difference in dip between the two crustal areas. The plots also show that there is no distinct difference in the trend or magnitude of scattering strength between the two crustal types, i.e. the relationships suggested in Figures 2-3(b-c) are not found.

We considered the possibility that only very high scattering strengths show a strong correlation to grazing angle. By choosing a threshold (based on the highlighting of steep dip features in map form (Figures 2-14 - 2-16)), we look for a more constrained relationship for signals above this threshold. The linear fit and correlation coefficients after including this constraint are also shown in Figures 2-8 - 2-10. Again the results do not suggest a functional fit between the parameters. In this case, the fact that the Hydrosweep bathymetry data does not define seafloor dip above $30 - 40^\circ$ may be strongly affecting the result.

In Figures 2-11 - 2-13 we test the idea that strong backscatter is produced primarily by the most directly 'back-looking' seafloor areas. In these plots, only signals from areas having dip azimuth within 10° of the return direction to the source were included in the stacks. The fact that the slopes of the regression lines and the breadth of the distributions in scattering strength do not differ from those in Figures 2-8- 2-10 suggests that 'back-looking' seafloor areas, as defined by Hydrosweep bathymetry, do not dominate the signals observed in monostatic reverberation backscattering.

2.6.2 Scattering Strength Maps

In spite of the lack of a clear functional relationship in crossplots, there is a correspondence between high scattering strength and steeply dipping seafloor features observed in all of the scattering strength maps (Figures 2-14 - 2-16). These maps suggest that the scattering strength can be used to constrain aspects of the interpretation of the shape of large-scale, highstanding seafloor morphology. The linear bathymetric ridges in Site A, Figure 2-14(b), correspond to linear scattering-strength highs, but only when insonified from directions at near normal angles to the ridge axis. When insonified from highly oblique angles, (Figure 2-14(a)), only isolated peaks, in particular the peak at the end of Blackjack Ridge ($26^{\circ}06.5' N$, $46^{\circ}14.5' W$), stand out as a scattering-strength high. Such isolated highs, which seem to be associated with changes in dip direction, may be indicative of diffraction scattering from edges. The linearity and strong dependence of scattering strength on source azimuth may be a useful qualitative indicator of OC crustal areas.

In Figure 2-15(a), the high-backscatter region wraps around the flank of the main peak of Syrian Knob, mimicking the shape of the topographic corner facing toward the North Source Group. A lower ridge, extending to the southwest, is also delineated by high scattering strength. In Figure 2-15(b), the arcuate scattering-strength high corresponds to a similar shape in the bathymetry facing the direction of the South Source Group. Because IC crustal areas have blocky rather than linear structures, strong scattering responses are observed from all source azimuths, although not necessarily corresponding to the same portion of a structure. We could conclude that the comparison of mapped spatial patterns of scattering strength for large changes in source azimuth can be used to distinguish shape characteristics of the seafloor and, in particular, to differentiate IC and OC crustal areas.

This conclusion must be tempered by the results of mapping in the Casa Grande area which is also described as being on the IC side of the discontinuity. The results for this area are somewhat problematic in that many of the beams from both source groups that intersected the area were within 30° of endfire and were rejected early in

the processing. This resulted in fewer beams in both North and South Source Group stacks. For the North Source Group (Figure 2-16(a)), the strong scattering strength generally corresponds with topographic corners, i.e., a change in dip azimuth. Even though Casa Grande is a steep feature, it does not have the blocky structure that is expected for IC crust. The dip azimuth of the seafloor structure facing the North Source Group is relatively oblique to the direction of insonification, and the results are similar to those for oblique insonification at Site A (Figure 2-14(a)).

The mapping of the South Source Group data (Figure 2-16(b)) suggests that the whole flank of Casa Grande has high scattering strength when insonified from the direction near normal to the strike of the seafloor dip. There is some striping which may indicate that some areas of the slope are more responsive than others. Higher-resolution bathymetry data would help to resolve whether there is detailed structure associated with this striping.

The map results for Casa Grande appear to be more similar to the response observed at Site A than at Syrian Knob. This seems to be the result of Casa Grande being a less blocky structure than Syrian Knob. Therefore, before using the difference in acoustic response of lineated vs. blocky structure to differentiate IC and OC crust, some further consideration of the scales of these features should be made.

2.6.3 Scattering Strength vs. Seafloor Dip

We estimate the direct relationship between seafloor dip and scattering strength by using the linear regression fit to each data set to remove the approximate effect of beam grazing angle from the scattering strength. In Figures 2-17 - 2-19, we plot the resulting scattering strength versus seafloor dip, where seafloor dip is the dip that would be observed by an acoustic beam travelling horizontally (beam grazing angle = 0°). If scattering strength is more, or less, dependent on beam grazing angle than on seafloor dip, then making this adjustment is expected to change the slope of the regression line. Instead, what we see is that the slope of the regression lines are essentially unchanged. This suggests that scattering strength either varies similarly with changes in grazing angle or seafloor dip, or that we cannot resolve the difference

due either to the insensitivity of the scattering strength to changes in dip or to the low resolution of dip as measured by Hydrosweep data.

2.7 Discussion and Conclusions

Our analysis of the monostatic backscatter signal from IC and OC crust, in the region of Site A, has led us to two seemingly contradictory conclusions. In map form (Figures 2-15 - 2-17) there is good correspondence between high scattering strength and source facing ('back-looking') slopes with steep dip, and the geometric patterns of high scattering strength mimic the shape of the bottom feature. This result agrees with results reported by other investigators (Makris et al., 1995; Preston et al., 1990; Shaw et al., 1993). Contrary to this, the analysis based on crossplots of scattering strength vs. true grazing angle and seafloor dip suggest that there is not a functional relationship between these parameters. The observed trend of increasing scattering strength with increasing seafloor dip or grazing angle is only about 0.1 dB/degree. This weak linear correlation is insufficient, given the broad distribution in scattering strength at each angle, to distinguish low dip areas from high dip areas.

We believe that these observations are not contradictory, but rather show the effect of geologic scale on the analysis of seafloor scattering. The lack of a stronger numerical correlation may indicate that the actual scattering mechanisms are only weakly dependent on dip at the scale measured by Hydrosweep. The good map correspondence is mainly due to the facts that steeply dipping slopes are part of large highstanding features with rough surfaces, and that steeply sloping areas are likely to be less thickly sedimented. Both of these conditions lead to stronger scattered signals. The correspondence of high scattering strength to these features does not define a quantitative relationship between scattering strength and seafloor dip at 200 m bathymetric grid spacing, but, it nevertheless suggests a useful relationship between reverberation backscatter signals and seafloor shape.

The observed variations in scattering strength are larger than can be explained by variations in seafloor dip from 200-m gridded bathymetry or data error. A significant

part of the variation in scattering strength observed in the crossplots is likely due to variations in seafloor and subseafloor properties at scales less than 200 m. Even in the case of what may be considered smooth and flat seafloor, volume density and velocity heterogeneities at wavelength scales (6 m for these data) produce anomalous backscattered signals (Swift and Stephen, 1994; Gensane, 1993).

For the data used in this analysis the peak acoustic wavelength was 6 m which is much smaller than the scale of resolution available from either the Hydrosweep data or the acoustic beam footprint. We did not, in this study, investigate the effects of small-scale (less than 200 m) features. Instead, we tried to quantify and understand the effects of large-scale features observed on IC and OC crust as a means of differentiating these crustal regions. The results of this study suggest that although scattering strength does in general increase with increasing seafloor dip, the trend is not strong enough to reliably predict seafloor dip from scattering strength when using 200-m gridded bathymetry. The difference in the mean dip of IC and OC crust is only a few degrees, and the overall distribution of dip and scattering strengths are so similar that no quantitative distinction between these areas, based on comparison of Hydrosweep data and backscatter data, can be made.

However, a qualitative analysis of the data based on mapping the scattering strength indicates that the reverberation signals may be useful in distinguishing IC and OC crust. The correspondence between steeply dipping features and high scattering strength can be used to delineate shapes of seafloor features. The long linear ridges characteristic of OC crust can be identified from backscattered data if at least two principle directions of insonification are used to acquire the data. We observed that when the high-standing ridge flanks are insonified at 'back-looking' angles, they produce much higher average scattering strength. In contrast, blocky seafloor regions associated with IC crust show high scattering strength when insonified from different source directions because at least some portion of high standing regions are insonified at 'back-looking' angles.

It has been our goal to determine a method for distinguishing IC from OC crust using acoustic backscatter signals. In doing so, we have focused our attention on

finding a relationship between seafloor dip and scattering strength at the scale of the resolution of Hydrosweep bathymetry data. Mapping data to the seafloor avoids making a quantitative judgement about any seafloor characteristic that might be controlling the level of backscatter. Contrary to this, plotting scattering strength versus seafloor dip is an explicit search for a quantitative relationship. There may be quantitative relationships between scattering strength and seafloor properties, but we conclude that we must look at wavelength scale variations, i.e. much smaller than Hydrosweep resolution, to determine them.

Figure 2-1: Inside-corner (IC) crust and outside-corner (OC) crust are found on opposite sides of mid-ocean ridge (MOR) segments. In this figure there are four segments denoted as A, B, C and D. When the displacement between segment ends is greater than about 30 km the discontinuity is usually the site of an active transform fault and is called a transform discontinuity. When the displacement is less than about 30 km, it is referred to as a second-order discontinuity and may or may not be the site of an active transform fault. In either case, IC is used to describe the crust formed adjacent to the active displacement zone of the discontinuity. OC crust is the portion of the crust formed adjacent to the inactive trace of the discontinuity and is coupled to IC crust in the adjacent segment across the discontinuity soon after being formed in the ridge axial valley. This figure represents the crust formed at a slow-spreading center, where IC crust is, usually, significantly higher than OC crust (Figure from Tucholke and Lin (1994))

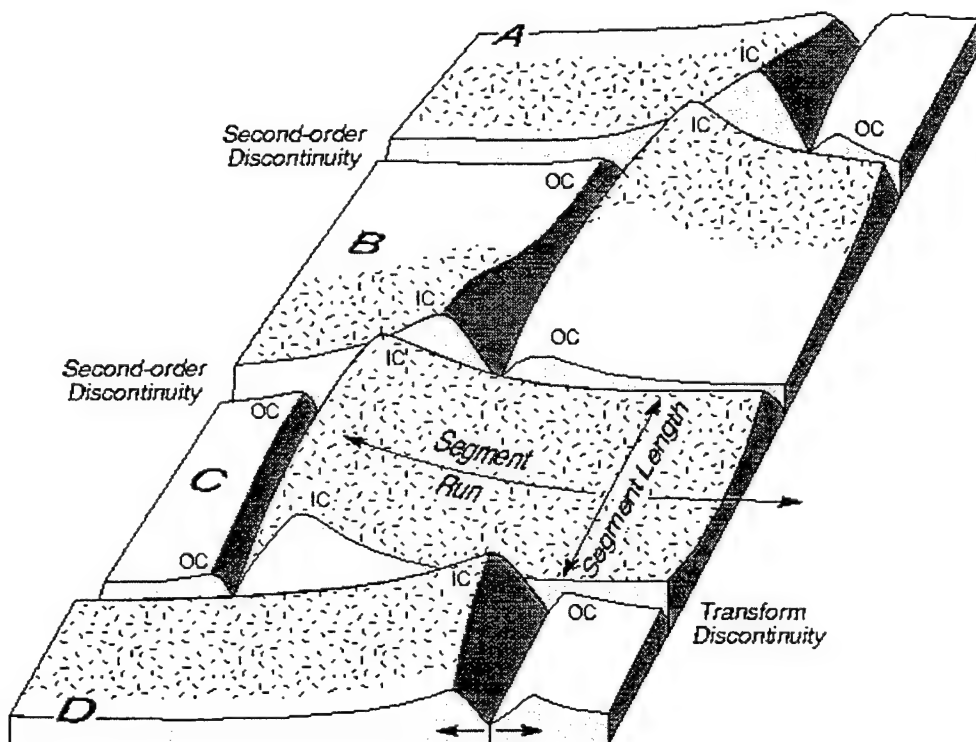


Figure 2-2: Site A is located on OC crust on the edge of a sediment pond which marks the trace of a second-order discontinuity. The figure shows seafloor bathymetry contoured at an interval of 25 m. Circles with flags indicate the receiver array location and orientation at each ship location during the Site A monostatic reverberation experiment (Run 1) of the 1993 ARSRP Acoustics Cruise. Backscattered signal from two areas located on IC crust, labelled as Syrian Knob and Casa Grande, are compared to signals from Site A. Source locations in two regions around Site A, the North and South Source Groups, are analyzed separately. Within each study area, the ranges and depths to 200 x 200m grid cells are used to find the corresponding acoustic backscatter signals.

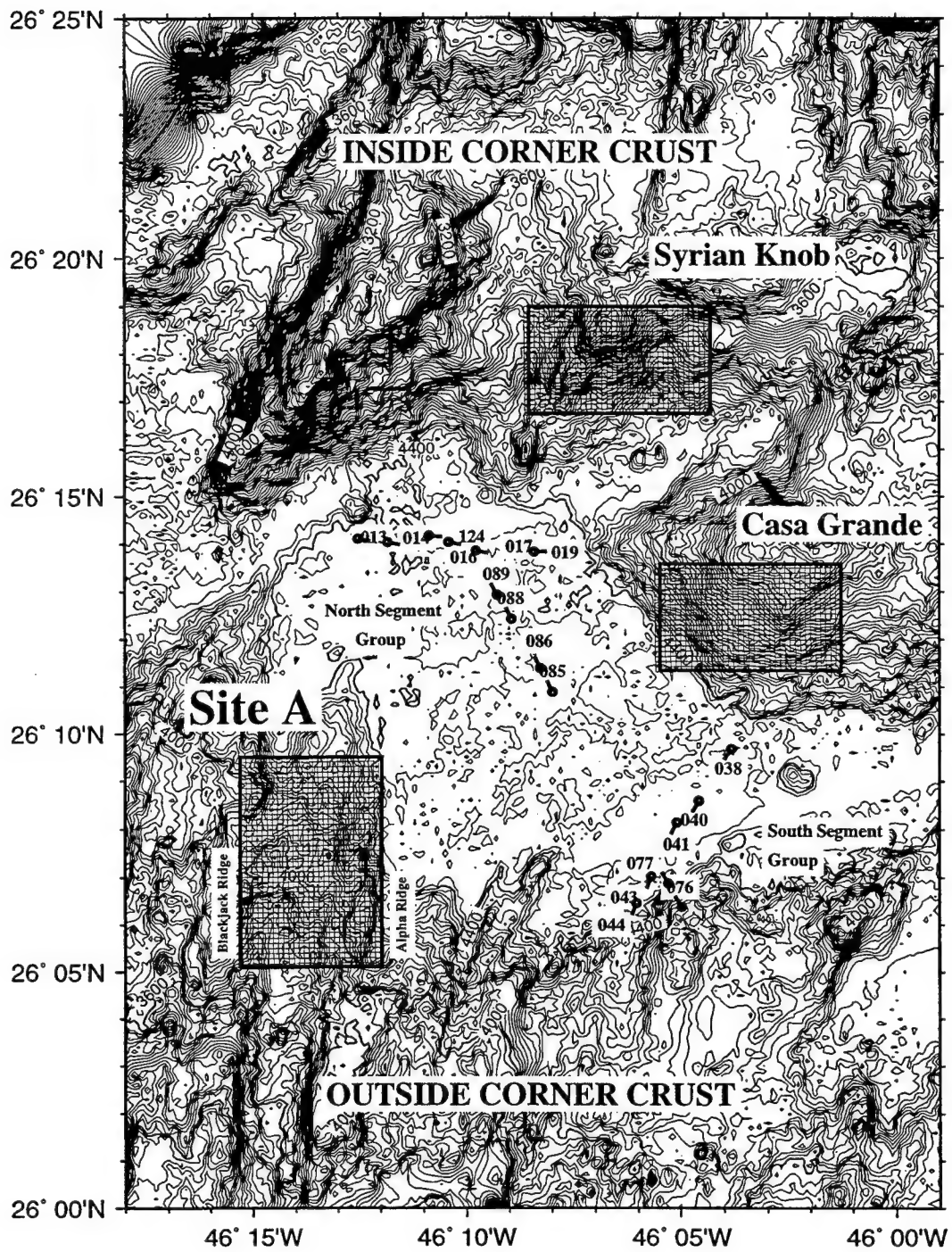


Figure 2-3: If IC and OC crust have distinct populations of seafloor dip, it may be possible to distinguish them on the basis of acoustic scattering strength, as in (a). If they have similar distributions of seafloor dip but have different scattering strengths due to surface characteristics, then it may be possible to distinguish the crustal regions by differences in scattering strength levels (b) or in the shape or slope of a functional relationship (c). If both dip distribution and scattering strength are similar, it may not be possible to distinguish the regions on any of these bases (d).

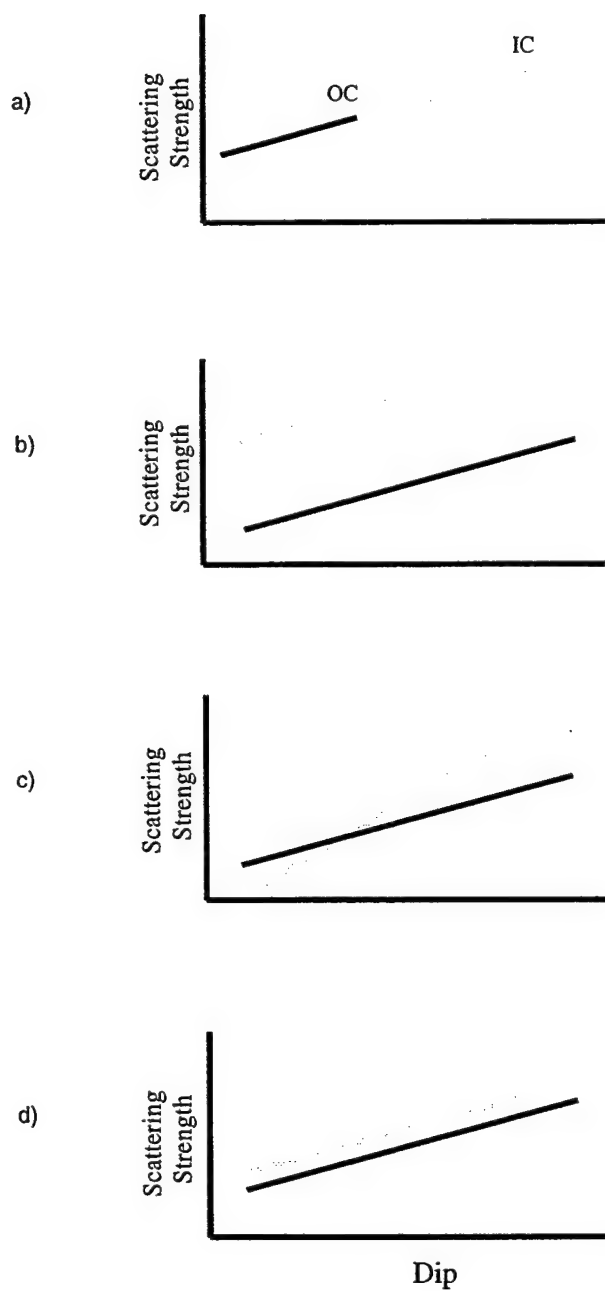


Figure 2-4: Bathymetry values at each corner of the grid cell are considered to be average values within 200 m diameter circles (dotted circles) on the seafloor. Four triangles defined by the corners of the grid cell are used to define four directional seafloor dips. For each incident acoustic beam, two of the dips defined in this way are assigned to the beam. Which dips are assigned depends on incident beam direction. a) Beams incident from the NW or SE are assigned dip 1 and dip 3 and b) beams incident from the NE or SW are assigned dip 2 and dip 4.

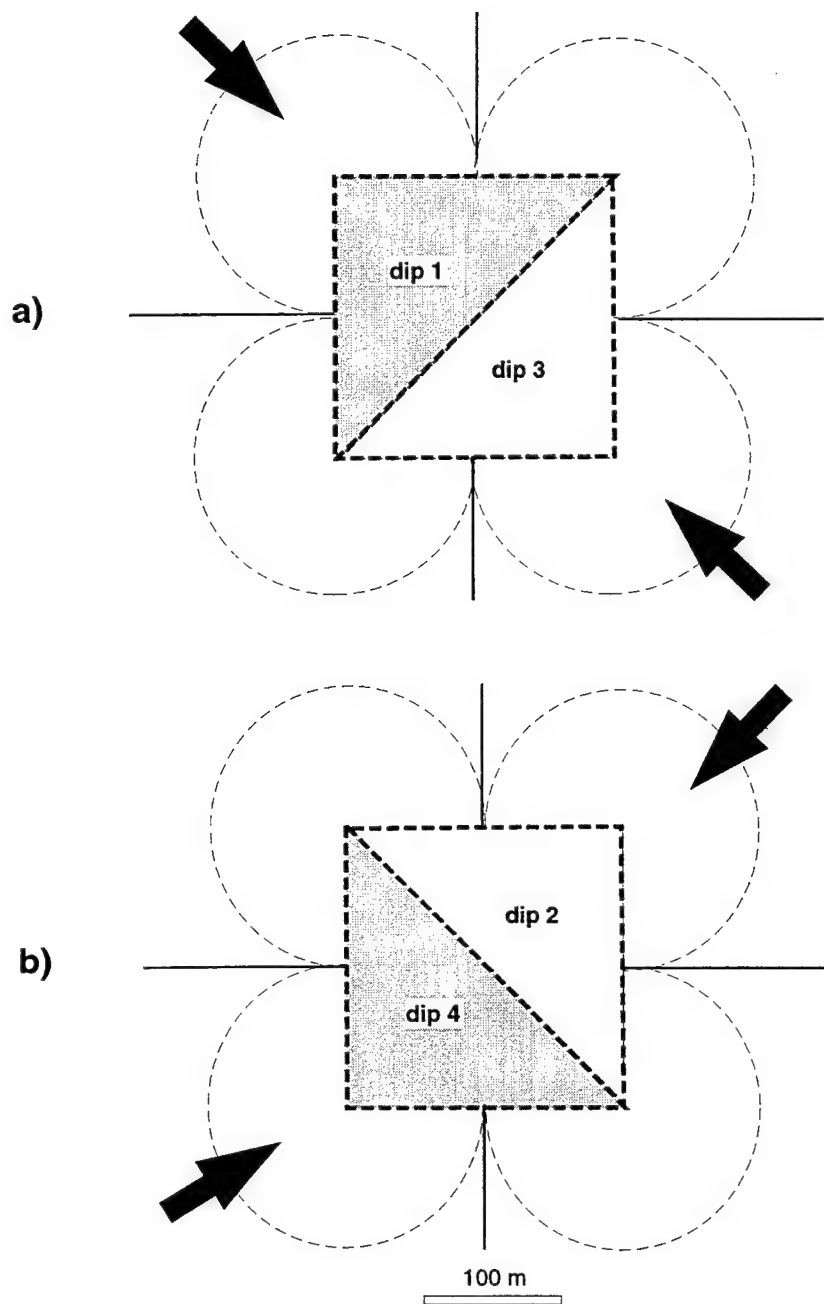


Figure 2-5: Approximate beam footprints, for a beamwidth of 1.1° , at 10 km (L1), 20 km (L2) and 30 km (L3), in comparison to the area covered in the seafloor dip calculations (Fig. 2-4). The dashed line circles enclose the area for which the bathymetry value at each corner of the square grid cell is an estimate of the local bathymetry. For the ranges and depths considered in this study, the width of the beam footprint is the same scale as the dip resolution of Hydrosweep bathymetry data. In the analysis, seven range-consecutive beam footprints (covering a range of about 100 m) are associated with each dip value.

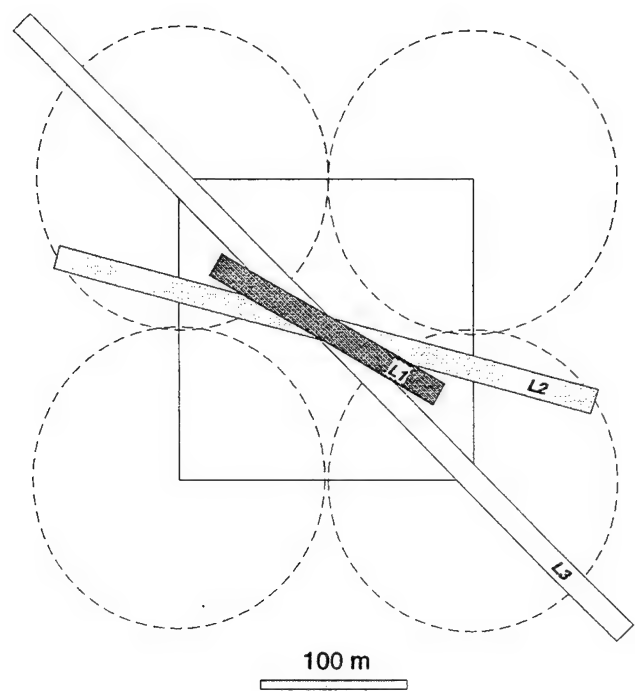


Figure 2-6: Comparison of observed dips calculated from Hydrosweep data in each study area. The vertical axis is the percentage of calculated dips within each area that fall within each 1° interval. Note that the mean dip of Site A, on OC crust, is smaller than the mean dip of both IC areas. Also, note that dip values greater than about 45° are not resolved in Hydrosweep data.

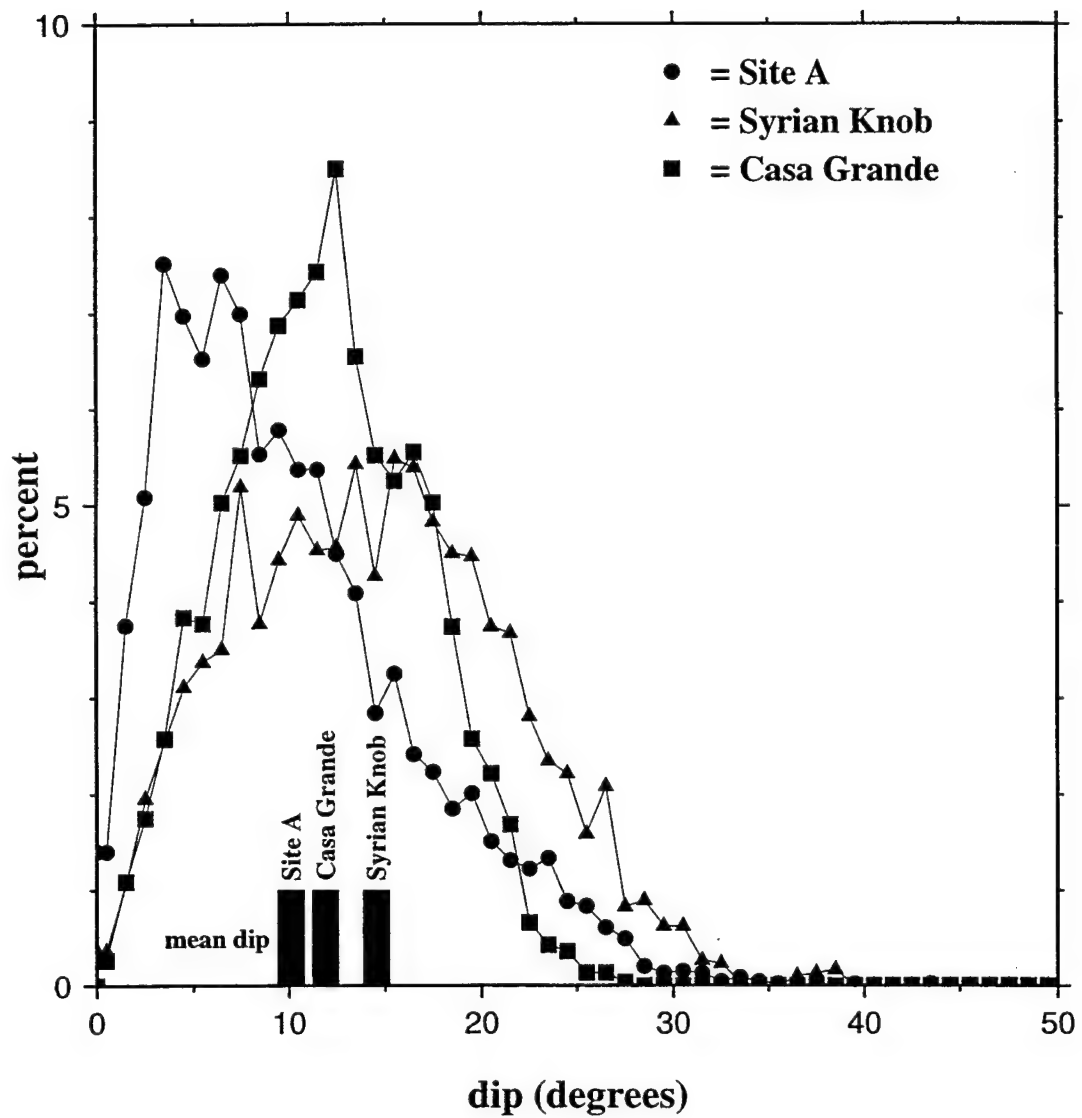
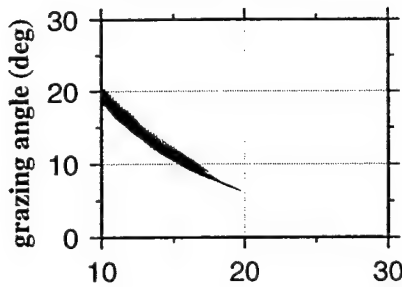


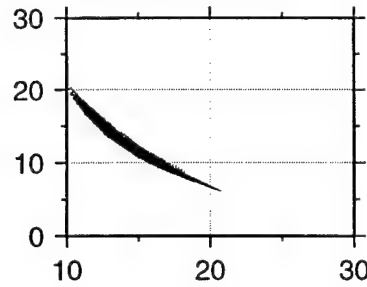
Figure 2-7: The distribution of grazing angles vs. range for each target area. These grazing angles are calculated using ray tracing in a layered ocean velocity model and assume a flat seafloor. The velocity profile used to generate this model is shown in Appendix A. The breadth of each curve indicates the range of observed depths. Note also that this plot shows that almost all of the horizontal offsets (range) actually used in our analysis lie within 10-20 km.

Site A

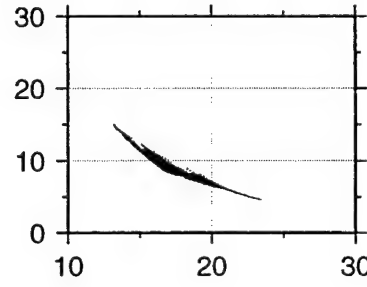
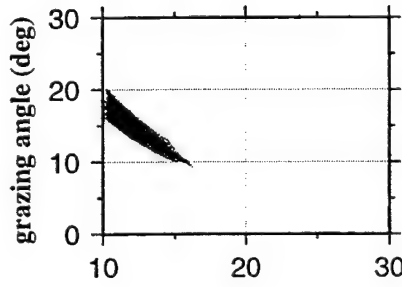
north segment group



south segment group



Syrian Knob



Casa Grande

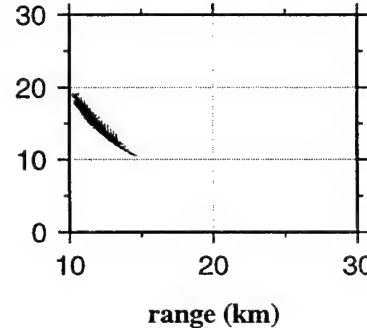
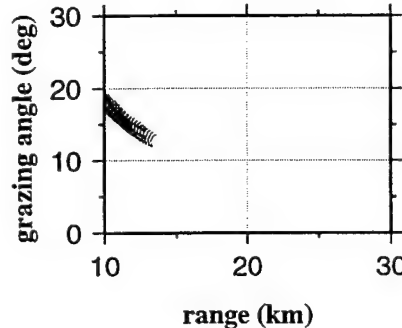


Figure 2-8: Scattering strength of stacked intersecting acoustic beams, in Site A, as a function of true grazing angle. The solid grey line is the linear regression fit, which for (a), the North Source Group data, has slope of $0.13 +/ - 0.01$ dB/deg with a correlation coefficient $r = 0.37$, and for (b), the South Source Group data, is $0.13 +/ - 0.01$ dB/deg and $r = 0.5$. Error of individual data values is estimated at $+/- 1$ dB in calculated scattering strength and $+/- 2^\circ$ in grazing angle. The standard deviation of the scattering strength when averaged over 1° intervals is about $+/- 2.5$ dB (not shown), which suggests that there is variation on the order of $+/- 1.5$ dB due to variations in seafloor properties other than true grazing angle. The dashed grey lines are the linear regression fits to the data that lie above a threshold (thin black line) chosen at -14.5 dB. In (a) the slope of this fit is $0.002 +/ - 0.02$ dB/deg with $r = 0.01$ and in (b) the slope is $0.06 +/ - 0.01$ dB/deg with $r = 0.3$. Note that thresholding the data in this way does not increase the slope of the trend in either case, nor does it improve the correlation coefficient.

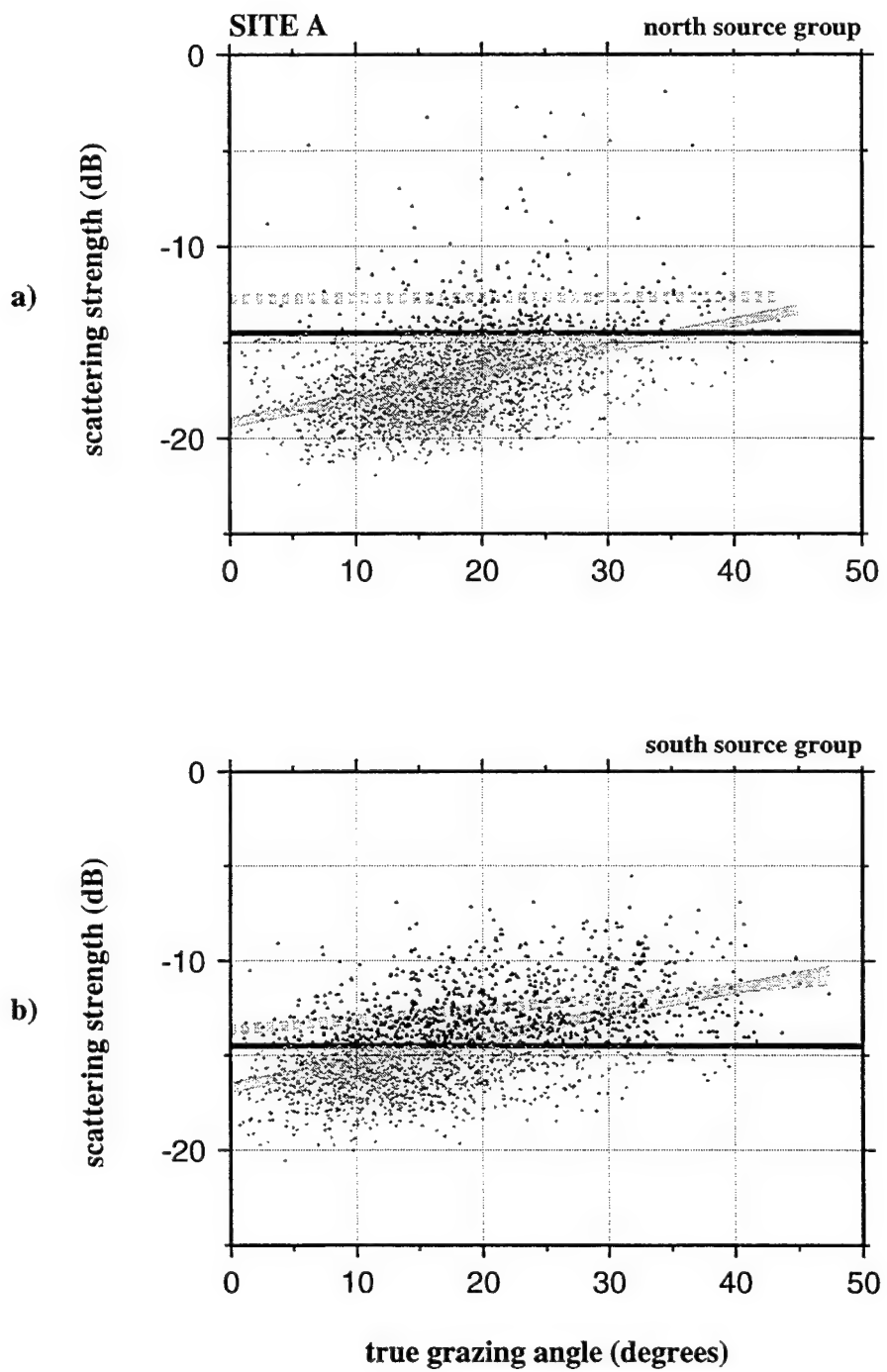


Figure 2-9: Same description as Figure 2-8 but for Syrian Knob. For the regression lines, in (a) slope= 0.08 ± 0.01 dB/deg and $r= 0.22$ and in (b) slope= 0.02 ± 0.01 dB/deg and $r= 0.06$. For signals above the threshold at -12.5 dB in (a) slope= $-0.005 \pm .01$ dB/deg and $r= -0.03$ and in (b) slope= 0.05 ± -0.01 dB/deg with $r= 0.23$.

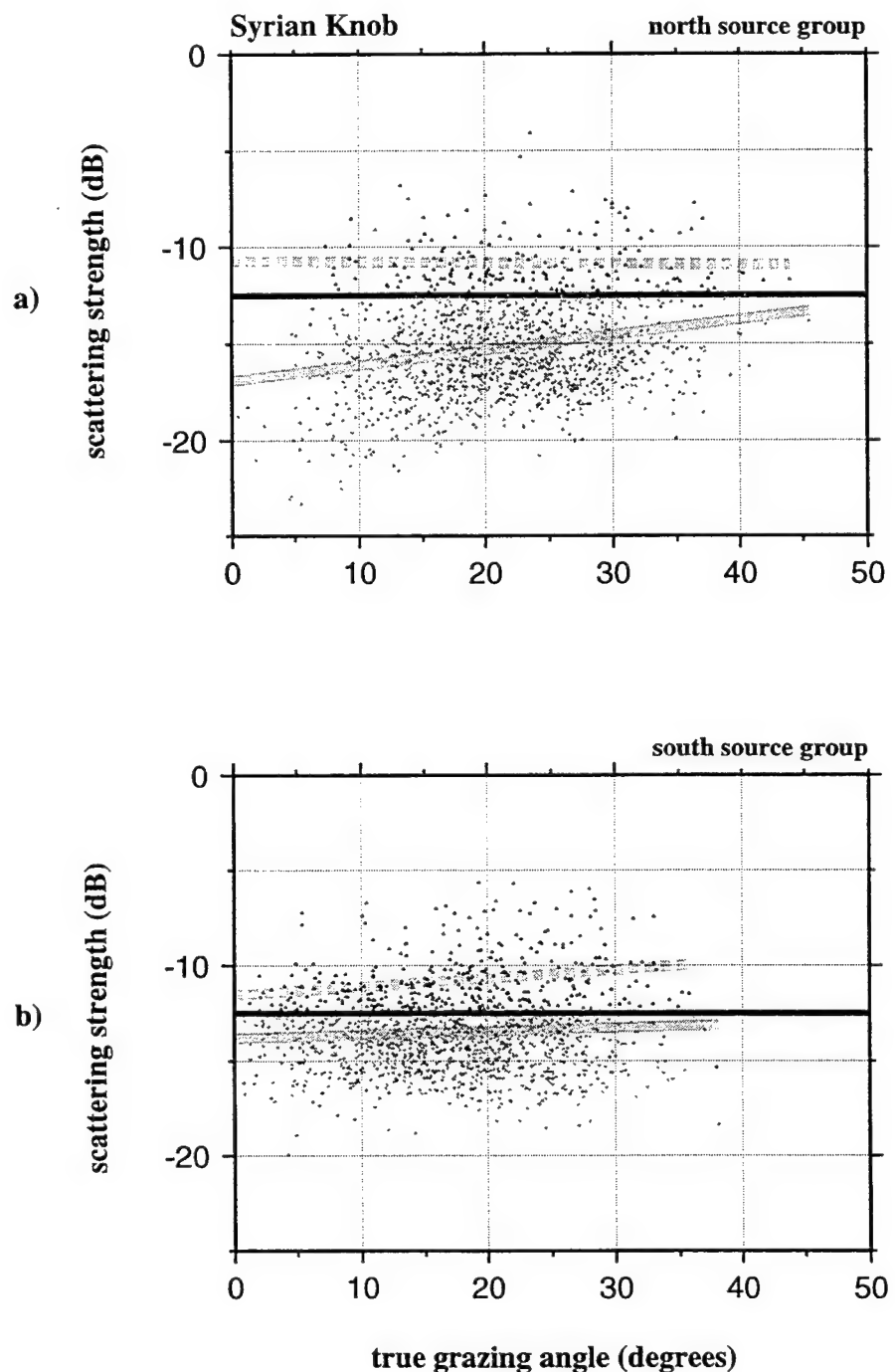


Figure 2-10: Same description as Figure 2-8 but for Casa Grande. For the regression lines, in (a) slope= $0.11 +/ - 0.02$ dB/deg and $r= 0.24$ and in (b) slope= $-0.08 +/ - 0.02$ dB/deg and $r= -0.13$. For signals above the threshold at -17.5 dB in (a) slope= $-0.04 +/ - .02$ dB/deg and $r= 0.18$ and in (b) slope= $-0.07 +/ - 0.01$ dB/deg with $r= -0.15$.

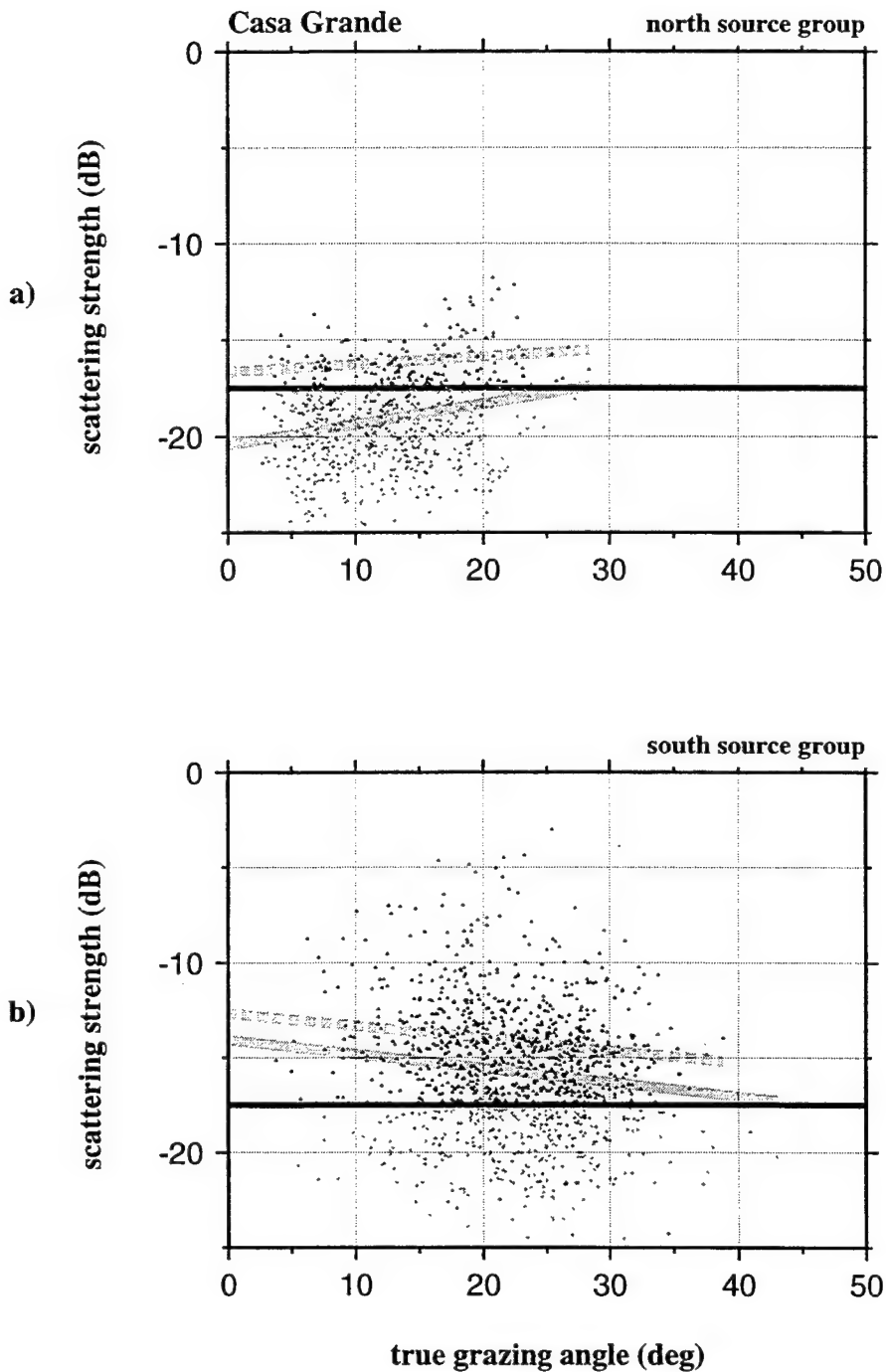


Figure 2-11: Scattering strength of stacked intersecting beams, in Site A, where only beams having source azimuth within 10° of being normal to the dip plane strike ('back-looking' dips) are included in the stack. The solid grey line is the linear regression fit, which for (a), the North Source Group data, has slope of 0.11 ± 0.02 dB/deg with a correlation coefficient $r = 0.36$, and for (b), the South Source Group data, has slope of 0.11 ± 0.01 dB/deg and $r = 0.39$. Note that reducing the stack to include only scattering from 'back-looking' seafloor areas does not improve the correlation nor does it significantly change the slope of the observed trend compared to Fig. 2-8.

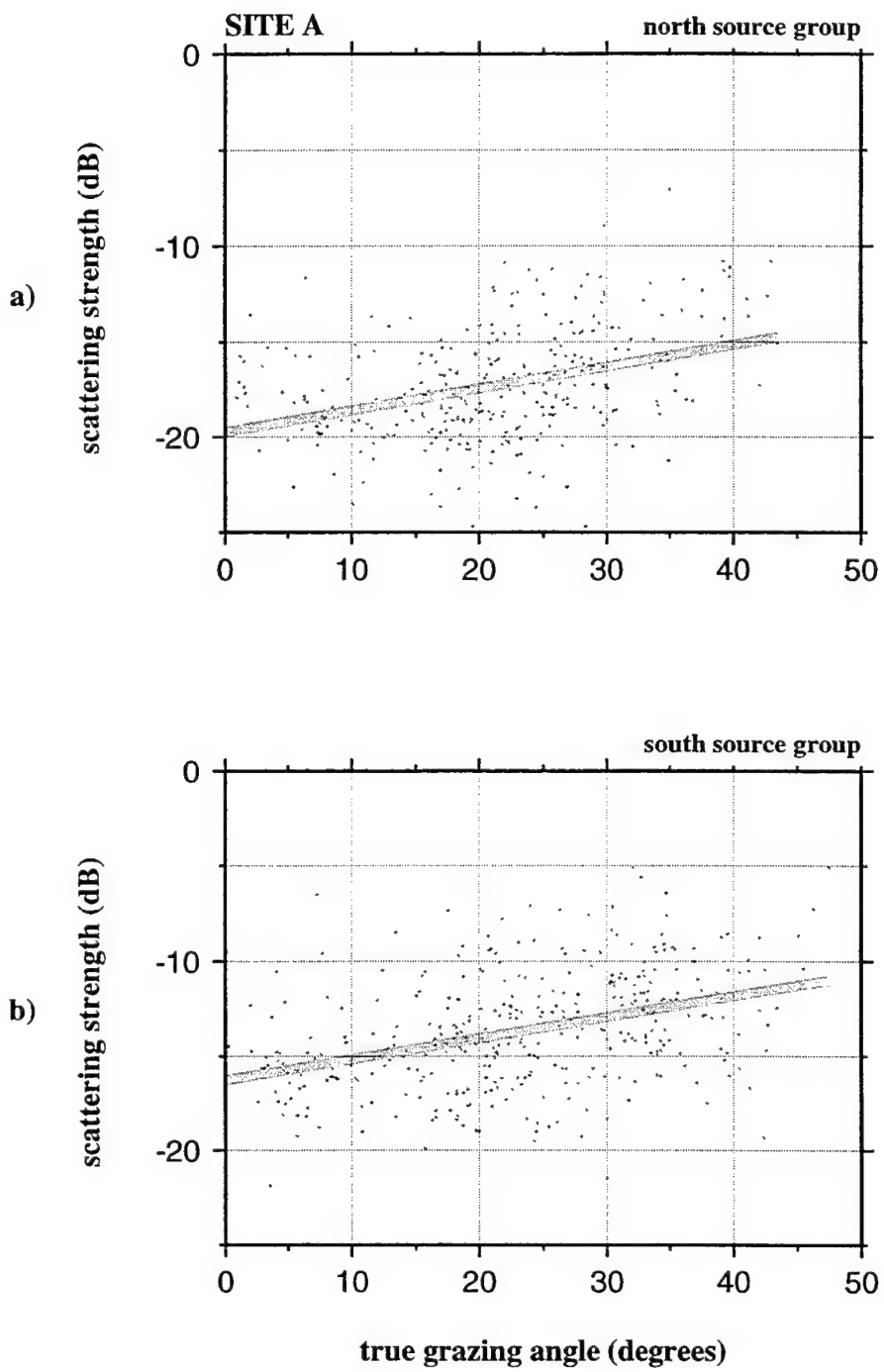


Figure 2-12: Same description as Figure 2-11 but for Syrian Knob. For the regression lines, in (a) slope= 0.10 ± 0.03 dB/deg and $r= 0.26$ and in (b) slope= 0.02 ± 0.03 dB/deg and $r= 0.04$. Note that the stack of data from only the 'back-looking' seafloor areas does not improve the correlation nor does it significantly change the slope of the observed trend compared to Fig 2-9.

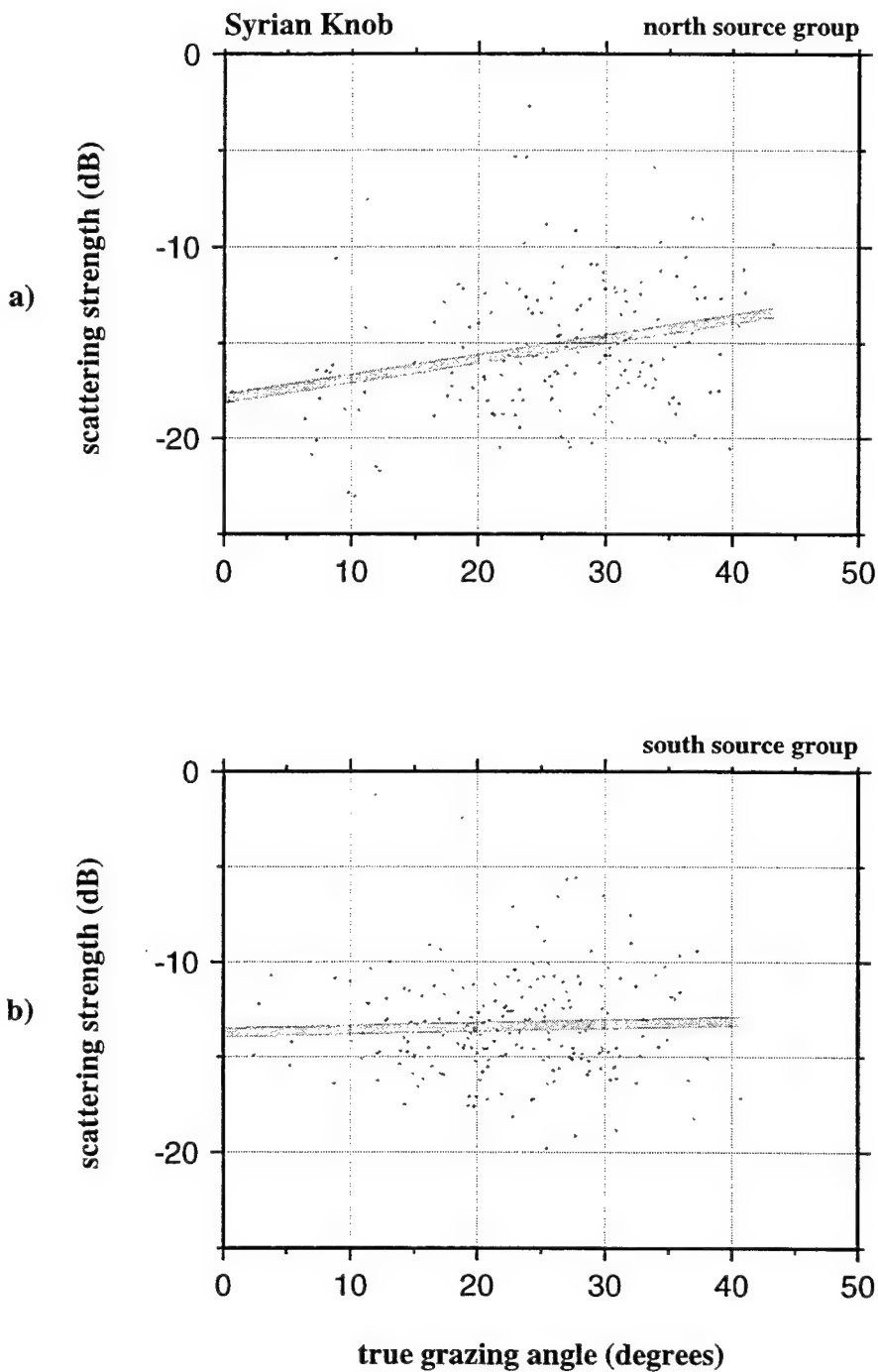


Figure 2-13: Same description as Figure 2-11 but for Casa Grande. For the regression lines, in (a) slope= 0.16 ± 0.09 dB/deg and $r = 0.39$ and in (b) slope= -0.11 ± 0.06 dB/deg and $r = -0.2$. Note that the stack of data from only the 'back-looking' seafloor areas does not improve the correlation nor does it significantly change the slope of the observed trend compared to Fig 2-10.

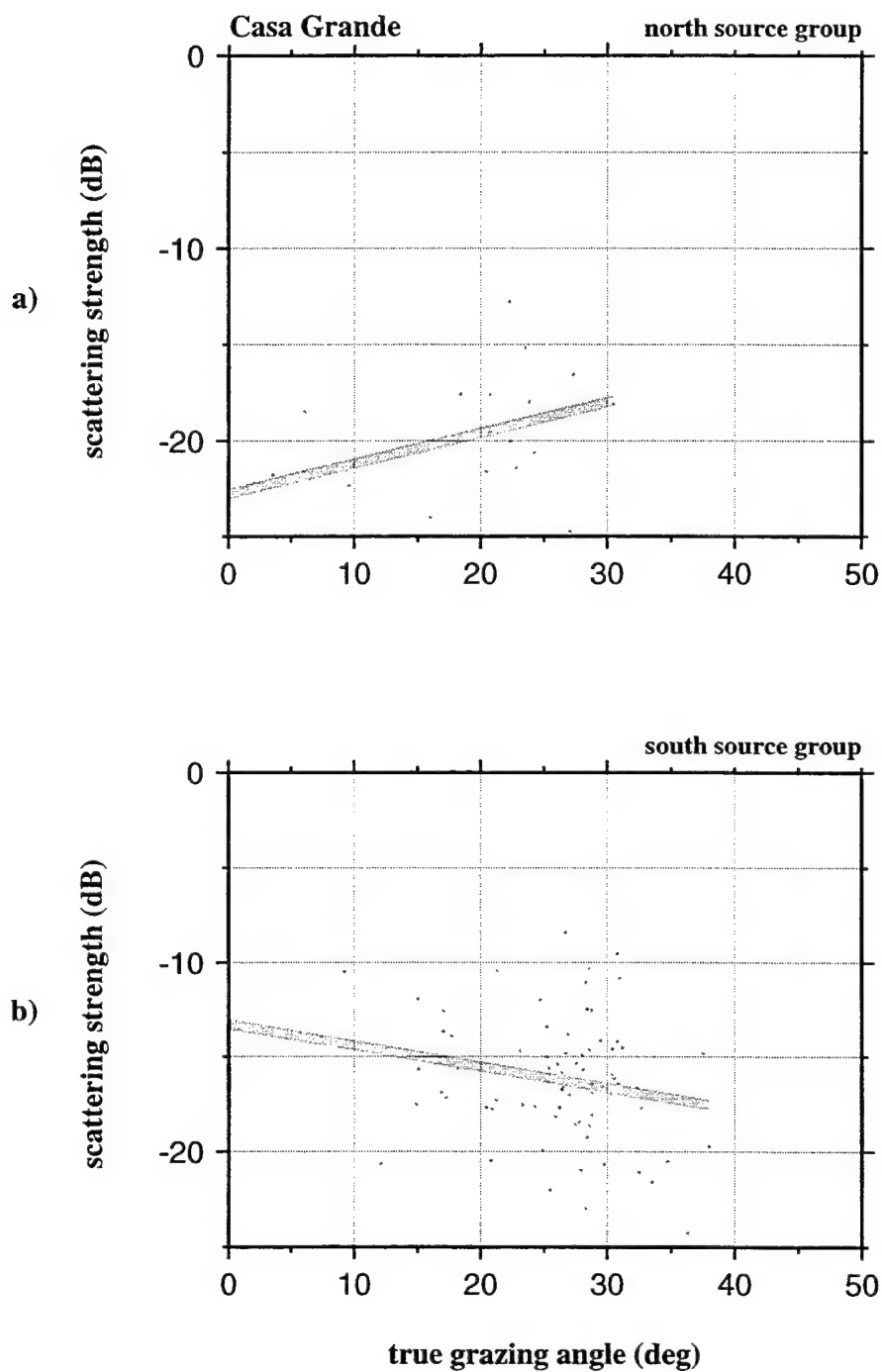


Figure 2-14: Average (per Hydrosweep grid cell) of stacked scattering strength of all intersecting beams mapped to Site A. The grey scale shows the locations of just the highest values (above a threshold at -14.5 dB). The arrows show the general direction of insonification from each source group. In (a) the North Source Group data shows a correspondence to a few isolated topographic highs that have steep dip facing the source direction. When insonified from the east by the South Source group, (b), the asymmetric linear ridges parallel to and facing the Mid-Atlantic Ridge (east) are highlighted. These long, linear ridges are characteristic of OC crustal areas.

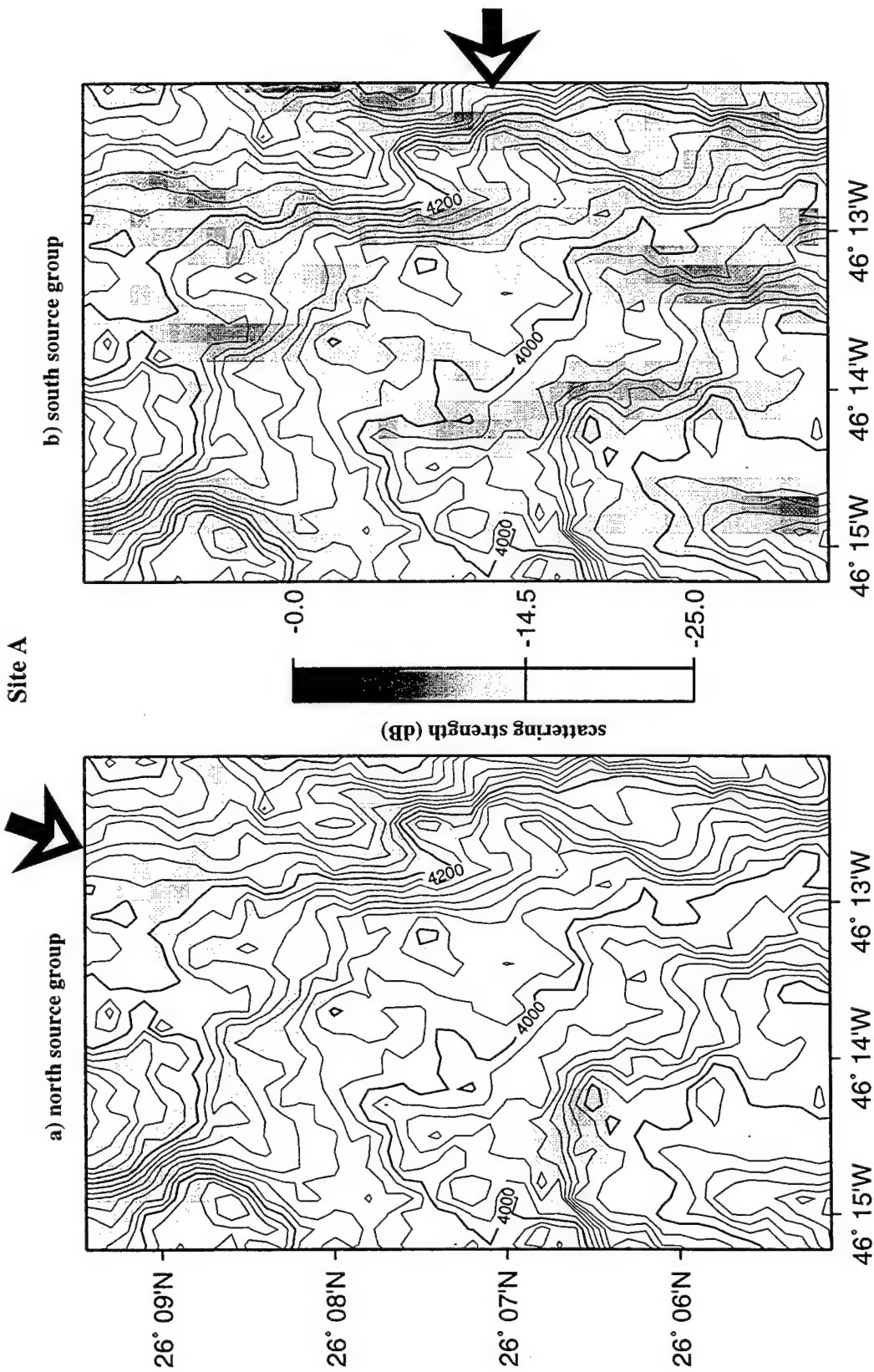
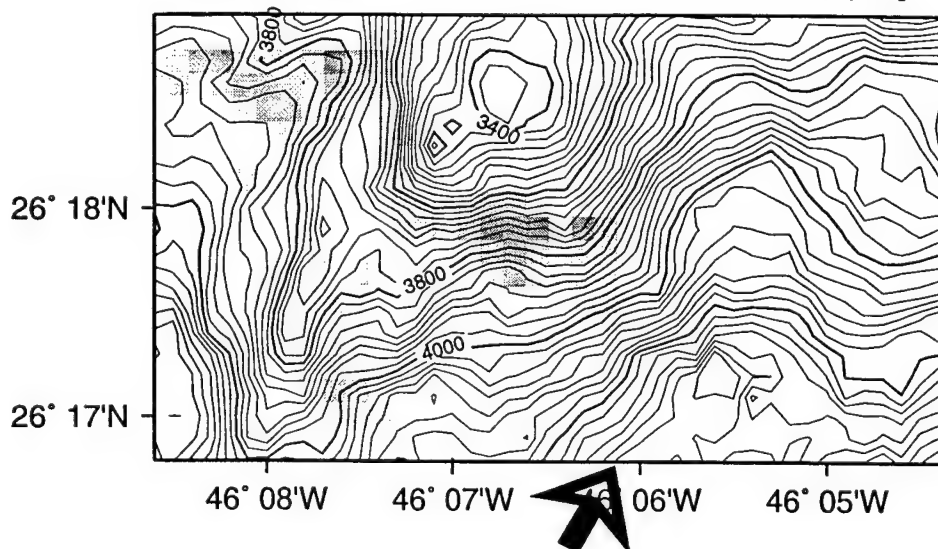


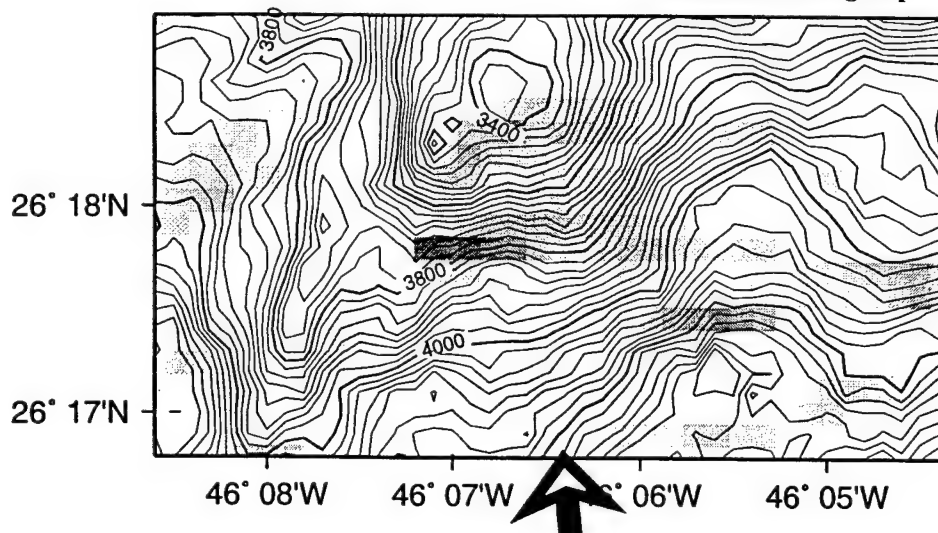
Figure 2-15: Average (per Hydrosweep grid cell) of stacked scattering strength of all intersecting beams mapped to Syrian Knob. The grey scale shows the locations of just the highest values (above a threshold at -12.5 dB). The arrows show the general direction of insonification from each source group. a) When insonified by the North Source Group the steep flanked corners facing the sources are highlighted. The shape of the peaks in the backscattered signals mimic the shape of the seafloor feature. b) When insonified by the South Source group, the south-facing ridge arms and back wall of the block produce a similar arcuate shaped scattering-strength high.

Syrian Knob

a) north source group



b) south source group



scattering strength (dB)



Figure 2-16: Average (per Hydrosweep grid cell) of stacked scattering strength of all intersecting beams mapped to Casa Grande. The grey scale shows the locations of just the highest values (above a threshold at -17.5 dB). The arrows show the general direction of insonification from each source group. a) The data from the North Source Group shows a highlight near the top of the slope where a corner is formed. Strong scattering associated with such sharp changes in slope direction are likely to be due to edge diffractions and may indicate the presence of a steep fault scarp. Most of the slope is at an oblique angle to the main source azimuth and shows little response, similar to Fig. 2-14a. b) When insonified from the direction of the South Source Group, which is more perpendicular to the strike of the dip, the entire slope appears to have relatively high scattering strength, similar to the response of the ridges in Fig. 2- 14b.

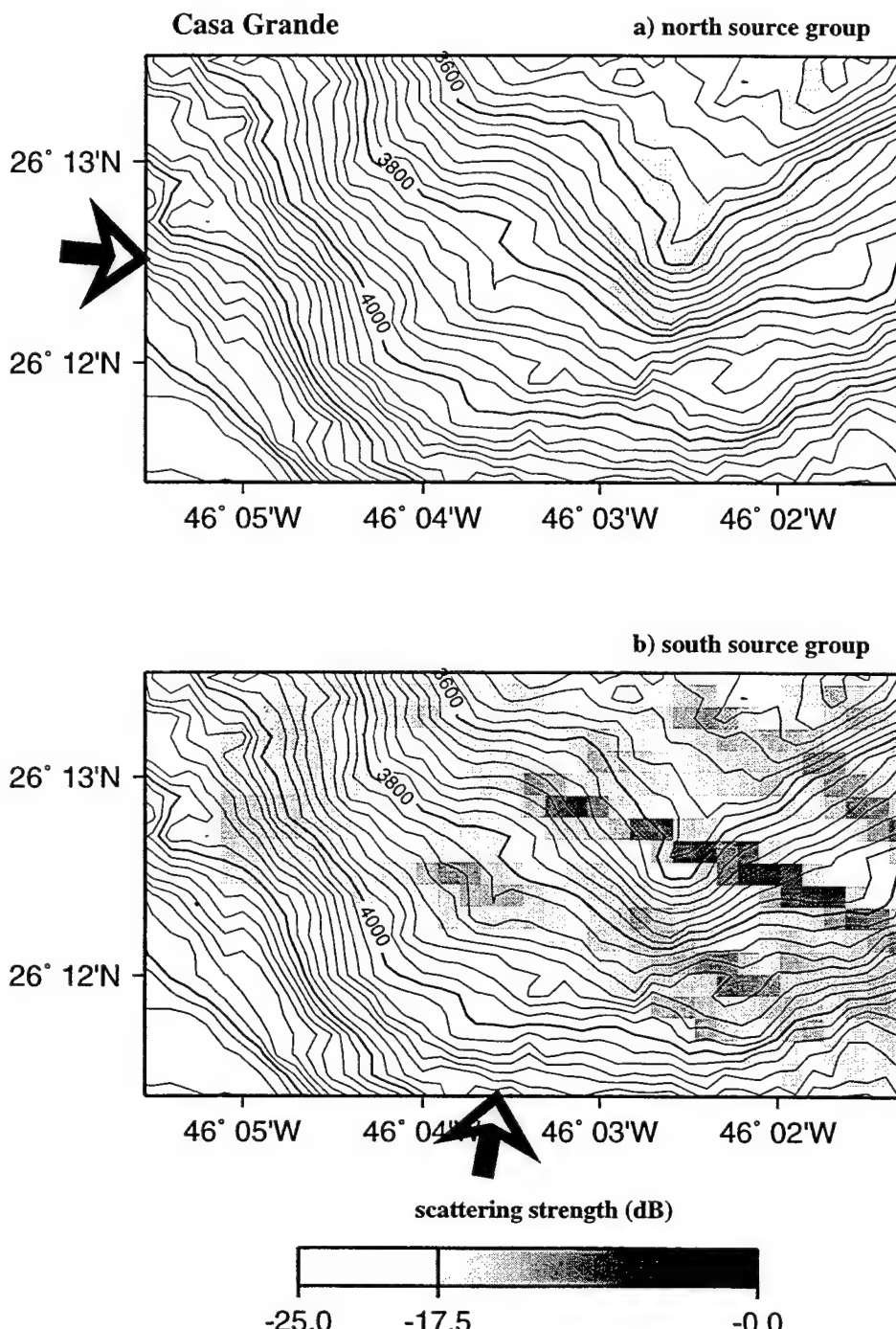


Figure 2-17: Scattering strength of stacked intersecting beams, with the estimated effect of beam grazing angle removed, versus seafloor dip for Site A. The linear fit shown in Figure 2-8 is used to estimate the scattering strength due to beam grazing angle relative to a flat seafloor. The observed scattering strength is then reduced by this amount and plotted relative to the seafloor dip. This is the dip that would be observed by a horizontally propagating (grazing angle = 0°) acoustic wave. After making this adjustment, the regression lines for the North Source Group (a) have slope of $0.12 +/- 0.01$ dB/deg and a correlation coefficient $r= 0.35$ and for the South Source Group (b) have slope of $0.13 +/- 0.01$ dB/deg and $r= 0.39$. The fact that these trends are the same as in Fig. 2-8 indicates that there is no distinction between the grazing angle and seafloor dip in terms of seafloor acoustic response.

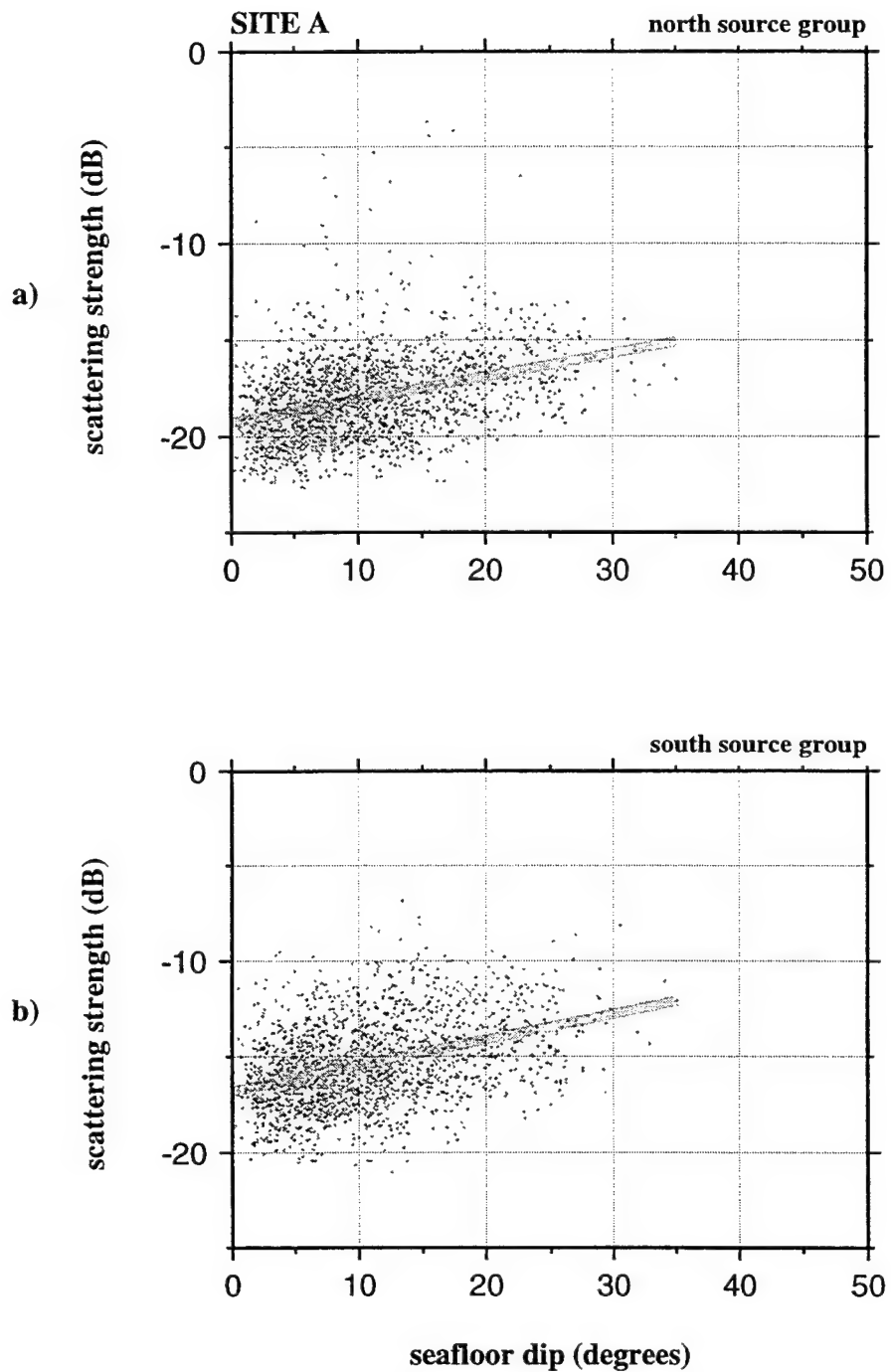


Figure 2-18: Same description as Figure 2-17 but for Syrian Knob. The linear fit shown in Figure 2-9 is used to estimate and remove the scattering strength due to beam grazing angle relative to a flat seafloor. For the regression lines, in (a) slope= 0.10 ± 0.01 dB/deg and $r = 0.27$ and in (b) slope= -0.04 ± 0.01 dB/deg and $r = 0.12$. These trends for seafloor dip are essentially the same as in those found for true grazing angle, shown in Fig. 2-9.

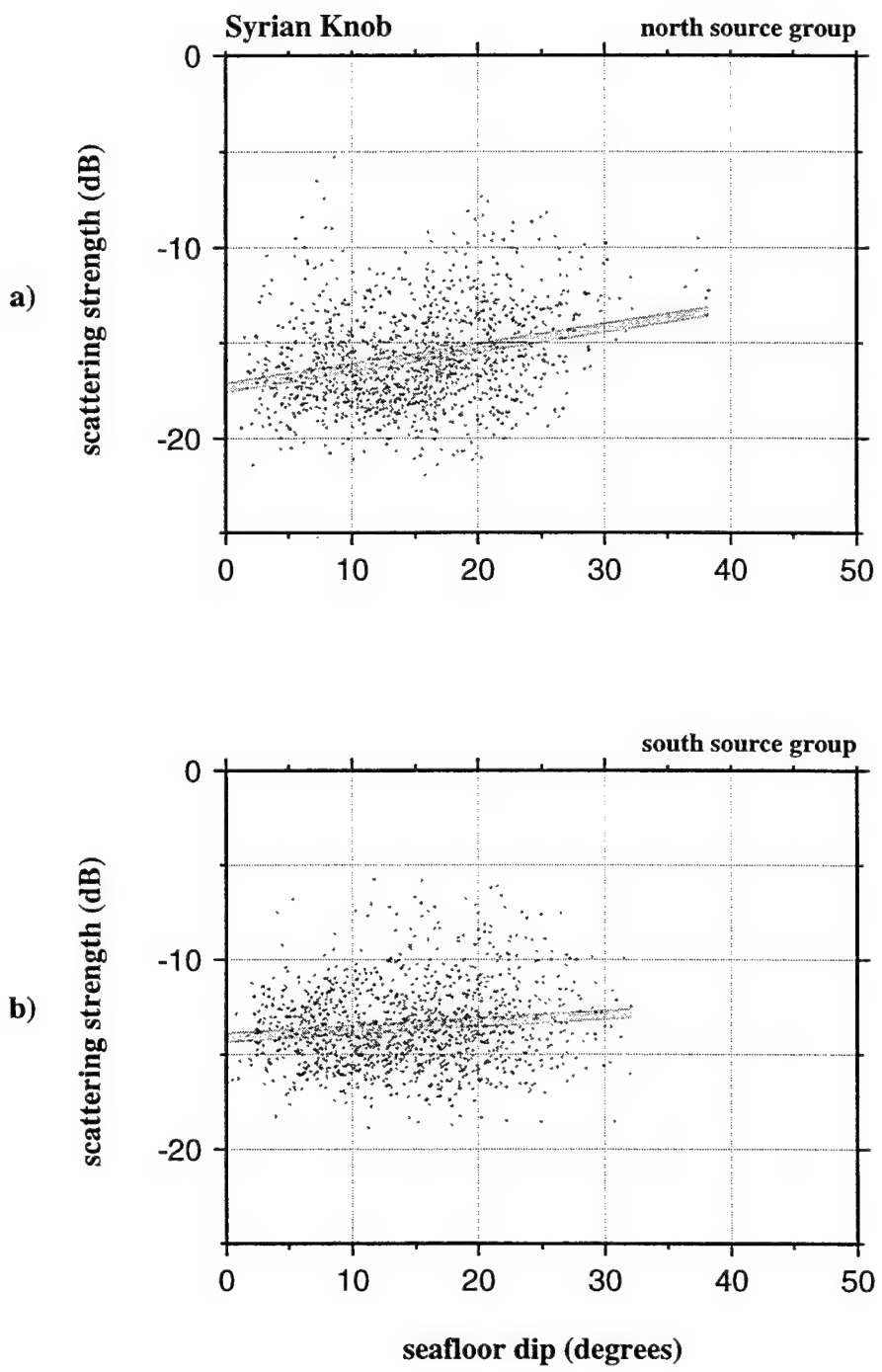
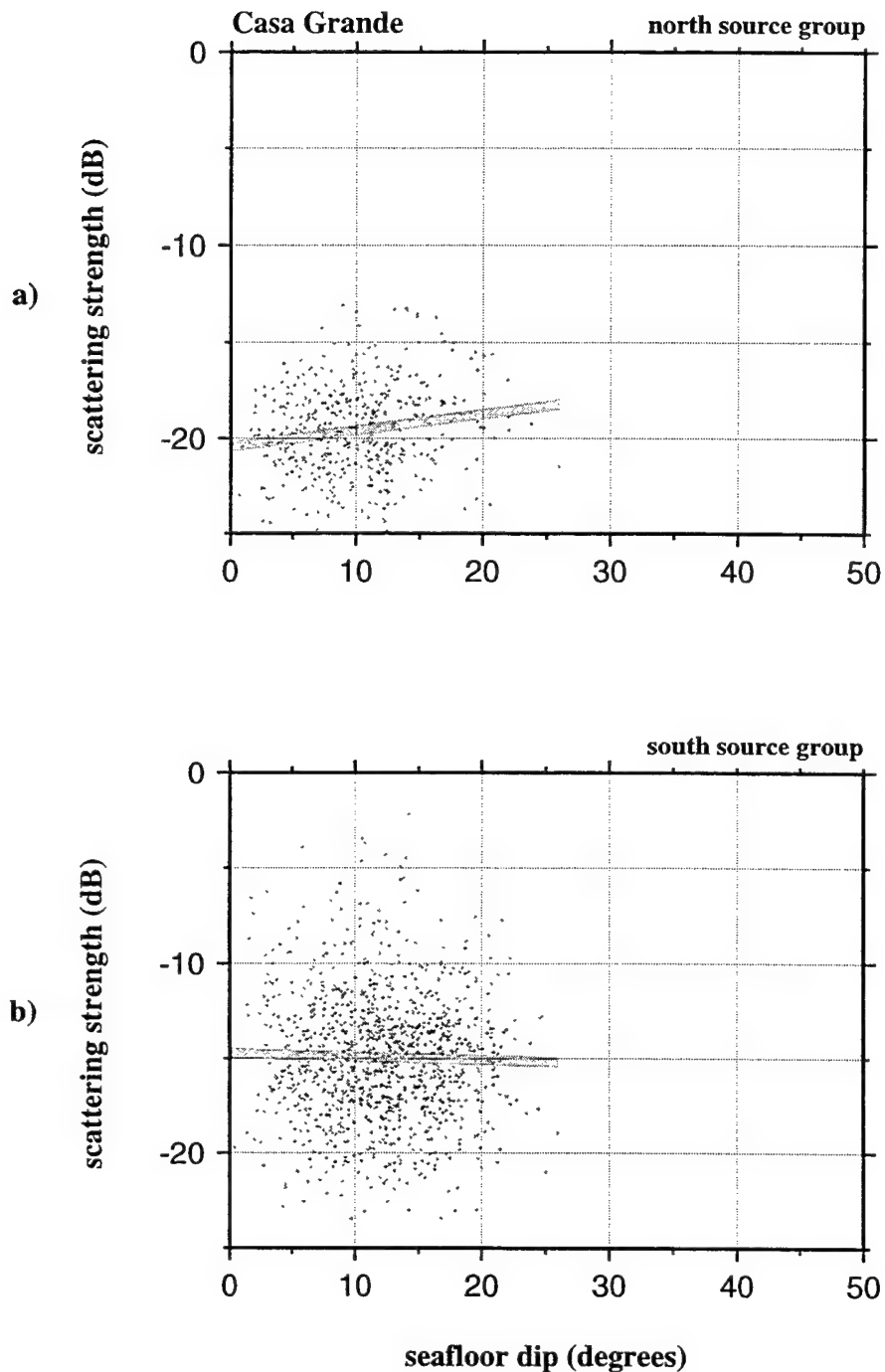


Figure 2-19: Same description as Figure 2-17 but for Casa Grande. The linear fit shown in Figure 2-10 is used to estimate and remove the scattering strength due to beam grazing angle relative to a flat seafloor. For the regression lines, in (a) slope= $0.09 +/- 0.02$ dB/deg and $r= 0.16$ and in (b) slope= $-0.02 +/- 0.02$ dB/deg and $r= -0.03$. These trends for seafloor dip are essentially the same as in those found for true grazing angle, shown in Fig. 2-10.



Chapter 3

The Geological Model

Introduction

In the previous chapter, we showed that the strongest backscattered signals are returned from steep, high standing areas of the seafloor (Figures 2-14 and 2-15). However, it was also shown that the strength of the backscattered signals are not strongly correlated to the seafloor dip measured at the scale of resolution of Hydrosweep bathymetry data (≈ 200 m). We also have observed that in this region, backscattered signals are also returned from low-lying seafloor areas, so that it cannot be argued that only the high-standing areas are insonified.

The premise of the remaining portions of this thesis is that the variation in observed signals scattered from the seafloor is primarily caused by variations in seafloor and subseafloor properties that occur at scales much smaller than the 200 m horizontal resolution of Hydrosweep data, and particularly at wavelength-scales, which for the ARSRP scattering data is about 6 m in the water column but varies in the subseafloor according to velocity. (The acoustic wavelength in water, of the ARSRP data, is between 6 and 7 m, corresponding to the source frequency bandwidth of 200-255 Hz.) This supposition is based on the theory of wave scattering and in particular on the principle that, in comparison to scattering from wavelength-scale heterogeneities, scattering from very large or very small heterogeneities is negligible (Aki and Richards, 1980; p. 749).

Therefore, in order to continue the investigation of mechanisms of acoustic backscattering from the seafloor it is necessary to define seafloor structural variation at much finer scales than available in Hydrosweep data, and to include subseafloor variations. We use numerical wavefield modeling to predict the scattered wavefield from a seafloor model with variations in interface and volume properties at wavelength-scales. This modeling allows us to compute backscattered signals for specific geological models and to quantify the sensitivity of these signals to changes in the geophysical parameters.

In this chapter, a 2-D geological model is defined from near-bottom, high resolution, bathymetry (Mesotech and DSL-120) surveys. The model has seafloor structure typical of the steep, fault-generated ridges that produce strong backscattered signal within Site A. The model definition includes wavelength-scale details of the seafloor morphology and seabed volume heterogeneities. This model is then passed to the Numerical Scattering Chamber (NSC), where the theoretical wavefield scattering is calculated. The NSC is described in detail by Stephen and Swift (1994). A complete geological model is defined in terms of interface morphology, spatial characteristics of volume heterogeneity, and the geophysical parameters (compressional-wave velocity, shear-wave velocity, attenuation, and density).

To accurately represent propagating waveforms and suppress numerical noise, the input model, which is represented in the NSC as a grid of material properties, is sampled at $\frac{1}{15}$ th of the compressional wavelength in water. For a 6 m wavelength, this means sampling the model every 0.4 m. The NSC uses a Gaussian pulse beam as the insonifying wavefield. As described by Stephen and Swift (1994), Gaussian beams provide realistic source wavefields with several advantages over planar wavefields and wavefields generated by arrays of point sources. In particular, side-lobe energy that is problematic in point source arrays is not present in Gaussian beams. Also, Gaussian beams propagate energy in a single direction like a simple plane-wave source, but unlike plane-waves the Gaussian beam is defined with a finite width, which reduces the unrealistic edge-effects that occur in numerical modeling of finite models with infinite plane-waves. Because the Gaussian beam is defined with a finite width, it also limits the size of the model necessary for accurate calculation of the scattered

wavefield. In our modeling we use a Gaussian pulse beam with a peak frequency of 250 Hz which is incident on the seafloor at 15° grazing angle. This beam has a minimum seafloor footprint of $72 \lambda_w$ or 432 m (where λ_w is the source wavelength in water). The minimum footprint is defined by the portion of the beam intersecting the seafloor that has amplitudes within 20 dB of the peak amplitude, which occurs along the axis of propagation at the center of the beam. This restricts the lateral extent of the geological model to 432 m. A longer model will not be completely included in the beam footprint. Decreasing either the frequency or the grazing angle would require a larger model space. There is no specific requirement for model (sub-seafloor) depth, except that it should be defined such that the wavefield can propagate at least several wavelengths through the subsurface media. In our modeling we include a depth of 12 $\lambda_w = 72$ m, which is sufficient depth to account for the interaction of the low-grazing-angle wavefield with subseafloor heterogeneity. With the spatial sampling rate of 0.4 m, a geological model 72 m x 432 m (model depth x length) translates to 181 x 1081 grid points in the NSC.

The size of the input model to the NSC is not sufficient to enclose a complete model of many typical seafloor features, like ridges. A single seafloor ridge, typical of the source of strong backscatterer in Site A, rises 100-300 m over a horizontal distance of 300-500 m. Modeling scattering from such a ridge requires that we divide the ridge model into smaller regions for the NSC calculation. Therefore, an initial geological model of a 'typical' seafloor ridge structure is developed and then subdivided into scattering models of suitable size.

Whenever possible, model characteristics are determined from data at or near Site A. The data available are near-bottom bathymetric surveys used to define the seafloor morphology; photographic images used to define seafloor material type; local estimates of sediment thickness; and shallow sediment velocity and density structure. Three types of bathymetry, Hydrosweep, DSL-120 and Mesotech, listed in order of increasing resolution but decreasing survey coverage, are available for defining the seafloor structure within Site A. Coincident with the Mesotech data are electronic still camera (ESC) and video images, showing bottom details along the track followed

by the JASON ROV (remotely operated vehicle) (ARSRP, 1992). The other local data are sediment-property measurements acquired in the sediment pond adjacent to Site A (Fu et al., 1996) and estimates of sediment thickness made from reflection profiling and side-scan sonar interpretation by Jaroslow (1997) and from statistical estimation by Webb and Jordan (1996).

Other model characteristics, such as subbottom heterogeneity and igneous basement velocity and density, are estimated from published analyses of regional data, including Ocean Drilling Program (ODP) and Deep-Sea Drilling Project (DSDP) reports, Office of Naval Research (ONR) publications and research journals. Some parameters, in particular the scale and characterization of volume heterogeneity and talus properties, can only be estimated.

In the following sections, the seafloor and shallow subseafloor (seabed) are defined as accurately as possible. It must be kept in mind that the resulting model is not an exact description of any specific seafloor structure. Instead, the model is defined as a reasonable and characteristic representation of a type of seafloor structure, with sufficient precision to carry out accurate numerical modeling. It is certainly true that exact seafloor and seabed properties depend on the specific seafloor location. However, it is also true that the exact properties at a specific location can be expected to lie within a limited range of values characteristic of the seafloor material, age and tectonic region. Therefore, in defining the physical properties of the material in the geological model, it is more important to define a reasonable range for their values than to determine a single, 'exact' value.

3.1 2-D vs. 3-D Modeling

Before describing the geological model, it is important to discuss the limitations and advantages of numerical modeling in 2-D, as done in the NSC, compared to a more exact, 3-D code.

Because the seafloor is obviously a 3-D structure, ideally the numerical wavefield modeling would be performed in 3-D rather than 2-D. Some of the limitations of

2-D numerical wavefield modeling are: (1) It does not account for wave types that have particle motion out of the plane of propagation, such as SH-waves and Love waves, and (2) it does not account for out-of-plane scattering and interference effects. 2-D numerical modeling is comparable to 3-D numerical modeling if there is little variability in the 3-D model in the direction normal to the strike of the 2-D profile model. In order to minimize the error in the our modeling, we choose a 2-D geological model that is normal to the strike of the local large scale (3-D) geological structure, i.e., normal to the ridges within Site A. The difference in scattering between our 2-D model and an exact 3-D model has not been explicitly determined. Bradley (1994) compared 2-D and 3-D numerical calculations of scattering from 3-D subseafloors with wavelength-scale volume heterogeneities and rms velocity perturbations of 10%, and he concluded that the 2-D modeling estimated the total scattered field within 10% of the value calculated in the 3-D modeling. He also compared 2-D and 3-D scattering from a 3-D rough-surface model and found that in general the numerical modeling in 3-D produced higher intensity scattering on the order of 3-5 dB. Considering this, we assume that the scattered field intensities we have calculated in our 2-D modeling are within about \pm 10-20% of the values that would be generated if the modeling had been done in 3-D.

The primary advantage of modeling wavefield propagation in 2-D as compared to 3-D is computational speed and feasibility. The NSC modeling code, running on a DEC/Alpha workstation, takes about 18 hours to compute the results for a single model. The size of this model, in wavelengths, is $72\lambda \times 12\lambda$. Although memory limitations preclude the possibility, a 3-D model $72\lambda \times 72\lambda \times 12\lambda$ would take at least 36 days to run on the same workstation. Even with 'state-of-the-art' multi-processor hardware, 3-D modeling is a very slow process. For example, Olsen et al. (1995) computed a 3-D wavefield model which was $38\lambda \times 23\lambda \times 8\lambda$ using all 512 processing nodes on an nCUBE-2 computer. Their calculation took 23 hours, computing at the rate of 17 seconds per time step for 4800 time steps. Our 3-D seafloor model, with the dimensions listed above, would be nine times as large as the Olsen et al. (1995) model and would need to be run for 15,000 time steps. We estimate that it would

take about 27 days to run this model on the nCUBE-2. This is clearly not a practical approach when we wish to compare the results of numerous models.

3.2 Geological Model

3.2.1 Seafloor Profile

The geological model is initiated by constructing a 2-D seafloor profile from the bathymetry data available within Site A. The seafloor profile is chosen with the following characteristics.

- 1) It is centered on a 'typical' seafloor structure at Site A that produces strong backscattered signals.
- 2) It is characteristic of a profile approximately normal to the local geological strike.
- 3) It has bathymetry defined with resolution at wavelength-scale.
- 4) To facilitate model vs. observed signal comparisons, it is representative of the structure intersected by a line of insonification (beam) originating at two ARSRP source locations.

Figure 3-1 summarizes the locations of data available at Site A, which include three types of bathymetry survey, a photographic seafloor survey, ARSRP acoustic backscatter data represented by the north and south source groups and locations of core and *in situ* acoustic sediment velocity measurements made by Fu et al. (1996). The Mesotech trackline is the path of the JASON ROV from which the Mesotech bathymetry measurements and photographic images were made.

Only the Mesotech bathymetry data has sufficient lateral resolution to define the seafloor at wavelength and sub-wavelength-scales. The Mesotech data (Figure 3-1) is available over only a very small region, but it is centered on one of the 'typical' strong backscattering areas within Site A. This feature is a long linear ridge typical of outside-corner crust which, as discussed previously (Chap. 2), is formed by co-linear normal faults trending parallel to the MAR. An E-W line, shown in the figure,

intersects both the south source group locations 76 and 44 and the JASON/Mesotech track. This 'insonification' line is also approximately normal to the strike of the predominant seafloor structure defined by the DSL-120 data (Figure 3-2).

To obtain finer-scale bathymetry along the insonification line, the Mesotech data along the most east-west portion of the JASON trackline are used to replace the corresponding section of DSL-120 data. To do so, the Mesotech data are projected onto the line marked in Figure 3-2 as the 'Mesotech bathymetry profile', which is a least squares fit through the Mesotech locations. Because the projection is over such a small distance, there is minimal distortion in the resulting bathymetry profile. (A further projection of these data to the insonification line was also done, but it distorted the Mesotech profile into an unrealistically steep slope and was not used.) The Mesotech bathymetry profile is then compared to the DSL-120 bathymetric profile along the insonification line, as shown in Figure 3-3(a). For reference, the range is plotted as horizontal distance from source location 76. In comparison, the Mesotech profile shows much finer scale details in both vertical and lateral directions, but it has the same basic ridge shape and seafloor steepness observed in the DSL-120 profile. To construct the seafloor profile for the model, the Mesotech data are shifted up 5.8 m and used to replace the matching segment of the DSL-120 profile. The final seafloor profile, shown in Figure 3-3(b), is an accurate representation of seafloor structure in this small area but is clearly not an exact description of the seafloor at a specific location.

3.2.2 Seafloor Type and Cross-section

The classification of the seafloor type is based on interpretation of photographic images recorded from the JASON cameras during the Mesotech survey. Two types of images are available; electronic still camera (ESC) images, recorded every 20 sec, and continuous video recording. The seafloor in each image was described in terms of characteristics such as surface morphology, material and texture, fracture and jointing patterns, and bioturbation. To reduce the image description into a form useful for geoacoustic modeling, the seafloor in each image was interpreted as either sedi-

ment, talus or basaltic basement. These are general classifications that can be used to describe almost any seafloor area and, most importantly, they can be assigned distinctive geophysical properties for geoacoustic modeling. The detailed descriptions of all of the photographic images are tabulated in the Appendix to this chapter. Example photographs from ESC and video cameras are shown in Figure 3-4. The time of each image can be used to find its corresponding seafloor location along the JASON trackline in Figures 3-2 and 3-5. Primarily, these images are from locations along the ridge slope which is a complex of fault scarps. The steep east-facing flank of the ridge is here referred to as a fault scarp even though it probably is made up of several degraded scarps. The upper portion of the scarp has very steep slope ($\geq 40^\circ$) and has a very rough surface of exposed pillow basalts and basalt fragments (Figures 3-4(a,b)). Fractured basalt pillows (Figure 3-4(c)), sediment-filled fissures or open fractures parallel to the ridge strike (Figure 3-4(d)), and bare fractured basalt (Figure 3-4(e)) are observed. The exposures of bare rock are a good indication that mass wasting is an ongoing process in this region. The scarp also has numerous terraces showing the tops of unbroken pillow flows (Figure 3-4(f)) and producing a steplike character on portions of the scarp (Figure 3-4(g)). Sediment is present on the scarp but primarily is in small chutes (Figure 3-4(e)), is trapped on small ledges (Figure 3-4(g)), or is a very light dusting over the surface. Most sediment on the scarp is less than a few tens of centimeters in thickness. Most of these details cannot be included in the geological model. Occasionally (for example Figure 3-4(h)), a larger ledge or chute will trap a significant amount of basaltic debris and sediment. These sediment-covered areas most likely are underlain by talus and are observed in various places along the lower portions of the scarp. The base of the scarp has markedly reduced slope ($\sim 20^\circ$). This slope is covered by pelagic sediment (Figure 3-4(i)) but probably is a talus ramp (following Tucholke et al. (1996)).

Both the plateau at the top of the ridge, beginning at the ridge crest (Figure 3-4(j)), and the base of the scarp are sediment-covered. Except on the high-slope scarp, sediment in the area of Site A is expected to be up to several meters thick, based on the crustal age and deposition rate in this region (Jaroslow, 1997). Pelagic

sediment found in this region of the Atlantic is nannofossil ooze (unconsolidated calcareous mud) (Tucholke et al,1993; Bowles, 1994). The surface of this fine-grained sediment is smooth or mottled by bioturbation and bottom-dweller tracks (Figure 3-4(k)) and occasional current-produced ripple marks. These details are not included in the geoacoustic seafloor model because they vary at much smaller scales than can be represented by the model grid spacing. It is important to note that the sediment supports cobbles and boulders on its surface. Thus, the sediment has non-zero shear strength and can support the propagation of shear waves.

The categorization based on the images is mapped to the seafloor (Figure 3-5) by projecting the camera (ESC) aperture (46° crosstrack and 30° inline) onto the seafloor. This projection includes adjustments for height, heading, pitch and roll of JASON. Seafloor dip has not been taken into account in these projections. The photographic data are recorded as a function of clock time which is then correlated with the JASON position. For reference, times at about five minute intervals are marked along the JASON track line in Figure 3-5. Each rectangle in the figure represents the bottom covered by a single ESC photograph. The ESC images were recorded every 20 sec and JASON was moving very slowly, so a great deal of image overlap occurs, and only image rectangles at one minute intervals are plotted in this figure. The video images are not mapped because they cover the same seafloor as the ESC images, but they are used to clarify the interpretation of the ESC images. Note that useable camera images were not recorded along all sections of the JASON trackline.

The seafloor types defined along the track from 16:10 to 17:40 in Figure 3-5 are used to define the seafloor along the model profile. Where the model profile extends beyond the JASON track, the seafloor type is extrapolated as sediment covered. This is considered reasonable because the whole region has been sedimented and the extrapolation extends into a low-slope area. To define the subseafloor cross-section, it is necessary to make some estimate of sediment and talus thickness. For Site A, two descriptions of sediment thickness are available. One is mapped from seismic reflection profiles and 3.5-kHz sonar (Jaroslow (1997)) and the other is statistical

estimation from Hydrosweep bathymetry (Webb and Jordan(1995)). These estimates of sediment thickness cover very large areas around and including Site A but are made at a much coarser spatial sampling than is appropriate for the geologic model needed in this study. We interpolated the data to a finer contour interval to produce the sediment thickness maps shown in Figures 3-6 and 3-7 for the Site A area. Neither of these maps shows much detail within the extent of the seafloor model profile. The map based on Jaroslow's data (Figure 3-6) suggests that sediment cover is very thin (i.e. most of the profile lies within a < 10 m contour). Contrary to this, the map based on the Webb and Jordan data (Figure 3-7) suggests 10-20 meters of sediment in the same area. Profiles extracted from these data sets, co-located with the seafloor model profile, are plotted in Figure 3-8 with $+/- 10$ m ranges shaded around them. From these profiles it was concluded that a maximum of 20 m of sediment could be expected in the low to the east of the ridge and 10 m on the plateau west of the ridge. It was also estimated that sediment thickness can increase at a rate of about 0.1 meter/meter east of the ridge but at a much slower rate on the plateau above the ridge. These constraints are used in the definition of the geologic model.

With these constraints on sediment thickness, the subseafloor model is defined in the following way (Figure 3-9(a)). Sediment at the base of the scarp is defined as increasing at a rate of 0.1 m/m up to a maximum of 20 m in thickness. On the plateau west of the ridge crest, the sediment is allowed to increase at a rate of 0.05 m/m up to a maximum of 10 m. The base of the sediment mimics the seafloor. The lateral extent of the talus ramp at the base of the ridge is interpreted from the change in slope of the scarp. The upper scarp has a slope of about 45° but the lower section (east of about 15200 m) abruptly decreases to about 16° . This change in slope is characteristic of the transition from the original scarp face to talus slopes observed in this region (Tucholke et al., 1996). Therefore, a wedge of talus, mostly overlain by sediment, is defined at the base of the scarp. The west side of this wedge is assumed to terminate at the edge of the average upper-scarp slope. We chose to terminate the base of the talus wedge where the sediment thickness reaches ten meters. This was an arbitrary choice and it is conceivable that, in fact, the talus extends under

the sediment much farther to the east. There is also a small perched talus fill defined about halfway up the scarp. The remaining portions of the model, below the sediment and talus, as well as the bare portion of the scarp, are defined as basaltic basement.

In Figure 3-9(b), the seafloor model is subdivided into appropriately sized models for the NSC. The incident wavefield is most intense in the center of the grid space, and therefore specific 'targets' of interest are chosen to occupy the center of each model. The 'target' in Model 1 is the layered sequence of sediment, talus and basement, in Model 2 the transition from sediment and talus to 'bare' basement, in Model 3 the steep, rough and bare slope, and in Model 4 the 'corner' at the ridge crest and the transition to increasing sediment cover.

3.3 Geoacoustic Volume Properties

To complete the geoacoustic model, the material properties of sediment, talus and basalt are defined in terms of appropriate ranges for each of the acoustic modeling parameters, i.e., compressional and shear wave propagation velocities and attenuation, and density. Porosity, volume heterogeneity and Poisson's ratio are also important parameters but are implicitly included in the velocity and density definitions. For the numerical modeling, the parameters are varied within these ranges to determine the sensitivity of the scattered signals to a wide variety of realistic combinations. In this section, physical properties are defined based on data acquired at Site A, on results from regional drilling sites, and on published studies of seafloor properties in the Atlantic Ocean Basin.

3.3.1 Sediment Properties

Sediment Properties: Fu et al. (1996)

The only direct measurements of sediment properties in the study area are those reported by Fu et al. (1996). Core samples and *in situ* 'acoustic lance' (compressional-wave velocity) measurements were collected at several locations within the large sed-

iment pond at Site A. These locations are marked in Figure 3-1. These data provide a good description of the top few meters of the sediment. Figure 3-10 is a plot of the core measurements (corrected by Fu et al. to *in situ* conditions) of P-wave (compressional wave) velocity, density and porosity, as well as the acoustic-lance velocity measurements. Of particular interest is the fact that velocity, as measured by the acoustic lance, decreases with depth in the first two meters of sediment before beginning to increase. It is also interesting that the velocity in these first few meters is less than the bottom-water velocity (1530 m/sec) that was measured by Fu et al. (1996). The velocity gradients below 2 m are quite large, on the order of 25 sec^{-1} . These sediment characteristics are probably not unique to Site A. For example, Tucholke (1980) showed that P-wave velocities of the topmost abyssal-plain sediments in the western North Atlantic are consistently lower than water velocity. This observation is consistent with a long history of similar observations (Nafe and Drake, 1963). Acoustic-lance measurements made in a sediment pond approximately 200 km west of Site A show the same low-velocity zone and steep velocity gradients (Fu et al., 1996). We assume that the low-velocity zone and steep velocity gradients in the first few meters of nannofossil ooze are characteristic of this type of sediment. However, we have found no previous numerical modeling of scattering that has included this velocity inversion in the descriptions of deep-water sediment properties.

Considering the close proximity of core measurements within the sediment pond, the measurement values are quite scattered. It is suggested by Fu et al. (1996) that this might be a consequence of core disturbance. Physical-property measurements of deep-sea sediments are difficult because they are very soft and consequently can easily be disturbed and deformed by coring. This is particularly true of the uppermost sediments which are important in this study. It is also possible that some of this variation may be caused by real heterogeneity in sediment properties. The sediment pond at Site A is flanked by steep ridges, and we would expect to find the nannofossil ooze to be interlayered with turbidites, which would add vertical and lateral heterogeneity to the sediment sequence. Detailed geological descriptions of the sediment cores were not included in Fu et al. (1996) however, they describe the sediment pond samples

as "soft, reddish-brown carbonate ooze".

We have used the acoustic-lance velocity and the core density measurements to generate one realistic possibility for the definition of sediment properties. To do this we calculated smoothed averages of the measurements, as shown in Figure 3-10. The average P-wave velocities, from the acoustic lance data, are about 10% lower than the average core measurements but converge above about 1.0 m subbottom. For the numerical modeling the average acoustic-lance velocity measurements and the core density values are extrapolated to the seafloor. As described in the next section, sediment properties below 5 m subbottom and shear-wave velocities can be defined by a model proposed by Bowles (1994).

It is of interest to consider the effect of a low-velocity zone in the sediment on wave propagation. For a compressional wavelength on the order of 6 m (and shear wavelength of 1.5 m or less), a low-velocity zone even a few meters thick in sediment is sufficient to substantially refract the incident wavefield downwards, thereby increasing the depth of penetration of energy and affecting the energy partitioning of the scattered field. Also, modeling results (e.g. Swift and Stephen, 1994) have shown that a velocity gradient in basalt basement has a substantial effect on the scattered field compared to a uniform velocity model. It is of considerable interest, therefore, to compare the numerical wave propagation results of a model with the detailed sediment description based on the Fu et al. data, against modeling results having simpler sediment descriptions.

Sediment Properties: Bowles (1994)

A general description of sediment properties in the ONR Atlantic Natural Laboratory is provided by Bowles (1994), who has summarized the majority of available physical property data appropriate to the description of calcareous sediment (i.e. nannofossil ooze) and has defined a geoacoustic model for sediment thickness up to 300 m. This is a compilation and summary analysis of Deep-Sea Drilling Project (DSDP) and Ocean Drilling Program (ODP) core measurements and previous analyses of similar data. The report includes data from the entire Atlantic Basin and other deep-ocean regions

where calcareous oozes are observed. The physical properties of such sediment are summarized in the form of tables and the following empirical functions:

$$v_p(z) = 1.487 + 0.00013369z + \Delta V_p(z) \quad (3.1)$$

where

$$\Delta V_p(z) = 0.66(1 - e^{(-0.00208z)}) \quad (3.2)$$

and

$$v_s(z) = 0.0625z^{0.3537} \quad (3.3)$$

$$\rho(z) = 1.5743 + 0.0008742z \quad \text{for } (z \geq 2 \text{ m}) \quad (3.4)$$

$$\phi(\rho) = 143.46 - 47.851\rho \quad (3.5)$$

where v_p and v_s are the P-wave and S-wave velocities, respectively, in km/sec, ρ is the density in kg/m^3 , and z is the depth below seafloor, in meters. Porosity, ϕ , is in percent volume. Shear-wave velocity at the seafloor is defined as $v_s(0) = 0.023$ km/s and at 1 meter depth as $v_s(1) = 0.067$ km/sec. The values for the top 20 m of sediment of the Bowles geoacoustic model are plotted in Figure 3-11. Within the top 20 m, the ranges of values from which these empirical functions have been derived are: $1.45 \leq v_p \leq 1.6$ km/sec, $0.023 \leq v_s \leq 0.28$ km/sec, $1.2 \leq \rho \leq 1.9$ kg/m^3 . Average values in the top 20 m of the Bowles model are: $\bar{v}_p = 1.490$ km/sec; $\bar{v}_s = 0.132$ km/sec; and $\bar{\rho} = 1.583$ kg/m^3 . Average values in the top 10 m of the model are: $\bar{v}_p = 1.488$ km/sec; $\bar{v}_s = 0.103$ km/sec; and $\bar{\rho} = 1.579$ kg/m^3 .

These properties are consistent with measurements made on calcareous sediments elsewhere. Average values and ranges of velocity, density and porosity of calcareous sediment on the Ontong-Java Plateau and in the eastern equatorial Pacific (Mayer, 1979; Hamilton et al., 1982; Milholland et al., 1980; Urmos and Wilkens, 1993) are very close to those derived from the compilation by Bowles. The Hamilton (1982) data are primarily from box cores, which sample only about the top 40 cm of the seabed. Richardson et al. (1991) observed shear-wave velocities as low as 0.20 km/sec in the top meter of sediment in shallow water. Agreement with these data suggests that the Bowles model is very representative for near-seafloor calcareous sediment. Even more

generally, it can be stated that the ranges of physical properties of the sediment are representative of a wide variety of unconsolidated deep-sea sediments. For example, Tucholke (1980) analyzed piston core samples of the top 13 m of turbiditic sediment in abyssal plains in the western Atlantic and reported distributions in velocity and density values that are comparable to the values listed above for calcareous sediment. Therefore, the results of numerical modeling performed using sediment properties appropriate for Site A can be considered representative of many seafloor regions.

Bowles' also provides an evaluation of compressional and shear-wave attenuation, but makes it clear that these are very poorly measured properties for near-seafloor sediment. Attenuation is described in terms of an attenuation parameter κ , which has units of $[\frac{dB}{m \text{ kHz}}]$. Bowles values for κ are also plotted in Figure 3-11. The average values of κ in the top 10 m of the model are: $\overline{\kappa_p} = 0.027 [\frac{dB}{m \text{ kHz}}]$ and $\overline{\kappa_s} = 12.59 [\frac{dB}{m \text{ kHz}}]$. In the top 20 m the average values are: $\overline{\kappa_p} = 0.027 [\frac{dB}{m \text{ kHz}}]$ and $\overline{\kappa_s} = 7.61 [\frac{dB}{m \text{ kHz}}]$. Hamilton (1972) showed that there is an approximately linear relationship between observed attenuation and frequency so that values for the attenuation coefficients, α_p and α_s , can be computed from κ_p and κ_s as

$$\alpha_p = \kappa_p f_{kHz} \quad (3.6)$$

and

$$\alpha_s = \kappa_s f_{kHz} \quad (3.7)$$

At $f = 250$ Hz ($f_{kHz} = 0.25$) the average values for the attenuation coefficients are: $\overline{\alpha_p} = 0.007 \frac{dB}{m}$ and $\overline{\alpha_s} = 3.15 \frac{dB}{m}$ in the top 10 m and $\overline{\alpha_p} = 0.007 \frac{dB}{m}$ and $\overline{\alpha_s} = 1.90 \frac{dB}{m}$ in the top 20 m. In our models the maximum thickness of sediment is less than 20 m, and the maximum path length of a compressional wave trapped in the sediment is on the order of 200 m, so that the maximum reduction in compressional-wave intensity would be only 1.4 dB. Contrary to this, attenuation of shear wave energy is very high in sediments and as such will have a very strong effect on scattered shear waves originating within or below the sediment layer. The very high $\overline{\alpha_p}$ and very low $\overline{\alpha_s}$ in the sediment suggests that including a more detailed description of attenuation in the numerical modeling would not significantly alter the modeling results.

In most numerical modeling programs that include attenuation as a model parameter, attenuation is included in the model description as the quality factor, Q , where Q^{-1} is defined as the fraction of energy lost per wavelength of travel through a medium, but being a ratio of energy values, Q is a unitless quantity. Values for Q can be computed from α_p and α_s using an approximate relationship given by Kibblewhite (1989)

$$Q = \frac{8.686\pi f_{kHz}}{\alpha v} \quad (3.8)$$

where v is the propagation velocity of the medium (i.e. v_p or v_s) in km/sec, frequency is in kHz, and α is in $\frac{dB}{m}$. Using the average velocities and attenuation coefficients listed above, the average Q values at 250 Hz are computed as: $Q_p = 654$ and $Q_s = 21$ in the top 10 m, and $Q_p = 654$ and $Q_s = 27$ in the top 20 m.

These values are consistent with other published reports on attenuation in marine sediments. Kibblewhite (1989) made a comprehensive review of measurements of attenuation in marine sediments. In Figures 9 and 10 of that report, compressional-wave attenuation (at ~ 250 Hz) in saturated sediment has an approximate range of $10^{-3} \leq \alpha_p \leq 10^{-1} (\frac{dB}{m})$ while shear wave attenuation ranges $10^{-2} \leq \alpha_s \leq 1 (\frac{dB}{m})$. Hamilton (1976) reported a range for sediments of $10^{-2} \leq \alpha_p \leq 10^{-1} (\frac{dB}{m})$ at 250 Hz. Mitchell and Focke (1980) found an average $\kappa_p = 0.03 (\frac{dB}{m})$ ($\alpha_p = 0.008 \frac{dB}{m}$ at 250 Hz) for calcareous sediments, and a range in the topmost sediment of $5 \times 10^{-3} \leq \alpha_p \leq 10^{-2} (\frac{dB}{m})$. Frisk et al. (1981) found a very low sediment attenuation coefficient of $\alpha_p = 0.0015 (\frac{dB}{m}$ at 220 Hz) in a very low-grazing-angle incident wave experiment. For comparison, the data compiled by Bowles for fine-grained sediment, shows a range in the top 20 m of about $10^{-4} \leq \alpha_p \leq 10^{-2} (\frac{dB}{m})$ and $0.25 \leq \alpha_s \leq 22 (\frac{dB}{m})$. These ranges are quite large, but they emphasize that the most important considerations for modeling are that shear-wave attenuation in sediment should be defined as very strong compared to compressional-wave attenuation (at least an order of magnitude difference), and that the value of Q_s in sediment should almost always be considered to be substantially less than 100.

3.3.2 Sediment Properties: Summary

From the preceding discussion, it is clear that there is more than one way to assign reasonable values to the sediment properties. The sediment model based on the Fu et al. (1996) data is a more precise description of the top few meters of sediment. However, because it is based on data from a single experiment it is treated as just one possible model to be tested along with other, more general models. Also, a large sediment pond flanked by ridges can be expected to have incorporated layers of turbidite flows and therefore these sediment property data may not be very representative of the top-of-ridge sediments. The Bowles sediment model is a 'best-fit' description of the calcareous sediment in the Atlantic Natural Laboratory based on the maximum amount of compiled data. As such, it is considered a likely 'average' model, but it lacks the possibility of interesting details such as the velocity inversion and steep gradients observed in the Fu et al. data. For comparison, a very simple layered model, consisting of one or two sediment layers is also defined. In summary the models are:

- 1) Simple sediment model: assigns constant or gradient values in the sediment layer.
- 2) Bowles sediment model: assigns values from Bowles (1994) geoacoustic model.
- 3) Fu sediment model: assigns values defined in the top 5 m from the Fu et al. (1996) data, with Bowles' model values at greater depth.

Figure 3-12 summarizes the three sediment models that are compared in the numerical modeling. This figure shows the range and variation with depth of v_p , v_s and ρ . Q_p and Q_s are not shown because attenuation was not successfully implemented in the NSC in our study. Both the Bowles model and the Fu model have inherent parameter gradients that vary with depth, so the entire curves are shifted within the appropriate ranges when parameter variations are tested. The simple sediment model is useful for comparison purposes and can be used to isolate the effect of parameter gradients on the scattered field.

Another limitation of the Bowles, and the Bowles and Fu models, is that the range of possible gradients is not well represented. In fact the gradients implicit in

the empirical Bowles functions are much smaller and the gradients observed in the Fu et al. data are much larger, by an order of magnitude, than the gradients usually observed in deep-sea sediments. Hamilton (1979) found that the velocity gradient in deep-sea sediment is depth dependent and derived an empirical function relating P-wave gradient and one-way traveltimes. His results for calcareous sediments suggest that the P-wave gradient decreases from 1.9 sec^{-1} at the surface to about 1.3 sec^{-1} at a one-way travel time of 0.5 sec ($\sim 750 \text{ m}$). Tang et al. (1995) calculate a gradient of 1.4 sec^{-1} in the sediment pond at Site A. Average P-wave velocity gradients are $1\text{--}2.5 \text{ sec}^{-1}$ for most marine sediment (Tucholke and Shirley, 1979; Houtz et al., 1968; Nafe and Drake, 1957). The data from Fu et al. (1996) indicate that a very high velocity gradient of about 25 sec^{-1} may exist in the first few meters.

Shear-wave velocity gradients are expected to be substantially greater than compressional wave velocity gradients in the shallow sediment. Hamilton (1976) found a shear-wave velocity gradient of 4.65 sec^{-1} in silt-clays and turbidites in the top 40 m of sediment, and estimates that shear-wave velocity gradients are 4 to 5 times P-wave gradients in all near-seafloor unconsolidated sediments. The density gradient predicted by the Bowles equation is about $0.0009 \text{ kg/m}^3/\text{m}$ which seems to be very low compared to other observations. Because density is directly related to porosity, and porosity is expected to decrease very rapidly in the shallow sediment, we expect a much steeper density gradient. In Nafe and Drake (1957), density is shown to increase non-linearly in the top 100 m of deep water sediment at a rate of about $0.005 \text{ kg/m}^3/\text{m}$ but the gradient decreases to an almost linear dependence at greater depths with a gradient of about $0.0001 \text{ kg/m}^3/\text{m}$. The Fu et al. data indicate that density gradients in the topmost sediment can be much greater, on the order of $0.1 \text{ kg/m}^3/\text{m}$ or more over sub-meter intervals. In order to investigate the effects of parameter gradients in sediment, a range of gradients for each of the geoacoustic parameters is defined within the parameter ranges shown in Figure 3-12. Examples are plotted for the simple model case.

It is possible that within the region represented by the models, there is some occurrence of lateral volume heterogeneity within the sediment. The scale and mag-

nitude of such heterogeneity are difficult to estimate. The spatial variation observed in core and acoustic-lance measurements made by Fu et al. (1996) is less than 10 % in density and less than 5 % in velocity, over distances of several kilometers, and it decreases noticeably with depth. This gives some sense of the possible magnitude of variations but does not define lateral spatial scales because the offset of sampling stations is so large. An approximate cyclicity of 0.5-1 m in depth is observed in the plots of velocity and density (Figure 3-10) which can be used as an estimate of the scale of spatial variation in the vertical direction. Variation in the lateral direction is probably at much longer wavelength, because sedimentation via turbidity flows in sediment ponds will extend over large areas. Pelagic sedimentation alone would not be expected to produce any significant lateral variations in sediment ponds or on the upper-ridge areas. Another view of sediment heterogeneity in sediment ponds is provided by Tang et al. (1995). Using data from a near-bottom backscattering experiment over the sediment pond at Site A, Tang et al. interpreted layered regions of irregular sediment structure that were responsible for significant portions of low-angle backscatter signals. The irregular layers are up to 20 m thick and are buried under undisturbed sediment layers at depths of 20 m to 60 m. The scale of the heterogeneity appears to be on the order of 2-5 m vertically but 10-100 m horizontally. No explanation of the origin of such irregular layers is given but we can speculate that they result from debris flows. From this discussion it seems reasonable to estimate lateral variability in sediment properties as occurring at spatial scales of 1-2 orders of magnitude greater than depth variability. However, this conclusion is based solely on descriptions of sediment data that is essentially exclusive of upper-ridge areas. For modeling heterogeneity in sediment in general, it seems most reasonable to assume that vertical gradients are the most likely the most common form of heterogeneity to be found in sediments, whether in sediment ponds or in the upper-ridge regions.

3.3.3 Basaltic Basement and Talus

The geophysical properties of the basaltic basement are estimated from DSDP reports of drilling in similar age oceanic crust (< 20 Ma), from published results of seismic

studies, and from general geological and geophysical descriptions of young oceanic crust.

Basaltic basement is the topmost section of igneous oceanic crust, usually referred to as oceanic 'Layer 2'. This layer is characterized by a relatively steep P-wave velocity gradient ($1\text{-}2 \text{ sec}^{-1}$) and is typically 1-2 km thick. In most areas it is highly fractured and faulted. The shallowest portions of the layer, i.e. the first few hundred meters below the sediment/basement or water/basement interface on 'normal' oceanic crust (i.e. outside-corner crust), are known from ocean drilling and bottom sampling to be primarily made up of basalt pillow and flow lavas, and basalt debris mixed with sediment. These overlie, but are not differentiated from, more consolidated basalt at depth. In regions where the crust has been formed at slow-spreading ridges, it may be that only about half of the oceanic crust is 'normal', in that inside-corner crust, potentially the 'other' half of oceanic crust, is dominantly made up of coarse-grained lower-crustal gabbros and mantle peridotites (Tucholke and Lin, 1994). In general, we would expect these inside-corner regions to have somewhat higher average velocity and density. For 'normal' oceanic crust, such as the outside-corner crust at Site A, the average P-wave velocity of Layer 2 is about 5 km/sec, with a nominal upper-interface velocity of 4 km/s (Fowler, 1990). However, significantly lower velocities are observed in the top \sim 200 m. Hyndman and Drury (1976) estimated velocity in the top 150 m to be about 2.8 km/sec in what is described as a 30% solid basalt and 70% sediment/basalt gravel mixture, increasing to 3.5 km/sec in the next few hundred meters made up of 60% solid basalt and 40% basalt fragments and gravel. Talwani et al. (1971) found a range of velocity from 2.3 km/sec to 3.7 km/sec in the upper 0.5 - 1 km of Layer 2. The lowest velocities tend to occur in areas of thick surface rubble which can be considered representative of talus properties.

The most important control on velocity and density variation in basaltic basement is porosity, which includes large-scale and small-scale fractures as well intergranular pore space. Spatial variation in velocity, density, and attenuation can be related to changes in porosity. Houtz and Ewing (1976) showed that seismic velocity of shallow oceanic crust increases with increasing crustal age, up to about 40 Ma where it levels

off at 5-6 km/sec. This lateral variation is attributed to a decrease in porosity with age (Schreiber and Fox, 1976; Purdy, 1987; Moos and Marion, 1994). There is no general agreement in how this change in porosity occurs. Many processes, including sediment infilling, chemical precipitation in voids and alteration via hydrothermal circulation, and tectonic compression have been proposed as mechanisms for reducing porosity with age. Moos and Marion (1994) suggest that porosity of zero-age crust may be as high as 20-40% and that it is filled over time with low-temperature alteration products, particularly in the upper few hundred meters of basaltic basement. Purdy (1987) found evidence that velocity increases much more rapidly with age in very young crust than predicted by Houtz and Ewing. Purdy concluded that it is the change in pore shape associated with changes in porosity that has the strongest influence on the change in velocity but that there is no dominant process that accounts for the change in either the shape or total porosity.

At the scale of the geoacoustic models, it is only necessary to define basaltic basement properties within the top 200 m below the seafloor. In order to determine more specific ranges for the model parameters, we use information from two DSDP drill sites located on the flanks of the MAR, in oceanic crust of roughly similar age as that found at Site A (\sim 11 Ma). DSDP Holes 395A and 396B are located about 400 km south of Site A on crust that is estimated to be 7 Ma and 10 Ma, respectively (Dmitriev et al., 1978), but on opposing flanks of the MAR. Hole 395A was drilled about 110 km west of the MAR axis and Hole 396B was drilled about 150 km east of the axis. Both holes are in sediment ponds such that the basaltic basement is buried by 100-150 m of calcareous pelagic sediment. Published analyses of laboratory measurements of core-sample properties and geophysical well logs are used to determine properties of the basaltic basement. Hole 396B is drilled into what can be considered outside-corner crust but is about in the middle of the adjacent spreading-ridge segment. As such it is most representative of the basaltic crust at Site A. Hole 395A is drilled in crust within the axis of maximum depth of a small-offset discontinuity, and it therefore may be less representative of the crust at Site A.

For Hole 396B, core measurements made at approximately *in situ* pressures by Christensen et al. (1978) are considered upper bounds on velocity and density, and lower bounds on porosity, because samples are cut only from cores with minimum fracturing. The drilled basaltic basement is described as interlayered pillow basalts and flow basalts overlying a thick zone of basalt fragments and breccia. At 0.4 kbar (a confining pressure of about 0.5 kbar is considered to be the confining pressure of the upper portion of Layer 2 (Schreiber and Fox, 1977) the range in P-wave velocity is $5.49 \leq v_p \leq 6.28$ (km/sec) with an average value of 6.02 km/sec. Shear-wave velocity ranges $2.79 \leq v_s \leq 3.40$ (km/sec), density is $2.67 \leq \rho \leq 2.88$ (kg/m^3), and porosity is $3 \leq \phi \leq 10$ (%). Another parameter that is very useful in describing basaltic basement, Poisson's ratio (σ), is calculated and ranges from 0.26 to 0.35. The results from these core samples agree very well with measurements reported by Schreiber and Fox (1977) performed on dredge samples from the FAMOUS study area on the MAR. They found ranges, at 0.5 kbar, of $5.2 \leq v_p \leq 6.0$ (km/sec) and $2.59 \leq \rho \leq 2.92$ (kg/m^3). Also, Hyndman and Drury (1976) found average velocity and density of $\overline{v_p} = 5.94$ km/sec and $\overline{\rho} = 2.8$ kg/m^3 in laboratory measurements of 4 to 9 m.y. old basalt samples recovered from drilling on the flanks of the MAR.

Geophysical properties measured by well logs are usually considered more representative of bulk properties than core measurements because they measure average properties of a comparatively large volume of rock around the borehole *in situ*. Well logs therefore are better sources of data for defining realistic geoacoustic modeling parameters. Well logs from Hole 396B, reported by Kirkpatrick et al. (1978), show that the upper 170 m of basement is made up of pillow basalts and basalt flows. In the upper 50 m of basement the P-wave velocity averages about 2.8 km/sec but can range from 2.5 km/sec to 4 km/sec in short intervals. Density in this section averages about $2.2 \text{ kg}/\text{m}^3$ with a range of 2.1 to $2.3 \text{ kg}/\text{m}^3$, and porosity ranges from 30-40%. Over the next 100 m, the averages are significantly higher and the ranges are $4.0 \leq v_p \leq 4.8$ (km/sec), $2.4 \leq \rho \leq 2.6$ (kg/m^3) and $13 \leq \phi \leq 21$ (%). These pillow basalts overlie a thick section of basalt breccia and gravel that has much lower velocity (~ 1.8 km/sec) and density ($\sim 1.55 \text{ kg}/\text{m}^3$) and higher porosity ($\geq 30\%$),

which can be considered representative of talus properties. In the top 100 m of the section logged, velocity increases at a rate of about 20 sec^{-1} , which is an order of magnitude greater than the nominal Layer 2 gradient of $1\text{-}2 \text{ sec}^{-1}$. Equally notable is that the velocity decreases at about the same rate in the lower half of the hole. These logs suggest that the most realistic model of the uppermost basaltic basement should include steep gradients and volume heterogeneity over a wide range of scales.

Geophysical logging results in Hole 395A are summarized by Moos (1990). This hole penetrated 93 m of sediment and 571 m of basement primarily made up of thick pillow basalts. Average properties in the upper 400 m of the basement are $\bar{v}_p = 4.41 \text{ km/sec}$ and $\bar{\rho} = 2.72 \text{ kg/m}^3$. In the bottom section ($> 400 \text{ m}$), shear-wave velocity was measured and the average was found to be $\bar{v}_s = 2.73 \text{ km/sec}$. Moos characterizes the sections of pillow basalts as being distinguished by their high porosities and low velocities at the tops of the sections, with porosity decreasing and velocity increasing steadily with depth. There are four distinguishable basalt sections, on the order of 100 m thick. The uppermost section has a range in velocity of about $2.0 \leq v_p \leq 5.5 \text{ km/sec}$ and an estimated gradient of about 3 sec^{-1} . The lower sections have more narrowly constrained range, $3.5 \leq v_p \leq 5.5 \text{ km/sec}$ and smaller gradients of $1\text{-}2 \text{ sec}^{-1}$. Density does not show as strong a gradient as the P-wave velocity and has a range throughout the logged section of $2.6 \leq \rho \leq 2.8$. Purdy (1987) performed a near-bottom refraction seismic experiment at this drill site and found the average P-wave velocity in the uppermost basement to be 4.12 km/sec , with the possibility of a velocity gradient up to 0.5 sec^{-1} . This value is similar to the average velocity in the upper 400 m found by Moos but is much higher than the well log values in the top 100 m. It must be noted that the wavelength of Purdy's refraction experiment is on the order of 100 m and therefore is measuring average properties over much larger scales than the well logs. As such, Purdy's value represents a good measure of \bar{v}_p in the top few hundred meters of basaltic basement, but it does not preclude the much stronger velocity gradients observed in the well log data, nor the intervals of much lower velocity in the top 50-100 m of basement which will have significant impact on wavefields with smaller wavelengths.

Measurements of attenuation in upper-crustal oceanic basalt are relatively rare. Christeson (1994) reports high attenuation, $10 \leq Q_p \leq 20$, in shallow seafloor near the East Pacific Rise. Jacobson and Lewis (1990) also report relatively high attenuation, $20 \leq Q_p \leq 50$, in the uppermost 650 m of 0.4 Ma crust near the Juan de Fuca Ridge. Their results also suggest that there is crustal heterogeneity present at scales of hundreds of meters. Wepfer and Christensen (1990) made laboratory measurements of Q_p and found that at seafloor pressures (≈ 0.4 kbar), Q_p ranges from 10 to 80. All of these measurements suggest much greater attenuations in the topmost portion of Layer 2 basalts than are usually considered for solid basalt. For example, Bowles (1994) uses values of $Q_p \approx 300$ and $Q_s \approx 180$ for average basaltic basement. It is likely that attenuation in the top few hundred meters of basement is, in fact, quite high in relatively young crust. In general, attenuation increases as porosity increases and as the volume of alteration products increases. Attenuation also increases as velocity and density decrease, which is partially attributable to increasing porosity. Low velocity in the top 0.5 km of crust is considered to be due to the high density of cracks and fissures in basalt. Fracturing is also considered the primary reason for the high Poisson's ratio, σ , in the upper 500 m of oceanic basement, interpreted from refraction seismic data to be $0.32 \leq \sigma \leq 0.38$ (Shearer, 1988). These factors are indications that shear-wave attenuation is very high and that shear-wave velocities are quite low. We estimate the range of shear-wave velocity in the upper 200 m to be $0.5 \leq v_s \leq 2.5$ km/sec. Given that the focus of the modeling in this study is on the effects of properties in the shallowest crust, values for basement Q considered most representative are $20 \leq Q_p \leq 50$ and $5 \leq Q_s \leq 30$.

A realistic model of basaltic basement must include volume heterogeneity. Core descriptions and well logs show that the scale of heterogeneity ranges from a few centimeters (scale of rubble) to more than 100 m (scale of lava flows). The magnitude of property variations at these scales can range as high as 50% or more but decreases with depth. The lateral heterogeneity of the upper crust probably has correlation lengths on the order of hundreds of meters as suggested by Jacobson and Lewis (1990). Most of the well log data suggests that there is fundamental heterogeneity

in the form of lava flows intermixed with layers of basaltic rubble. Goldberg and Sun (1997) analysed well log data from the flank of the East Pacific Rise and found that the subseafloor was dominated by variations having correlation lengths of 1 m and 10 m. They associated these correlations with pillow basalts and basalt flows. Few direct measurements of lateral heterogeneity, particularly in the shallowest crust, have been made. One example of such a measurement is reported by Stephen (1988), in which lateral heterogeneity in P-wave velocity is found to vary over distances from 1 to 3 km in the upper 600 m of 5.9 Ma basaltic crust. Stephen also shows that the heterogeneity can be explained by lateral velocity gradients from 1 to 2.5 sec^{-1} , which are comparable to observed vertical gradients. Stephen suggests that a primary cause of the heterogeneity in seafloor basalt is lateral variation in crack (fracture) density. With this in mind, we also include models with fault zones in our study. These fractures are modeled as low-velocity, low-density vertical strips within the ridge structure. Figure 3-13 shows an example of this type of heterogeneity included in Model 3.

Using a technique similar to that described by Dougherty and Stephen (1988) and Swift and Stephen (1994), we model heterogeneity as random parameter variations occurring at various scales. The random heterogeneity can be added to the talus and basalt in the model, with or without fracture heterogeneity and with or without gradients. Because real heterogeneity occurs over a broad range of scales, it may be most appropriate to use a self-similar correlation function to define the randomness. The power spectra of a Gaussian correlation function and a self-similar correlation function are given by Frankel and Clayton (1986). A plot of the spectra of these functions for a fixed wavenumber is shown in Figure 3-14. The plot shows that a Gaussian description of heterogeneity focuses attention on a single or narrow range of correlation lengths. This might be most appropriate in modeling the talus zone. Contrary to this, the self-similar correlation gives equal weight to a broad range of correlation lengths and is a better method of modeling a region, such as basaltic basement, that has heterogeneity at many scales. However, the Gaussian models have a distinct advantage when we are trying to quantify the effects of spatial characteristics

because they allow us to focus on specific and well defined correlation lengths.

3.3.4 Basaltic Basement and Talus: Summary

Realistic models of basaltic basement and talus should have geoacoustic parameters defined with gradients and volume heterogeneity. Models using constants for parameter values are useful for comparison purposes but are not realistic descriptions of the subsurface. Constraints on the ranges of parameters are estimated as follows. The P-wave velocity range for talus is $2.2 \leq v_p \leq 3.6$ km/sec and for the top 200 m of basalt is $2.5 \leq v_p \leq 4.8$ km/sec. For simplicity, shear-wave velocities are calculated from compressional-wave velocities using v_p/v_s ratios defined by

$$\frac{v_p}{v_s} = \left(\frac{1 - \sigma}{0.5 - \sigma} \right)^{\frac{1}{2}} \quad (3.9)$$

where Poisson's ratio, σ , ranges in the upper crust over $0.32 \leq \sigma \leq 0.38$ (Shearer, 1988). The range in shear-wave velocity is estimated to be $0.3 \leq v_s \leq 2.0$ km/sec for talus and $0.5 \leq v_s \leq 2.5$ km/sec for basalt. The range in density for talus is taken to be $2.0 \leq \rho \leq 2.4$ kg/m³ and for basement is $2.2 \leq \rho \leq 2.8$ kg/m³.

In order to simplify the definition of model parameters, they are defined as linear functions of depth

$$v_p = v_0 + \Delta v_p \cdot z \quad (3.10)$$

$$v_s = \left(\frac{v_p}{v_s} \right)^{-1} \cdot v_p \quad (3.11)$$

$$\rho = \rho_0 + \Delta \rho \cdot z \quad (3.12)$$

where initial values of velocity and density, v_0 and ρ_0 , are chosen such that the maximum parameter values, for given gradients $\Delta \rho$ and Δv_p , do not exceed the parameter ranges. P-wave velocity gradients as high as 20 sec^{-1} may exist in the very top of basaltic basement even though the average gradients in the upper crust are usually observed as less than 2.5 sec^{-1} .

An alternative description of density is to calculate it as a function of velocity. Dougherty and Stephen (1988) use a relationship of the form $\rho = \text{constant} + 0.38v_p$. Wepfer and Christensen (1990) show a linear relationship of the form $\rho = \text{constant} +$

$0.27v_p$. Bowles in an unpublished report derived the function $\rho = \text{constant} + 0.32v_p$. It is expected that density will vary most rapidly in the shallow crust so the Dougherty and Stephen (1988) function is used to relate velocity and density in the model definition. This also ties the density gradient to the velocity gradient. An example of the geoacoustic parameters for talus and basaltic basement defined in this way is shown in Figure 3-15.

3.4 Conclusion

The geological model has been defined sufficiently to proceed with the numerical wavefield modeling. The constraints on the ranges for each parameter are broader than expected, but this probably indicates real variability in ocean sediment and basaltic basement properties. Hamilton (1980) listed the requirements of a complete geoacoustic model as

- 1) Identification of sediment and rock types at the seafloor and in the subseafloor.
- 2) Thickness and shapes of the layers.
- 3) Compressional-wave velocities.
- 4) Shear-wave velocities.
- 5) Compressional-wave attenuation.
- 6) Shear-wave attenuation.
- 7) Density

All of these parameters have been defined in this chapter and except for attenuation are included in the Numerical Scattering Chamber. Even though seafloor and subseafloor heterogeneity are incorporated in the geoacoustic model via the definition of the velocity and density parameters, the description of heterogeneity, correlation length and amplitude could be considered separate parameters in model definition. These parameters are more thoroughly discussed as they apply to the modeling in the following chapter.

Figure 3-1: Site A bathymetry and ARSRP data locations. Data available at Site A include Hydrosweep, DSL-120 and Mesotech bathymetric surveys. DSL-120 data covers only the area within the large box labeled as Site A. Mesotech data was acquired only within the very small box, shown in the expanded view, along the JASON vehicle track. In the sediment pond, 'acoustic-lance' velocity measurements (triangles) and short cores (squares) were obtained by Fu et al. (1996). ARSRP source/receiver locations are indicated by the numbered, filled circles. From these locations, monostatic acoustic reverberation data were acquired during the 1993 Acoustic Reverberation Special Research Program (ARSRP) cruise. The transect of the geological model profile is shown in the expanded view. The projection of this transect, shown in the large map, intersects ARSRP locations 44 and 76.

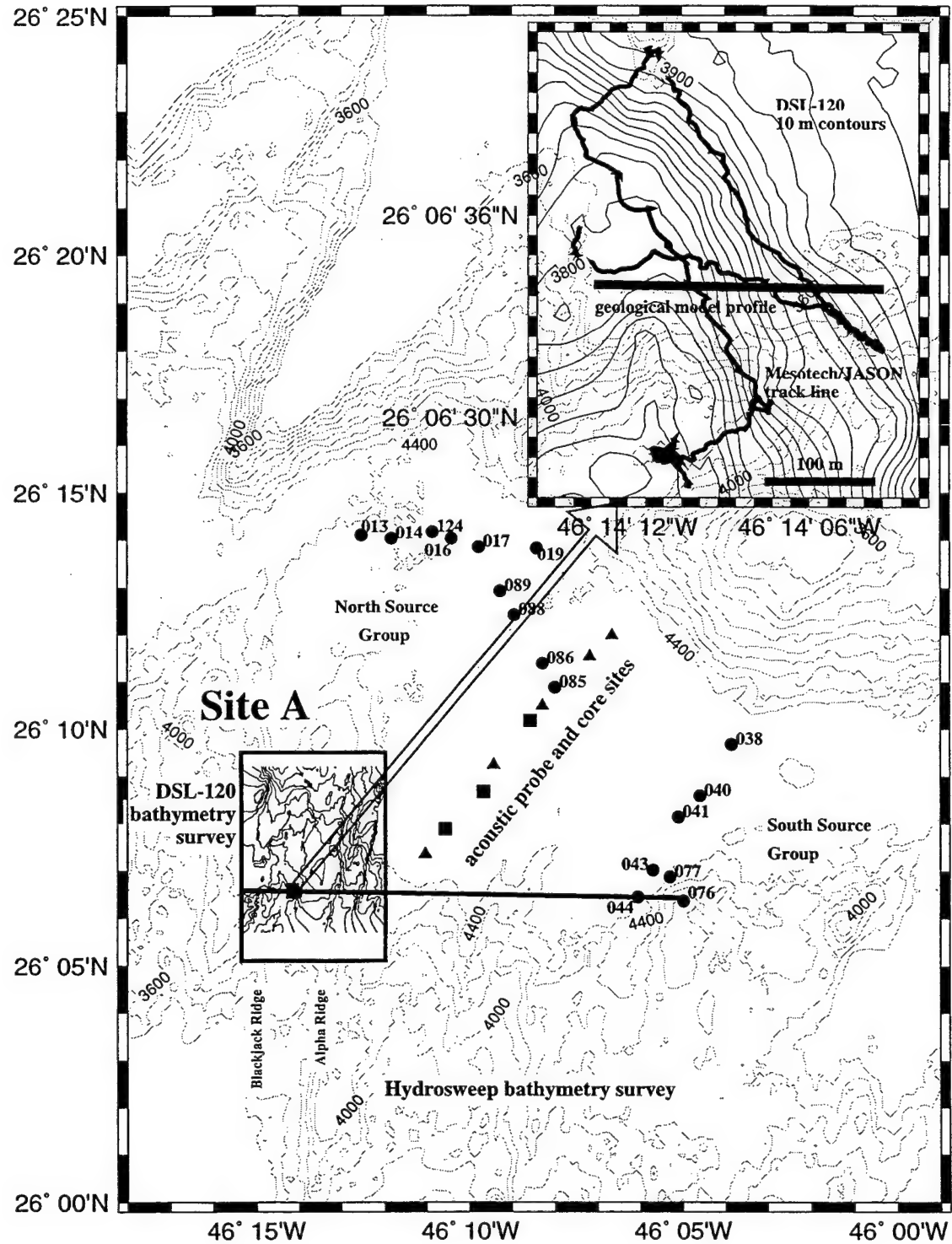


Figure 3-2: Bathymetry around the JASON trackline. DSL-120 bathymetric data along an E-W 'insonification line' is chosen as the basis of the seafloor profile. This line is approximately perpendicular to the strike direction of the local seafloor structure as defined by DSL-120 bathymetry contours, and when projected to the east it passes through ARSRP source locations 44 and 76. The most E-W portion of the Mesotech bathymetric data is projected onto a best fit line (the Mesotech bathymetry profile line) and used to replace the adjacent portion of DSL-120 bathymetry along the insonification line.

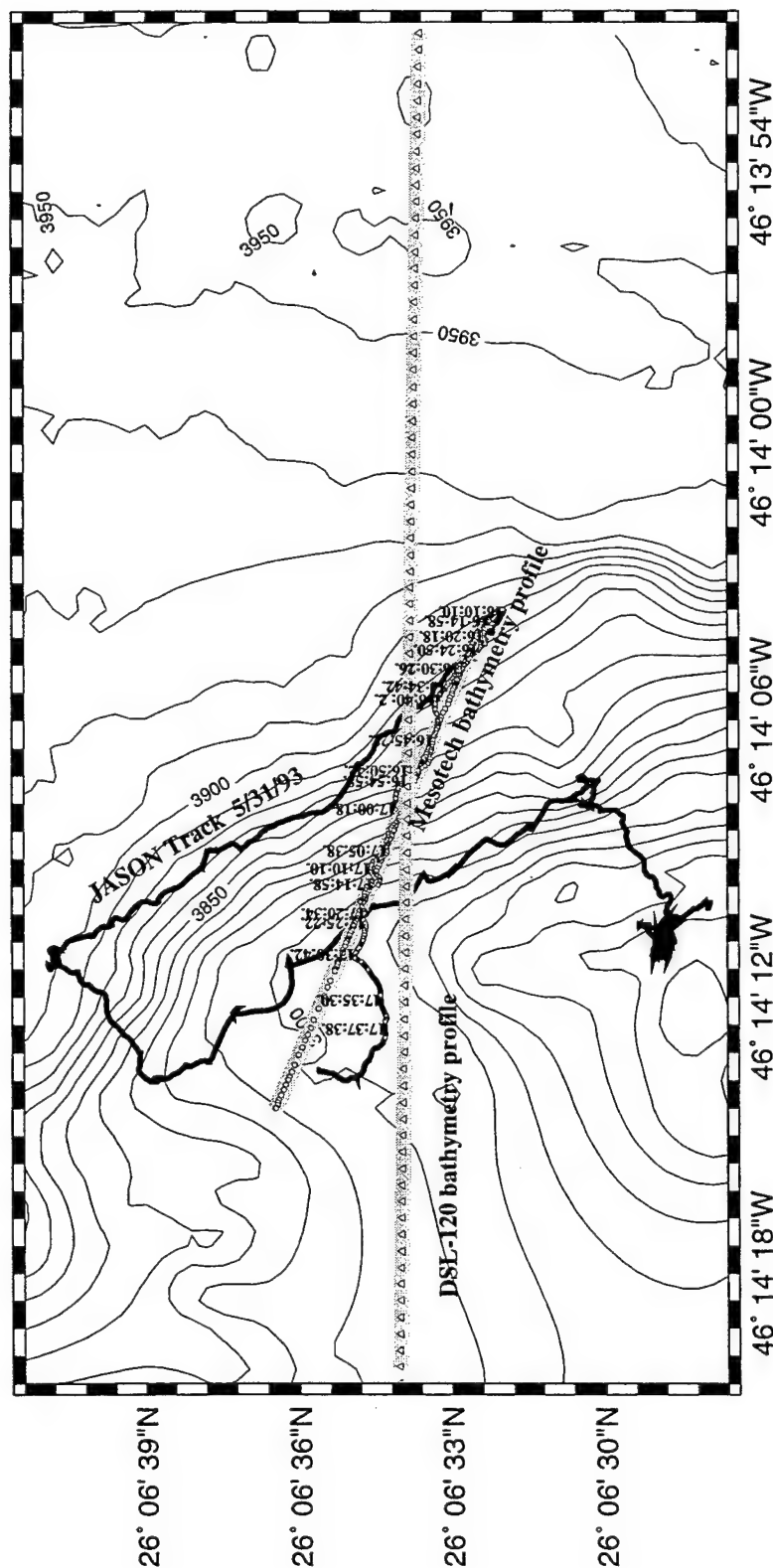


Figure 3-3: Generating a seafloor profile. (a) The DSL-120 and Mesotech bathymetry profiles clearly show the difference in resolution between the two types of data. The profile range is plotted as horizontal distance from ARSRP source location 76. The vertical scale is exaggerated by a factor of 1.2. In (b) the Mesotech data has replaced the DSL-120 data in the region marked. Only an upward shift of 5.8 m in the Mesotech profile was needed to make the replacement. Note that the ridge rises about 100 m above the seafloor to the east and forms a plateau to the west.

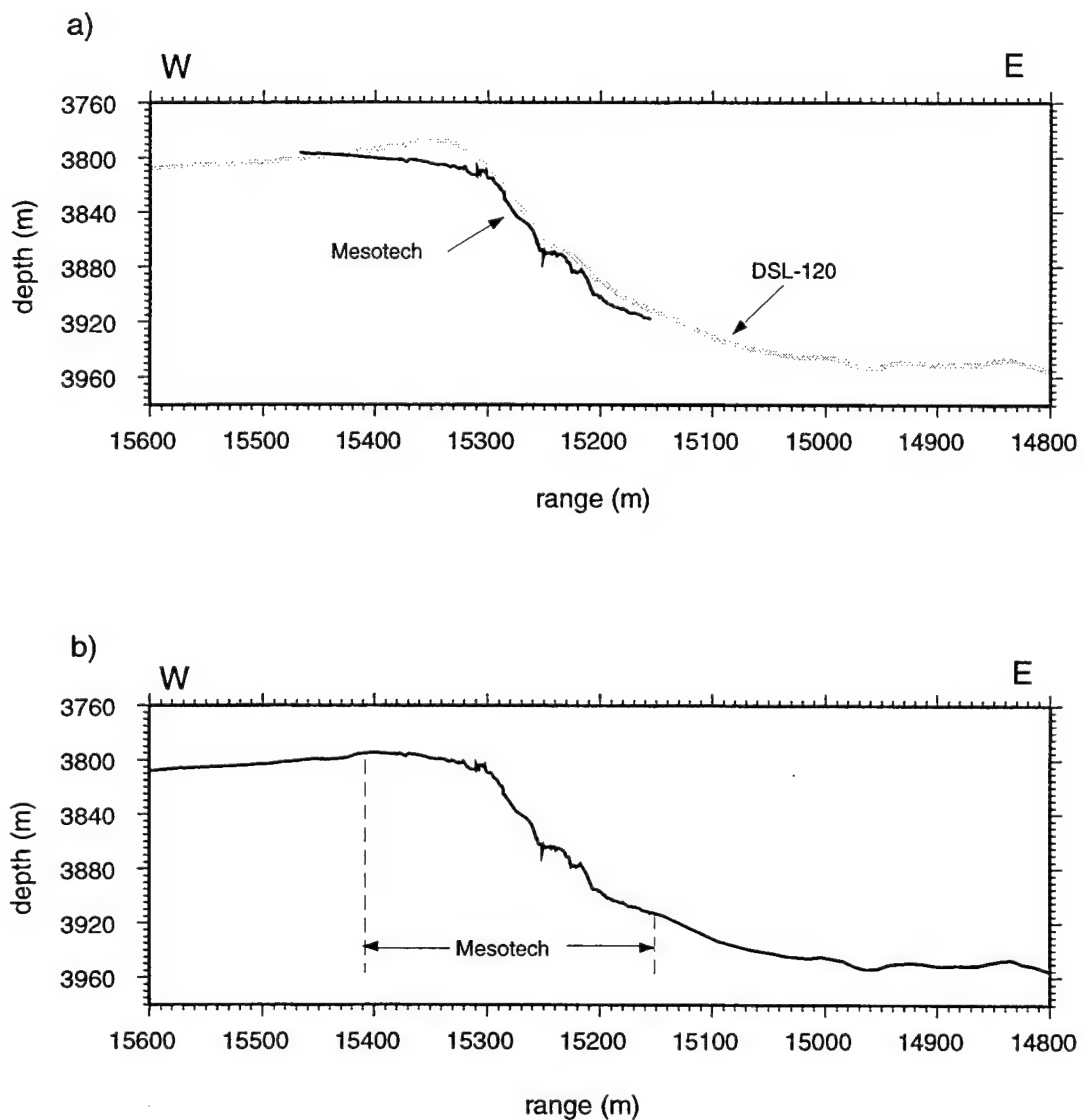
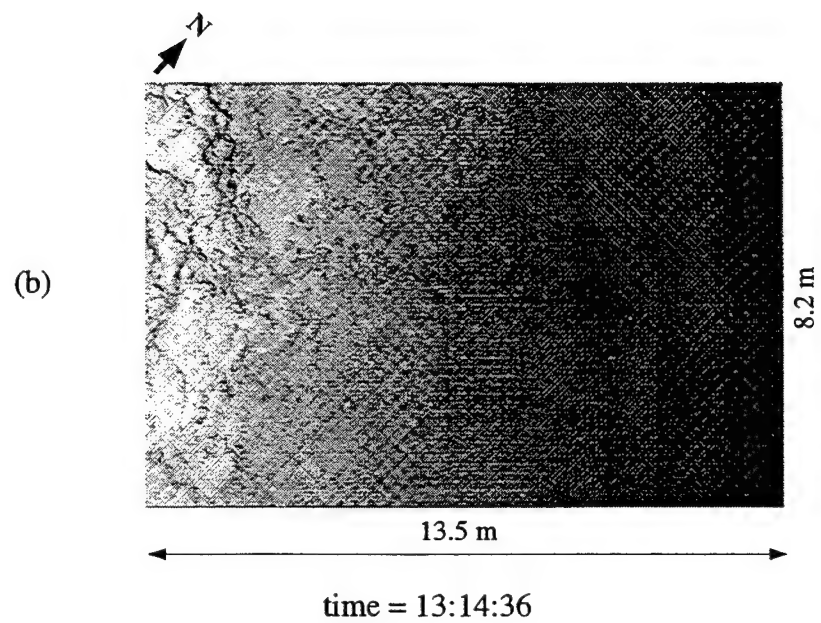
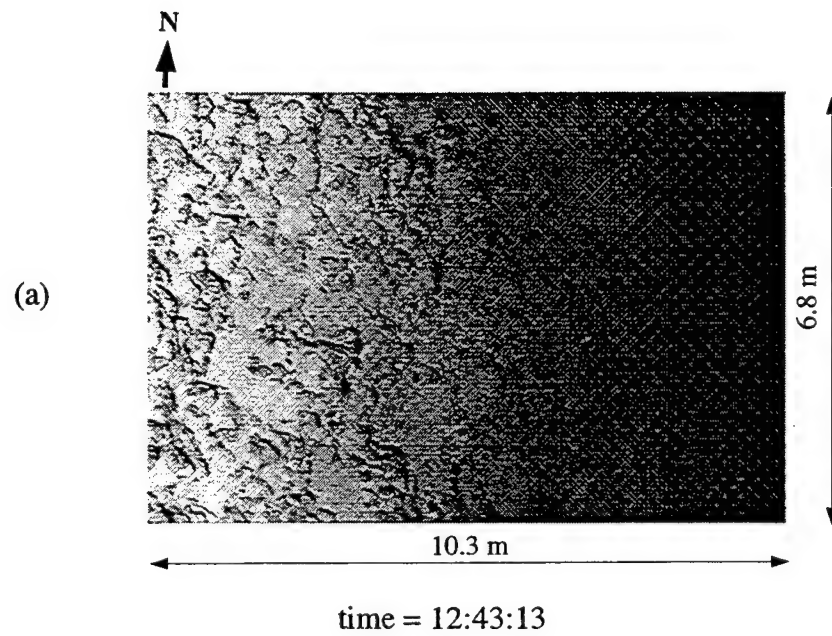
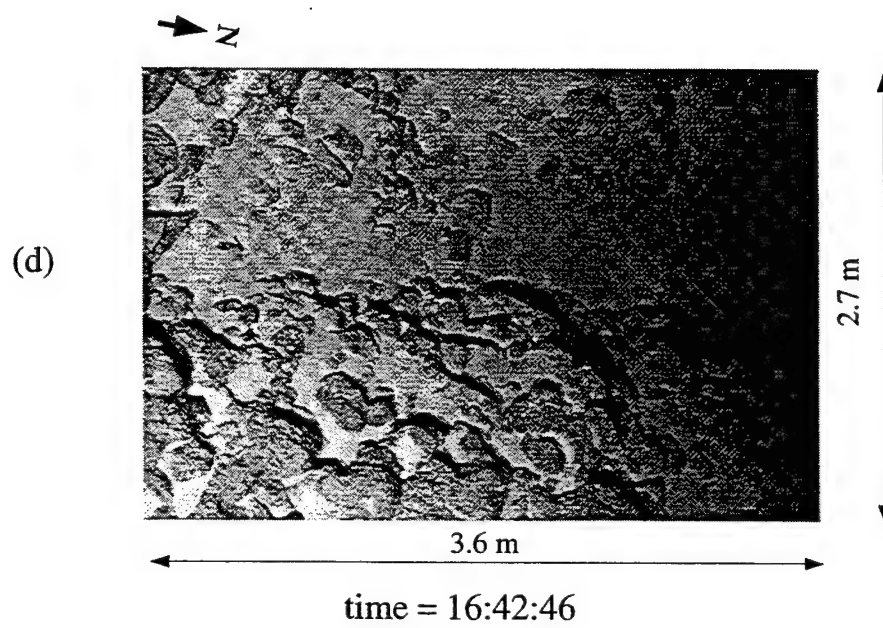
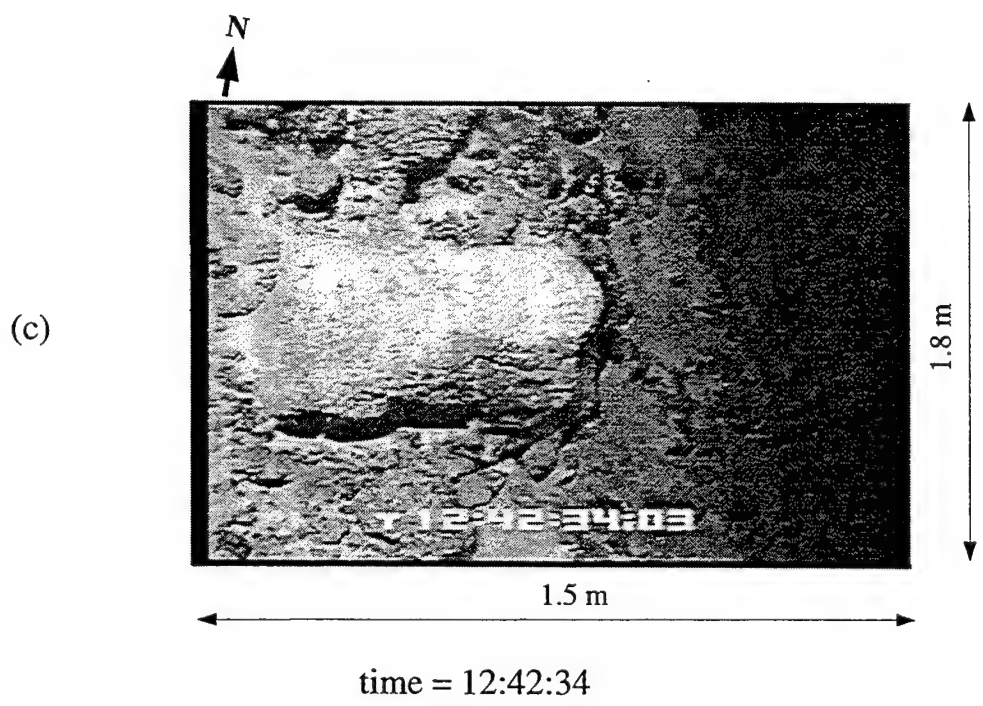
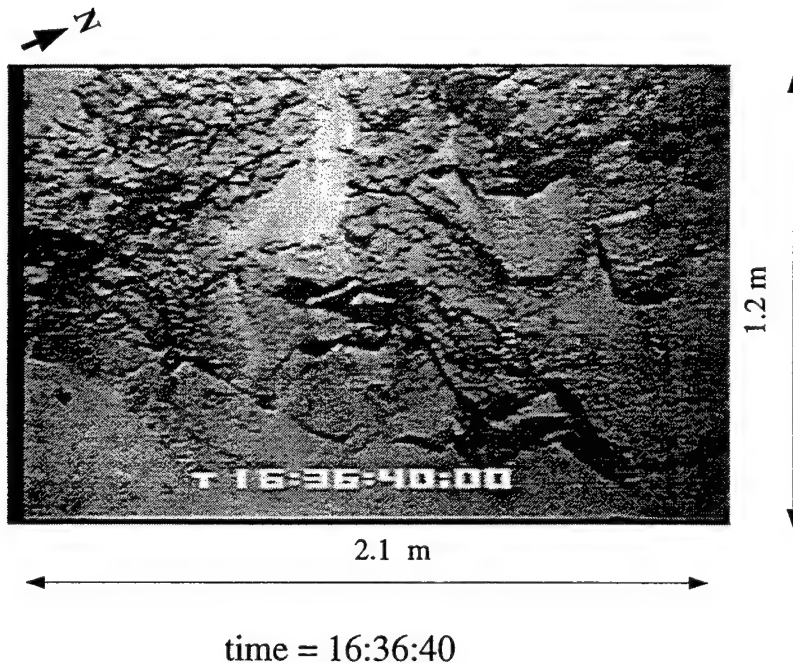


Figure 3-4: Photographs of seafloor features at Site A. Examples of seafloor images from ESC (electronic still camera) and video cameras attached to the JASON submersible vehicle. Video frames have a time stamp in the image while ESC images do not. The upper portion of the ridge shows a very steep and rough surface covered by basalt pillows and fragments (a). In places the ridge is almost vertical (b), suggesting remnants of fault scarps or fracturing caused by mass wasting. Fractured pillow basalts (c) and other exposed basaltic debris at the edges of steep slopes are more evidence of continued mass wasting from the face of the scarp. Sediment-filled fissures or fractures (d) and jointing of massive basalt (e) are observed in some areas on the ridge flank. Sediment is trapped in small chutes (e), as a light coating between pillows and fragments (f) and on terraces (g) which give a stair-step character to the ridge face. In some areas, large chutes (h), filled with sediment and talus, are in some cases large enough scale (i.e. ≥ 1 m) to be included as details in the numerical geological model. Sediment covering at the base of the steep upper ridge (i) is interpreted to be the top of a talus ramp based on profile slope changes. From the ridge crest westward, uniform sediment covers the seafloor (j). In most areas the sediment surface has a mottled appearance and shows signs of bioturbation and bottom-dweller tracks (k).



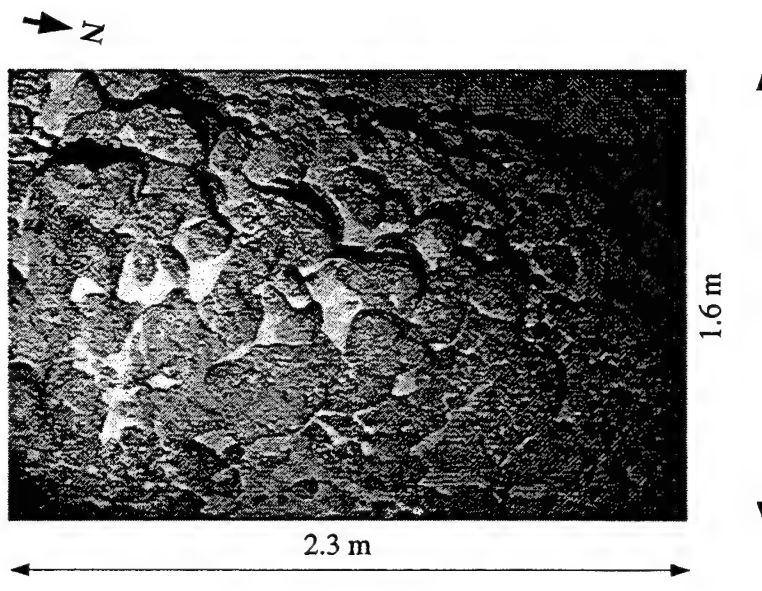


(e)



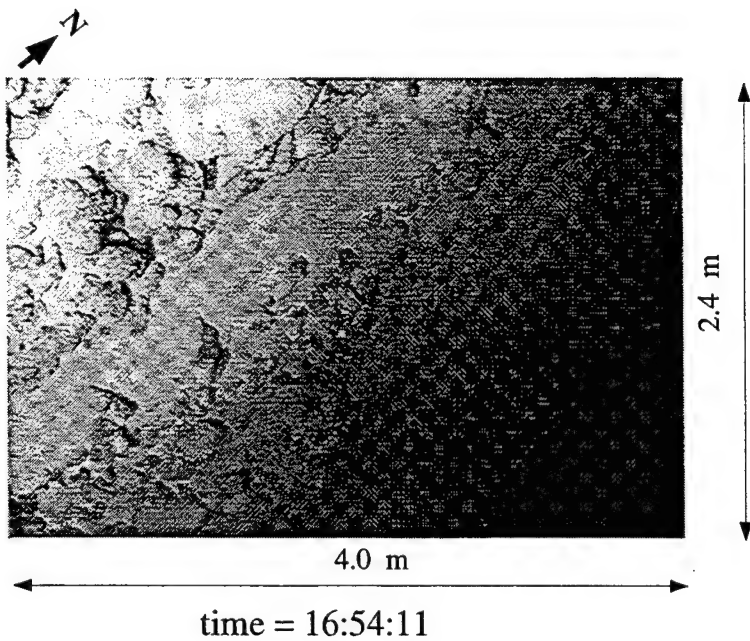
time = 16:36:40

(f)

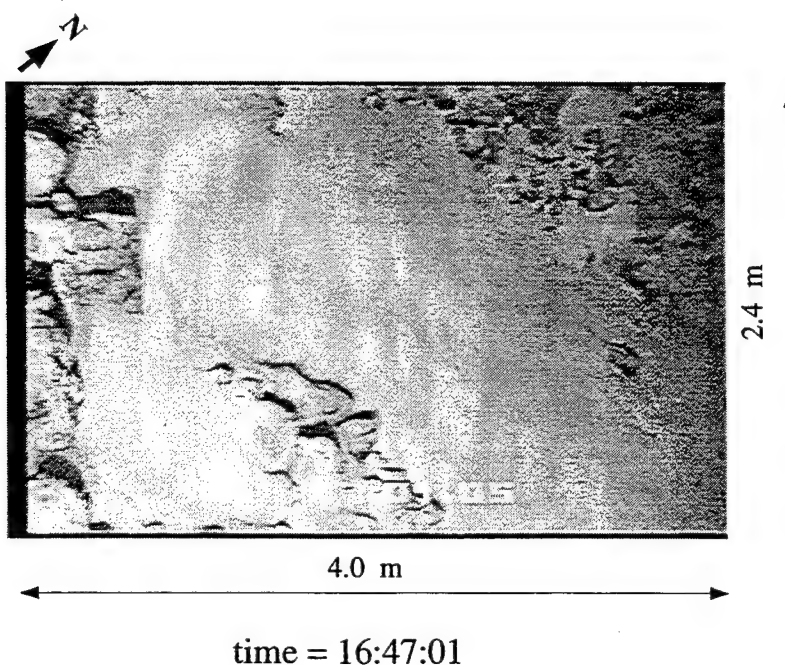


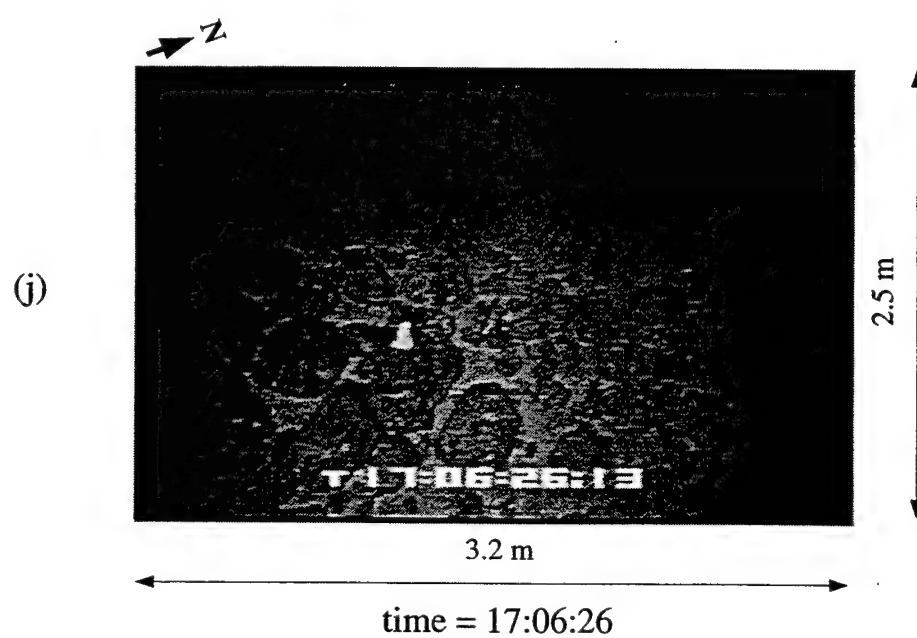
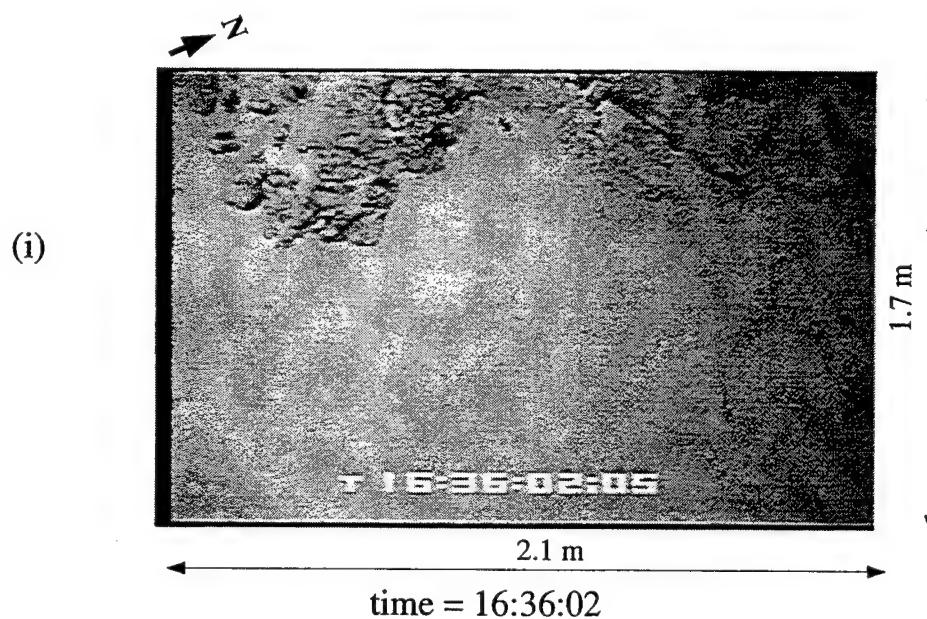
time = 16:42:26

(g)

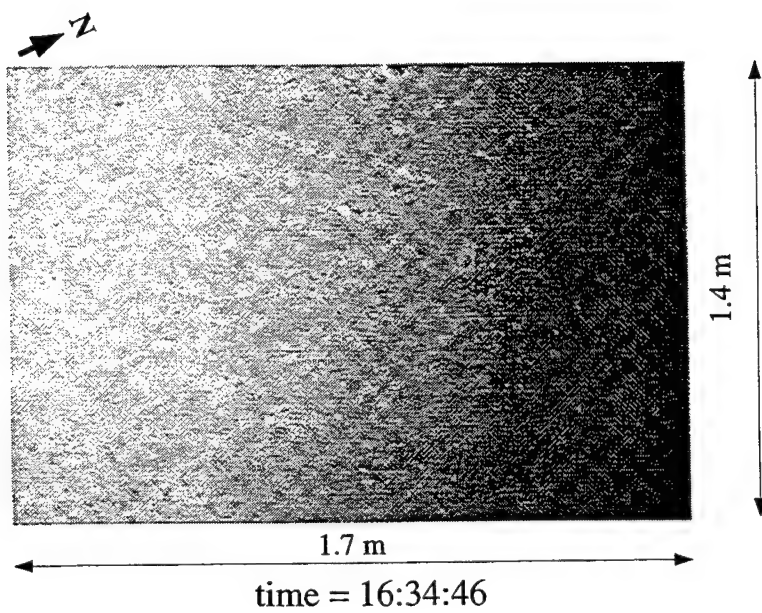


(h)





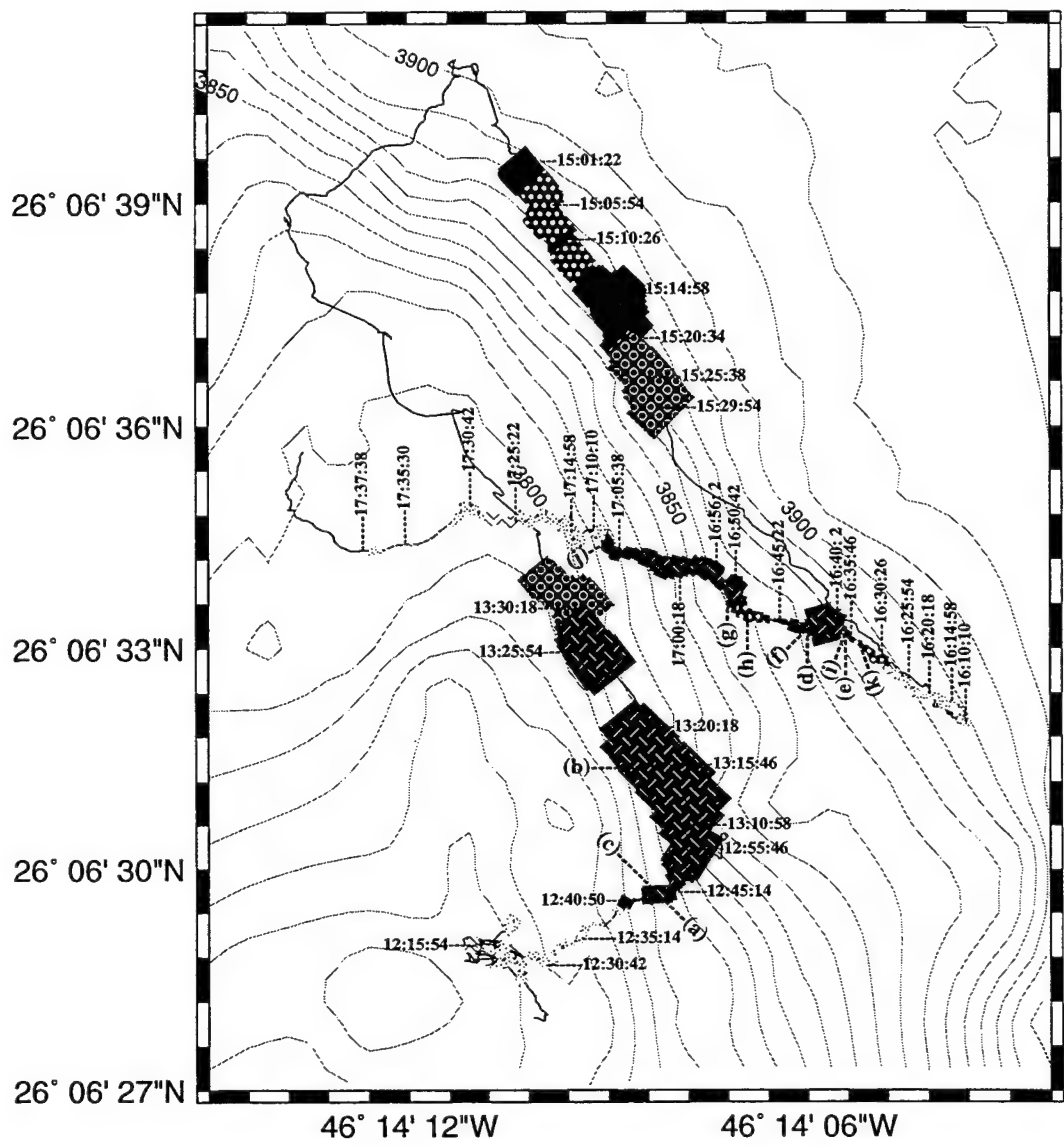
(k)



1.7 m
time = 16:34:46

Figure 3-5: Surficial seafloor geology based on photographic data. For modeling purposes, the seafloor classification is reduced to three categories: sediment, talus and basaltic basement. ESC images are projected onto the Jason track at the corresponding time in this map. Image sizes and orientations indicated depend on the elevation and orientation of JASON above the seafloor and the camera aperture. The letters (a)-(k) correspond to the locations of the seafloor photographs in Fig. 3-4.

Observed Seafloor Geology



sediment: smooth mottled rippled

talus: [dotted gray square]

basement: massive basalt basalt pillows fractured pillows

Figure 3-6: Site A sediment thickness mapped from seismic and side-scan sonar observations. The contour interval is 10 m, interpolated between 50 m contours of Jaroslow (1997). Thick sediment occurs in the center of the boxed area, but most of the area is within the nominal 'zero' contour (≤ 10 m).

**Mapped Sediment Thickness
based on Jaroslow, 1997.**

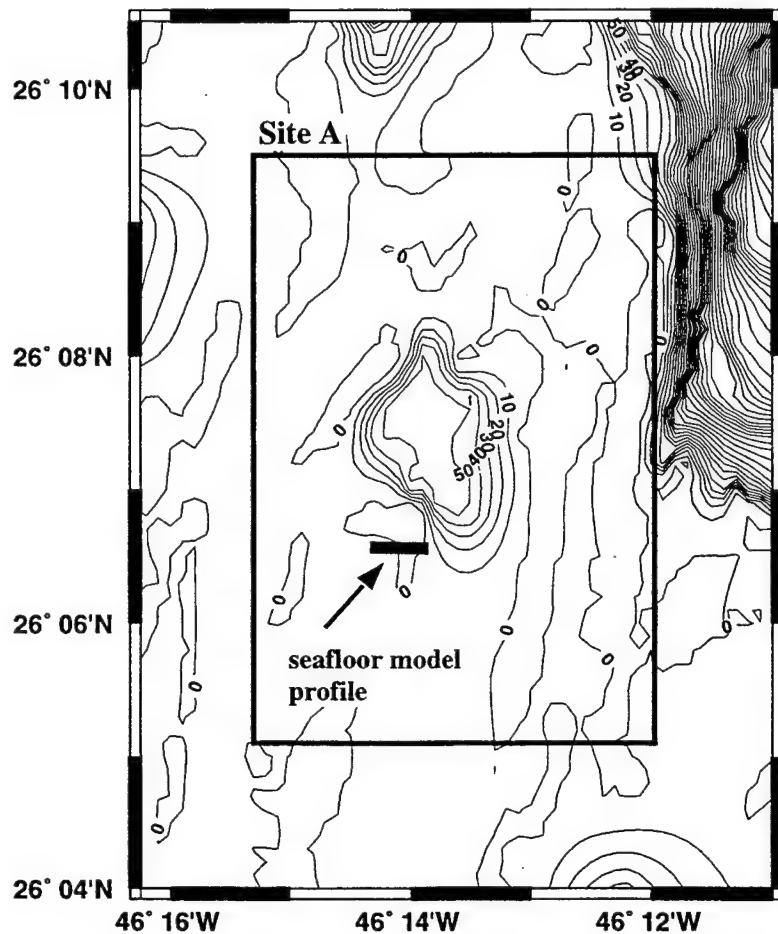


Figure 3-7: Sediment thickness at Site A based on the statistical description of Webb and Jordan (1995). The bathymetry contour interval is 10 m. This estimate of sediment thickness is derived from Hydrosweep bathymetry and as such, cannot have lateral resolution better than 200 m. However, it shows a 'probable' distribution of sediment that fits the local morphological features well.

**Predicted Sediment Thickness
based on Webb and Jordan, 1995**

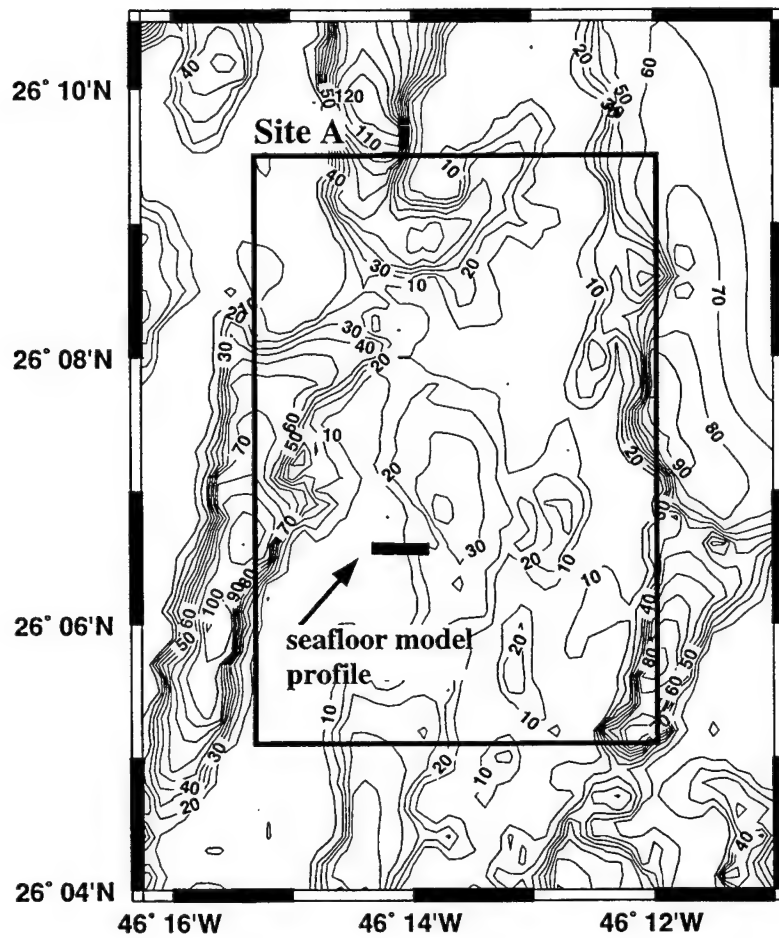


Figure 3-8: Profiles of estimated sediment thickness. Sediment thickness profiles extracted from Webb and Jordan (1995) and Jaroslow (1997) data after gridding. These profiles are only crude estimates of sediment thickness at this scale but both predict more sediment east of the ridge than on the plateau west of the ridge. The shaded zones suggest the possible range (+/- 10 m) of sediment thickness. From these profiles we interpret a limit of realistic sediment thickness to be about 20 m east of the ridge and 10 m west of the ridge. The slope of the Webb and Jordan profile suggests that sediment thickness can increase at a rate of up to 0.1 m/m.

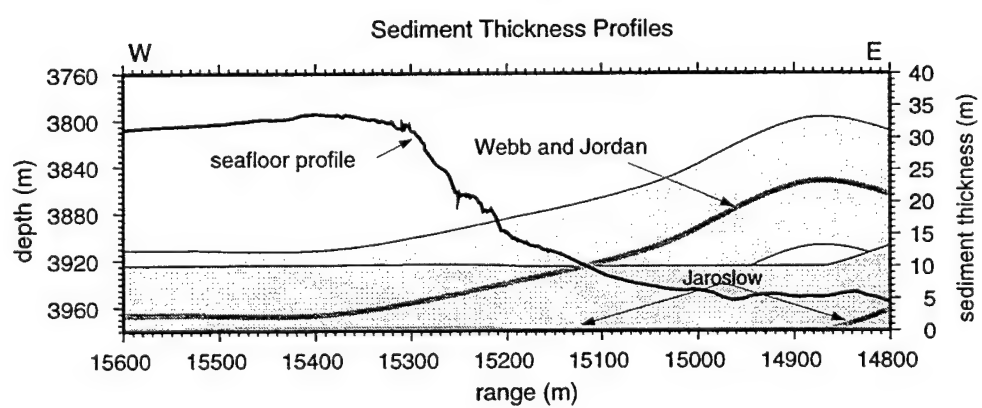


Figure 3-9: The seafloor geological model. (a) The seafloor categories of sediment, talus and basaltic basement are applied to the seafloor profile to create the geologic model. The plot is vertically exaggerated by a factor of 1.2. Sediment thickness is allowed to increase away from the ridge, up to 20 m east of the ridge and 10 m on the west side. A talus ramp is interpreted at the foot of the ridge where the average slope has decreased from about 40° to less than 20° .

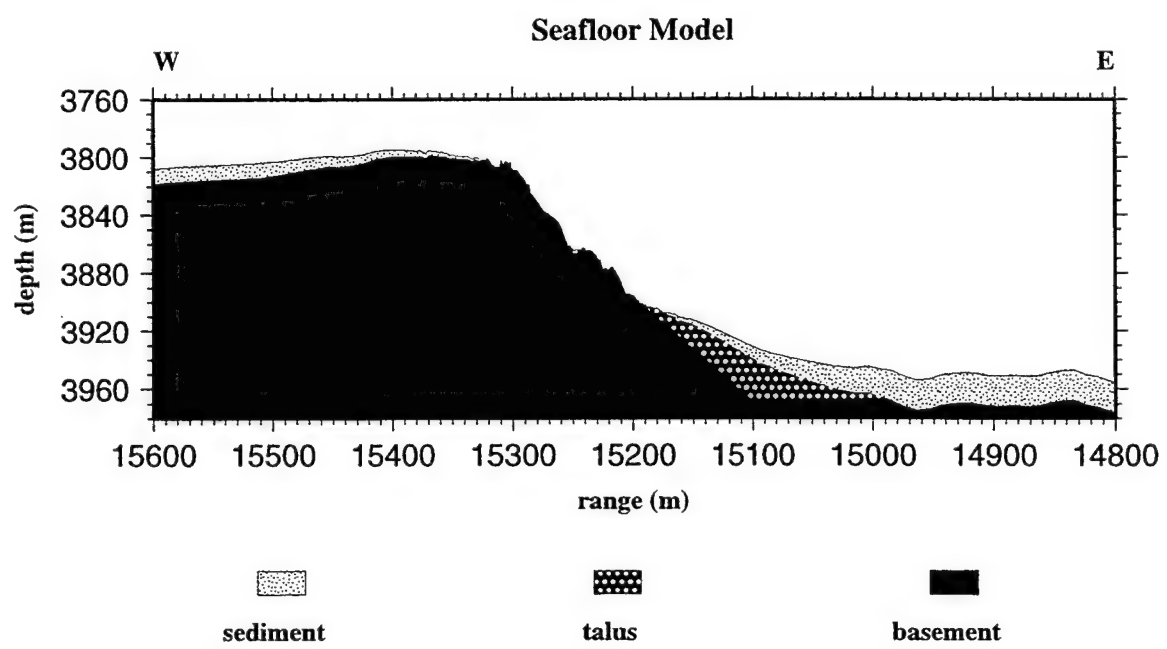


Figure 3-9: (b) The Numerical Scattering Chamber accommodates models with dimensions of 72 m x 432 m. The seafloor model in (a) is subdivided into four appropriately sized models as shown here: Model 1 targets the sediment-covered talus ramp; Model 2 targets the transition from the talus ramp to bare basaltic basement; Model 3 targets the steepest and barest basement portion of the ridge; and Model 4 targets the corner and transition to sediment cover at the ridge crest.

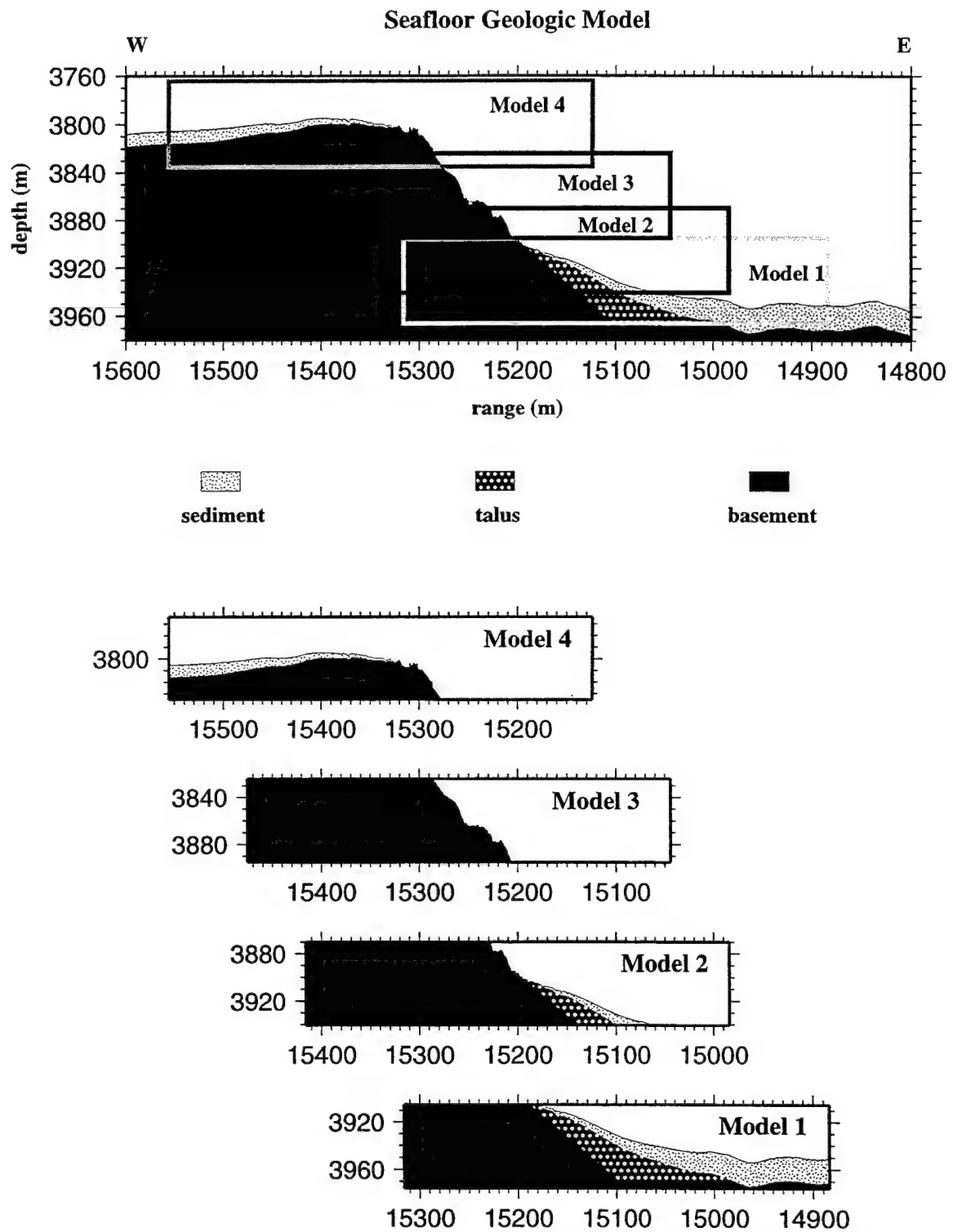


Figure 3-10: Sediment core and acoustic-lance data. Sediment-property data are from the sediment pond at Site A, reported by Fu et al. (1996). The open symbols represent the laboratory measurements of compressional-wave velocity, density and porosity from three sets of core samples. The averaged values are plotted as dark-grey lines. The filled symbols are the 'acoustic-lance' measurements (Fu et al., 1996) of sediment compressional-wave velocity made *in situ*. Water velocity at 4000 m (estimated from the CTD profile shown in the appendix to Chapter 2) is plotted (light-grey line) for reference. Particularly interesting is the low-velocity zone observed below the seafloor surface in the acoustic-lance data.

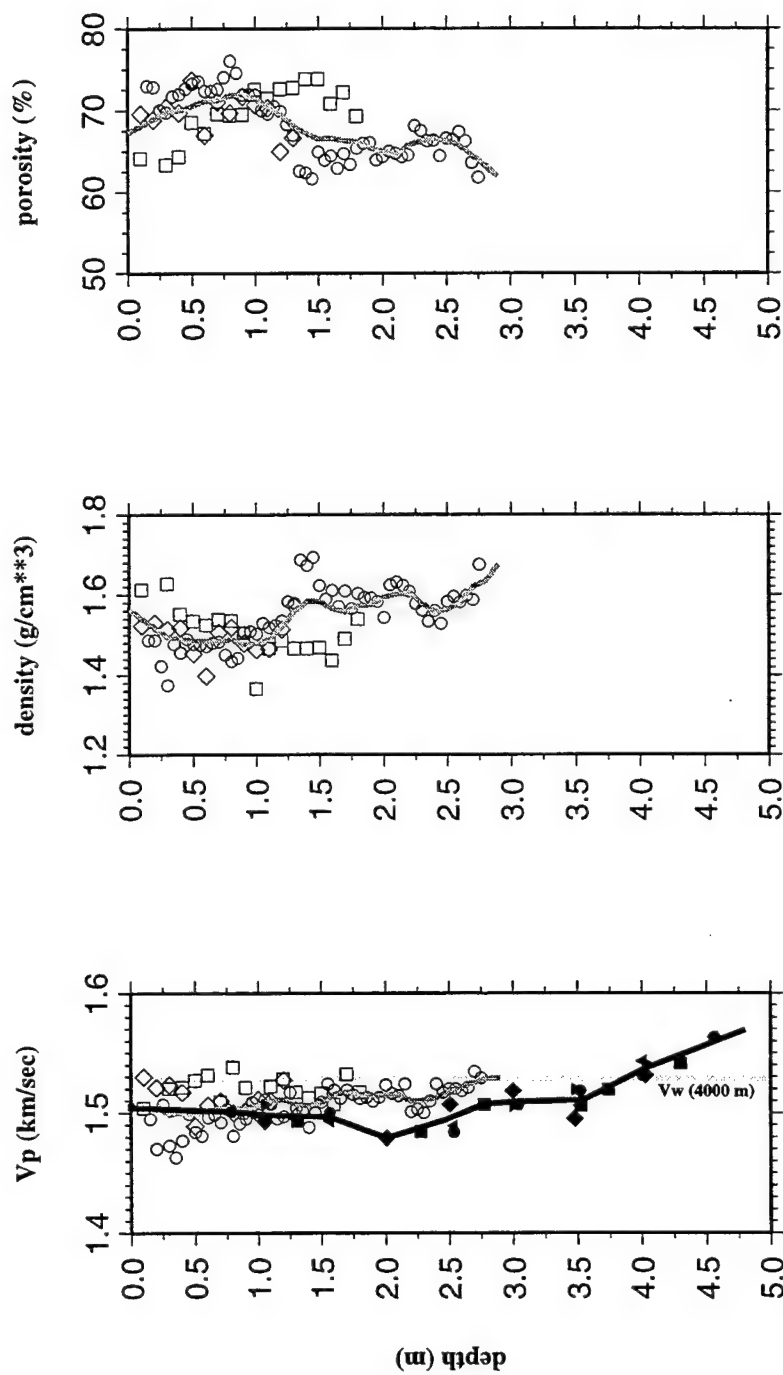


Figure 3-11: Geoacoustic parameters of nannofossil ooze. Sediment properties in the top 20 m as defined by Bowles (1994), for calcareous nannofossil ooze in the Atlantic Natural Laboratory. κ_p and κ_s are the compressional and shear-wave attenuation parameters. Only shear-wave properties are distinguished as being strongly non-linear within the upper portion of the sediment.

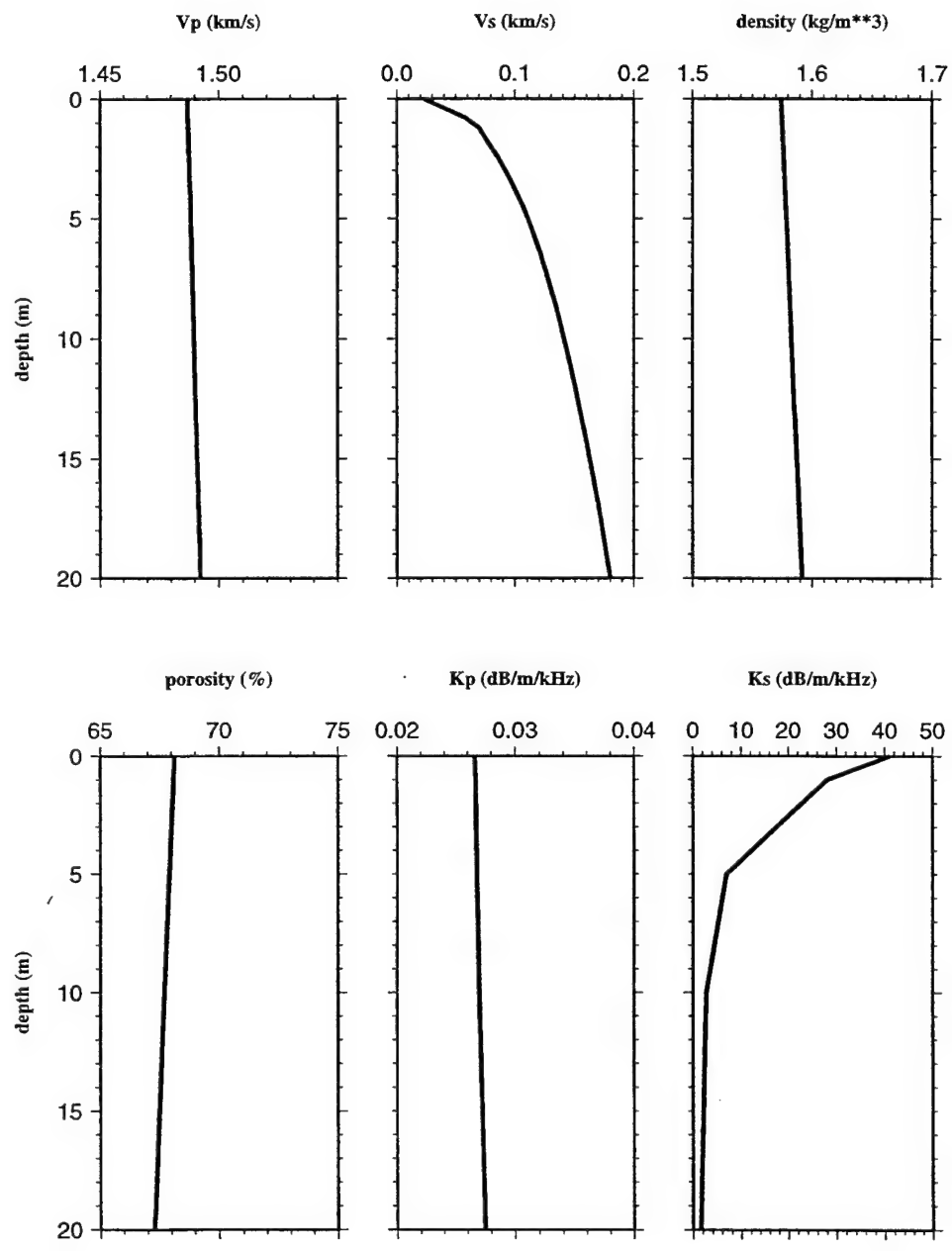
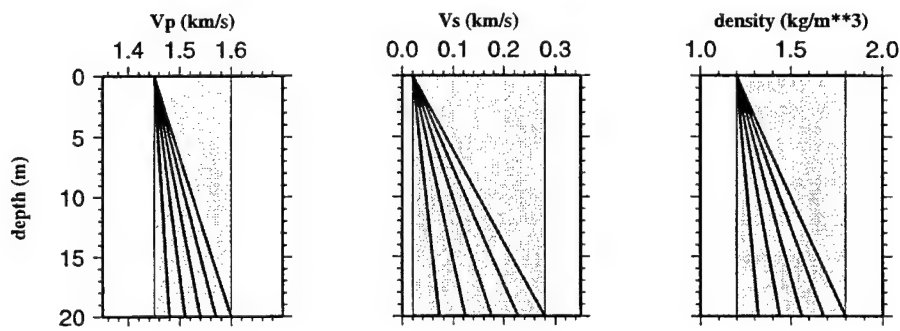
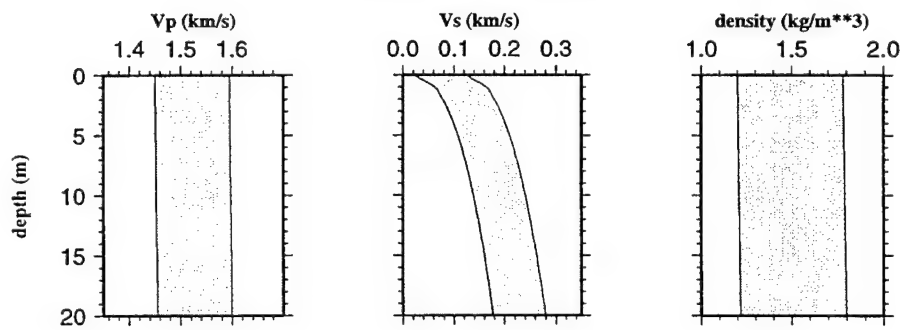


Figure 3-12: Geoacoustic parameters of sediment models. Three different models are used to define geoacoustic parameters of sediment. All variations of properties are constrained within the same ranges (highlighted in gray). The simple sediment model defines all properties as constant or having constant gradients (lines in plot are examples of properties defined with constant gradients) within a single layer or multiple layers (not shown). The Bowles (1994) geoacoustic model has only small linear gradients in P-wave velocity and density, but a strong non-linear gradient in S-wave velocity. In the bottom model, data from Fu et al. (1996) are used to define details of P-wave velocity and density in the top 5 m of sediment, with the remaining depths and the S-wave velocity defined from the Bowles model. For each model type, all combinations of v_p , v_s and density that stay within the constraints are valid descriptions of calcareous (nannofossil ooze) sediments.

Simple sediment model



Bowles sediment model



Fu et al + Bowles sediment model

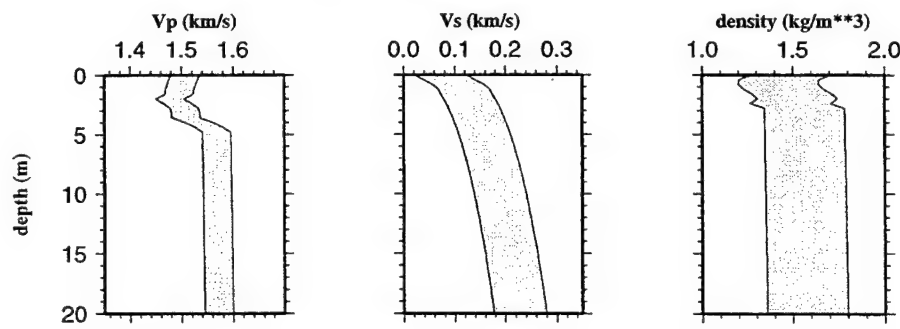


Figure 3-13: A simple model of fault zones in seafloor basement. Fault-generated fracturing, or other localized variation in porosity/density in basaltic basement, can be modeled as heterogeneity in the form of vertical strips of varying width with lower velocity and density than the surrounding basalt.

Model 3 with Fracture Heterogeneity

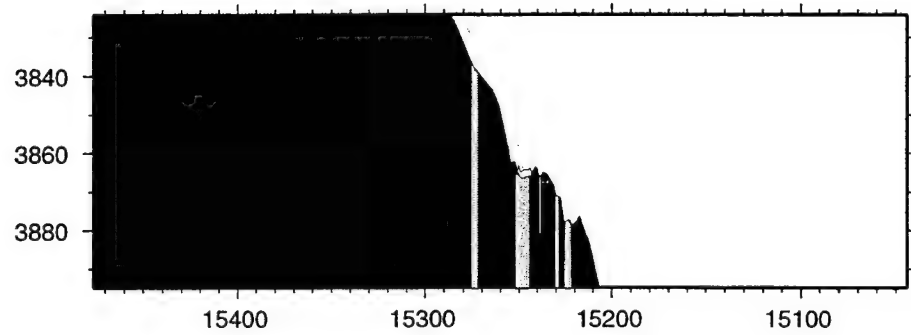


Figure 3-14: Gaussian vs. self-similar correlation functions. A comparison of the spectra of a Gaussian autocorrelation function and a self-similar autocorrelation function, as a function of correlation length, a . These plots are generated assuming the wavenumber, k , is equal to 1 in the 1-D Fourier transform equations:

$$F.T.[Gaussian] = (\pi)^{\frac{1}{2}} a e^{\frac{-k^2 a^2}{4}}$$

and

$$F.T.[self - similar] = \frac{a}{(1+k^2 a^2)^{\frac{1}{2}}}$$

This plot shows that the Gaussian autocorrelation function is best suited to generating random heterogeneity with a narrow range of correlation lengths while the self-similar autocorrelation function will produce a distribution in random heterogeneity over a much larger range of possible correlation lengths.

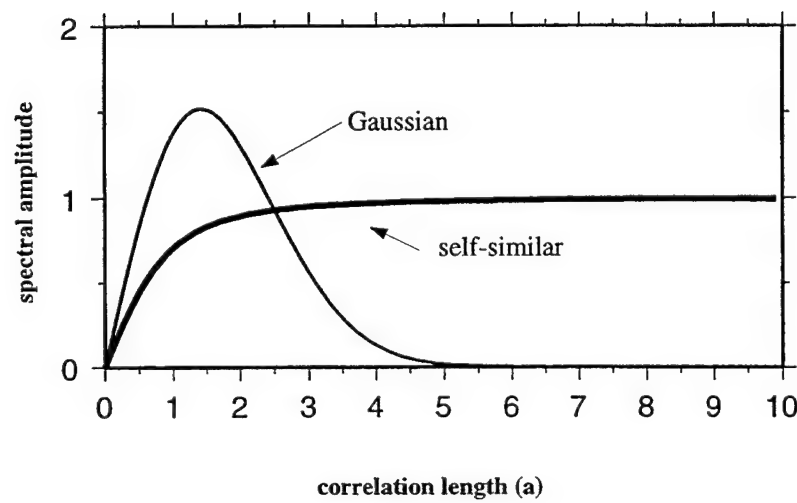
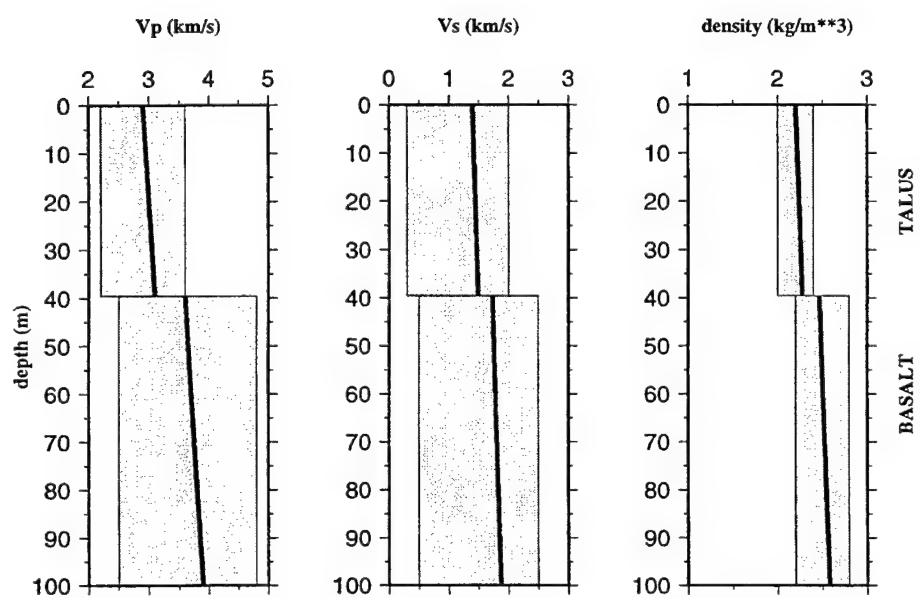


Figure 3-15: Geoacoustic parameters of upper-most crustal basalt and talus. Basalt basement and talus geoacoustic model parameters are defined with linear gradients in this model. V_s and density are further defined as linear functions of v_p . The areas in gray are the ranges over which the velocity and density can be allowed to vary within the definition of shallow basaltic crust.



Chapter 4

Numerical Elastic Wavefield Modeling of Seabed Scattering

4.1 Introduction

Numerical wavefield modeling, based on the full elastic wave equation, is used to investigate and quantify the sensitivity of acoustic/elastic scattering to variations in geological properties of the seabed. 'Seabed' in this case refers to the seafloor and the subseafloor penetrated by energy from the incident wavefield. The modeling is used to simulate low-grazing-angle ($< 20^\circ$) monostatic reverberation experiments. The quantification of the backscattered signals is necessary to establish the interpretability of actual data in terms of seabed geological characteristics. The primary focus of this chapter is the sensitivity of the backscattered signal to variations in correlation length and standard deviation of seafloor roughness and subseafloor volume heterogeneity that occur at wavelength scales.

The scale over which geological variations occur is a very important parameter in any study of scattering of sound propagating in the earth. Most important is the scale of spatial variations relative to the scale of the wavelength of the propagating sound. From the standpoint of scattering, the term 'wavelength-scale' is really meant to include all spatial variations that act as sources of significant scattering. Since there is no clear and absolute way to decide on 'significance' of a scattered signal, it is not

really possible to make an absolute definition of the boundaries of wavelength scale. For descriptive purposes, an acceptable definition of 'wavelength scale' is the range of individual features or variations in properties at the scale of about $\frac{1}{10}\lambda$ to 10λ , where λ is the wavelength. In this study the dominant wavelength in water of the incident and scattered field is 6 m. In the subseafloor, wavelength increases as the propagation velocity increases, and there are different wavelengths for compressional waves and shear waves. Thus in describing variation in seafloor structure, this range would include all features from about 0.6 m to 60 m. With this constraint, small-scale then refers to all features or variations smaller than $\frac{1}{10}\lambda$ and large-scale to those larger than 10λ . As discussed by Goff and Jordan (1988), that part of the seafloor bathymetry that varies over scale lengths in the range of the wavelength scale described above can be reasonably described as a stochastic spatial distribution. In this paper, stochastic distributions are used to model both bathymetry and subseafloor heterogeneity that occur at wavelength scales.

The hypothesis for this study is that wavelength-scale heterogeneity of the seafloor and subseafloor produces variations in backscattered signal intensity from low-grazing-angle insonification that are of sufficient magnitude to explain the fine-scale, high-intensity variations observed in monostatic reverberation data. This hypothesis is consistent with a fundamental concept of scattering theory that the maximum energy level of the scattered wavefield, in non-specular directions, occurs when the wavenumber ($k = 2\pi/\lambda$) multiplied by the scale dimension of the interface or volume heterogeneity approaches unity. Frankel and Clayton (1986) and Dougherty and Stephen (1988) showed, using finite-difference modeling, that this peak in scattering does in fact occur in the vicinity of $ka = 1$, where a is the correlation length of volume heterogeneity defined with a Gaussian stochastic spatial distribution. However, the most important concept is that the scattering increases when heterogeneity approaches wavelength scales and that scattering from small-scale and large-scale heterogeneity is much less significant (Aki and Richards, 1980, p. 748-750).

Recent analyses of monostatic reverberation data have been focused primarily on the correlation of high-intensity backscatter to the locations of relatively high-

standing bathymetric features, in particular seamounts, deep ocean ridges and continental margins (e.g., Preston et al., 1990; Makris and Berkson, 1994; Makris et al., 1995; Smith et al., 1996). Most of these analyses do not offer explanations for the detailed variations in the backscatter time-series intensity data. To a great extent, variation in signal is treated as a problem of finding the locations of specific large-scale bathymetric features that intercept the insonifying wavefield. Issues concerning the resolution of the insonification field, especially at ranges exceeding the 1/2 CZ (convergence zone), seem to have inhibited attempts to correlate fine-scale signal variations (up to 20 dB in reverberation level) to seafloor features less than 1 km in size (Smith et al., 1996).

At the same time, other researchers using finite difference wavefield modeling have demonstrated that variations in much smaller seabed characteristics ($<< 1$ km) can produce monostatic backscatter signals at magnitudes equal to those observed in real data. For example, Stephen and Dougherty (1993) showed that realistic wavelength-scale seafloor roughness can produce high-intensity backscattered signals, and that variations in sediment thickness produce strong variations in those signals – as strong as those observed in reverberation data. They also demonstrate that shear energy, in both interface and body waves, is partially converted to acoustic waves when re-scattered at the seafloor, and it can comprise a significant contribution to the total backscattered acoustic wavefield. This result suggests that accurate modeling of seabed scattering requires that modeling algorithms be based on the full elastic wave equation, rather than the acoustic wave equation. Robertsson and Levander (1995) investigated the effects of sediment thickness on scattering from rough, basaltic seafloor and show that scattering strength can be decreased by as much as 15 dB by even thin layers of attenuating sediment. Swift and Stephen (1994) show that wavelength-scale volume heterogeneity in basaltic basement can also produce variations in backscatter signal intensity on the order of 15 dB. They showed that the observed intensity level is clearly dependent on the correlation length of the heterogeneity and that gradients in the subseafloor also affect the volume-scattered wavefield. However, the average signal strength of their model results is much smaller than seafloor scattering signals

observed in monostatic reverberation experiments.

In this study, we use the Numerical Scattering Chamber (NSC), described by Stephen and Swift (1994), to generate scattered wavefields from a variety of seabed models with well defined seafloor roughness and subseafloor volume heterogeneity. The source wavefield in the NSC is a Gaussian beam that is incident at a particular low grazing angle. In order to simulate a monostatic reverberation experiment, a beamforming process is applied to the scattered-field time-series data to calculate scattering coefficients as a function of scattering angle. The scattering coefficient in the monostatic backscatter direction is then compared as specific geologic parameters are varied. These sensitivity studies are then used to analyze the backscatter coefficients produced by realistic seafloor models (described in the previous chapter).

4.2 The Numerical Scattering Chamber

The Numerical Scattering Chamber (NSC) is an elastic-wavefield-propagation forward-modeling program, and it was introduced by Stephen and Swift (1994) specifically to address problems of seabed scattering at low grazing angles. The wavefield propagation algorithm is based on a finite difference formulation, with model parameters defined on a staggered grid, as described by Virieux (1986).

The source wavefield is initiated at the edge of the chamber as a Gaussian pulse beam in order to constrain the insonification to specific grazing angles. The Gaussian beams are approximations to plane waves with the advantages that "they have finite width, they do not have sidelobes, and they represent energy propagating at a single angle, in homogeneous media, or ray parameter, in stratified media" (Stephen and Swift, 1994). These are important characteristics because monostatic reverberation signals in the deep ocean represent scattering associated with a limited range of grazing angles, depending on the water depth and velocity profile (Jensen et al, 1994). For this study, the source pulse in pressure is defined as the third derivative of a Gaussian curve, with the peak frequency at 250 Hz and half-power bandwidth of one octave (170-340 Hz). The grazing angle was maintained at 15°, which, as shown

in Chapter 2, is an appropriate angle for simulating the monostatic reverberation experiment at the water depths found at Site A.

The NSC (Figure 4-1) consists of a 2-D grid in which the particle displacements, defined by the elastic wave equation, are calculated at all grid intersections at a series of specified times. Within the total grid is a limited region defined as the 'scattering chamber'. This is surrounded by an absorbing region that attenuates wavefield energy as it exits from the scattering chamber, in approximate fulfillment of the Sommerfeld radiation condition (Pierce, 1989, p. 177-178). The geological model is defined only in the region labeled as the heterogeneous transition zone, by defining the compressional and shear wave velocities and density at each grid point. The regions around the transition zone are defined as homogeneous water and homogeneous solid, and they incorporate absorbing boundary conditions. The Gaussian pulse beam source is introduced as a time-dependent boundary condition in the upper right corner such that it is incident on a flat-seafloor model at a specified grazing angle.

The numerical wavefield can be 'recorded' in two ways. One way is to store the particle displacements at each grid point at specified time steps. These 'snapshots' of the time progression of the wavefield are particularly useful for gaining insight into the mechanisms of scattering, and they show the full variety of wave types that occur. Rather than displaying displacement vectors at each grid point, the snapshots display 'amplitude density'. Compressional (E_c) and shear (E_s) wave energy densities are defined by Morse and Feschbach (1953, p. 150) (also see Stephen and Swift, 1994, Appendix):

$$E_c = (\lambda + 2\mu)(\nabla \cdot \vec{u})^2 \quad (4.1)$$

and

$$E_s = \mu(-\nabla \times \vec{u})^2 \quad (4.2)$$

where \vec{u} is the displacement vector and λ and μ are Lame's elastic constants. These expressions are accurate only for homogeneous wave types (i.e., that have separable compressional and shear components) such as elastic body waves. Inhomogeneous

propagation modes, such as interface waves, have inherently coupled shear and compressional components, and therefore have both E_c and E_s components. Interface wave energy is therefore observed as having both shear and compressional wave energy. In order to retain the polarity of the divergence and curl operators, Dougherty and Stephen (1988) define 'amplitude density' as the quantities

$$P - \text{wave amplitude density} = \text{sign}(\nabla \cdot \vec{u}) E_c^{\frac{1}{2}} \quad (4.3)$$

$$S - \text{wave amplitude density} = \text{sign}(\nabla \times \vec{u}) E_s^{\frac{1}{2}} \quad (4.4)$$

These quantities are then displayed as snapshots, with color density of the plots increasing with amplitude, which is proportional to the square root of the energy density. Snapshots are similar to and can be referred to as 'schlieren' diagrams (see definition of schlieren in Sheriff, 1991).

The other way that the propagating wavefield is recorded simulates 'receivers' that would be used during actual data acquisition. In this case, the displacements or pressure at any chosen grid points are recorded at each time step, producing a time series of the wavefield amplitude observed at a point in space. In our modeling, the time series are recorded at grid locations along the sides and top of the scattering chamber, as indicated in Figure 4-1. Only time series at grid locations in the water column (dependent on the shape of the model) are recorded in our modeling. These time series can be displayed as wiggle traces, but for comparison to monostatic reverberation data they require further processing. Stephen and Swift (1994) defined a beamforming process that reduces the time-series data to a scattering coefficient defined as a function of scattering angle. Scattering angle is defined as the rotation angle relative to a horizontal vector pointing in the direction of the source. This is illustrated in Figure 4-2. All scatter directions greater than 90° correspond to forward scatter and less than 90° to backward scatter. The scattering coefficient is the time average pressure field intensity, calculated as a function of propagation (scattering) angle, normalized by the intensity of the incident (reference) field. The intensity of

the incident field has been calibrated such that it is equivalent to the field of a plane wave in water with an rms pressure of $1\mu\text{Pa}$ and intensity of $0.667 \times 10^{-16} \text{ W/m}^2$.

As previously discussed, the grid spacing is constrained by the need to minimize grid dispersion and yet maximize the speed of model computation. The grid spacing was chosen as 0.4 m which is 1/15 of the source (dominant) wavelength (6 m) in water. Kelly et al. (1976) showed that grid dispersion effects are acceptable if the grid spacing is at least ten grid points per wavelength, i.e., $\Delta x \leq \lambda_{min}/10$. This suggests that the lowest propagation velocity that should be included in the geological models in order to limit grid dispersion is $v_{min} = \lambda_{min}f_p$, i.e., $v_{min} \geq 10\Delta x f_p$, where f_p is the peak frequency of the source wavefield. In our modeling $f_p = 250 \text{ Hz}$, so that $v_{min} = 1 \text{ km/sec}$ is the minimum velocity for which there is an acceptable level of grid dispersion.

A finite difference calculation can also become numerically unstable if the time step chosen is too large. The stability criteria for propagation in homogeneous media using the second-order staggered grid scheme is (Virieux (1986)):

$$\Delta t \leq \frac{\Delta x}{\sqrt{2v_{max}}} \quad (4.5)$$

where v_{max} is the maximum compressional velocity in the model. For our modeling, Δt was chosen as 0.00004 seconds, which satisfies this stability criteria for $v_{max} \leq 7 \text{ km/sec}$. However, according to Stephen (1990), "Sufficient (stability) conditions for heterogeneous media are not known". Therefore, numerically stability in the modeling of heterogeneous media must be judged for each model computation. Within the range of heterogeneous models used in this study, the NSC proved to be numerically stable.

4.2.1 Limitations to the Numerical Modeling

The numerical modeling presented in this study has several limitations that must be considered. As previously discussed in Chapter 3, the modeling is done in 2-D, even though scattering is really a 3-D process. This is primarily due to the extremely long computation times that would be necessary to do the numerical wavefield modeling if

appropriately scaled 3-D geological models were used. We believe that the scattering coefficients calculated in our modeling are within 10 – 20% of the values that would be calculated for 3-D models with similar wavelength-scale roughness.

Another limitation to ideal modeling is that we were not able to successfully include intrinsic attenuation as a parameter in the finite-difference code. Since the propagation distances within the solid region of the models are quite short, this is not considered a strong limitation in the modeling. In future work both homogeneous and heterogeneous attenuation will be included in the code to quantify its influence on the scattered field.

As discussed in the previous section the minimum velocity that is included in the geological models is 1 km/sec, in order to reduce the problem of grid dispersion. This requirement made it not possible to include the very low shear-wave velocities that are realistic for sediment just below the seafloor (0.1 - 0.3 km/sec). The only way to include such low velocities in this modeling is to use finer grid spacings and time steps that would have made computation times of the models impractical.

4.3 PART 1:

Models with Homogeneous Subseafloor

The scattered acoustic wavefield returned from the seabed contains products of both seafloor and subseafloor interaction with the incident and transmitted wavefield. In order to simplify the quantification of this scattered field in terms of seabed geological characteristics, we consider the problems of seafloor (interface heterogeneity) scattering separately from subseafloor (volume heterogeneity) scattering. The results from highly constrained models are then used to interpret the scattered wavefields from realistic seabed models that include both seafloor roughness and subseafloor volume heterogeneity.

In this section, interface scattering from a rough seafloor with a homogeneous subseafloor is described and quantified in terms of seafloor roughness parameters, seafloor slope and the velocity and density of the subseafloor. Rough-seafloor models are defined by stochastic height distributions with the characteristic dimensionless parameters, ka and $k\sigma$, where $k = 2\pi/\lambda$ is the wavenumber of the incident field having wavelength λ , a is the (auto)correlation length and σ is the standard deviation of the distribution. These distributions are created by filtering normalized random distributions to create stochastic (band-limited) random distributions having Gaussian autocorrelation functions. The stochastic distributions are then scaled such that their standard deviation in amplitude is the desired height, σ . The Fourier transform of a Gaussian function is itself a Gaussian function, and therefore the height distribution is also Gaussian in models defined with Gaussian autocorrelations (Bracewell, 1978). This method of model generation is adapted from the work of Frankel and Clayton (1986) and Dougherty and Stephen (1988).

Correlation length of a function having a Gaussian autocorrelation is defined as the lag distance at which the autocorrelation amplitude has decreased to $1/e$ of its peak value (Ogilvy, 1991, p.14). This explicit definition of correlation length is a strong motivation for using Gaussian distributions in modeling where quantification of model characteristics is needed. Goff and Jordan (1988) showed that seafloor models can

be adequately represented by random distributions having Gaussian autocorrelation functions, with the exceptions that seafloor asymmetry caused by fault scarps and flatness of sediment ponds are not fully represented. However, in our modeling such features would be classified as large-scale because they would usually have dimensions much larger than the wavelength. Other distributions, such as the exponential and von Karman self-similar models described by Frankel and Clayton (1986) might be somewhat more realistic representations of variations in seabed properties, but they do not have easily measured correlation lengths.

An example of a self-similar seafloor model is compared in Figure 4-3 to its corresponding Gaussian model. The most notable difference between these seafloor models is that the self-similar model contains more high-frequency variations (i.e., more small- and wavelength-scale features). Both models are initiated with the same random series before the filters are applied. The Gaussian model has a correlation length of 6 m that is determined exactly from the lag distance in the autocorrelation function (Figure 4-3(c)). The standard deviation of the height is represented in the height distribution (probability density function) by the black region centered at zero (mean) height. It should be noted that even though the Gaussian and self-similar models differ in the details of their height distributions, the second moments of these distributions are specified to be exactly the same. The standard deviation and correlation length are completely distinct parameters in all of our models, i.e., variation in either standard deviation or correlation length does not imply any corresponding variation in the other parameter. Therefore, in any comparison of the Gaussian and self-similar models shown here, the only statistical difference is in the distribution of spatial scales represented by the shape of the frequency spectra and the autocorrelation functions. The reciprocal of the spatial frequency at the base of the initial steep roll-off of the power spectrum for the Gaussian distribution (0.16 cycles/m) is equal to the correlation length. The asymmetric shape of the power spectrum of the Gaussian function makes the location of this frequency clear. Contrary to this, correlation length of the self-similar distribution is not defined by the width of its autocorrelation function, and the symmetric shape of its power spectrum suggests that a much higher frequency

limit (and smaller correlation length) should be chosen to describe the distribution. The correlation length of non-Gaussian media is defined by the corner wave number of its fluctuation spectra (see Figure 3-14) (Frankel and Clayton, 1986), but it can be approximated as the inverse of the corner frequency of its power spectrum. The corner frequency is defined as the frequency at the intersection of the lines to which the power spectrum is asymptotic (Oldham and Schwarz, 1972, p. 85). For this spectrum, the corner frequency is approximately 0.25 cycles/m, which would suggest a correlation length of about 4 m, even though the majority of the power is in spatial frequencies below 0.16 cycles/m. The difference in the scattered field produced by these two models is discussed in a later section. For our purposes, the explicit definition and constraint of correlation length provided by the Gaussian model definition is better suited to quantification of scattering.

4.3.1 Wavelength-Scale Properties of Realistic Seafloor

The seafloor profile shown in Figure 4-4(a) is constructed from DSL-120 and Mesotech bathymetry data at Site A in the Atlantic Natural Laboratory (see Chapter 3). In order to identify the dominant scales of seafloor variation within the range of the wavelength scale, this profile was high-passed filtered with a cut-off frequency of 0.01 cycles/m (100 m wavelength). We use the high-pass profile to estimate the wavelength-scale characteristics of the seafloor. These characteristics are then used to constrain the stochastic distributions used as models of the seafloor. The remaining (low-pass) profile then represents the underlying ridge (large-scale) feature. The filtered profiles have been shifted to a zero mean depth in the figure. The boxes labelled Model 1-4 represent the regions to be modeled in the NSC. We note that only Model 3 contains seafloor entirely defined by the high resolution Mesotech bathymetric data.

Figure 4-4(b) shows the autocorrelations, height distributions and power spectra calculated from the seafloor within each model region. The slow roll-off at high frequencies of the power spectra is suggestive of the self-similar model. However, the initial asymmetric steep roll-off at low frequencies is more suggestive of the Gaussian model. It is not surprising that real seafloor does not fit any particular model exactly.

If we assumed that the correlation length could be estimated by the half-width of the autocorrelation functions, the correlation lengths corresponding to Models 1-4 would be 15 m, 10 m, 5 m and 30 m, respectively. On the other hand, if we assume the distributions are self-similar, a choice of corner frequency at 20 dB in each power spectra would yield correlation length estimates of 3 m, 5 m, 3 m and 2 m, respectively. As a compromise, we chose instead to estimate correlation length by the corner frequency, chosen as the base of the initial steep roll-off. These choices (dashed lines in plots) produce estimates of correlation lengths of 9 m, 7 m, 6 m and 5 m, respectively. The standard deviations of the height distributions are 1.5 m, 1.9 m, 3.2 m and 2.5 m for Models 1-4.

Based on these estimates, we limited the parameters of the stochastic seafloor models to the ranges, $1 \leq a \leq 12$ m for correlation length, and $0.5 \leq \sigma \leq 6$ m for standard deviation. Note that for modeling with a 250 Hz sound signal, $k \approx 1$, so that $ka \approx a$ and $k\sigma \approx \sigma$. For Site A, these can be considered the parameter constraints that define typical seafloor spatial characteristics.

4.3.2 Baseline Model

As a reference, we consider first the most basic seafloor model, consisting of a smooth horizontal (flat) interface between two homogeneous media, as shown in Figure 4-5(a). Because all numerical methods have numerical errors such as round-off error and finite resolution, the scattered wavefield from this model provides a measure of the background numerical noise level in all other models. One source of numerical noise is the truncation error associated with computations on machines having finite floating point precision. This noise places a lower limit on the wavefield amplitude variations that can be considered meaningful. Another source of noise is scattering produced by the microroughness of the interface due to the model definition occurring only at discrete gridpoints. Dougherty and Stephen (1991) investigated this problem and showed that scattering from this microroughness can only be eliminated if the grid spacing (and consequently the time step) is reduced to intervals very much smaller than necessary for numerical stability. This quickly makes the model computation

time impractical. However, they also suggest that this microroughness can be considered a realistic contribution to the seafloor model. As such, the microroughness adds a low level of background noise to the scattered field that is realistic, although not quantified in our analysis.

Figure 4-5(b) shows schlieren diagrams for the wavefields in the model space after propagating 160 ms (400 time steps). The Gaussian beam source pulse (P_1), was introduced at a grazing angle of 15° on the right side of the diagram and propagates from right to left (this propagation direction is the same in all subsequent schlieren diagrams). The water column, the upper half of the model, has compressional velocity, $v_p^w = 1.5 \text{ km/sec}$, density, $\rho^w = 1.0 \text{ kg/m}^3$ and no shear velocity. The lower half is a homogeneous solid basement with properties appropriate for igneous (basalt) basement rock, $v_p^b = 4.0 \text{ km/sec}$, $v_s^b = 2.0 \text{ km/sec}$ and $\rho^b = 2.5 \text{ kg/m}^3$. Such seafloor is considered a 'hard bottom' because $v_p^b \geq v_s^b \geq v_p^w$. If $v_p \geq v_p^w \geq v_s$, the seafloor is considered to be a 'soft bottom'. The compressional and shear critical grazing angles for a model with these properties are, respectively

$$\theta_c^p = \cos^{-1}\left(\frac{v_p^w}{v_p^b}\right) = 68^\circ \quad (4.6)$$

and

$$\theta_c^s = \cos^{-1}\left(\frac{v_p^w}{v_s^b}\right) = 41^\circ \quad (4.7)$$

such that the 15° source wavefield is incident at a subcritical grazing angle and is totally internally reflected. Consequently, there is no transmission of either compressional or converted shear waves into the subseafloor. The only scattered field produced in the water column is the specular reflection, P_1P_1 . In this notation for waves the subscript '1' refers to the propagation in the upper (water) medium, and a subscript of '2' refers to propagation in the subseafloor. Also note that we use the nomenclature P_1P_2 and P_1S_2 to denote diffracted body waves rather than transmitted or converted, transmitted body waves.

In spite of being totally internally reflected, in both the compressional and shear schlieren diagrams there is energy present in the subseafloor just below the contact of

the source pulse with the seafloor. This is the direct wave root (DWR) that exists only when an incident wavefield interacts with an interface at subcritical grazing angles. This is an 'evanescent wave' and does not exist as an independently propagating wave (Stephen and Bolmer, 1985). Like interface waves, it contains coupled shear and compressional wave energy and is evanescent away from the interface, with depth of penetration dependent on the compressional and shear wave velocities at the interface. Typical penetration is on the order of $\lambda_p/4$ (λ_p being the compressional wavelength in the solid), which in this model would be about 4 m. The importance of the DWR in the study of seafloor scattering is that it provides a source of energy for subseafloor scattering from volume heterogeneity, even when the grazing angle of the incident wavefield is subcritical.

The pressure time series is recorded at the receivers at the top and sides of the scattering chamber (Figure 4-1) that are located within the water column. The time series is recorded for 15,000 time steps (600 ms or 150 wave periods), which is a sufficient time for essentially all of the scattered wavefield energy to pass into the bordering absorbing region. The beamforming process is then applied to calculate the scattering coefficients as a function of scatter direction. Figure 4-6 shows the scattering function calculated for this baseline model. As expected, the only event with significant energy is the seafloor specular reflection which corresponds to the peak at 165° . Monostatic backscatter, i.e., scatter directly back towards the source, is then always at 15° , which is indicated by the labelled vertical grey line in each plot.

The width of the reflection peak is a function of the bandwidth of the source pulse and the wavenumber content of the Gaussian beam, i.e., the wavelet resolution. The numerical noise 'floor' is about 55 dB down from the reflection peak. This model represents total internal reflection, and there should be no energy propagating in any other direction, which suggests that this is the dynamic range of the NSC, i.e., about 55 dB. As a reference, the baseline model scattering function is included in the scattering function plots for all other models.

4.3.3 Scattering vs. ka

Figure 4-7(a) shows a series of horizontal, rough-seafloor models with variable correlation lengths and constant standard deviation (rms height for zero mean distributions) in height. The dimensionless parameters ka and $k\sigma$ are used to parameterize these surfaces. The velocity and density of the water and homogeneous subseafloor are the same as in the hard-bottom baseline model. Each seafloor model has been initiated from the same random distribution such that as ka decreases, the low frequency features are maintained while high frequency variations are increased. The surface characteristics of these Gaussian models are illustrated by the plots of autocorrelation, height probability distribution, and power spectra in Figure 4-7(b). In each case, the rms height was scaled to $\sigma = 1.91$ m so that $k\sigma = 2$. Correlation lengths were varied from $ka = 0.5$ to $ka = 6$, but only distributions for $ka = 1, 2$, and 6 are shown in these plots. As correlation length decreases, power is distributed over a wider range of length scales, as indicated by the broadening of the spectra and lowering of its peak value. The details of the height probability distribution vary but always have 68% of height values falling within the standard deviation, as expected for Gaussian distributions.

The snapshots of wavefield amplitude density after 160 ms of propagation in the scattering chamber are shown in Figure 4-7(c). The energy represented in these schlieren diagrams corresponds to a variety of elastic and acoustic waves. The types of acoustic and elastic propagation that are possible at a homogeneous liquid-solid boundary, insonified by a point source above the interface, are described in Brekhovskikh (1960). With a point source in the fluid, and a smooth boundary, these include the direct, reflected, and transmitted compressional waves, converted transmitted shear waves, as well as compressional and shear head waves and interface waves. When the incident wavefield is described as a plane wave or approximation to a plane wave (Gaussian beam), the existence and relative amplitude of each wave type depends on the grazing angle of the source wavefield and the propagation properties of the media, in particular the velocities defining the critical angles at the interface. When

the grazing angle of the source wavefield is less than either critical angle, a direct wave root is also generated. Although theoretical analysis can be used to predict all of the possible wave types that occur for very simple models such as a flat smooth interface or a point scatterer, it quickly becomes an intractable problem if the model is more complex. For this reason, predicting wave propagation in heterogeneous media, including rough surfaces, must rely on numerical approximation methods such as numerical wavefield modeling. If we think in terms of Huygen's Principle, all of these wave types are the result of constructive interference of wavefields emanating from secondary point sources along the flat interface. However, if the interface is not flat, this interference may or may not yield all of these wave types predicted for simple models. For a rough surface, some energy will be diverted into scattered energy recognized as diffractions. The occurrence of diffractions always implies the presence of a rough interface or volume heterogeneity. In general, diffractions occur where the heterogeneity has a radius of curvature comparable to the wavelength scale (Aki, 1982).

Two types of independently propagating interface waves are possible at a liquid-solid boundary: Stoneley waves and pseudo-Rayleigh waves. It is important to note that Stoneley waves are generated only if a wavefield energy source is located at, or near, the interface, because they require a source of inhomogeneous energy that is present only within the evanescent field of a source. Scattering of the incident wavefield on a rough surface provides secondary point sources for this evanescent energy. Given this condition, Stoneley waves will always be present at the seafloor interface. These (Stoneley) waves are evanescent in both the water column and the solid medium, and they propagate independently along the interface. Their decay depends on geometric spreading in 2-D as well as energy being lost to intrinsic attenuation and secondary scattering from surface roughness encountered. They propagate just slower than the lowest velocity occurring at the interface. For hard-bottom cases this will be the compressional velocity of the water, but for soft bottoms it will be the subseafloor shear velocity.

The other possible wave type, pseudo-Rayleigh waves, can occur only if the shear

wave velocity of the solid is greater than the fluid velocity, i.e., $v_s \geq v_p^w$. This wave travels along the interface with an apparent velocity just below the shear wave velocity. In the fluid it looks like a head wave, but in the bounding solid it is evanescent.

In rough-seafloor models, scattering of the Stoneley and pseudo-Rayleigh waves generates acoustic waves in the water column and compressional and shear body-waves in the subseafloor. This secondary scattering contributes energy to the total scattered wavefield energy that can continue to arrive at receivers long after the initial direct wave and reflected waves.

In Figure 4-7(c), the direct wave (P_1) is reflected (P_1P_1) from the seafloor as well as being diffracted from the surface roughness into the water column. Strong point diffractions occur where the half-width of a particular seafloor bathymetric feature is on the order of the incident wavelength (Dougherty and Stephen, 1987). Scattering at the seafloor also acts as the local source of interface waves that propagate in both the forward and backward directions. In this figure, Stoneley waves are clearly identifiable.

Although the grazing angle of the insonifying field at the seafloor is still subcritical, some of the incident energy is diffracted into the subseafloor. Wavefields propagate in the subseafloor primarily as diffracted compressional and converted shear waves but the direct wave root is also observed in this case. Some of the diffracted energy in the subseafloor interacts with the seafloor from below, generating a new set of secondary point sources which produce more Stoneley waves and both compressional head waves (pHW) and converted shear head waves (sHW) in the water column. Another shear body wave ($P_1P_2S_2$) is generated by the interaction of the diffracted compressional wave with the interface. Pseudo-Rayleigh waves are possible for these models but are not positively identified in these figures because they are kinematically very close to the shear waves propagating along the interface. The total scattered wavefield in the water column is a combination of primary diffractions of the direct wave from seafloor features, internal reverberation within these features, and secondary diffractions of interface waves.

Comparison of the schlieren diagrams shows that as the value of ka decreases, the

number of individual diffractions propagating in the water column increases. This suggests that the total scattered energy is increasing as the correlation length of the surface roughness decreases. It is expected that if the correlation length is decreased sufficiently, the scattering would again begin to decrease.

It is important to remember that each seafloor model is just a particular deterministic realization of all possible seafloor models having the same values for the parameters ka and $k\sigma$. In numerical modeling, different realizations are generated by initiating the model-building process with different random series. For example, Figure 4-8(a) shows three realizations of seafloor characterized by $ka = 4$ and $k\sigma = 2$. The similarity of the models is evident in comparison of the characteristics of the functions shown in Figure 4-8(b). It is not possible to distinguish or parameterize the 'randomness' of each realization, so that the scattering from three realizations is used to estimate a level of variation in scattered energy below which we cannot distinguish one realization from another. We refer to this as the 'realization error'. Signal variation at or below this level cannot be used to estimate seabed property variations.

The schlieren diagrams (Figure 4-8(c)) for these three realizations clearly show that the scattered fields differ in the locations of strong diffractions propagating in the backward directions. In Figure 4-9(a) the scattering functions for all models with $k\sigma = 2$ are plotted. In general, the scattering functions of the three realizations for each model remain grouped within a few decibels. In the 15° backscatter direction the realization error is estimated at ± 1 dB, for these models. In the backward scatter directions, the scattering coefficients for distinct seafloors diverge as a function of ka , with a maximum in this divergence occurring in the region around the monostatic (15°) backscatter direction.

Variation in scattering coefficient at 15° as a function of ka is shown in Figure 4-9(b). The results for $k\sigma = 2$ show clearly that the scattering decreases in a regular manner as ka increases. Results from other models calculated with $k\sigma = 4$ and $k\sigma = 0.5$ show a similar trend. Between $ka = 2$ and $ka = 0.5$ the scattering coefficients are almost constant, suggesting that this region may be the peak of the backscattering,

although we have no results for smaller values of ka to prove this. The grid spacing of 0.4 m does not allow definition of models with $ka < 0.4$. Within the realization error, models within $ka = 0.5$ and $ka = 2$ cannot be clearly distinguished based on scattering coefficients. For $ka > 2$, a linear approximation to the sensitivity gives the scattering coefficient decreasing at a rate of about $-3 \text{ dB}/ka$.

4.3.4 Scattering vs. $k\sigma$

In the next series of models, the correlation length is held constant while the seafloor rms height is varied. Velocity and density of the subseafloor are the same as the baseline model. Figure 4-10(a) shows examples of models with $ka = 6$ and variable $k\sigma$. Figure 4-10(b) shows that as σ decreases the probability height distribution narrows. With a fixed correlation length, the corner frequency of the power spectra is also constant. However, as σ decreases, the relative power of low spatial frequencies compared to higher spatial frequencies also decreases.

The schlieren diagrams corresponding to the models at 160 ms (Figure 10(c)) show that the energy diffracted from individual surface features increases strongly as $k\sigma$ increases. In general, the same set of wave types are observed as for variation in ka . However, the model with the lowest amplitude roughness, i.e., where $k\sigma = 0.5$, produced an identifiable pseudo-Rayleigh wave in the backward propagation direction, with its head wave appearance in the water and evanescent tail in the solid. Also, secondary diffraction produced by the interaction of the Stoneley waves with the seafloor roughness can be identified.

The scattering functions for all realizations of models with $ka = 6$ and variable $k\sigma$ are plotted in Figure 4-11(a). Again, the realizations remain grouped with differences in detail and realization error of about $\pm 1 \text{ dB}$ at 15° . Scattering coefficients are divergent as a function of $k\sigma$, as scattering decreases in the backward scatter directions. The propagation directions of head waves, predicted by Snell's law, are marked on the plot. When the surface is not very rough, the scattered signal propagating in these directions constructively interferes. As $k\sigma$ increases above unity the peaks at head-wave angles disappear, suggesting that the interference in these directions in no

longer constructive.

These model results provide an opportunity to compare our full elastic wavefield modeling to an acoustic modeling case. Thorsos (1988) computed scattering strength as a function of scattering angle for a variety of rough surface models with a pressure release boundary condition assumed. The results shown in Fig. 14 of that paper are for a source grazing angle of 20° and a model with roughness parameters very similar to those of the $k\sigma = 1$ model in Figure 4-11(a) (black solid lines). Thorsos' calculations suggest that scattering in the backward directions is a continuously decreasing function of scattering angle, i.e., as scattering angle decreases down to the monostatic backscatter direction and below, the scattering strength is always decreasing. Our results show that when elastic properties are included in the model and a full elastic wave equation formulation is used, that scattering in the backward directions does not continuously decrease. In fact, in the monostatic backscatter direction, a relative peak in scattering intensity is achieved. This result suggests that acoustic modeling of rough surfaces does not adequately predict scattering for use in monostatic acoustic reverberation studies. A significant part of the explanation for this is that, acoustic modeling does not account for the scattering introduced into the water column by interface waves, in particular Stonely waves (Stephen and Dougherty, 1993).

In the 15° backscatter direction, scattering coefficients increase rapidly as $k\sigma$ increases (Figure 4-11(b)). A similar trend is found when scattering from models with $ka = 1$ and variation in $k\sigma$ is calculated. From $k\sigma = 1.0$ to $k\sigma = 6$, scattering increases by about 13 dB, which is more than double the variation observed over the range in ka . This suggests that backscattering is much more sensitive to variation in surface height than to correlation length.

It is interesting that the highest level of backscattered energy in all of these models (both variation in ka and $k\sigma$) occurs in the direction of the source wavefield. This suggests that the monostatic reverberation experiment may always record the maximum variation and divergence of the backscattered field intensity, and as such it is a superior geometry to bistatic reverberation experiments for determining and resolving seafloor characteristics. However, in order to prove this it would be necessary to

model the monostatic scattering from the same models with different source grazing angles.

4.3.5 Gaussian vs. Self-similar

As previously discussed, a self-similar distribution of seafloor height variation may be a more realistic representation than the Gaussian distribution. But, as shown in Figure 4-3, Gaussian and self-similar models with approximately the same correlation length and rms height differ primarily in frequency components. Similarly, the difference between their corresponding wavefields, shown in Figure 4-12(a), is primarily that the self-similar model produces a greater number of small diffractions. The stronger diffractions associated with larger seafloor features are common to both model types. A comparison of scattering coefficients (Figure 4-12(b)) shows that the difference between the time-averaged intensity is quite small, even in the 15° backscatter direction. Because the difference between Gaussian and self-similar representations of the seafloor is no greater than the realization error, we conclude that any improvement in modeling that might be made by using self-similar models could not be resolved in the resulting scattered field intensities.

4.4 Large-Scale Seafloor Characteristics

Values of seafloor slope and subseafloor velocity and density measured over distances greater than about ten times the wavelength are considered large-scale features that do not produce significant scattering of the incident wavefield. However, large-scale features do have an effect on the partitioning of scattered energy because average slope changes the grazing angle of the insonification, and velocity and density define the critical angles and impedance contrast at the seafloor.

4.4.1 Variation in Velocity and Density

As discussed in the previous chapter, we consider only three main groups of subseafloor types: basalt, sediment and talus. The modeling discussed to this point has been limited to 'hard-bottom', basalt seafloor. Swift and Stephen (1994) suggest a basic breakdown of seafloor material into sediment, defined as seabed with $\frac{v_s}{v_p} < 1.0$, and igneous (basaltic) rock, defined as $\frac{v_s}{v_p} > 1.0$. By this definition, sediment-covered seafloor has no shear critical grazing angle, so that conversion of compressional wave energy to transmitted shear wave energy at the seafloor is always possible. Seafloors with sediment velocity and density characteristics are always considered 'soft-bottom' seafloors. Talus, being a mixture of fine grained pelagic sediment and coarse basaltic debris, has intermediate velocity and density, but in our modeling these parameters have been set such that talus would also be described as a 'soft bottom'.

To represent sediment in the subseafloor models, we use $v_p^s = 1.52 \text{ km/sec}$, $v_s^s = 1.0 \text{ km/sec}$ and $\rho^s = 1.5 \text{ kg/m}^3$. Talus is represented by $v_p^t = 2.0 \text{ km/sec}$, $v_s^t = 1.0 \text{ km/sec}$ and $\rho^t = 1.74 \text{ kg/m}^3$. To represent basaltic basement, we have used several velocity and density values besides the baseline model values, but we have maintained $\frac{v_p}{v_s} = 2$ in all cases. This gives a Poisson's ratio of 0.33, which is higher than the value for a Poisson solid (0.25). This value was chosen based on the evidence presented by Shearer (1988) that the Poisson's ratio in the upper 500 m of oceanic basement is within the range of 0.32 and 0.38, due primarily to fracturing in these upper-crustal regions. All of the parameter values used are within the ranges of realistic geological

parameters discussed in Chapter 3. The one exception is that the minimum velocity that could be included in the model for stability reasons was 1.0 km/sec, so the sediment shear velocity was set at this value. This gives the sediment in models an unrealistic Poisson's ratio of 0.1.

Figure 4-13 compares schlieren diagrams of the same seafloor structure (the Gaussian model in Figure 4-3) when the subseafloor is defined with the properties of basalt, talus and sediment. The points of origin for individual scattering events are the same for all three cases, but their amplitudes decrease as the subseafloor parameters decrease. When $\theta_c^s \Rightarrow 0^\circ$ for $v_s < v_p^w$, which is the case for both talus and sediment, 'transmitted' shear waves are clearly observed. The sediment model also generates transmitted compressional waves, because $\theta_c^p = 9^\circ$ is below the 15° grazing angle of the source wavefield.

Results of modeling with the same subseafloor properties, but with a smoother ($k\sigma = 0.5$) interface, are shown in Figure 4-14. In comparison to the rougher seafloor in Figures 4-13, both the scattering into the water column and into the subseafloor are much reduced. Again, transmission of P_1P_2 and P_1S_2 occurs as the shear and compressional velocities are decreased (Figure 4-14(ii) and (iii)). In this modeling the Stoneley waves are more clearly observed because there is less interference from seafloor diffractions. In fact, secondary diffractions of the interface waves can be distinguished in some locations, as noted on the figures.

Figure 4-15 summarizes the variation in scattering coefficients in the 15° backscatter direction as a function of subseafloor compressional velocity. The results include a variety of seafloor models represented by the stochastic distribution parameters $k\sigma$ and ka . In all of these models, the shear wave velocity and density of the subseafloor are defined by linear relationships to compressional velocity (see Chapter 3), and therefore, plots of scattering coefficients relative to v_s or ρ would show the same variation. Although only two values of ka are modeled, the results suggest that the sensitivity of the backscatter signal to average subseafloor velocity is not strong above $v_p = 2$ km/sec. A consistent exception to this is that the variation from $v_p = 2$ km/sec (talus) to $v_p = 1.52$ km/sec (sediment) is always large. In this range the

backscattering decreases on average by about 7 dB. We might attribute this to the fact that at this low velocity much more energy is transmitted. This would imply that seabeds with thick uniform sediment cover will produce much less backscatter than seabeds made up higher velocity materials such as talus or basalt. It is interesting that this transition seems to depend on the compressional velocity rather than on whether the bottom is 'soft' or 'hard' i.e., both the sediment and talus properties are considered those of a soft bottom. However, for these particular model results, it is also necessary to add a cautionary note. The unrealistically low Poisson's ratio of the soft-bottom models gives them more a more 'stiff' response to shear stress than could be expected from soft sediment. Considering this, the scattering coefficients calculated may in fact be somewhat higher than models with a more realistic Poisson's ratio.

The results of the modeling also show an anomalous result at $v_p = 3$ km/sec for small values of $k\sigma$. Multiple realizations of models with these characteristics all produce similar results. We can offer, at this stage, no explanation for this anomaly. Given the regularity in all the other model results, it may be an indication of some form of resonance set up within these models. In order to investigate the meaning of this anomaly, much more modeling would be required.

Within the limitations of the modeling shown here, we conclude that variation in backscattering is not a strong function of the average subseafloor velocity and density, for $v_p > 2$. An important exception is that very low-velocity seafloor, i.e., sediment covered, will generally have a substantially reduced backscatter signal.

4.4.2 Variation in Seafloor Slope

Much of the analysis of acoustic reverberation data has been focused on the correspondence of strong backscattering to steeply sloping seafloor areas (e.g., Makris and Berkson, 1994; Preston et al., 1990). In fact, in our own analysis of monostatic reverberation data (Chapter 2) we also showed this correspondence but also found that the intensity of the backscatter could not be quantified as a strong function of the large-scale slope as measured from Hydrosweep bathymetry data. In many

analyses of acoustic reverberation, the urge to find some simple relationship between the backscattered signal and seafloor characteristics is so strong that the role of wavelength-scale heterogeneity in strong scattering is quickly forgotten and approximations such as Lambert's rule (Jensen et al., 1994) in various forms are invoked to predict scattering as a function of seafloor slope and/or grazing angle. But these slopes are usually measured over distance scales much larger than the incident wavelength. The result is that scattering from large-scale deterministic features, caused by small and wavelength-scale features, is not considered. In this section, we investigate the effect of seafloor slope on scattering from a seafloor that also has roughness at wavelength scales.

Smooth Sloping Seafloor

Figure 4-16(a) shows a series of smooth-seafloor models with different slope. In each model, the middle of the sloping portion of the model is centered within the NSC grid space. As the schlieren diagrams in Figure 4-16(b) show, the only scattering observed for these models is due to the inherent microroughness of the grid itself and the corner diffractions emanating from the terminations of the models within the model space. Both of these sources of scattering are artifacts of the finite difference modeling. As previously discussed, the scattering from the microroughness can be considered a background 'noise' level from geologically reasonable small-scale roughness. The only non-artifact waves are the incident and reflected waves, the direct wave root, and the transmitted P_1P_2 and P_1S_2 body waves. The scattering coefficients for the complete set of smooth, dipping models are shown in Figure 4-17(a). For each model, the scattering function is dominated by a peak in the specular reflection direction. The amplitude of each peak is a function of the reflection coefficient which varies as a function of angle of incidence. Strong backscatter, well above the background level, in the source direction only occurs when the seafloor slopes at 75° , i.e., is normal to the 15° incident beam. Figure 4-17(b) shows that the scattering coefficient attributable to the grid microroughness and the corners of the model is about 25 dB above the scattering coefficient of the 0° slope baseline model.

Rough Sloping Seafloor

The rough, sloping-seafloor models shown in Figure 4-18(a) were generated by rotating the horizontal, Gaussian-seafloor model in Figure 4-3(a) to the desired slopes. Given that the horizontal model is described by $ka = 6$ and $k\sigma = 4$, these are the nominal descriptions for the dipping models also. However, a problem with modeling dipping interfaces in a finite model space is that it is not possible to present exactly the same surface to the incident wavefield, because the length of the actual dipping surface included in the model space varies with the dip. Also, the footprint of the incident beam varies with the dip of the seafloor. In order to minimize this problem, we have rotated the original horizontal, rough-seafloor model about the center grid space, such that at least the most central portion of each sloping rough model contains the same surface and interacts with the most central portion of the incident beam. For description of the stochastic portion of each of these dipping models, the actual values of ka and $k\sigma$ for each case are determined from the autocorrelations of the interface with large-scale dip removed. The distributions of the roughness characteristics with dip removed are shown in Figure 4-18(b) and the values are written at the top of each frame in Figure 4-18(a). The difference between $k\sigma$ of the original rough surface (Figure 4-3(b)) is less than about 10%. The difference in ka is larger, up to about 20%. However, these differences are not so large that the results of the numerical modeling cannot be compared.

Comparison of the schlieren diagrams (Figure 4-18(c)) to the case of no surface roughness (Figures 4-16(b)) clearly shows that the addition of the wavelength-scale stochastic roughness causes the simple interface reflection to be destroyed by interference. Also, a much higher proportion of energy is transmitted (scattered) into the subseafloor. The comparison of scattering coefficients in Figure 4-19(a) shows that in all cases the addition of dip increases the average scattering in backward directions in comparison to the same surface with no dip. However, it also appears that in the 15° backscatter direction (Figure 4-19(b)) there is very little distinction in scattering coefficient as a function of seafloor slope for slope greater than 15° , including the

case of normal incidence (75° slope). In comparison to smooth dipping seafloor (with backscattering from the grid microroughness), the overall backscatter is at least 15 dB greater in all cases. This is about 40 dB greater than the numerical error of the baseline (smooth and flat) model. It is also very clear from these plots that the peaks associated with the reflected wave have been essentially eliminated by the interference and scattering effects of the rough surface.

Alternatively, scattering coefficients can be plotted as a function of true grazing angle. The true grazing angle includes the grazing angle of the incident beam relative to the horizontal, θ_b , and the large-scale slope, θ_s .

$$\theta_g^{true} = \theta_b + \theta_s \quad (4.8)$$

At this point, we take a somewhat phenomenological step in our analysis in order to incorporate some measure of the seafloor roughness parameters in the definition of the grazing angle. This is purely an attempt to include the geologically significant wavelength-scale seafloor features in the interpretation of the backscatter data, and it is not based on wave propagation theory. Although there is no precedent for doing so, we add to the grazing angle an estimate of average (rms) slope (magnitude) of the interface roughness. For a seafloor defined by a stochastic Gaussian distribution, an rms slope, θ_{rms}^s , is defined by

$$\theta_{rms}^s = \tan^{-1}\left(\sqrt{2}\frac{\sigma}{a}\right) \quad (4.9)$$

(Broschat and Thorsos, 1997). This rms slope can be attributed to either the forward or backward direction relative to the incident wavefield (i.e. $\pm \tan^{-1}\left(\sqrt{2}\frac{\sigma}{a}\right)$), but we have used it only in the sense of the backward (i.e., beam facing) direction. An effective grazing angle, defined here as θ_g^{eff} , is then estimated as

$$\theta_g^{eff} \approx \theta_b + \theta_s + \theta_{rms}^s \quad (4.10)$$

For the horizontal, rough-seafloor model discussed above, with nominal correlation length ($ka = 6$) and rms height ($k\sigma = 4$), the rms slope is $\theta_{rms}^s = 43^\circ$. For the

same seafloor incorporated into the sloping-seafloor models, the resultant correlation lengths and rms height vary somewhat, such that the rms slope differs for each model slope and realization. The calculated rms slope for each model realization is plotted in Figure 4-20(a) as a function of the large-scale slope. The average rms slope is close to that of the horizontal model (43° in all cases), but any particular realization can deviate by as much as five degrees. In Figure 4-20(b), the scattering coefficients for all of the rough dipping models are plotted as a function of the effective grazing angle. The result still suggests that the backscattering is much less sensitive to changes in large-scale slope above about 15° (corresponding to $\theta_g^{eff} \approx 73^\circ$). Below 15° the scattering coefficients increase with θ_g^{eff} at a rate of about 0.5 dB/degree, but above 15° the rate decreases to about 0.2 dB/degree.

These results suggest that the backscatter signal from a smooth, flat seafloor, such as a lava flow, will produce at least 5 dB less signal than adjacent rough, sloping seafloor. It also suggests that changes in slope of an already dipping rough seafloor cannot change the backscatter signal by much more than 5 dB.

Another question is whether the variation in backscattered signal from rough sloping surfaces depends on the impedance contrast at the interface. To consider this, some of the rough, sloping-seafloor models were re-computed with the velocity and density of a sedimented seafloor. The scattering coefficients calculated are compared in Figure 4-21 to the coefficients for the same models with the baseline basalt-bottom properties. Although the difference in signal levels due to velocity change is substantial (10 dB), both the basalt and sedimented seafloor have about the same sensitivity to seafloor slope (Figure 4-21(b)).

4.5 Backscatter and Effective Rayleigh Roughness

In the previous sections, it has been shown that the backscattered monostatic signal is sensitive to both large-scale seafloor characteristics, viz. seafloor slope and subseafloor velocity, and the stochastic seafloor parameters, correlation length and rms height. The model studies have shown that variation in any one of these parameters, within the range of the realistic geological model, can cause variations in the backscattering intensity from 5 to 20 dB. If the actual values of all of these seafloor parameters except one is known, then it would be possible based on these sensitivity studies to predict the remaining parameter from observed backscatter signals. In general, we would not expect to already have such a complete seafloor description. An alternative approach is to reduce the problem by combining a number of these independent parameters into a single variable that can be used to describe the seafloor. In this section we combine all of the seafloor structural parameters into a single descriptive variable. The end result is that we then can consider the scattering from the seafloor in terms of the subseafloor velocity (and density) and a single surface-structure parameter.

One characterization of surface roughness is the Rayleigh roughness parameter, R_a , defined as

$$R_a = k\sigma \sin \theta_g \quad (4.11)$$

(Ogilvy, 1991). Surfaces with larger Rayleigh roughness parameters are expected to produce stronger scattered fields for a fixed impedance contrast. If we replace the grazing angle, θ_g , with the effective grazing angle, θ_g^{eff} , the Rayleigh parameter then incorporates all of the spatial characteristics of the seafloor, i.e., $k\sigma$, ka , and large-scale slope. We call this modified Rayleigh roughness parameter the 'effective Rayleigh roughness parameter', defined as

$$R_{eff} = k\sigma \sin \theta_g^{eff} = k\sigma \sin(\theta_b + \theta_s + \tan^{-1}(\sqrt{2}\frac{\sigma}{a})) \quad (4.12)$$

For the case of flat seafloor, $\theta_s = 0^\circ$ and $\theta_b = 15^\circ$, the variation of the effective Rayleigh parameter as a function of ka or $k\sigma$ is shown in Figure 4-22. This plot

shows clearly that effective Rayleigh roughness is only a slowly varying function of correlation length with a peak dependent on $k\sigma$. Note that the decrease in R_{eff} for small values of ka falls outside the range of values of ka appropriate for Site A. Contrary to this, effective Rayleigh roughness is a strong and almost linear function of $k\sigma$ for a fixed value of ka . This functionality is reflected in the modeling results, which show that the backscatter strength is more sensitive to variation in $k\sigma$ than ka and that scattering increases with decreasing values of ka for a fixed value of $k\sigma$. This suggests that local variation in monostatic data is more likely to be indicative of seafloor height variations than changes in correlation length.

The effect of large-scale slope on R_{eff} is also interesting. If large-scale slope increases to sufficiently large values, then θ_g^{eff} will be greater than 90° , at which point R_a begins to slowly decrease. In other words, the surface roughness appears to be at its maximum when the insonification is at 90° relative to the sum of the slope and the rms slope of the roughness. Such response is suggestive of what is observed in the modeling results. That is, for $\theta_b = 15^\circ$ and $\theta_{rms}^s = 45^\circ$, the backscatter response is almost flat beyond 30° , which corresponds to $\theta_g^{eff} = 90^\circ$ (Figure 4-20(b)).

In order to correlate effective Rayleigh roughness to scattering coefficients, R_{eff} is calculated from the parameters of each model. Figure 4-23(a) shows a 'wire' diagram for horizontal, hard-bottom seafloor models with $ka = 1$ and $ka = 6$ for a range of $k\sigma$ values. Although this plot is limited to the ranges of our model parameters, it does provide a simple basis for interpreting scattering coefficients in terms of wavelength-scale seafloor structural characteristics. For example, a scattering coefficient of -22 dB would correspond to a seafloor with $1.25 \leq R_{eff} \leq 2.25$. If in this example we believed that $ka = 6$, then $k\sigma = 3$ would be a best estimate of seafloor height variation. However, this diagram would only be applicable for scattering from a rough horizontal seafloor with the velocity and density of the basalt baseline model.

A more general interpretation method must take both large-scale seafloor slope and subseafloor velocity into account. One approach is use other data to remove the influence of these parameters from the observed intensity. If large-scale seafloor slope is known from bathymetry data such as Hydrosweep, then it is possible to estimate

and remove its effect on the backscattered signal. In Figure 4-23b(i), the average (of realizations) scattering coefficient for the rough, sloping-seafloor models are plotted with arrows leading to the approximate scattering coefficient that would be predicted (from the wire diagram itself) for horizontal rough seafloor with the same values (average of realizations) of ka and $k\sigma$. Determining the 'slope corrected' scattering coefficient requires both a change in R_{eff} , to account for the removal of the large-scale slope, and a change in scattering coefficient. Figure 4-23b(ii) summarizes the magnitudes of the changes in these parameters corresponding to each seafloor slope. For example, scattering from seafloor having a slope of 30° would require a change in effective Rayleigh roughness of -0.6 and a change in scattering coefficient of -8 dB to remove the effects of this slope in the R_{eff} vs. scattering coefficient plot.

In order to consider subseafloor velocity in detail, it is necessary to generate a new wire diagram for each velocity considered. Figure 4-24 shows wire diagrams for the same horizontal rough seafloors but with different subseafloor velocity and density values. The variation in backscatter as a function of velocity or density is small for any particular model, with the exception of the very low-velocity case. This is clearly reflected in the figure, in which the wire diagram for $v_p = 1.52$ km/sec is significantly shifted away from the other cases. A possible geological interpretation of scattering coefficients is also shown in this figure. This interpretation is based on the notion that when velocity and effective Rayleigh roughness are considered together, then sediment ponds will be areas of low velocity and low effective Rayleigh roughness, fault scarps or hummocky basaltic bottom will be areas of high velocity and high effective Rayleigh roughness, and basaltic sheet flows or talus might be areas of high velocity and low effective Rayleigh roughness.

Figures 4-23 and 4-24 can be used as a basis for interpreting of the monostatic backscattered signal returned from realistic seafloor. Such interpretation is reasonable, but approximate, because it assumes that the subseafloor is homogeneous, and because it is based on a limited number of seafloor models. To test the effectiveness of the interpretation scheme, we consider backscattering from the realistic seafloor models in Figure 4-4(a).

4.5.1 Seafloor Scattering: Models 1-4

The realistic seafloor profile generated in Chapter 3 is divided into four segments that fit within the model space of the NSC. These segments (Models 1-4) are shown in Figure 4-25(a) for the case of homogeneous subseafloor. The average large-scale slope for each model is shown by the dashed lines in the figures. The schlieren diagrams in Figure 4-25(b-e) show the scattering from these models when they have seabed velocity and density parameters simulating (i) basaltic (hard bottom), (ii) talus (soft bottom), and (iii) sediment (soft bottom) seabeds. These parameters are listed in Table 4-1.

The comparison of scattering coefficients for each case is shown in Figure 4-26. The results show that, as could be expected, the relatively smooth seafloor of Model 1 consistently generates lower backscatter for all seabed types. Also, as the velocity and density values decrease, all of the models produce lower scattering coefficients. Of particular interest in the schlieren diagrams is that, in most cases, a substantial proportion of energy is transmitted into the subseafloor. This implies that 'typical' seafloor on the flanks of mid-ocean ridges will in fact be penetrated by wavefields incident on the seafloor even at low (grazing) angles, for any of the seabed material types.

Figure 4-26(d), shows that the sensitivity of these seafloor models to velocity is very similar to that of a horizontal rough seafloor with $ka = 6$ and $k\sigma = 4$. Model 2 at $v_p = 4$ km/sec is an exception to this regularity. Model 2 is almost 5 dB higher than Model 3 in this case, whereas for the other velocity models it has lower scattering coefficients than Model 3. This anomalous result seems to be related to the response of the sharp seafloor peak at about 240 m, in range, to the incident wavefield. Except for this peak, Model 2 has relatively smooth seafloor, much like Model 1. Such a model might not be considered capable of generating scattering levels similar to the very rough seafloor of Model 3. The fact that it does suggests that not all backscattering can be explained by scattering from stochastic models of wavelength-scale features on the seafloor. A possible explanation for the strong backscatter for Model 2 is that at

this velocity the peak develops an internal resonance that radiates more energy than a single diffraction event. Stephen and Swift (1994) noticed that 'reverberation' in a single-facet seafloor model produced continuous scattered signals for long periods after the passing of the direct wave. It is conceivable that at some velocities, such reverberation could transform into a resonance and broadcast anomalously strong and long-duration signals. Such events may be an explanation for the anomalous 'highlight' signals observed in monostatic reverberation. Such events would only occur when the velocity and size of the feature are such that an internal reverberation within the particular feature occurs at a resonant frequency. Such events may also be an explanation for the anomalous backscattering from rough-seafloor models with $v_p = 3$ km/sec, as seen in Figure 4-15.

If we assume that the subseafloor is homogeneous, then the scattering coefficient at 15° can be used to estimate some seafloor characteristics. However, if nothing at all is known about the seafloor, only general characterizations can be made. For example, if the scattering coefficients measured in the monostatic experiment are consistently smaller than about -30 dB, then from Figure 4-24 the seafloor is most likely covered by low-velocity material (viz. sediment). If signals are consistently higher than -30 dB, the seafloor is most likely made up of higher-velocity (basaltic) material. The scattering coefficients at 15° for Models 1-4 are consistent with this generalization, that is, most of the models produce less than about -30 dB backscatter when the seabed is sediment covered (Figure 4-26(c)), and they have backscatter levels greater than -30 dB for higher-velocity seabeds. If variations in the backscatter signal greater than 10 dB are observed, then we can also be sure that some seabed characteristic besides seafloor slope must be varying. In areas with large-scale slope consistently greater than 15° , we could claim that signal variations greater than 5 dB should be attributed to variations in geological parameters other than slope.

In order to make a more specific interpretation, it is necessary to have some information about seabed characteristics. For example, in Figure 4-27 we consider the possible interpretations of the scattering coefficients from each of the realistic seafloor models when we know, or can estimate, the large-scale slope, the seafloor

stochastic roughness and the mean subseafloor velocity and density. With this much *a priori* information, it is possible to determine both the seafloor correlation length and standard deviation directly from the scattering coefficient. The average (least-squares fit) large-scale slope calculated for each (entire) model (shown in Figure 4-25(a)) is used to find approximate shifts in roughness, R_{eff} , and scattering strength (from Figure 4-23b(ii)) that should be applied to the scattering coefficient at 15° for each model. When these shifts are applied, as indicated by the arrows in Figure 4-27, the new location within the wire diagram can be used to estimate the values of ka and $k\sigma$ for the stochastic wavelength-scale roughness of each model. In this figure, the vertical grey lines, labeled Model 1-4, correspond to the correct value of R_{eff} for each model. These values are calculated from the actual stochastic parameters for each model and assume a 15° grazing angle and 0° large-scale slope. If the shifts based on Figure 4-23(ii) are accurate, the shifted scattering coefficients should be on, or near, one of these vertical lines. Table 4-2 summarizes the estimates of ka and $k\sigma$ determined by this procedure for each model. For this table, linear interpolation and extrapolation is used within the wire diagram to find ka and $k\sigma$ for each model.

The results shown in Table 4-2 imply that the procedure can lead to a correct interpretation in the majority of cases. The average absolute deviation, $\overline{|\Delta|}$, is much smaller for $k\sigma$ than for ka , indicating that resolution is much better for $k\sigma$. However, it also shows that we cannot expect to be precise in the quantification of scatter. The predicted values of ka and $k\sigma$ for these models are within about 20% and 10%, respectively, of the actual values. Also, there are the anomalous cases, such as the response observed in Model 2 for $v_p = 4$ km/sec, that are unpredictable responses to individual seafloor features rather than a response to the statistical average seafloor.

A more realistic scenario is to make the interpretation starting with much more limited *a priori* information. For example, we might know large-scale seafloor slope based on coarse bathymetry data such as Hydrosweep. The shift in observed scattering coefficients to account for this slope can be made, but the results then correspond to the horizontal grey lines in Figure 4-27. In this case, each shifted scattering coefficient could be generated by seafloor having stochastic parameters found anywhere

along the corresponding horizontal line. The modeling of horizontal seafloor showed that variation in backscatter is a stronger function of variation in rms seafloor height than correlation length, so that one further step in the interpretation would be to choose a fixed value for correlation length and then attribute signal variation to variation in $k\sigma$. For example, the average value of ka in the stochastic portion of Models 1-4 is $ka = 7$. Table 4-3 summarizes the values of $k\sigma$ that are then interpreted for each model. The results of this analysis are satisfactory in that, for most of the examples, the predicted rms height is at the expected physical scale, i.e., the predicted σ is ≤ 4.5 m and the measured σ (from spatially filtered seafloor models) is ≤ 3.37 m. The average absolute deviation, $|\bar{\Delta}|$, suggests that $k\sigma$ can be resolved in such an interpretation only to within about 40% of its true value.

The analysis described above can be applied to actual monostatic reverberation data only if some means can be found to scale the real data intensity to be equivalent to the intensities in this model study. One approach might be to assume that some signal level in the real data corresponds to a particular geological model and interpret all other signals relative that model. A general description of the application of this interpretation scheme that can be applied to such scaled monostatic reverberation data is as follows: If the seabed is assumed to be approximately homogeneous, then a signal greater than -25 dB would be indicative of high-velocity seafloor (i.e., basaltic basement or talus). A signal consistently less than this would be indicative of a region with sediment cover. Variation in signals of more than about 5 dB, within an area considered to have a laterally uniform velocity and density seabed, can be considered an indication of a change in roughness of the stochastic seafloor. Within about 5 dB, variations in signal due to roughness changes cannot be distinguished from variations in large-scale seafloor slope. However, if seafloor slope is known, a shift can be applied to the signal such that variations in seafloor roughness can be estimated from the remaining signal. From seafloor roughness the parameters ka and $k\sigma$ can then be estimated. This procedure provides a method for determining at least an approximation to seafloor spatial characteristics.

4.6 PART II:

Models with Heterogeneous Subseafloor

The numerical calculation of scattering effects of rough seafloor with homogeneous subseafloor has shown that a significant portion of energy from low-grazing-angle incident wavefields penetrates into the subseafloor in realistic seafloor models. Even in the case where total internal reflection occurs, energy is present in the shallow subseafloor via the direct wave root. All energy reaching the subseafloor is then available for elastic wavefield scattering if volume heterogeneity in velocity and density is encountered. When such scattering occurs, some of the scattered waves are directed upwards and return to the seafloor. Dougherty and Stephen (1988) showed that scattering from volume heterogeneity excites interface waves, which propagate along the seafloor and scatter back into the water column when heterogeneity at the surface is encountered. Energy that is emitted from the seafloor into the water column from this interaction is observed as seabed volume scattering. As energy is also scattered into the subseafloor and some of it returns to the seafloor, the process is repeated until all wavefield energy has been dissipated.

As with seafloor scattering, the spatial scales over which the heterogeneity occurs, compared to the wavelength in the subseafloor medium, are expected to have a significant effect on the characteristics of the volume scattered wavefield. In this study, volume heterogeneity at wavelength scales is defined as isotropic heterogeneity, with correlation length and rms perturbation amplitudes constrained to Gaussian stochastic distributions. Volume heterogeneity in the subseafloor can also include such characteristics as layering, gradients, and faulting. Large-scale variations such as gradients can influence the scattering that is generated by the wavelength-scale heterogeneity but do not in themselves produce scattering. Geological subseafloor models with vertical gradients in velocity and density, in addition to stochastic variation, are calculated. Models with other heterogeneous characteristics, such as layering and localized fault zones, are also considered.

Bathymetry data was used to define the ranges of correlation length and rms

height variation for realistic models of the seafloor. Unfortunately, there are no direct measurements of subseafloor properties within the boundaries of Site A. Furthermore, there are essentially no measurements of fine-scale (in the sense of 6 m wavelength) lateral variation in subseafloor properties anywhere in the deep ocean. As discussed in the previous chapter, realistic ranges of subseafloor properties, in particular velocity and density, can be interpreted from core and well log data. The acoustic lance and sediment core data from Fu et al. (1996), shows that vertical variation in sediment velocity and density, in a large sediment pond environment, can be on the order of 20% over cycles of 0.5-1.0 m within the first few meters of the seafloor. Core descriptions from DSDP drilling in the region (e.g., DSDP Holes 295A and 396B (Moos, 1990; Kirkpatrick, 1978) indicate that the basement below thick sediment ponds consists primarily of pillow basalts, basalt flows, and volcanic breccia at scales of 10-100 m thickness. Well logs in these drillholes, however, show that large variations in sonic velocity and density (as much as 100%) occur over much finer scales. Goldberg and Sun (1997) analyzed well log data from ODP Hole 504B (on the flank of the East Pacific Rise) to estimate the scales of vertical heterogeneity in the shallow crust (< 2.1 km). They found that the subseafloor was dominated by variations having correlation lengths of 1 m and 10 m. Their interpretation of this is that the 1 m heterogeneity is characteristic of pillow basalts and the 10 m heterogeneity is characteristic of lava flows and large-scale faulting. For our modeling, we suggest that the high slope, exposed igneous basement areas at Site A can be described as having isotropic heterogeneity with correlation lengths predominantly at the scale of 10 m and speculate that talus wedges are better described as having smaller correlation lengths on the order of 1 m. We also consider vertical gradients as high as 20 sec^{-1} in the shallow igneous basement to be likely. Within a region as small as Site A, pelagic sedimentation should produce essentially homogeneous sediment volumes in the perched sediment ponds. Therefore, sediment layers in our final models are treated as uniform layers with vertical gradients in velocity and density.

4.6.1 Scattering from Isotropic Volume Heterogeneity

Seabed models with heterogeneous distributions of subseafloor velocity and density are constructed by defining 2-D distributions of perturbations in these properties, relative to a specified homogeneous background model. To create isotropic heterogeneity, 2-D stochastic distributions with Gaussian autocorrelations are generated having specified correlation length (a_v) and standard deviation of the perturbation amplitude (σ_v), equal in all directions within the subseafloor. The rms perturbation amplitude in these models is described as a percentage of the mean (homogeneous) velocity and density, except in the case of models with gradients, when it is a percentage of the initial (seafloor) values. In all models, the range of perturbed velocity is constrained to $1.0 < (v_p, v_s) < 7.0$ km/sec to maintain numerical stability and acceptable grid dispersion in the NSC.

4.6.2 Scattering vs. a_v

Figure 4-28(a) shows three examples of a flat seafloor with isotropic volume heterogeneity. In each case, the background homogeneous (mean) model is defined with the baseline 'hard-bottom' properties. The perturbation amplitude of $\sigma_v = 10\%$ applies to all three propagation parameters, i.e., compressional and shear velocity and density. The model variable is the correlation length of the perturbation. For volume scattering, the dimensionless descriptor, ka , depends on the velocity of the subseafloor, whereas in the seafloor (interface) modeling ka was only dependent on the water velocity. For compressional waves, $k_p a_v = \frac{2\pi a_v}{\lambda_p}$, where λ_p is the wavelength defined by the mean compressional velocity. For shear waves, $k_s a_v = \frac{2\pi a_v}{\lambda_s}$, where λ_s is the wavelength defined by the mean shear velocity. For the following discussion we use the values of $k_p a_v$ when referring to volume heterogeneity and ka when referring to seafloor roughness.

The schlieren diagrams in Figure 4-28(b) show that the scattered field observed in the water column increases significantly as the correlation length of the heterogeneity decreases from $k_p a_v = 4.63$ to $k_p a_v = 0.69$. If we were to continue decreasing the

correlation length of the volume heterogeneity we would again expect the scattering to begin to decrease as it gets much smaller than wavelength scales. This figure also brings out an inherent problem in determining the scattering effects of volume heterogeneity. In order to isolate the scattering due to volume heterogeneity from surface scattering, the seafloor is assumed to be flat. Therefore, these models are actually comparisons of volume scattering when the majority of wavefield energy reaching the subsurface is via the direct wave root (DWR). The DWR is evanescent away from the seafloor and consequently, it makes direct contact with only the shallowest portion of the subseafloor model. The resulting scattered-field intensity varies as the correlation length varies, but the magnitude of the scattered field is very small and does not reflect the magnitude of volume scattering that could occur if more energy penetrated the seafloor, as would be the case with a rough seafloor or a low-velocity subseafloor.

In order to estimate the resolution of the modeling, multiple realizations of these models were computed. Figure 4-29(a) shows three realizations of a model having $a_v = 4.2$ m and $\sigma_v = 10\%$. Comparison of schlieren diagrams (Figure 4-29(b)) for these models shows that different model realizations produce scattering that does not vary significantly.

Figure 4-30(a) shows the scattering coefficients calculated for all of the hard, flat-seafloor models with isotropic subseafloor having $\sigma_v = 10\%$ and variable a_v . In general, scattering increases in all scattering directions as the correlation length of the volume heterogeneity decreases from $k_p a_v = 4.63$ to $k_p a_v = 0.3$. It is notable that the volume heterogeneity produces strong headwaves in both forward and backward directions for most of the correlation lengths modeled. This effect of scattering from subseafloor volume heterogeneity was first pointed out by Swift and Stephen (1994). It suggests that analysis of head wave amplitudes may be a means by which volume heterogeneity could be interpreted from bistatic reverberation data.

When variation of the 15° scattering coefficient is plotted as a function of $k_p a_v$ (Figure 4-30(b)), we see that, in fact, there is some indication of a peak in the scattering coefficient in the vicinity of $k_p a_v \approx 1$. This plot also shows that volume scattering decreases above $k_p a_v \approx 1$ at a rate of about -3 dB/ $k_p a_v$. This sensitivity is as strong

as that observed for variation in rms height of the seafloor. However, the magnitude of the volume scattering is more than 10 dB down compared to signals produced by seafloor scattering. Variations in scattering coefficients attributable to different realizations are about ± 1 dB, suggesting that changes in ka greater than one unit would be significant. The fact that the scattering coefficient of the reflection in each model (Figure 4-30(a)) is the same magnitude as for the baseline seafloor model is confirmation that essentially all of the energy involved in the volume scattering in these models is from the DWR. It is also noted that the introduction of volume heterogeneity produces higher levels of head waves, in particular the backward-propagating shear head wave. This is more evidence that most of the energy conversions in the subseafloor are occurring very close to the seafloor.

4.6.3 Scattering vs. σ_v

The same series of isotropic heterogeneous models discussed above were re-computed with perturbation amplitudes of $\sigma_v = 5\%$ and $\sigma_v = 50\%$. Figure 4-31(a) shows examples of these models in the case of $\sigma_v = 50\%$. The large perturbations in these models transform the flat seafloor into what is effectively a rough seafloor, that is; variations in subseafloor velocity and density at the seafloor cause the seafloor to appear to the incident wavefield as an irregular boundary. This allows incident energy to scatter into the subseafloor as converted shear and compressional waves, i.e., more energy than is available in just the DWR. The schlieren diagrams in Figure 4-31(b) show that there are strong diffraction events, but they are generated primarily by the scattering of the direct wave from heterogeneity at the seafloor. There is also a higher intensity of scattering observed in the subseafloor, with some portion of this generated by interaction with the DWR. However, it is not obvious that much of the energy being scattered in the subseafloor is being returned to the seafloor. It is clear, however, that these models are producing stronger scattered fields in the water column than the models with $\sigma_v = 10\%$.

Figure 4-32(a) compares the scattering coefficients in all directions for models with 5%, 10% and 50% perturbations for two values of the volume heterogeneity correlation

length. For the cases of $\sigma_v = 50\%$, it is notable that the strong head wave events have disappeared, which is also observed when seafloor roughness is increased (see Figure 4-11). Also, when $\sigma_v = 50\%$, the scattering coefficient in the reflection direction is reduced by about 12 dB compared to the baseline model, confirming that energy other than the DWR is penetrating the seafloor. The rapid increase in the scattering coefficients as the perturbation amplitude is increased (Figure 4-32(b)) suggests that volume scattering is very sensitive to this parameter (just as seafloor scattering is strongly sensitive to variation in σ). However, even with an intentionally flat seafloor, the subseafloor velocity variation creates an irregular (rough) velocity and density boundary at the seafloor. This suggests that it may not be possible to distinguish between scattering from the irregular impedance boundary of a volume-heterogeneity model and scattering from a rough-seafloor (interface) model. Also, as in the case of variation in $k_p a_v$, these signal levels are 5-10 dB smaller than those observed in all the seafloor scattering models. These results raise the question of whether volume scattering from heterogeneity significantly below the seafloor is actually contributing any significant signal to the scattered field observed in the water column.

4.6.4 Rough Seafloor and Isotropic Volume Heterogeneity

In order to consider the combined effects of volume heterogeneity and rough seafloor, the two rough, hard-bottom seabed models shown in Figure 4-33(a) were computed. These models have both seafloor roughness, with $ka = 6$ and $k\sigma = 4$, and isotropic volume heterogeneity, with $k_p a_v = 6.6$. The models differ only in the volume perturbation amplitudes, which are (i) $\sigma_v = 10\%$ and (ii) $\sigma_v = 50\%$. The rough surface is the same as that in the Gaussian homogeneous model of Figure 4-3(a). The schlieren diagrams at 160 ms (Figure 4-33(b)), when compared to the homogeneous model (Figure 4-12(a)), suggest that the rough-surface scattering dominates the total scattered field in all cases, even with large perturbation in heterogeneity. Figure 4-34 compares the scattering coefficients for these models to the flat-seafloor models with the same heterogeneity. When the rough seafloor is added to the $\sigma_v = 10\%$ volume model, the resulting scattering function is almost identical to the case of the homogeneous

rough surface. This implies that even with more energy penetrating the seafloor, the 10 % volume heterogeneity has had almost no effect on the total scattered field. The rough-surface model with $\sigma_v = 50\%$ shows an increase of only about 2 dB over the homogeneous model. Because the rough homogeneous model and the flat heterogeneous model with $\sigma_v = 50\%$ have very similar scattering levels, particularly in the backscatter directions, we might expect that the model with both the rough surface and volume heterogeneity would yield much higher scattering coefficients than either of the original models. This scattering coefficient is only increased slightly relative to the homogeneous model, which suggests that the 'volume scattering' is predominantly scattering from the volume heterogeneity very close to the seafloor. When volume heterogeneity is included in a rough-seafloor model, it essentially adds more roughness to the seafloor from the standpoint of interaction with the incident wavefield.

Although this is a very limited set of possible models, these observations strongly suggest that volume heterogeneity, at least in hard-bottom models, cannot be distinguished in any way from surface-roughness scattering. Nor does scattering from volume heterogeneity substantially increase the net scattering observed from a rough seafloor without subseafloor volume heterogeneity. It seems that most of the signal that is scattered into the subseafloor becomes trapped there, undergoing multiple scattering with little or no signal returning to the seafloor. It is true that the backscattered signal has sensitivity to volume heterogeneity correlation length and perturbation amplitude as strong as that of seafloor correlation length and rms height variation, but the intensity level of the volume scattering intensity is not significant compared to that produced by seafloor scattering unless the perturbation amplitude is in the range of 50%.

4.6.5 Isotropic Volume Heterogeneity with Sloping Seafloor

It might be argued that even rough-seafloor models do not allow much energy to penetrate into the subseafloor, and they therefore do not show the maximum possible effect of volume scattering. One way to increase the energy penetrating the seafloor is to increase the large-scale seafloor slope. To investigate this, volume heterogeneity

with perturbation amplitudes of $\sigma_v = 10\%$ and $\sigma_v = 50\%$ and a range of correlation lengths are added to the 45° sloping models with smooth (Figure 4-16a(ii)) and rough (Figure 4-18a(ii)) seafloor. An example with $k_p a_v = 0.7$ and $\sigma_v = 10\%$ and their corresponding schlieren diagrams at 160 ms are shown in Figure 4-35. These should be compared to the schlieren diagrams in Figures 4-16b(ii) and 4-18c(ii). The similarity to scattering from models with homogeneous subseafloor again suggests that the effect of volume scattering is quite small in comparison to the seafloor scattering. Internally, i.e., within the subseafloor, the volume scattering certainly affects the coherence of the propagating waves, but the net energy returned to the seafloor and scattered into the water column is small.

The scattering coefficients for all of the 45° models computed are plotted in Figure 4-36. A strong sensitivity of the scattered field to changes in the correlation length of the volume heterogeneity for smooth, sloping models is observed. Compared to the smooth, horizontal models with volume heterogeneity (Figure 4-30), the intensity level of the scattering is much higher. The scattering coefficients of rough, sloping seafloor with and without volume heterogeneity are also shown in the figure. For the rough-seafloor models, when $\sigma_v = 10\%$, the resulting scattering function is almost identical to that of the homogeneous model. When $\sigma_v = 50\%$, the scattering coefficients differ by less than 2 dB from the homogeneous model in directions less than 40° . These results again suggest that volume scattering does not appreciably change the level of scattering from that attributed to the rough seafloor.

4.6.6 Variation in Mean Volume Properties: Hard vs. Soft Bottoms

If the subseafloor has both low compressional and shear wave velocity, the seafloor becomes essentially transparent to the incident wavefield because the critical grazing angle is always exceeded. In these cases the energy transmitted into the subseafloor, and available for volume scattering, is at its maximum. Figure 4-37(a) compares the scattering coefficients calculated for models computed with and without volume

heterogeneity, for seabeds with hard- and soft-bottom parameters. For both $\sigma_v = 10\%$ and $\sigma_v = 50\%$, the difference between the scattering coefficients for flat seafloors shows very little sensitivity to the mean velocity of the models, particularly in the 15° backscattering direction. The plots for multiple realizations of the hard bottom with $\sigma_v = 10\%$ shows that the sensitivity is, in fact, less than the realization error.

However, if we consider models that include surface roughness and seafloor slope, somewhat different results are obtained. Figures 4-37(b-c) compare scattering functions of rough heterogeneous models to those of rough homogeneous models for both soft and hard bottoms with $\sigma_v = 10\%$ and $\sigma_v = 50\%$. Also included are results of modeling with talus subseafloor properties with $\sigma_v = 50\%$. Figure 4-37(d) compares the scattering coefficients of rough, soft-bottom seafloor with 45° slope. The hard-bottom models show (solid lines in Figure 4-37), as in Figure 4-34, that volume heterogeneity has little effect on the net scattered field when the seafloor is rough. Contrary to this, the heterogeneous soft-bottom models (dashed lines in Figure 4-37) produce significantly higher scattering coefficients than the homogeneous models. In the 15° backscatter direction, the difference is about 8 dB for the $\sigma_v = 50\%$ model and about 2 dB for the $\sigma_v = 10\%$ model. This is also true for the sloping soft bottom, where the scattering coefficient of the heterogeneous model ($\sigma_v = 10\%$) in the 15° direction is about 9 dB higher than its homogeneous counterpart. The talus model, which has mean volume properties between the hard-bottom and soft-bottom values, shows an increase of about 4 dB in scattered energy when volume heterogeneity with $\sigma_v = 50\%$ is added to the homogeneous talus, rough-seafloor model.

Figures 4-37(e) and 4-37(f) show the sensitivity of the 15° backscattered signal to variation in v_p and σ_v for these rough-seafloor models. The plots show that as the perturbation amplitude of volume heterogeneity increases, the backscatter signal increases, but simultaneously, the sensitivity to mean subseafloor velocity decreases. Except at very low velocity (where the maximum penetration of sound into the subseafloor occurs), the level and variation of the backscatter intensity can be attributed to seafloor (surface) scattering. The fact that the high-velocity models with $\sigma_v = 50\%$ are so insensitive to subseafloor velocity might, in fact, be another indication that

volume scattering is not generating much of the scattered field. Our interpretation of these results is that there is a practical limit to the amount of scattering that can be produced by interface roughness. That is, there is some point at which increasing interface roughness does not increase the scattered field. The models having both seafloor roughness and $\sigma_v = 50\%$ may have reached that limit.

4.6.7 Models 1-4 with Isotropic Volume Heterogeneity

The results of modeling isotropic volume heterogeneity suggest that there should be little difference between scattering from realistic seafloor with homogeneous subseafloor and scattering from the same seafloor with heterogeneous subseafloor. In fact, it can be said that the main contribution of volume heterogeneity below an interface is that it adds to the 'apparent roughness' of the interface, and consequently alters the surface scattering to some small extent. When the low velocities in variable-velocity seafloor approach water velocity, an apparent rough surface is created that interacts with the incident wavefield just as a rough surface would.

Figure 4-38(a) shows the realistic seafloor models (Models 1-4) with volume heterogeneity having the characteristics of $\sigma_v = 10\%$, $k_p a_v = 0.7$ ($a = 1.7$ m), and the hard-bottom mean velocities and density. This might be thought of as a subseafloor predominantly made up of pillow basalts and basaltic fragments.

Schlieren diagrams for each model with $\sigma_v = 10\%$ and $\sigma_v = 50\%$ are shown in Figure 4-38(b-e). These are compared to the homogeneous model results in Figure 4-25. In both cases, the principal propagation modes are the same as in the homogeneous models. In the subseafloor, the volume scattering disrupts the coherence of the body wave modes, but only in the case of $\sigma_v = 50\%$ in Model 1 do we see a significant difference in the scattered field in the water column. At this point, we would argue that this is probably due to the increase in the apparent roughness of the relatively smooth seafloor of Model 1 (in comparison to Models 2-4).

The comparison is shown more quantitatively in Figure 4-39. For $\sigma_v = 10\%$, all of the models except Model 1 have scattering functions almost identical to their homogeneous counterparts. When $\sigma_v = 50\%$, the scattering functions for Model 2 and

Model 3 are still within a few decibels of the homogeneous models. However, Model 1 and Model 4 now show differences greater than 6 dB. All of these variations, however, are within the limits of signal variation that can be attributed to changes in interface roughness (e.g., Figure 4-11). If isotropic volume heterogeneity has a significant impact on the scattered field, we would expect this effect to be observed in all models. The facts that scattering is not consistently affected when volume heterogeneity is added and that the models with the smoothest seafloor are most strongly affected can be interpreted as indications that volume heterogeneity only affects scattering by changing the apparent roughness. If volume heterogeneity changes laterally, it will alter the scattered field from place to place, but this variation will not usually be distinguishable from changes in actual surface roughness, unless the surface roughness has been previously determined from some other data.

4.6.8 Scattering from Large-Scale Volume Heterogeneity

In this section, scattering from geological models with vertical gradients in velocity and density, in addition to isotropic heterogeneity, is calculated. If isotropic volume heterogeneity really only affects scattering into the water column by altering the apparent roughness, then we would not expect gradients in the solid volume to impact scattering significantly. Finally, models with lateral variation in large-scale characteristics, such as layering and fracture zones, are also considered.

Gradients in Mean Velocity and Density

Gradients in subseafloor velocity and density, are considered 'normal' characteristics of the seabed. The magnitude of the gradients depends on such factors as the type of seabed, e.g., igneous or sediment, its age, and secondary processes such as hydrochemical alteration. In the previous chapter, we estimated that gradients in the upper 100 m of basaltic rock can be as high as 20 sec^{-1} . Gradients in sediment are expected to be only about $1\text{-}2.5 \text{ sec}^{-1}$, with the exception that a very strong gradient ($\sim 25 \text{ sec}^{-1}$) may exist in the first few meters. We might also expect that there will be a gradient in the perturbation amplitude of rock properties, such that the perturbation decreases with depth. However, Swift and Stephen (1994) showed that a gradient in perturbation produces negligible change in scattering coefficients, so it is not included in our modeling.

Figure 4-40 shows the calculated scattering functions for flat-seafloor models with $\sigma_v = 10\%$, $a = 1.8 \text{ m}$, initial (seafloor) parameters, $v_p = 3.2 \text{ km/sec}$, $v_s = 1.6 \text{ m/sec}$, and $\rho = 2 \text{ kg/m}^3$ and vertical gradients ranging from 0 sec^{-1} to 20 sec^{-1} . As the gradient increases, the response decreases and the sensitivity is very low, as shown in Figure 4-40(b). The maximum change in the 15° backscatter direction is 4 dB, but the signal levels are always at least 10 dB down relative to scattering from rough homogeneous seafloors. Included in Figure 4-40(a) is a comparison of a rough, heterogeneous seafloor model with and without the 20 sec^{-1} gradient. The addition of the gradient has almost no impact on the scattering function, particularly in the

backscatter directions.

Figure 4-41 shows the results from models with $\sigma_v = 10\%$, $a = 11.8$ m, and initial velocity and density values corresponding to the soft-bottom seafloor. In this series we include the sediment model based on the Fu et al. (1996) data. This model has a very steep gradient ($\sim 25 \text{ sec}^{-1}$) and reversal in v_p in the top few meters. These models produce scattering coefficients that are as small as the baseline model, suggesting that flat, soft-bottom seafloor with heterogeneity and gradients will not produce significant backscatter signals. We also note that the Fu et al. (1996) sediment model produces essentially the same response as a simple gradient, so the velocity inversion does not have a strong effect on scattering.

Figure 4-42 compares the same model with gradients of 20 sec^{-1} but with different seafloor initial velocities. These results suggest that there is no increase in the sensitivity of the scattering to velocity when a gradient is added to the model. It also shows that changing velocity does not increase the scattering to levels comparable to surface scattering.

It might again be argued that these flat models only compare the volume scattering generated from the energy available in the DWR. Figure 4-43 shows the scattering functions of sloping, rough-seafloor models with homogeneous subseafloor compared to the same models with heterogeneous subseafloor and a gradient. The results show that gradients in subseafloor properties do not significantly alter the scattering from a rough seafloor.

Fault Heterogeneity

Another form of heterogeneity that is considered an important characteristic of the seafloor is fracturing along faults. Fracturing along faults produces zones of higher porosity. These are modeled as localized regions having low velocity and density.

For the sake of simplicity, we model faults as vertical features that are one or two wavelengths wide. Figure 4-44 shows the realistic Model 3 with one (i) and several (ii) fault zones. Other than the fault zones, the subseafloor is parameterized as a homogeneous hard bottom. Figure 4-44(b) shows corresponding schlieren diagrams which

should be compared to the homogeneous model result in Figure 4-25d(i). The fault zones are clearly interacting with the body waves in the subseafloor, but there is no substantial change in the diffractions observed in the water column. The comparison of scattering functions (Figure 4-45) shows that these fault zones do not significantly alter the scattered field.

4.6.9 Realistic Layered Models

The primary objective of this modeling has been to provide a basis for understanding and interpreting backscattered signals from realistic seabed models. The most realistic models include layering, variation in volume heterogeneity and gradients. In Figure 4-46, we show seabed Models 1-4 with sediment, talus, and basalt layers included. In these models sediment is defined as soft bottom with the vertical gradients in velocity and density defined by the Fu et al. (1996) data, but with no wavelength-scale volume heterogeneity. Talus is defined as heterogeneous subseafloor with $\sigma_v = 50\%$, $a_v = 1.7$ m, and a vertical gradient of 20 sec^{-1} . The basalt regions are defined as hard-bottom heterogeneous subseafloor with $\sigma_v = 10\%$, $a_v = 11.8$ m and a vertical gradient of 20 sec^{-1} .

The scattering functions computed for these very realistic and complex models are compared in Figure 4-47 to the scattering functions of the hard-bottom homogeneous model and to the uniform layered model (i.e., Figure 4-46(a) but with no heterogeneity or gradients in the sediment, talus and basalt layers). Even with such a high level of complexity, the response of all models, except Model 1, can hardly be distinguished from the response of the simple homogeneous models. As previously discussed, the scattering function for Model 1 seems to be more strongly affected by the addition of volume heterogeneity. However, we suggest that this difference is still due to an increase in the apparent roughness. Here the sediment layer is uniform except for the gradients, so that the apparent roughness is now occurring at the top of the talus layer. The fact that the other models produce responses so similar to the homogeneous models strongly suggests that volume characteristics cannot be interpreted from the backscatter signal.

4.7 Discussion

The motivation for this study has been the hypothesis that much of the signal intensity variation observed in monostatic reverberation data is produced by the scattering effects of wavelength-scale heterogeneity. It was also believed that both seafloor (interface) heterogeneity and subseafloor (volume) heterogeneity generate comparable scattered field intensities and variations in intensity. For most of the modeling study, heterogeneity is defined as isotropic and having a Gaussian distribution such that it can be parameterized in terms of correlation length and standard deviation of amplitude. However, heterogeneity is only part of a complete description of a real seabed. The seabed also has large-scale characteristics such as average seafloor slope and average subseafloor velocity and density, to which wavelength-scale heterogeneity is added. Although seabed characteristics that vary over scales much larger than the incident wavelength do not produce scattering, they do have an effect on the scattering caused by the wavelength-scale heterogeneity. Therefore, in our attempt to quantify scattered fields as functions of wavelength-scale variation, we have also tried to quantify the effects on this scattering due to large-scale characteristics.

For rough-seafloor models, we found that backscatter is most sensitive to variation in the rms height of the stochastic seafloor structure. The maximum range in intensity associated with height variation is about 15 dB, whereas the maximum range observed for variation in correlation length is only about 5 dB. For a seabed that is assumed to be uniform in all other characteristics, monostatic signal intensities that vary more than 5 dB are a certain indication that seafloor height is varying. The sensitivity measured with these models also suggests that scattering can be characterized as a function of the effective Rayleigh roughness parameter, which is most strongly a function of rms height. Our results suggest that as seafloor roughness (quantified by the effective Rayleigh roughness parameter) increases, the backscatter signal seems to approach some limiting value (Figure 4-24) that depends on the correlation length.

The effects of average seabed properties on the scattered field are more difficult to quantify. Very low-velocity and low-density subseafloor produces a backscatter signal

that is consistently at least 6 dB down from the same seabed with higher velocity and density. A reasonable explanation for this is that the critical grazing angles for the soft-bottom seafloor are consistently less than the incident wavefield grazing angle, even when the seafloor is rough. In this case, the seafloor is essentially transparent to the incident wavefield and relatively little seafloor scattering occurs. There is also variation in the sensitivity to seabed velocity that is a function of seafloor correlation length, which does not have an obvious explanation. When $ka = 1$ and $v_p > 2$ km/sec, there is essentially no sensitivity to velocity, but for $ka = 6$ the sensitivity is about 2 dB/(km/sec). For most interpretations of intensities, it is reasonable to assume that scattering is not sensitive to the average subseafloor velocity and density, because it would require a difference of at least 3 km/sec to produce a signal variation greater than 5 dB. The exception to this is the transition from a sediment bottom to a higher-velocity bottom such as talus or basalt.

The effect of large-scale seafloor slope on backscattering can be summarized as follows. Transitions in large-scale slope from 0° slope up to 15° will produce an increase in backscatter intensity up to a maximum of 5 dB. Above 15° slope, the rate of increase in intensity decreases, suggesting that backscatter is not very sensitive to changes in slope above 15°. Transitions from seafloor with very small average slope (i.e., almost horizontal), to seafloor with slope greater than 15° will increase the backscatter signal by 5-10 dB. These results suggest that the effect of seafloor slope can be considered a two-scale problem. That is, variation in slope in regions where the seafloor slope is below 15° will have a strong influence on the backscattered signal while variations in slope in regions where the slope is greater than 15° will affect the scattered signal much less. However, in all of our modeling the beam grazing angle was 15° so that this transition point in terms of true grazing angle, rather than seafloor slope, is 30°. In order to more definitely determine the transition point for scattering influence of slope variations at large and small seafloor slope a more detailed study, with variation in true grazing angle below 15°, will be done in the future.

It is also very important to distinguish between scattering as a function of seafloor

slope and scattering as a function of scattering angle. The idea that scattering is a two-scale function of seafloor slope is based on the plot of backscattering in the monostatic reverberation direction (Figure 4-19(b)). As seafloor slope varies the true grazing angle (and effective grazing angle for a rough surface) varies. The scattering coefficients for different scatter directions for a single seafloor model, with or without seafloor slope, when plotted as a function of scatter direction, as any of the individual scattering functions in Figure 4-19(a), must not be interpreted as equivalent to variation in seafloor slope, because the true grazing angle is not changing.

The most striking result of all the modeling performed for this study is that rough seafloor, with or without subseafloor volume heterogeneity, produces essentially the same scattered fields. In particular, the backscatter intensity is always within a few decibels, even when the rms perturbation amplitude is as large as 50%. This is also true when gradients in average velocity and density, or fault zones, are added to the subseafloor heterogeneity. The scattering from flat-seafloor models with subseafloor heterogeneity does show strong sensitivity to variation in correlation length and rms perturbation amplitude of the volume heterogeneity. In fact, this sensitivity is the same level as that measured for seafloor rms height variation. But the fact that adding volume heterogeneity to rough-seafloor models does not significantly increase the scattered field observed in the water column leads to the conclusion that the volume scattering is not contributing any substantial energy to the observed scattered field. This sensitivity is very similar to that of seafloor-height variation, which suggests that the primary effect of volume heterogeneity is to increase the apparent roughness of the seafloor. This suggests that energy scattered into the subseafloor is trapped in the multiple scattering environment such that very little energy is returned to the seafloor from below.

The combination of these results suggest that the interpretation of monostatic reverberation data is best limited to the effects of seafloor scattering. A procedure was outlined for interpretation of signal intensity, in terms of seafloor roughness. This procedure can be applied to all backscatter data. In order to make the most useful interpretation in terms of variation in seafloor roughness, it is necessary to have a good

estimate of the local seafloor slope and the subseafloor velocity.

4.8 Conclusion

The results of the numerical wavefield modeling of a large variety of seabed models with geologically realistic characteristics have led to several important conclusions that impact the interpretation of monostatic reverberation data.

The most important conclusion is that the scattering generated by insonification of the seabed with low-grazing-angle wavefields is dominated by seafloor (interface) scattering. Volume scattering, produced by subseafloor volume heterogeneity, can produce strong backscatter signals when the perturbation amplitude is high ($\sim 50\%$), but when combined with surface roughness, volume scattering does not have a strong effect on the total backscattered signal. An exception to this seems to be when the volume heterogeneity occurs in low-velocity materials such as sediment. However, sediment is also expected to be highly attenuative, so that any scattering from volume heterogeneity would be diminished. The real impact of volume heterogeneity is that the velocity variation at the seafloor adds to the apparent roughness of the seafloor, which increases the backscattered field.

Variations on the order of 5-20 dB observed in monostatic reverberation data can be attributed to lateral variation in wavelength-scale seafloor roughness parameters, average seafloor slope, and average subseafloor velocity and density. In general, the backscatter intensity is not very sensitive to velocity variation, except in the transition from soft- to hard-bottom seafloors which will yield at least 6 dB difference in intensity. Scattering is sensitive to average seafloor slope, but primarily to the difference between a low-slope ($< 15^\circ$) and a high-slope ($> 15^\circ$) environment. The intensity difference between these two areas can be as much as 10 dB; however, within the high-slope region, variations will be smaller than 5 dB. Variation in seafloor roughness, in particular variation in the standard deviation in height, can account for intensity variations up to 15 dB. Intensity variation can be interpreted in terms of stochastic seafloor roughness if some measure of local large-scale seafloor slope is available for

the slope correction.

Finally, the extremely strong backscatter signals, i.e., more than 20 dB above local scattering levels, referred to in some publications as 'highlights', cannot be accounted for by variation in either stochastic wavelength-scale or large-scale parameters. Our conjecture is that these singularly strong intensities may be due to a resonant response of particular seafloor features that depends on the size, shape and subseafloor velocity of the feature, and the frequency of the incident wavefield.

Table 4.1: Velocity and density of sediment, talus and basalt used in modeling realistic seafloor with homogenous subseafloor.

Media	Basalt	Talus	Sediment
$v_p(\frac{km}{sec})$	4.0	2.0	1.52
$v_s(\frac{km}{sec})$	2.0	1.0	1.0
$\rho(\frac{kg}{m^3})$	2.5	1.74	1.5

Table 4.2: A comparison of ka and $k\sigma$ calculated from bathymetry (listed as 'bathy' values in the table) to estimates of ka and $k\sigma$ derived from scattering coefficients. Shifts in effective Rayleigh roughness parameters and scattering coefficients were derived from numerical modeling of rough and sloping, basalt-bottom models (Figure 4-23b(ii)). In Figure 4-27, appropriate shifts are applied to the scattering coefficients calculated for the realistic seafloor models (Models 1-4) having homogeneous sediment, talus and basalt subseafloors. The slope is the least-square estimate of average large-scale slope for each model. The shifted locations of each scattering coefficient are then compared to the corresponding wire diagram for each velocity (Figure 4-24) to find an estimated value for ka and $k\sigma$. This table compares these estimates to the values of ka and $k\sigma$ that were calculated from the model bathymetry data. $|\Delta|$ is the average of the absolute value of the deviation of each estimated parameter (ka or $k\sigma$) from the value calculated from the bathymetry and % is this deviation as a percentage. Values excluded from the calculation of averages are listed in parentheses. Excluded values are those that were far outside the region of the wire diagrams.

Model		bathy	basalt	talus	sediment	$ \Delta $	%
Model 1	ka	9.42	4.8	14.7	14.3	4.92	52
	$k\sigma$	1.56	1.0	1.4	2.3	0.49	31
Model 2	ka	7.33	(<< 1)	9.	6.3	1.35	18
	$k\sigma$	1.99	(0.5)	1.5	2.	0.25	12
Model 3	ka	6.28	6.	7.4	8.	1.04	17
	$k\sigma$	3.37	3.5	3.7	3.7	0.26	8
Model 4	ka	5.24	5.5	6.	6.3	0.69	13
	$k\sigma$	2.66	3.25	2.5	2.8	0.3	11

Table 4.3: A comparison of $k\sigma$ calculated from bathymetry to estimates of $k\sigma$ derived from scattering coefficients when only large-scale seafloor slope is known. This table is the same as Table 4-2 except that in this case, it is assumed that $ka = 7$ in the analysis. This is the average value of ka calculated from the bathymetry in Models 1-4.

Model		bathy	basalt	talus	sediment	$ \Delta $	%
Model 1	ka	9.42	7.	7.	7.	-	-
	$k\sigma$	1.56	1.6	(< 0.5)	(<< 0.5)	0.04	3
Model 2	ka	7.33	7.	7.	7.	-	-
	$k\sigma$	1.99	(>> 4)	1.5	2.	0.25	12
Model 3	ka	6.28	7.	7.	7.	-	-
	$k\sigma$	3.37	4.	2.4	3.3	0.56	17
Model 4	ka	5.24	7.	7.	7.	-	-
	$k\sigma$	2.66	3.2	4.5	4.	1.06	40

Figure 4-1: The Numerical Scattering Chamber (NSC) consists of an inner 'scattering chamber', in which a geological model is defined, surrounded by an absorbing boundary region. The scattering chamber includes a homogeneous fluid zone, a heterogeneous transition zone (seafloor model) and a homogeneous solid zone at its base. A Gaussian beam pulse is introduced into the scattering chamber in the upper right corner of the model space. Receivers are located in the water column along the top and sides of the scattering chamber.

Numerical Scattering Chamber

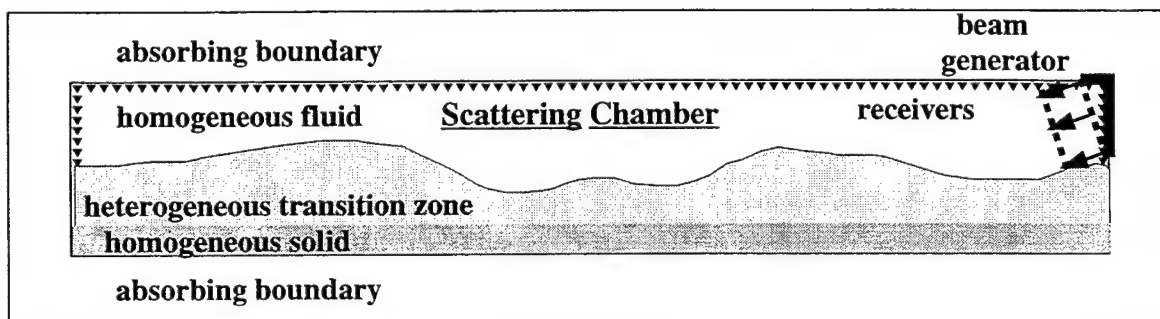


Figure 4-2: Scatter direction in the NSC is measured as the counterclockwise grazing angle relative to the propagation direction. All scattering that propagates in the scattering chamber in directions from 0° to 90° is referred to as backward scatter. All scattering that propagates in directions from 90° to 180° is considered forward scatter.

Scattering Coefficients

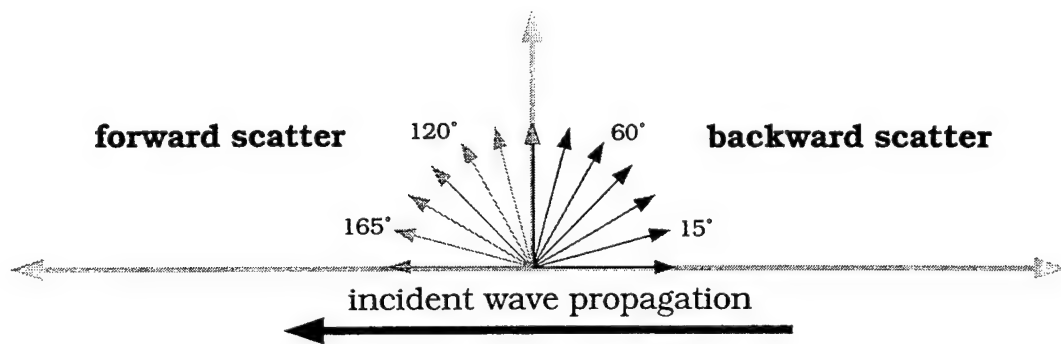


Figure 4-3: A random seafloor defined with a Gaussian autocorrelation function (a) compared to the same seafloor defined with a self-similar autocorrelation (b). The Gaussian model has correlation length $a = 6$ and standard deviation in height $\sigma = 4$. The self-similar model has the same $k\sigma$ but correlation length is less well defined.

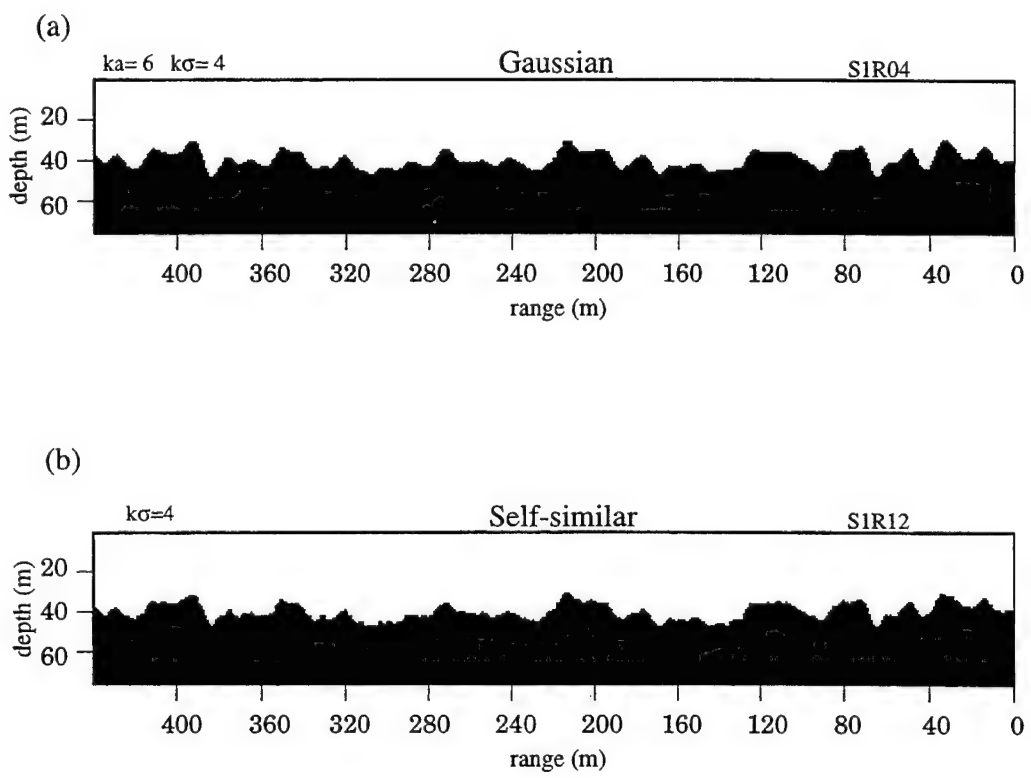
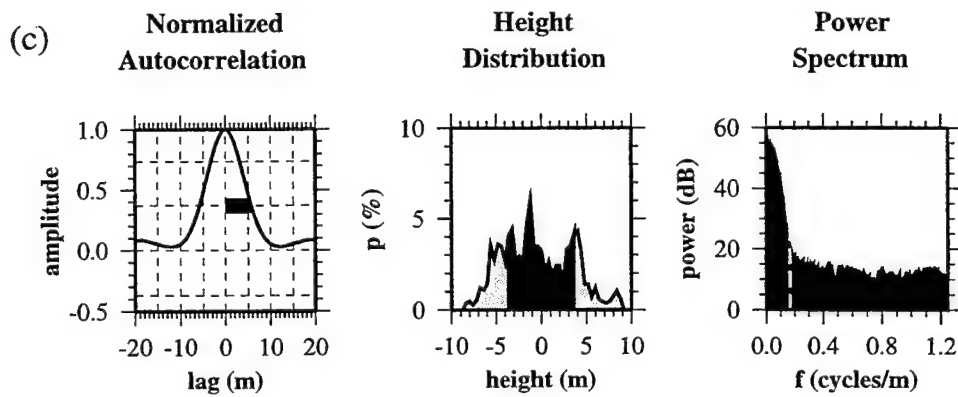


Figure 4-3: (c) The correlation length of a Gaussian model is defined as the lag distance at which the amplitude of its autocorrelation has decreased to $\frac{1}{e}$ of its peak value (black bar). This corresponds also to the corner frequency (dashed line) in the power spectrum. The height distribution (probability density function) is also approximately Gaussian, such that 68% of the heights are within one standard deviation (darkened zone around the origin) of the mean. The roll-off in the power spectrum of the self-similar model (d) is more gradual and symmetric, allowing more energy in the higher spatial frequencies. The corner frequency is the frequency at the intersection of the lines to which the power spectrum is asymptotic. The estimated correlation length for the self-similar model would be $a = \frac{1}{0.25} = 4$ m (dashed lines). This cannot be estimated from the width of the autocorrelation.

Gaussian Interface Model



Self-Similar Interface Model

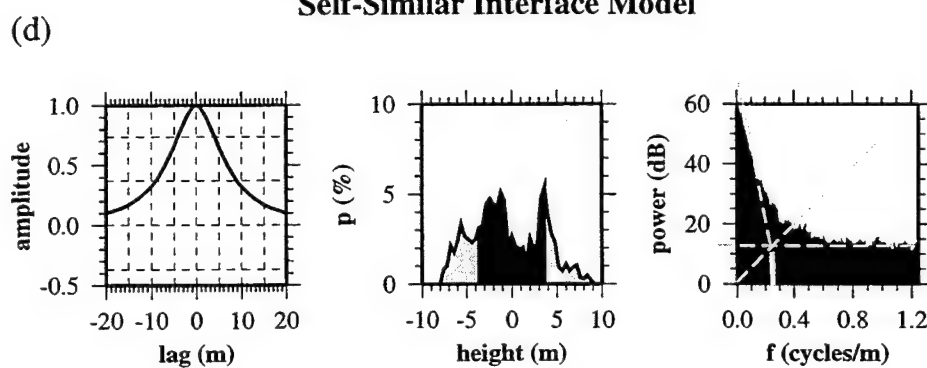


Figure 4-4: (a) The realistic seafloor profile (i) is high-pass filtered to remove the large-scale ridge feature. High-resolution Mesotech bathymetry data (black profile) is incorporated into the lower-resolution DSL-120 bathymetry data (grey profile) in generating the realistic profile. The filter low-cut was set at 0.01 cycles/m (100 m) and the resulting filtered seafloor was shifted to a zero-mean level (ii). The realistic model is divided into four sections (Models 1-4) for the numerical modeling.

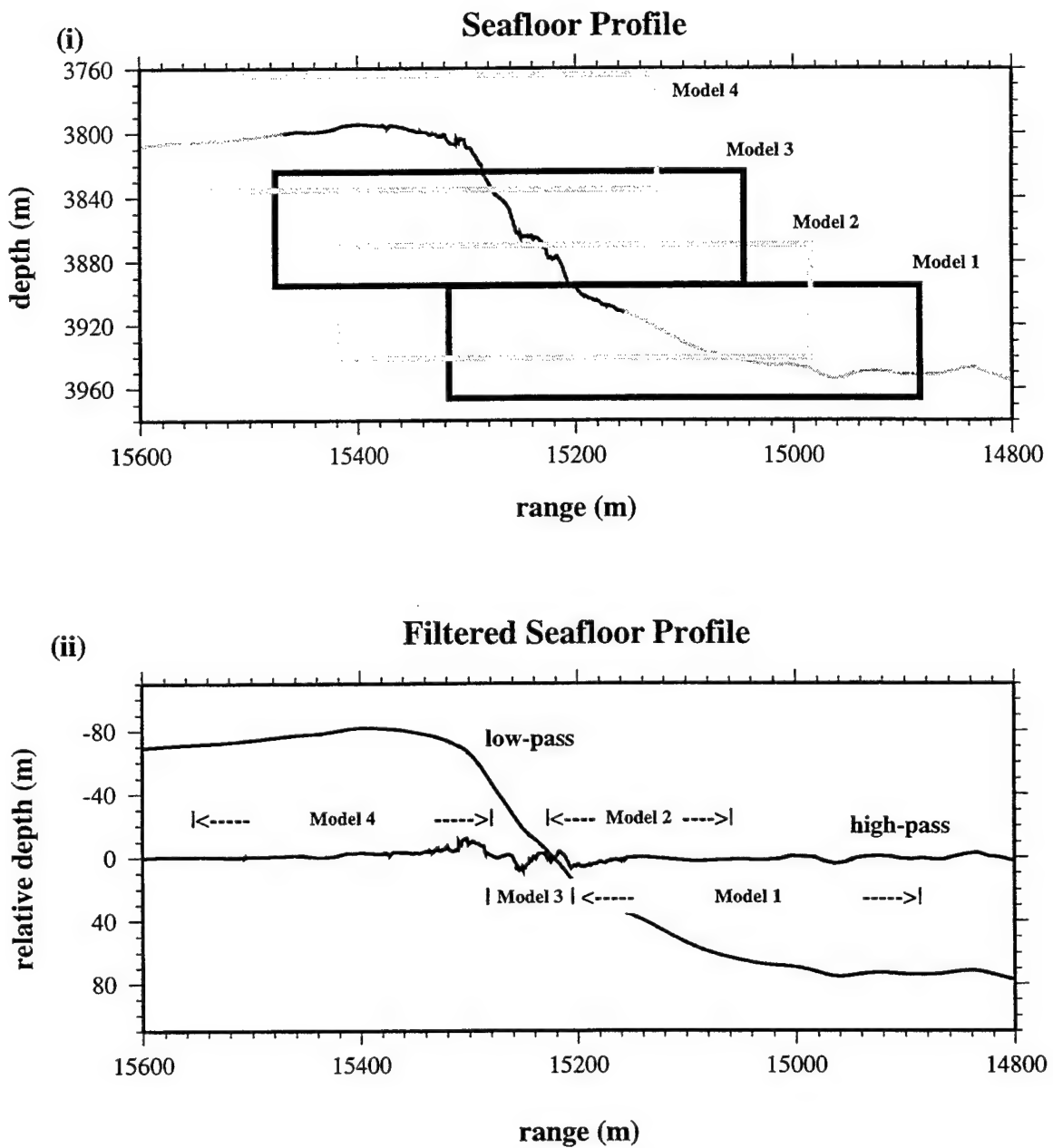


Figure 4-4: (b) The shape of the power spectra calculated for Models 1-4 suggest that a most precise representation of the real seafloor would be a self-similar model. However, for $f < 0.4$ Hz, the power spectra roll off more rapidly, suggesting that the seafloor is dominated by features with correlation lengths larger than about 2.5 m and that this portion of the seafloor can be well represented by a Gaussian distribution. Picking corner frequencies as shown in the figure gives correlation lengths of $a_{Model\ 1} = 9$ m, $a_{Model\ 2} = 7$ m, $a_{Model\ 3} = 6$ m, and $a_{Model\ 4} = 5$ m.

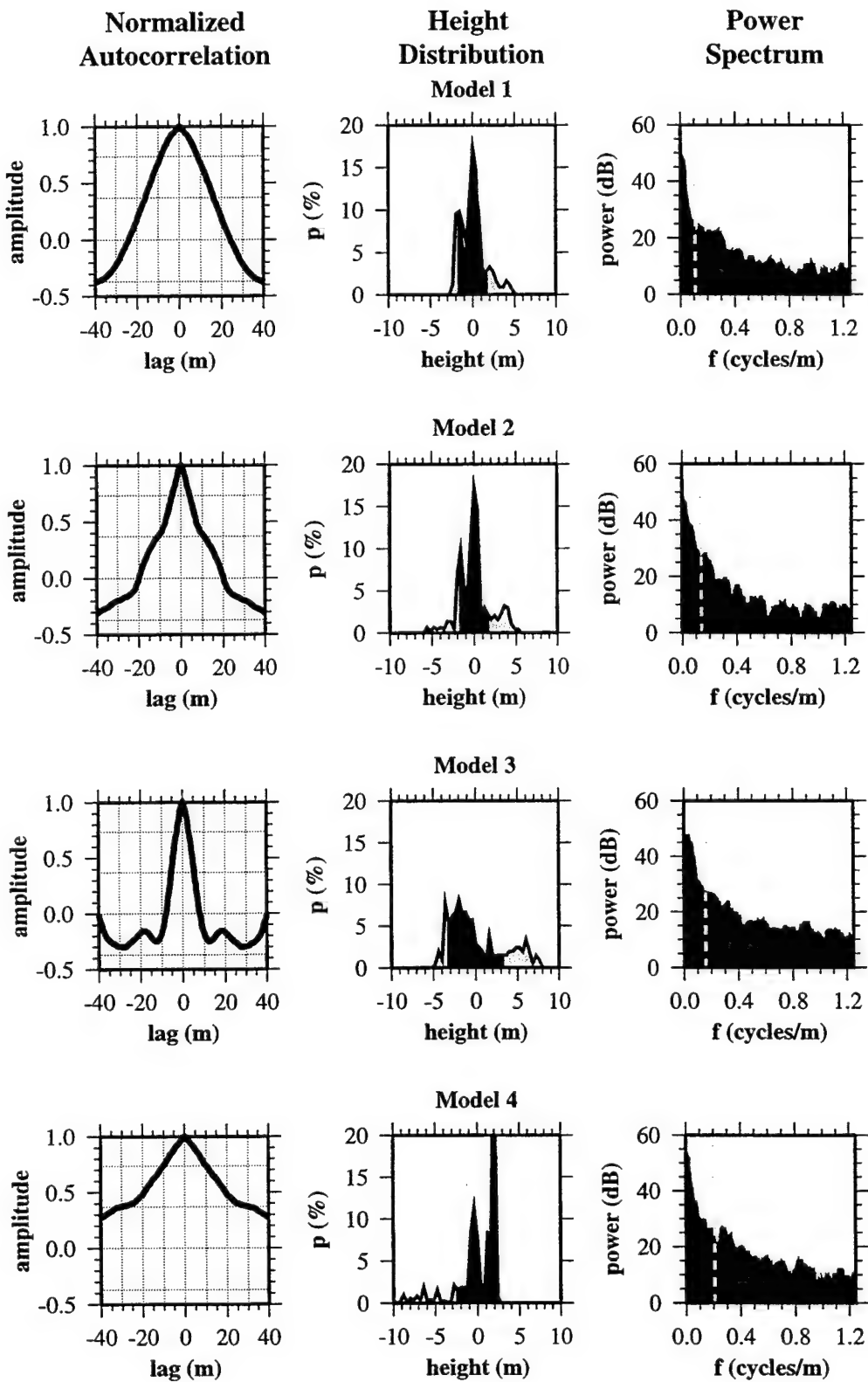


Figure 4-5: (a) The baseline model is a flat seafloor with 'hard-bottom' (basalt) properties. The water column is defined with parameters $v_p = 1.5 \text{ km/sec}$, $v_s = 0.0 \text{ km/sec}$, and $\rho = 1.0 \text{ kg/m}^3$. The hard-bottom homogeneous seabed parameters are $v_p = 4.0 \text{ km/sec}$, $v_s = 2.0 \text{ km/sec}$, and $\rho = 2.5 \text{ kg/m}^3$.

(b) The compressional and shear 'amplitude density' (see Appendix of Stephen and Swift, 1994) at 400 ms propagation is represented by this 'schlieren' diagram. Amplitude is represented by color density and polarity by color. The source wavefield, P_1 , is a Gaussian pulse beam incident at a grazing angle of 15° and is initiated on the right side of the diagram. For a flat, hard bottom, this is a subcritical grazing angle (supercritical incidence angle) so that all P-wave energy is reflected (P_1P_1). At subcritical grazing angles there is energy present in the subseafloor called the direct wave root, DWR. (The DWR is a disturbance in the sub-bottom caused by pressure on the surface induced by the incident wavefield.)

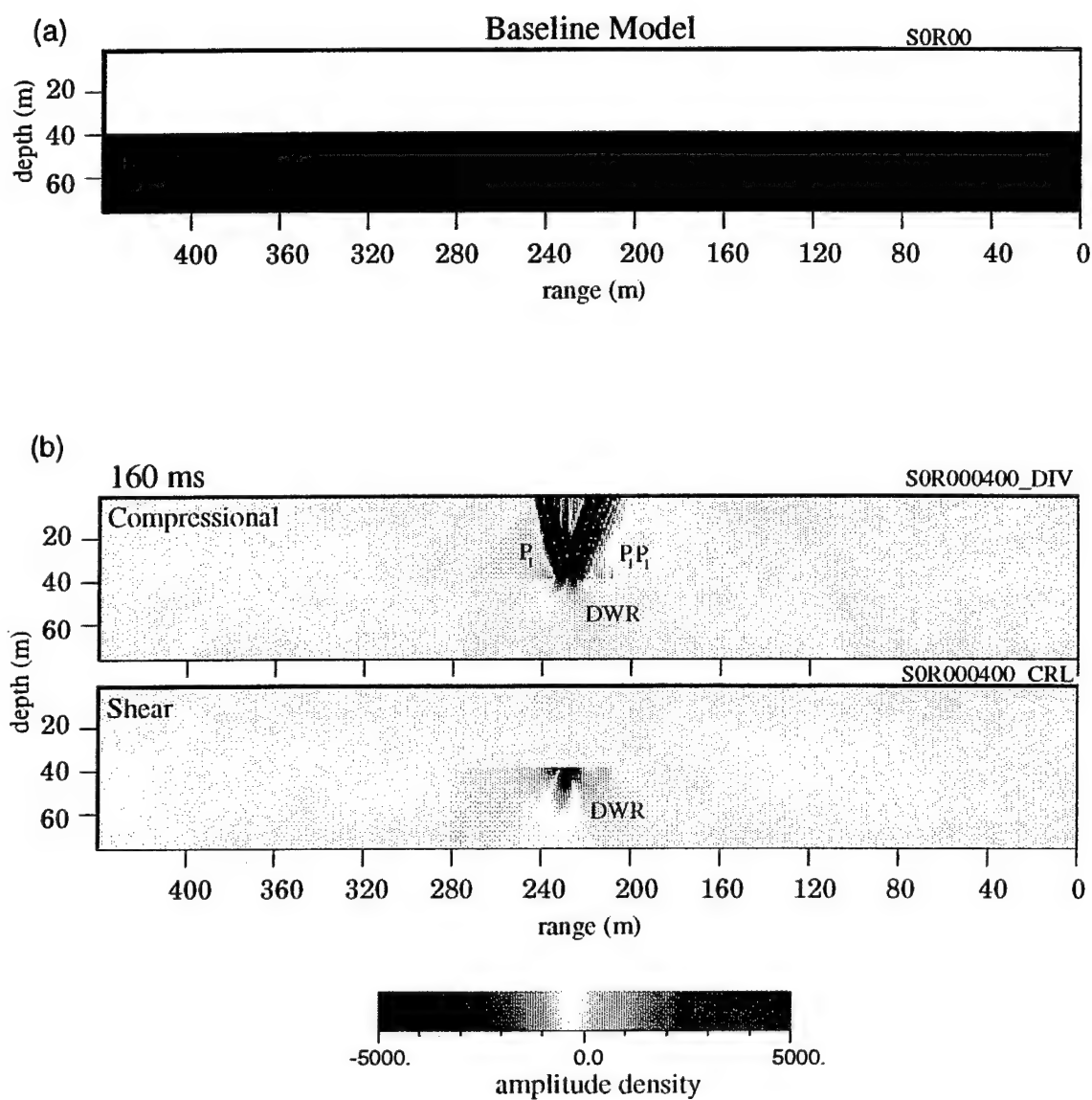


Figure 4-6: Scattering coefficients are calculated as a function of scattering direction. For the Gaussian beam incident at 15° , the scattering coefficient at 15° represents the monostatic reverberation experiment, i.e., the backscatter signal directed back toward the source. The scattering coefficient at 165° is the specular reflection. The width of the reflection peak is a function of the bandwidth and wavenumber content of the Gaussian beam, i.e., the resolution of the incident wavefield.

Baseline Model: Hard Flat Bottom

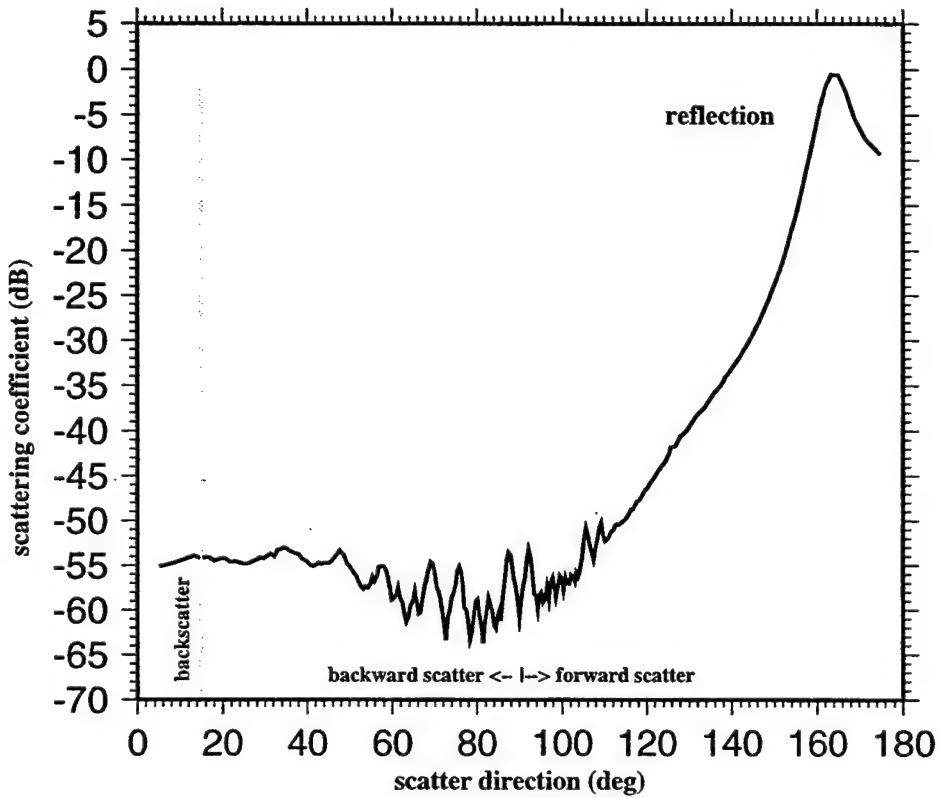


Figure 4-7: (a) These models have horizontal rough seafloor with different correlation lengths. The seafloor models have Gaussian autocorrelations with different correlation lengths such that in (i) $ka = 6$, (ii) $ka = 2$, and (iii) $ka = 1$. The rms height distribution has been fixed such that $k\sigma = 2$. As ka decreases, higher frequency variability is observed overriding the same low frequency characteristics. Subseafloor velocity and density are the same as the hard-bottom baseline model.

Models with Varying Correlation Length and Constant RMS Height

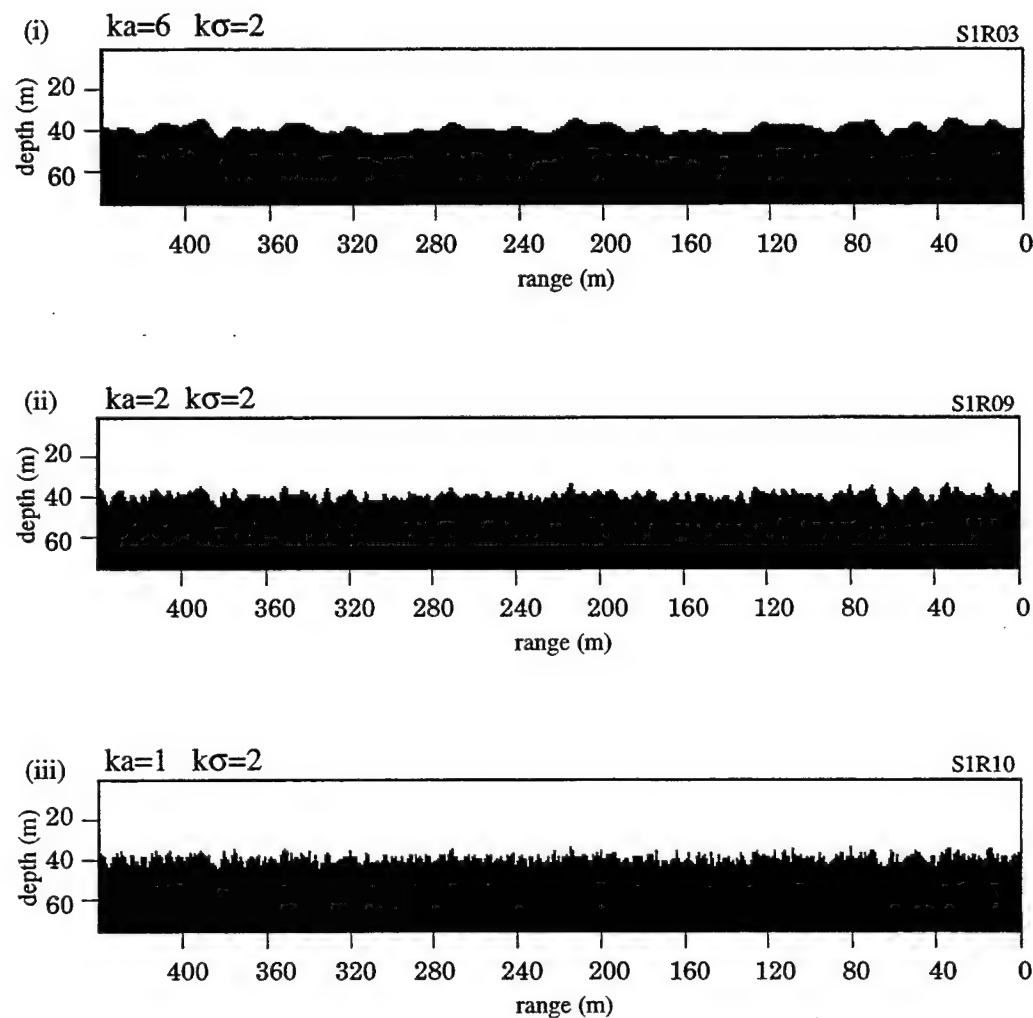


Figure 4-7: (b) The statistical properties of the seafloor models in (a) show that as the correlation length (black bar in autocorrelation plots) decreases, the corner frequency of the power spectrum increases. The models are defined by filtering a random series such that its autocorrelation function has a Gaussian distribution and then scaling to the desired rms height. Although the height distributions are not exactly the same in each model, they do have exactly the same rms height and 68% of the height values fall within this rms height range (blackened zones).

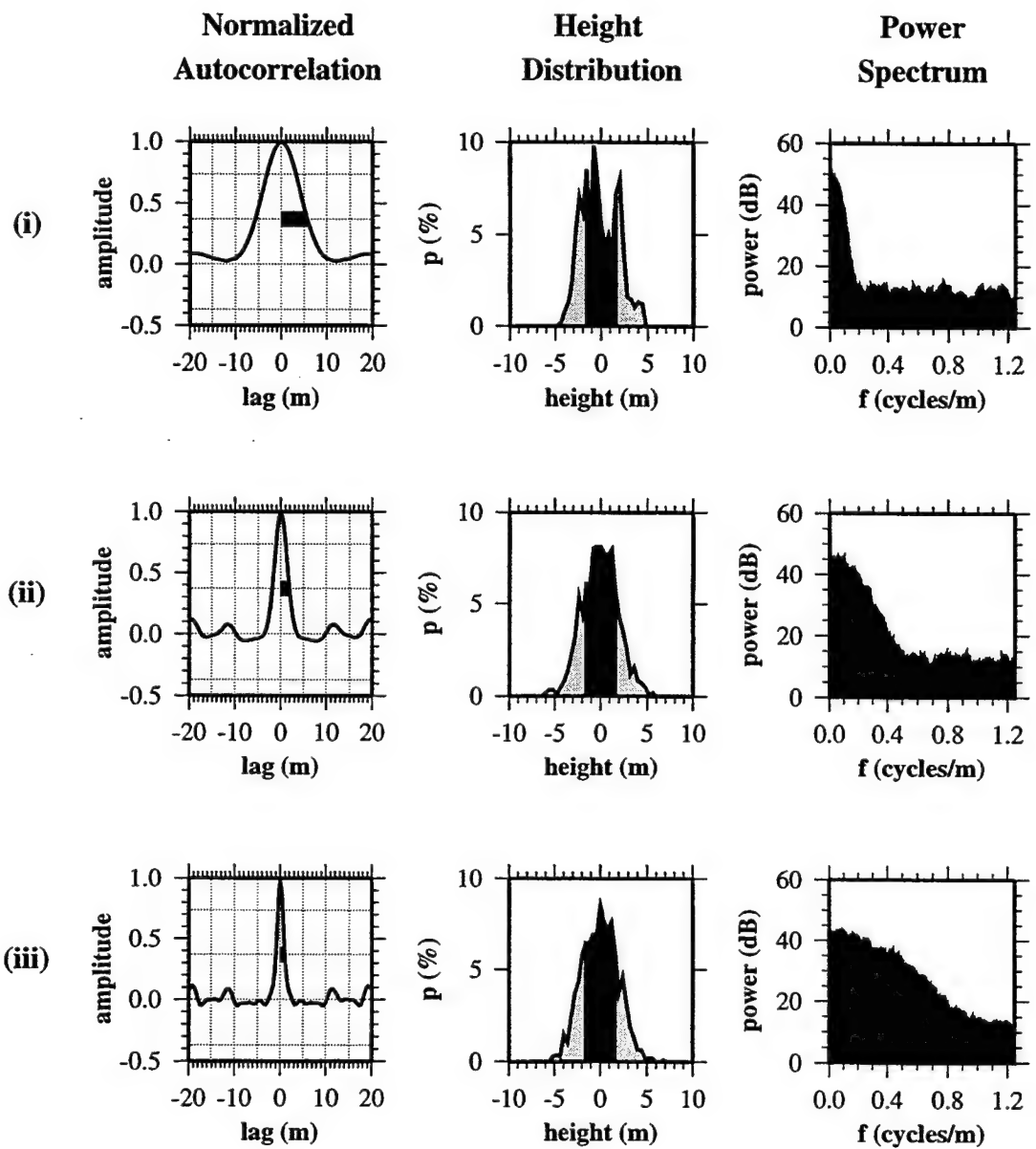


Figure 4-7: (c) These schlieren diagrams show the distribution of compressional and shear amplitude density at 160 ms (400th time step). The incident beam wavefield (P_1) is reflected from the seafloor (P_1P_1) and has a direct wave root (DWR). The surface roughness in each model produces primary diffractions in the water column and diffracts energy into the subseafloor. Both diffracted compressional (P_1P_2) and diffracted shear (P_1S_2) waves are observed in the subseafloor. Surface (Stoneley) waves propagate in both the forward and backward directions and produce secondary diffractions that add to the total scattered wavefield in the water. Both compressional head waves, pHW ($P_1P_2P_1$), and shear head waves, sHW ($P_1S_2P_1$), are observed in the water column, as well as a shear head wave ($P_1P_2S_2$) in the solid. These wave types occur in each model but differ in detail.

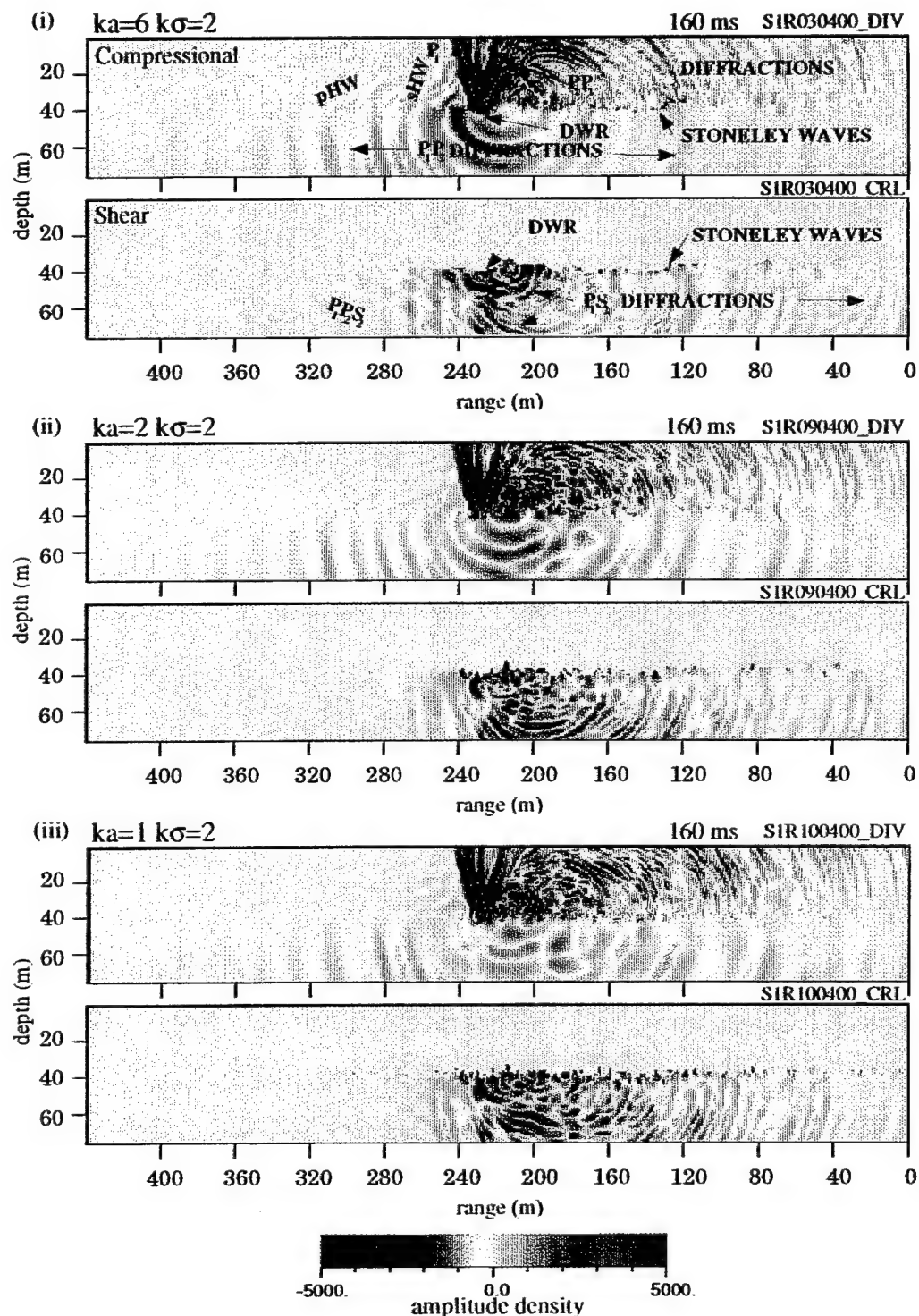


Figure 4-8: Three realizations of a horizontal, rough-seafloor model. (a) Different realizations of a seafloor model are created by initializing the model generation process with different random series. These series are then filtered to produce interface models with the same correlation lengths and scaled to the same rms height.

Three Realizations of Seafloor with $ka=4$ and $k\sigma=2$

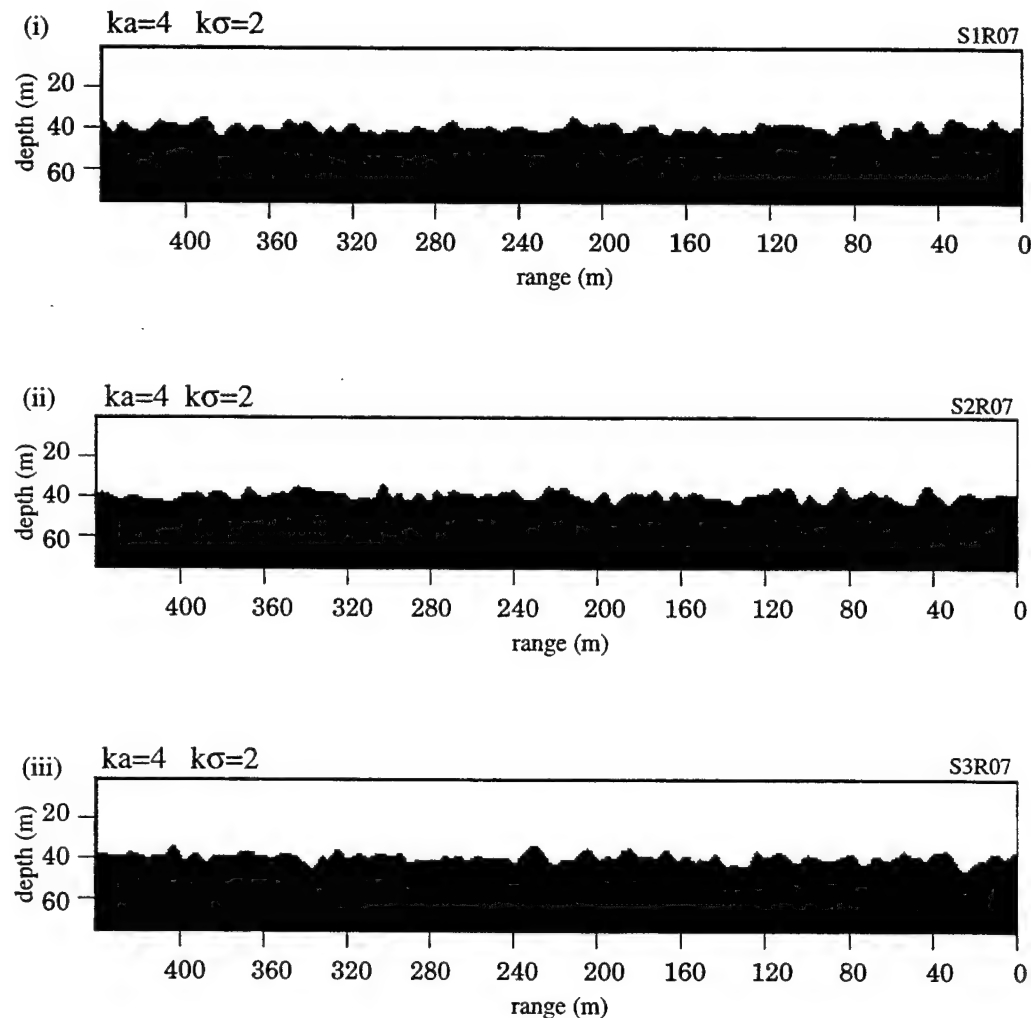


Figure 4-8: (b) The models in (a) have the same autocorrelation length and rms height. The only distinguishing characteristic is the detailed variation in the height distribution, which cannot be parameterized.

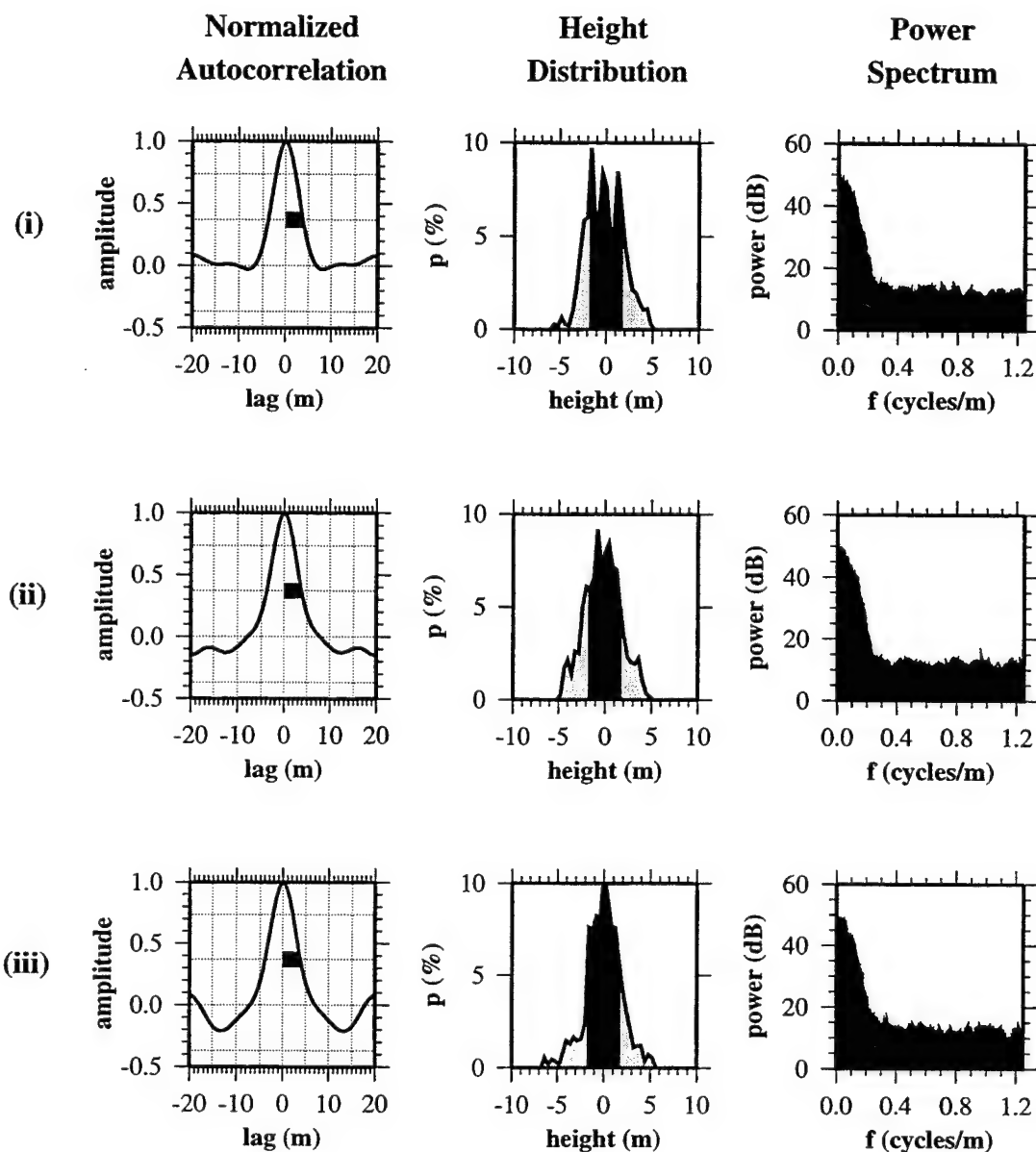


Figure 4-8: (c) Even though the models in (a) have the same statistical parameters, the scattered fields produced by them differ in the locations of primary scattering sites. However, all of the models produce the same basic wave types. Because the variations in the random character of these different realizations cannot be parameterized, the difference in scattering produced by them must be considered a fundamental noise level, referred to here as realization error.

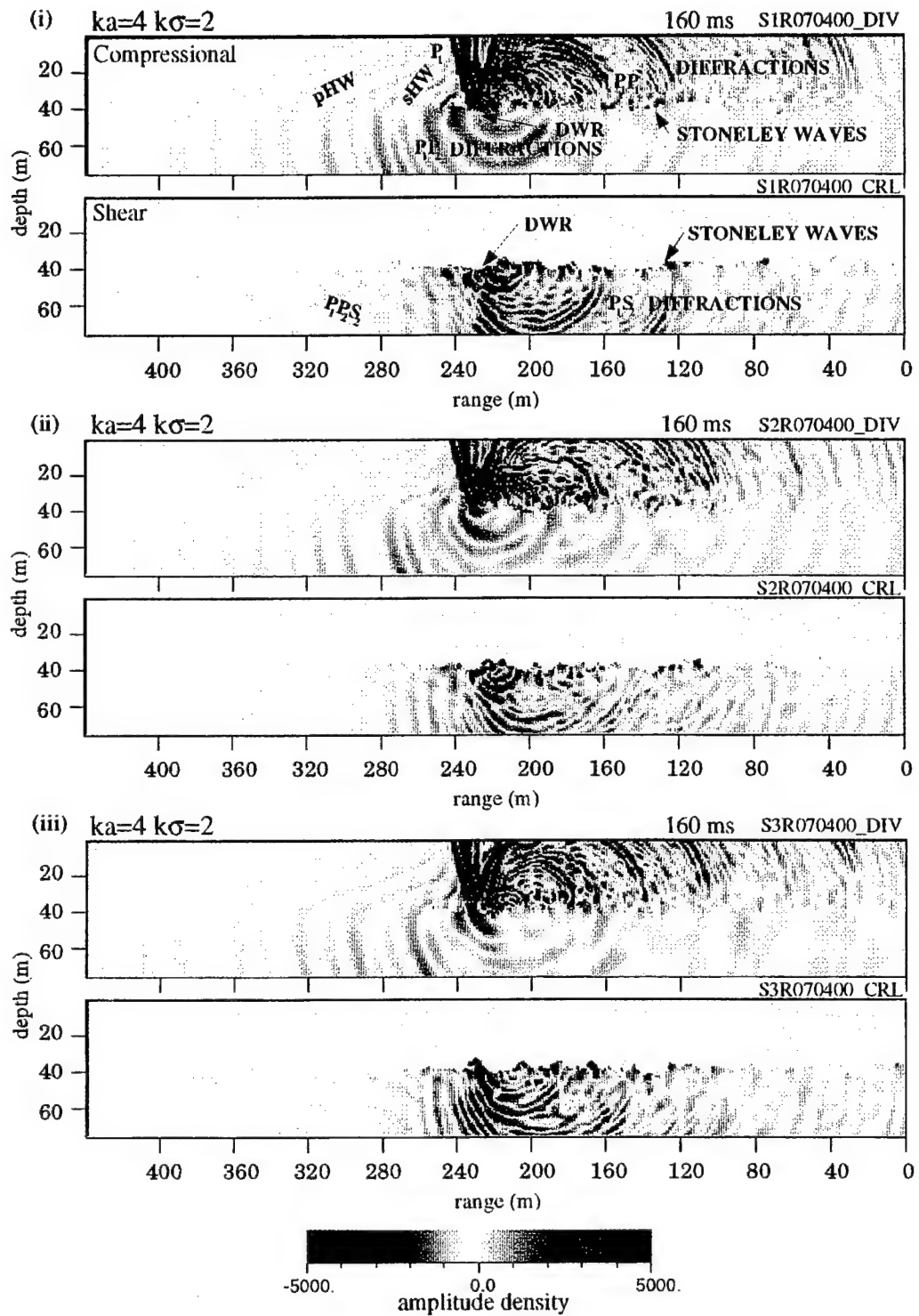
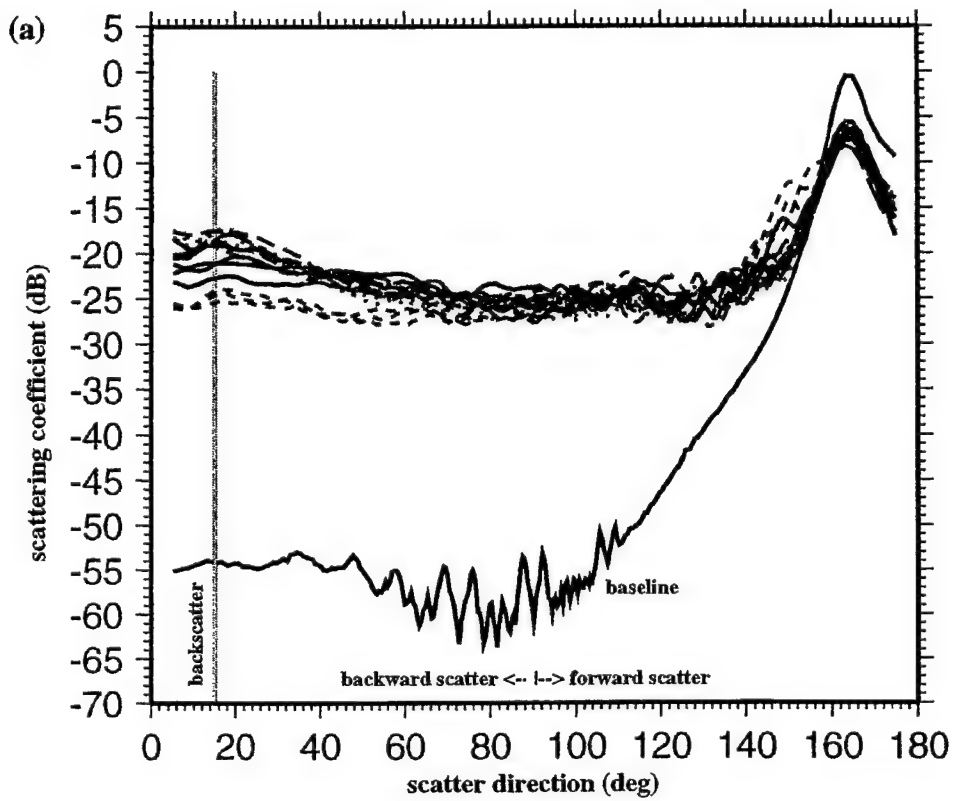


Figure 4-9: Scattering coefficients for horizontal, rough seafloor with different correlation lengths. (a) The scattering functions of the rough-surface models are much higher than that of the flat baseline model. The results from three realizations of each model are plotted for $ka = 0.5$ (pink dots), $ka = 1$ (medium blue dash), $ka = 2$ (long green dash), $ka = 4$ (solid black) and $ka = 6$ (short red dash). The reflection at 165° is still the strongest event but as scattering approaches 15° the scattering coefficients also reach a peak.

(b) In the direct backscatter direction (15°) the variation in scattering coefficient as a function of ka shows an approximately linear decrease as ka increases. The black line corresponds to the results for $k\sigma = 2$ shown in (a). The grey lines and symbols correspond to results for models with the same ka but scaled such that $k\sigma = 4$ and $k\sigma = 0.5$. The spread in the scattering coefficients for different realizations is about ± 1 dB.

Horizontal Seafloor: vary ka , $k\sigma = 2$



15 ° Backscatter vs. ka

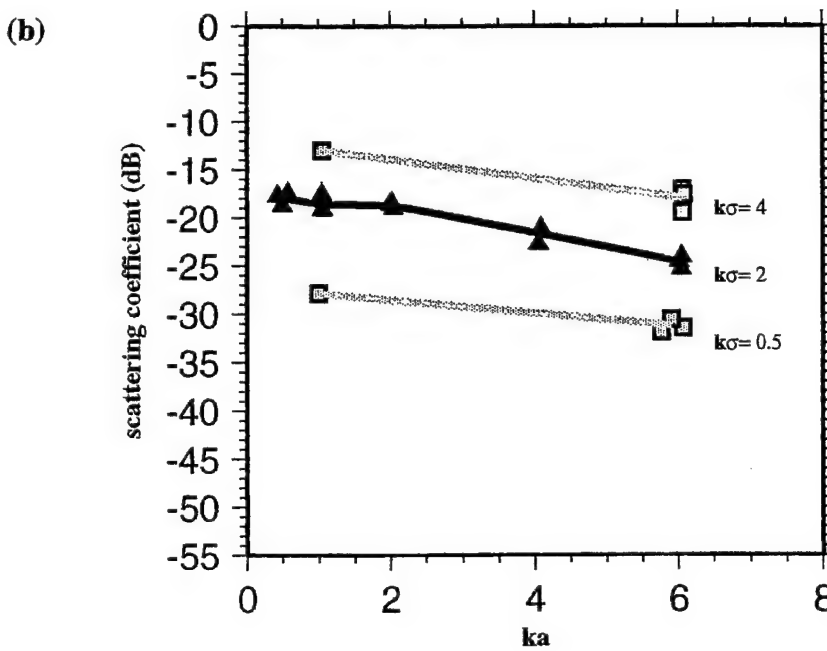


Figure 4-10: (a) These models have horizontal rough seafloor with different rms heights. The roughness has Gaussian autocorrelations with constant correlation length ($ka = 6$) and variable rms height distribution: (i) $k\sigma = 6$, (ii) $k\sigma = 1$ and (iii) $k\sigma = 0.5$. Subseafloor parameters are the same as the hard-bottom baseline model.

Models with Varying RMS Height and Constant Correlation Length

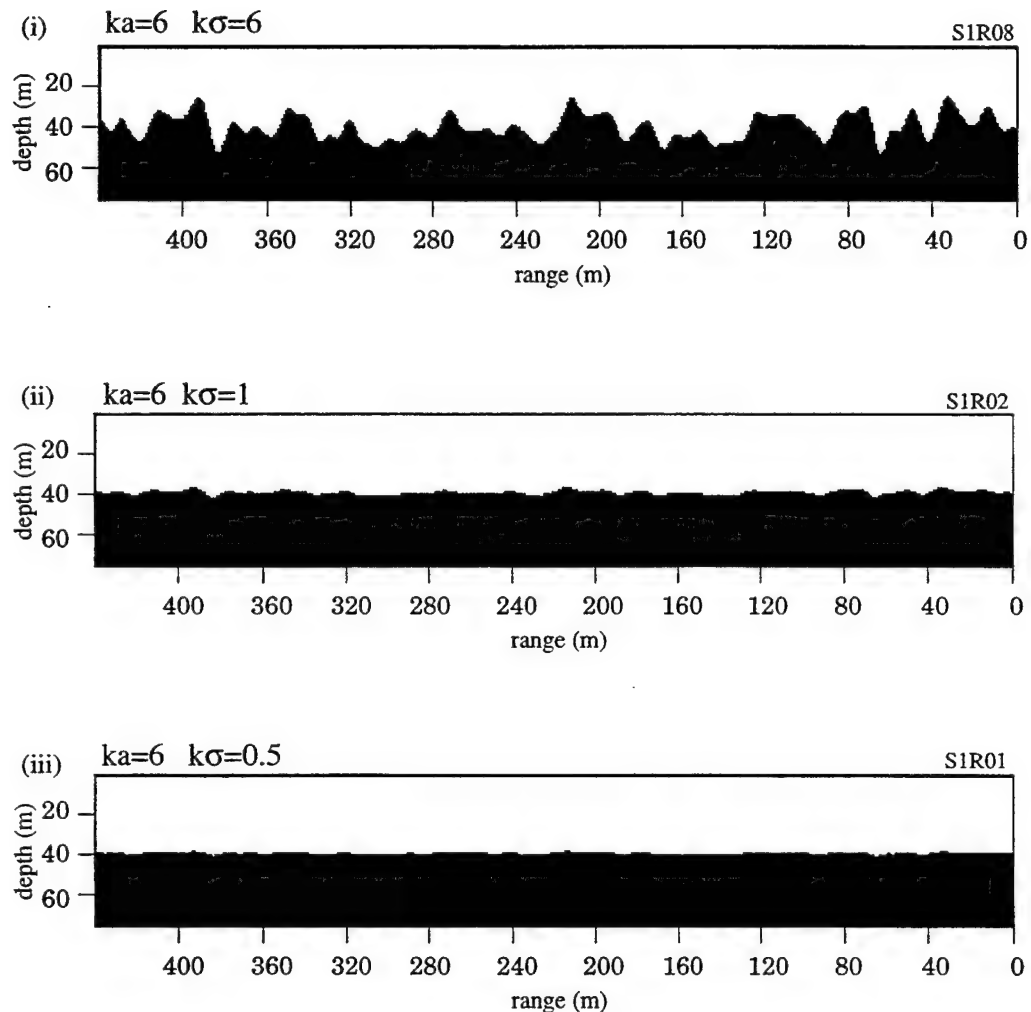


Figure 4-10: (b) As the rms height is decreased the probability distribution narrows. The distributions have the same autocorrelation functions and therefore the same corner frequencies in the power spectrum. However, note that the power levels at low frequencies decrease as the rms height decreases.

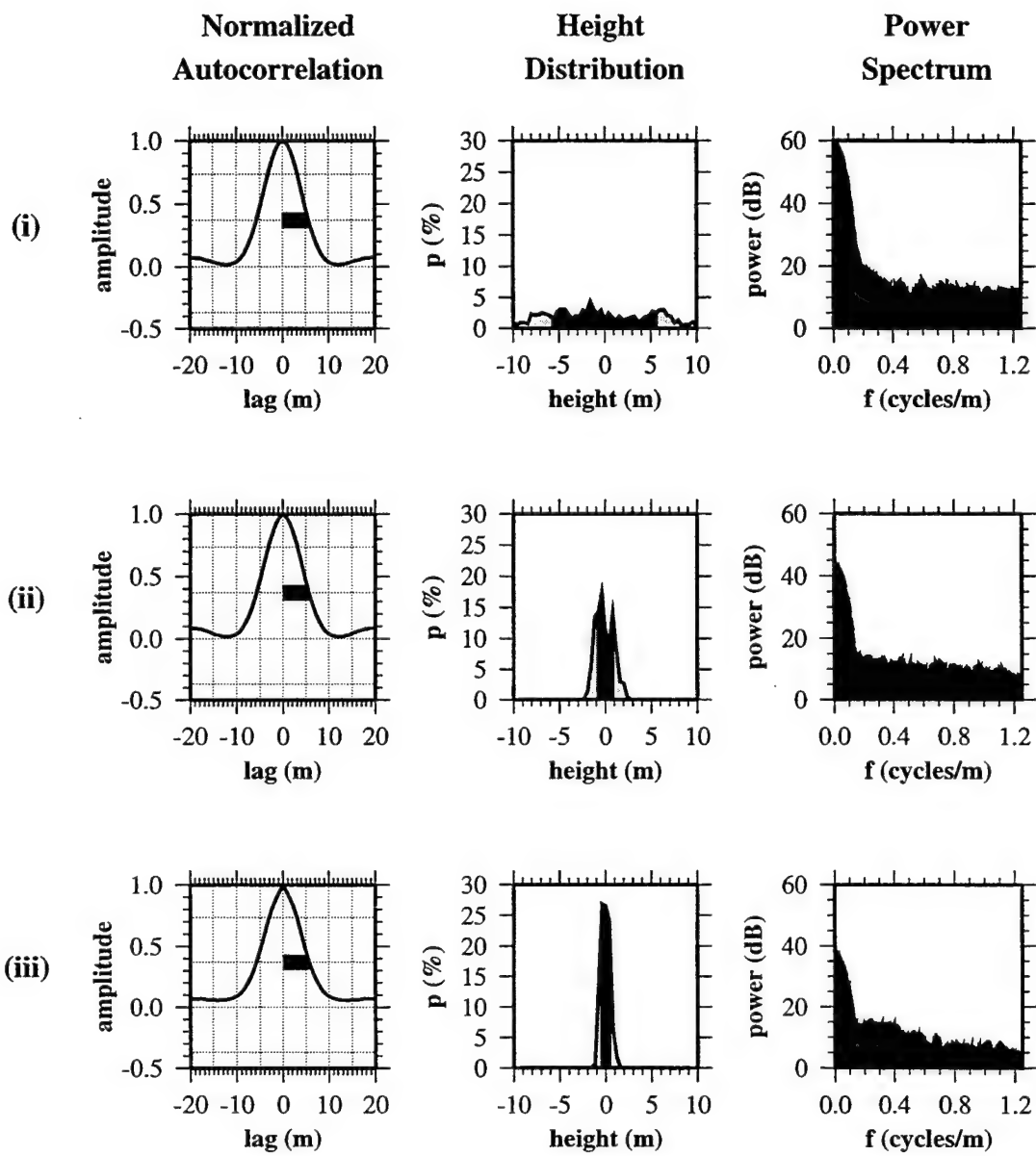


Figure 4-10: (c) These schlieren diagrams show that the rougher (higher $k\sigma$) surfaces generate significantly stronger primary diffraction events in the water column as well as stronger body wave diffractions. Stoneley waves are observed in all cases and produce secondary diffractions at low energy levels which contribute to the total scattered wavefield. Some of these secondary diffractions are distinguishable in (iii). Head waves in the water column (pHW) and the subsurface ($P_1P_2S_2$) are also seen in each case. The direct wave root is also observed. Models with small $k\sigma$ also have events identified as back-propagating shear head waves (sHW) as well as a pseudo-Rayleigh wave.

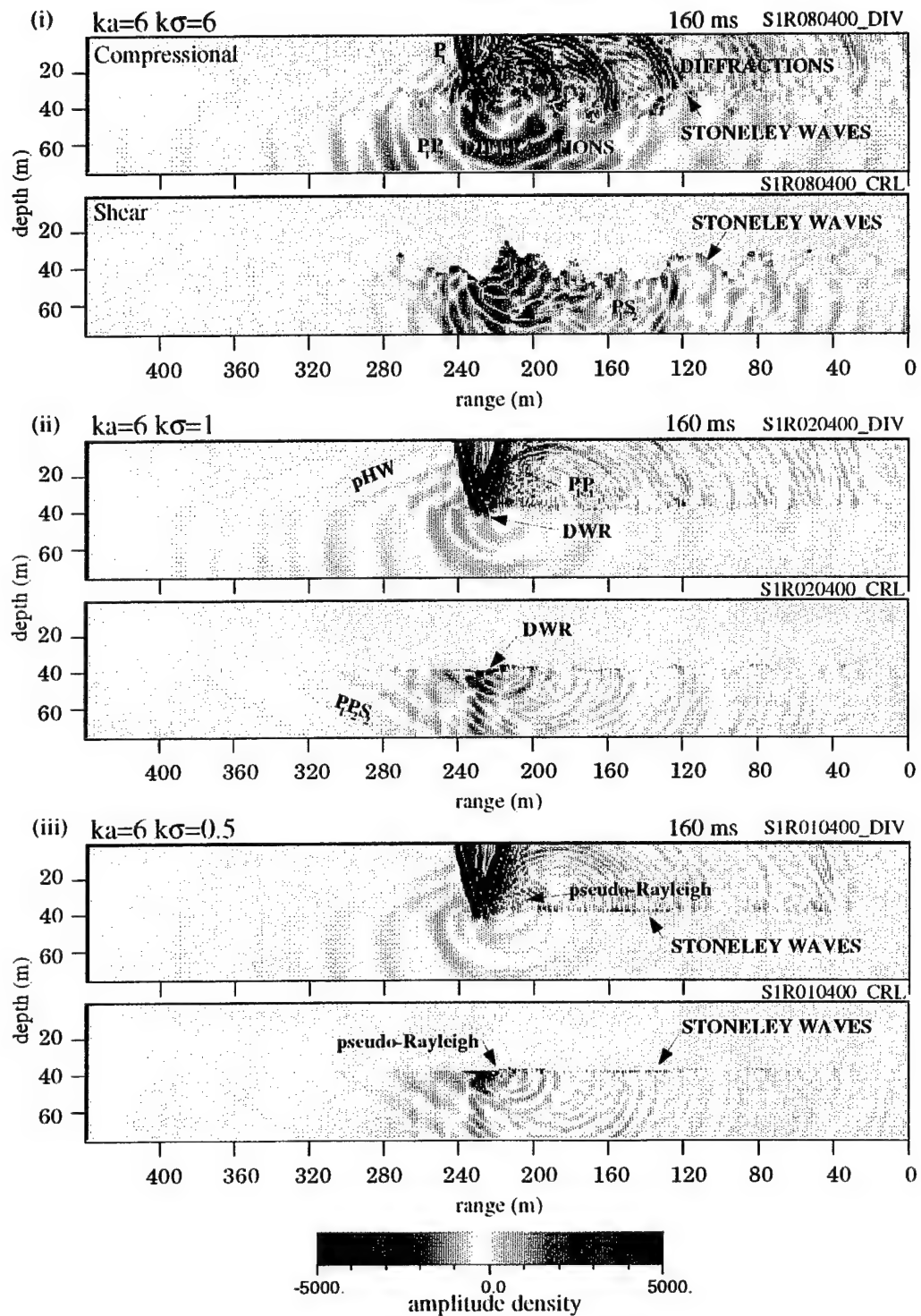
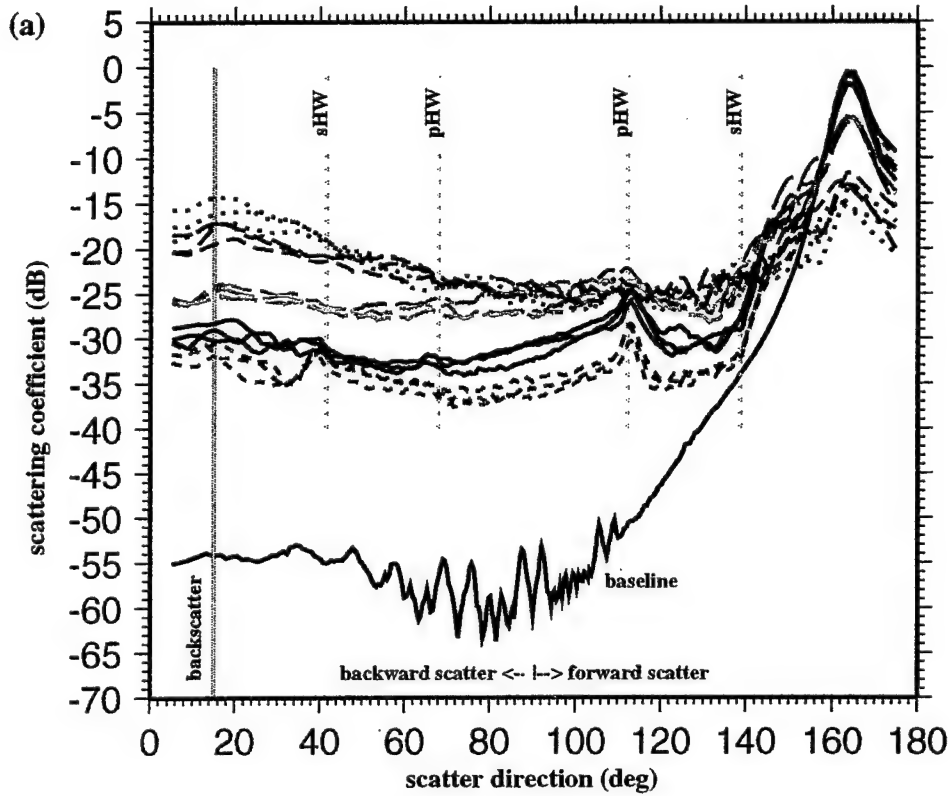


Figure 4-11: Scattering coefficients for horizontal rough seafloor with different rms heights. (a) The scattering functions of rough surface models with a fixed correlation length ($ka = 6$) decrease as the rms height decreases. The results from three realizations of each model are plotted for $k\sigma = 6$ (black dots), $k\sigma = 4$ (medium blue dash), $k\sigma = 2$ (long green dash), $k\sigma = 1$ (solid black) and $k\sigma = 0.5$ (short red dash). The reflection at 165° is still the strongest event but as the 15° scatter direction is approached the scattering intensity also rises. Variation in intensity for different realizations is on the order of ± 1 dB. For low-roughness models, local peaks in the scattering coefficients correspond to forward and backscattered head waves, which match quite well with the Snell's law predictions (light grey dash lines) for the model velocities.

(b) In the direct backscatter direction (15°) the variation in scattering coefficient as a function of $k\sigma$ shows an increase in backscatter intensity as $k\sigma$ increases. The black line corresponds to the results for $ka = 6$ shown in (a). The grey line and symbols correspond to results for models with $ka = 1$ and show the same variation. The flattening of the trend suggests that there is some limit to the level of backscatter that is reached when $k\sigma$ becomes large.

Horizontal Seafloor: vary $k\sigma$ for $ka = 6$



15 ° Backscatter vs $k\sigma$

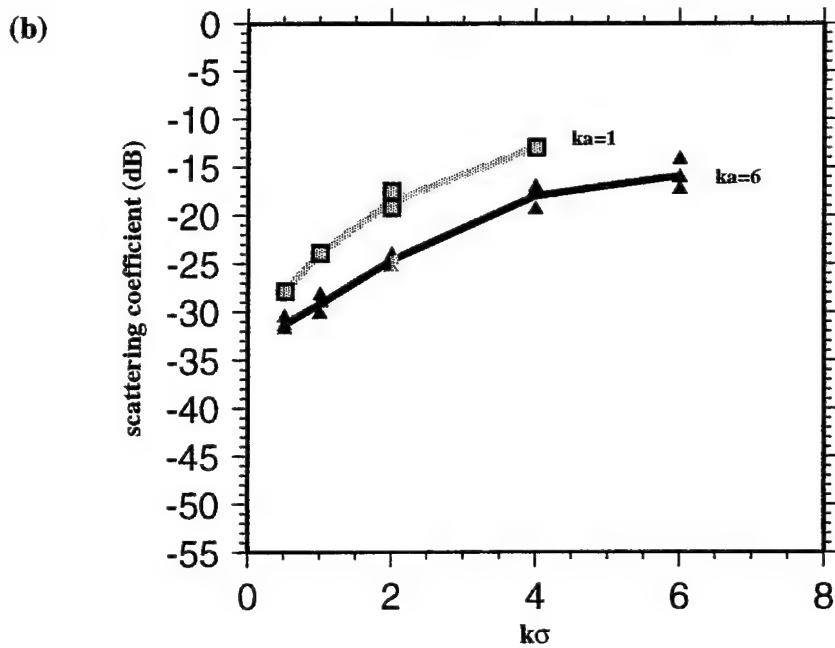
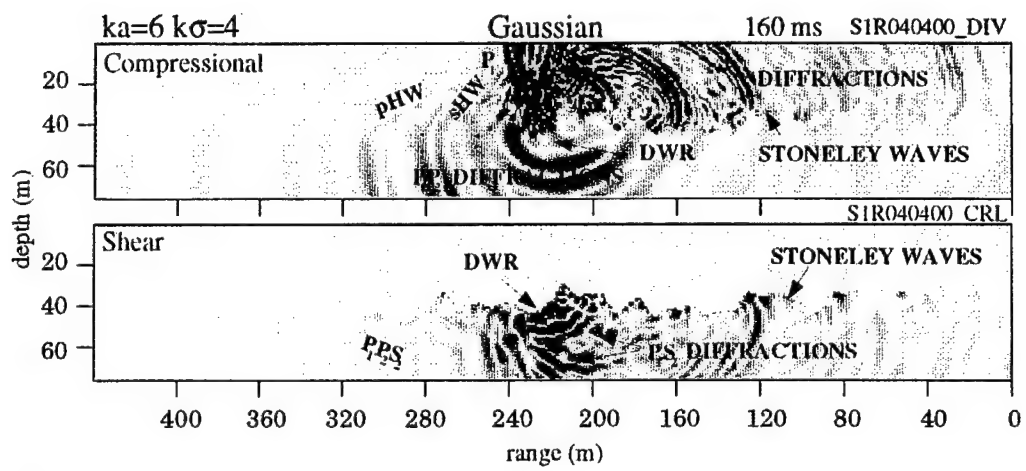


Figure 4-12: (a) A comparison of the scattered wavefields from Gaussian vs. self-similar models (Fig. 4-3(a)) shows that the scattering in the water column and body wave in the subseafloor differ primarily in the greater number of low-energy diffraction events created by the self-similar model.



(a)

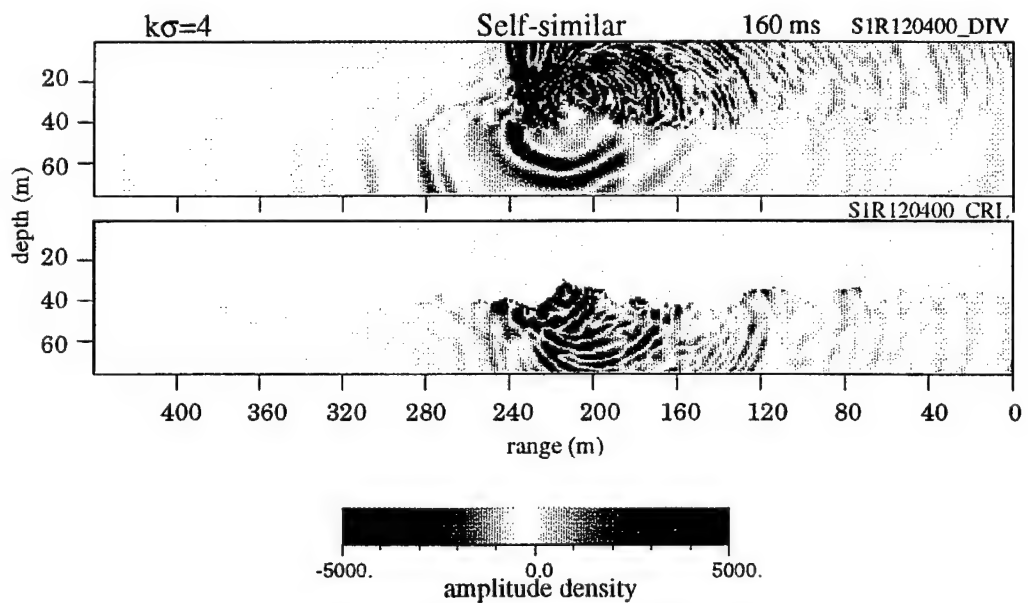


Figure 4-12: (b) The comparison of scattering functions of the Gaussian (solid line) and the self-similar model (dashed line) shows clearly that they produce almost indistinguishable time-averaged scattered energy. Within the approximations of this study, in particular the realization error, a Gaussian seafloor model response cannot be distinguished from its corresponding self-similar model response.

Gaussian vs Self-similar: $ka = 6$ $k\sigma = 4$

(b)

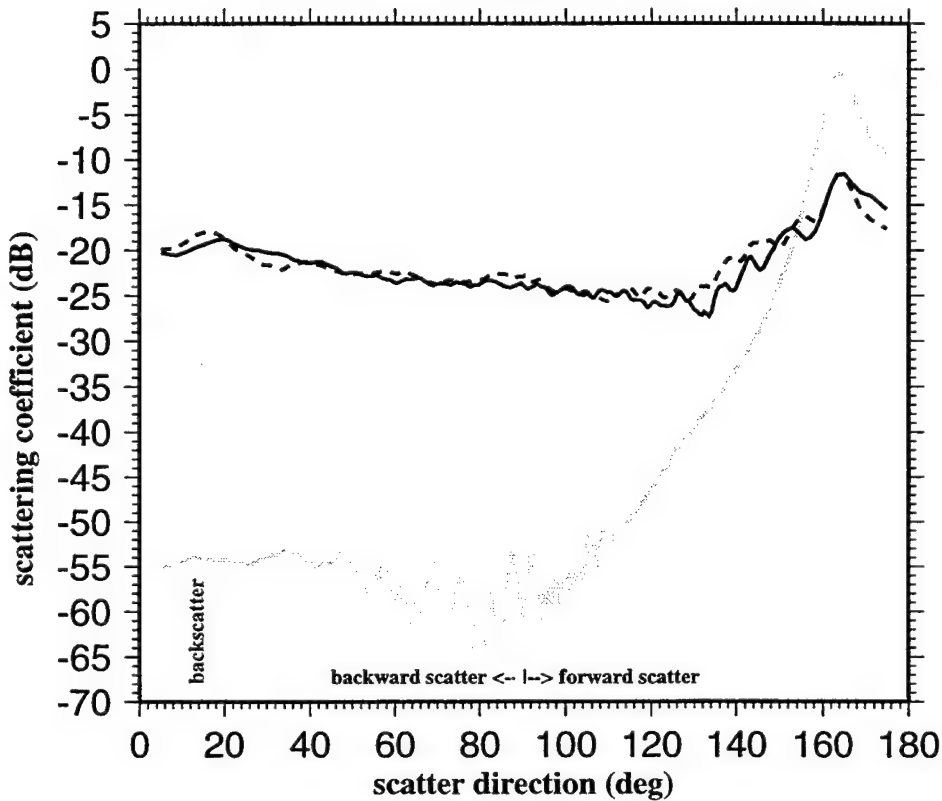


Figure 4-13: Variation in the subseafloor propagation velocity and density of a homogeneous, rough-seafloor model alters the scattered and transmitted wavefields. These schlieren diagrams show the wavefields at 160 ms for the $ka = 6$, $k\sigma = 4$, Gaussian seafloor model (Fig. 4-3). In (i) the subseafloor parameters correspond to a basalt bottom: $v_p = 4.0$ km/sec, $v_s = 2.0$ km/sec, and $\rho = 2.5$ kg/m³; in (ii) they correspond to an intermediate (talus) bottom: $v_p = 2.0$ km/sec, $v_s = 1.0$ km/sec, and $\rho = 1.74$ kg/m³; and in (iii) they correspond to a sediment bottom: $v_p = 1.52$ km/sec, $v_s = 1.0$ km/sec, and $\rho = 1.5$ kg/m³. For these models the critical grazing angles are (i) $\theta_c(P_1P_2) = 68^\circ$ and $\theta_c(P_1S_2) = 41^\circ$, (ii) $\theta_c(P_1P_2) = 41^\circ$ and (iii) $\theta_c(P_1P_2) = 9^\circ$. For (ii) and (iii), converted S-wave diffraction (P_1S_2), can occur at all grazing angles. For these models a 'transmitted' shear wave is generated at all incident angles even for a flat, homogeneous bottom. In (iii) the grazing angle is supercritical and a 'transmitted' compressional wave is also observed. The figures show that scattering of the incident wave into P-wave and S-wave energy increases as velocity decreases. However, even at subcritical grazing angles (i), both compressional and shear energy is scattered into the subseafloor. In general, as the subseafloor velocity decreases, the amplitude of the backscattering appears to decrease.

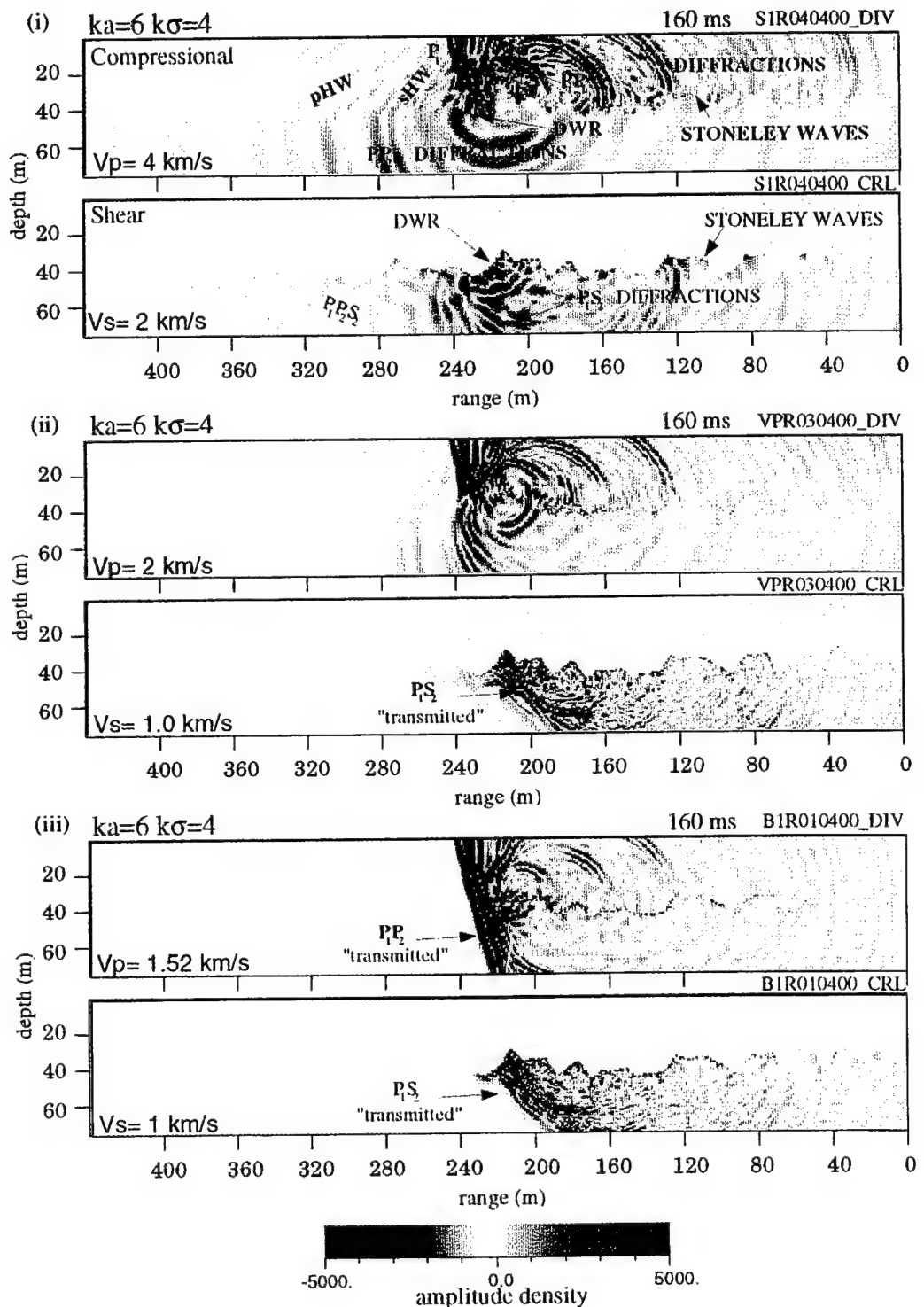


Figure 4-14: This figure shows wavefield energy at 160 ms for the $ka = 6$, $k\sigma = 0.5$ Gaussian model (Fig. 4-10a(iii)), for the same subseafloor velocity and density parameters as listed in Fig. 4-13. In all of the velocity models, diffractions of P-wave and S-wave energy into the subseafloor are observed, but in lower-velocity models, (ii) and (iii), transmitted shear waves are also observed. For the lowest-velocity model, the transmitted P-wave energy is observed as well. The decrease in roughness due to the smaller value of $k\sigma$ produces less scattering in the water column (compare to Fig. 4-13).

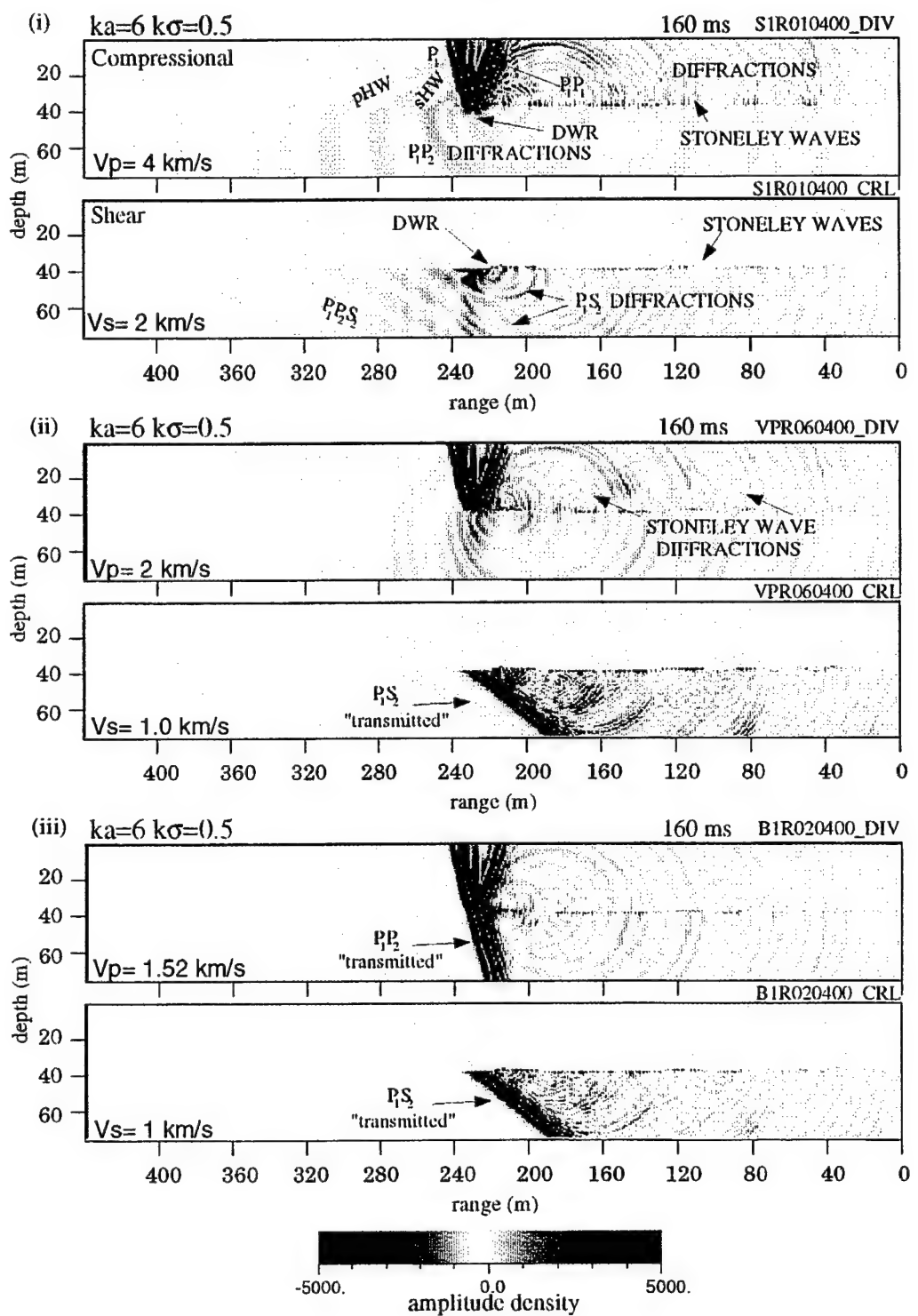
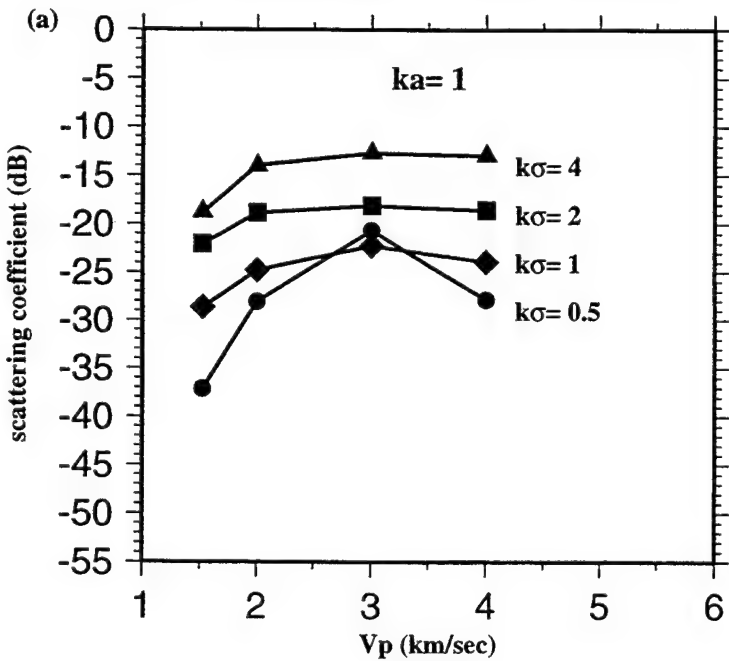


Figure 4-15: In general, scattering coefficients in the 15° backscatter direction increase as subseafloor velocity and density increase. The sensitivity is slightly weaker for models with correlation length of $ka = 1$ (a) than for models with larger correlation length, $ka = 6$ (b). These results also show that the backscattered signals of the lowest (sediment) velocity models are always at least 7 dB down relative to the same models with higher subseafloor velocity. In most cases, the points plotted represent average values from three realizations. The anomalous response at 3 km/sec of models with small $k\sigma$ values is observed in all realizations.

15° Scattering vs. P-wave Velocity



15° Scattering vs. P-wave Velocity

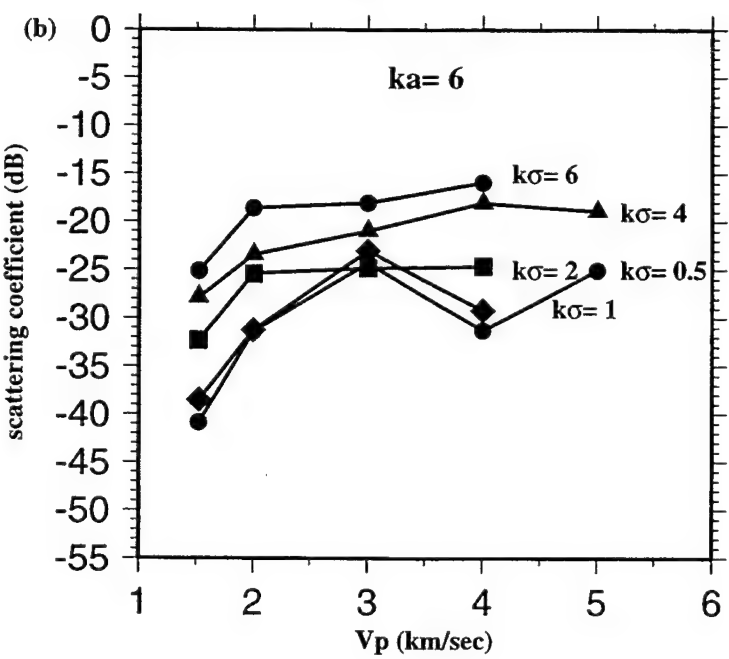


Figure 4-16: (a) Models with sloping smooth seafloor, where the slope is measured over large scales, i.e., much larger than wavelength-scale of the insonifying wavefield. This slope affects the scattering from stochastic representations of the seafloor because it alters the effective grazing angle and apparent roughness of the surface. To quantify this effect, scattering from models with slopes from 0° – 75° , are compared. In this figure three sloping models with smooth surfaces are shown. In each case the models are centered in the NSC in order to have the same portion of the Gaussian beam interacting with the surface. Note that the finite grid spacing adds a certain amount of 'microroughness' to any model, except at 0° . Model (iii), sloping 75° , represents a surface normal to the 15° incident beam.

Models with Sloping Smooth Seafloor

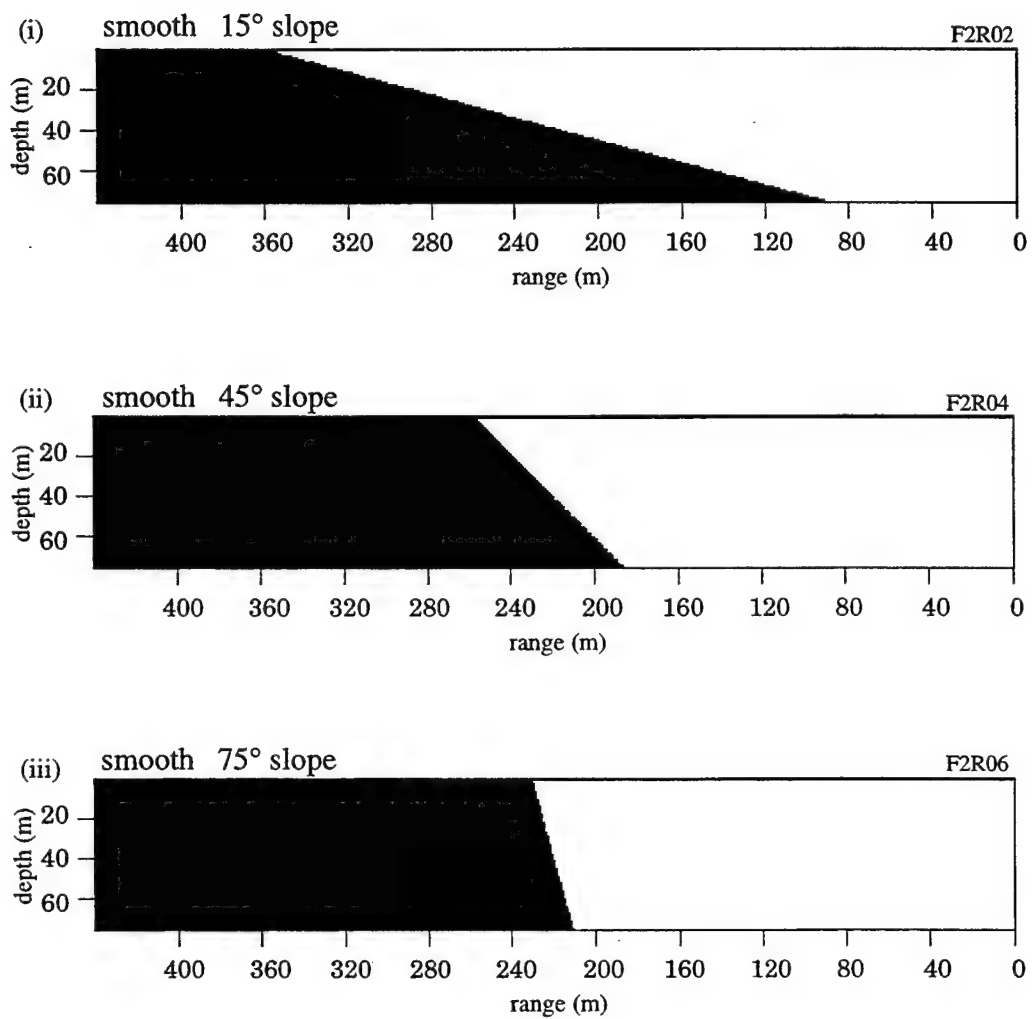


Figure 4-16: (b) The dominant waveforms in these schlieren diagrams are the surface reflections (P_1P_1). When the true grazing angle, $\theta_g = \theta_{beam} + \theta_{slope} > \theta_c$, transmitted compressional and shear wave body waves are also produced. For these models $\theta_c^p[P_1P_2] = 68^\circ$ and $\theta_c^s[P_1S_2] = 41^\circ$. In (i) $\theta_g = 30^\circ$ and no P -wave or S -wave transmission is observed. The direct wave root is present, as are low level diffractions due to the grid microroughness (referred to as grid diffractions in the figure). In (ii), $\theta_g = 60^\circ$ such that transmission of converted S -wave energy occurs. Scattering from the microroughness also generates some P -wave energy in this case and yet the direct wave root still exists because the grazing angle is subcritical for P -waves. In (iii), $\theta_g = 90^\circ$ and the P -wave is reflected directly back in the source direction as well as being transmitted. Note that shear wave energy in (iii) is due to scattering from the microroughness into the subseafloor. Note that there are some wavefield artifacts, such as the corner diffractions and the reflection from the model base at the toe of each model.

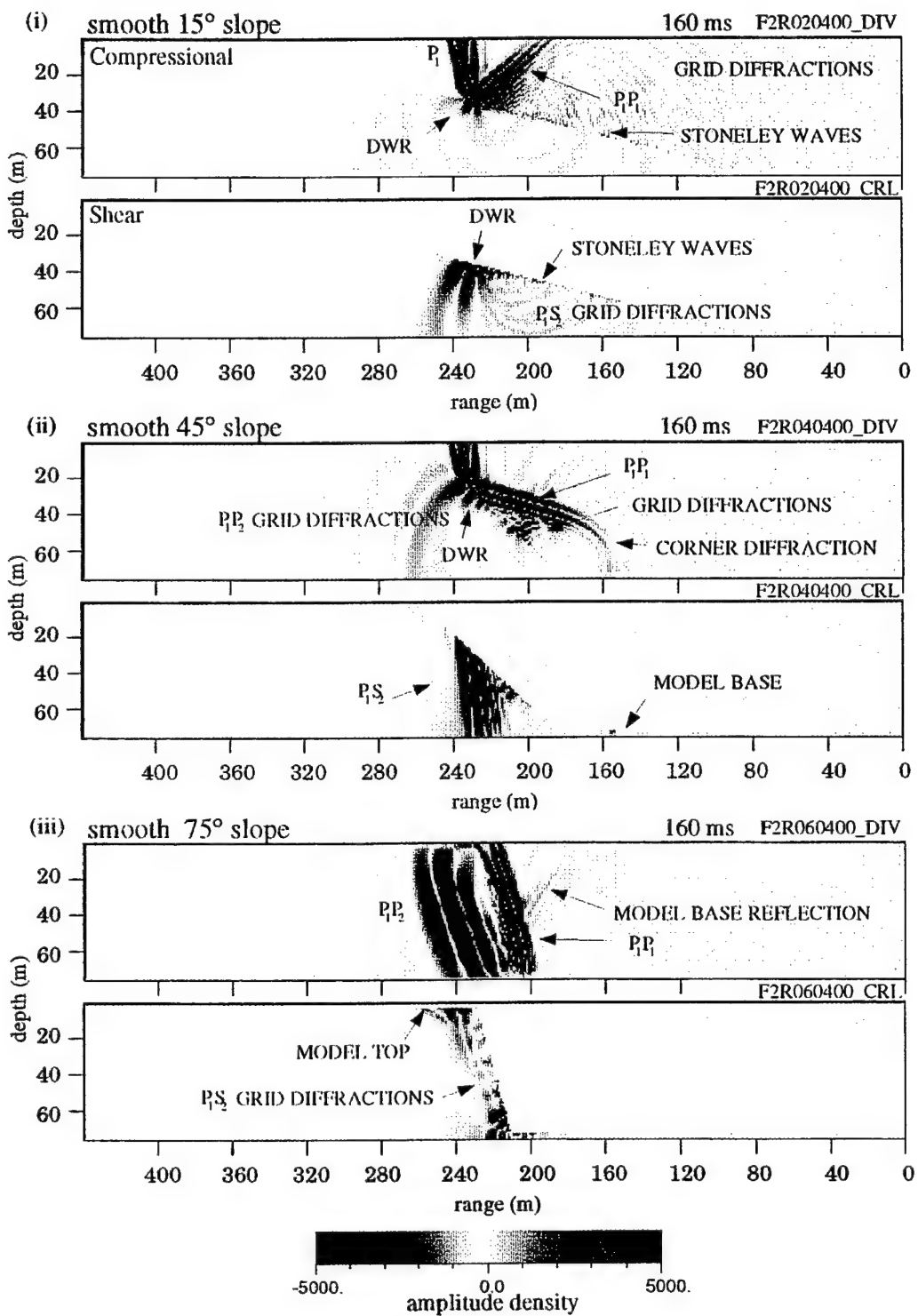
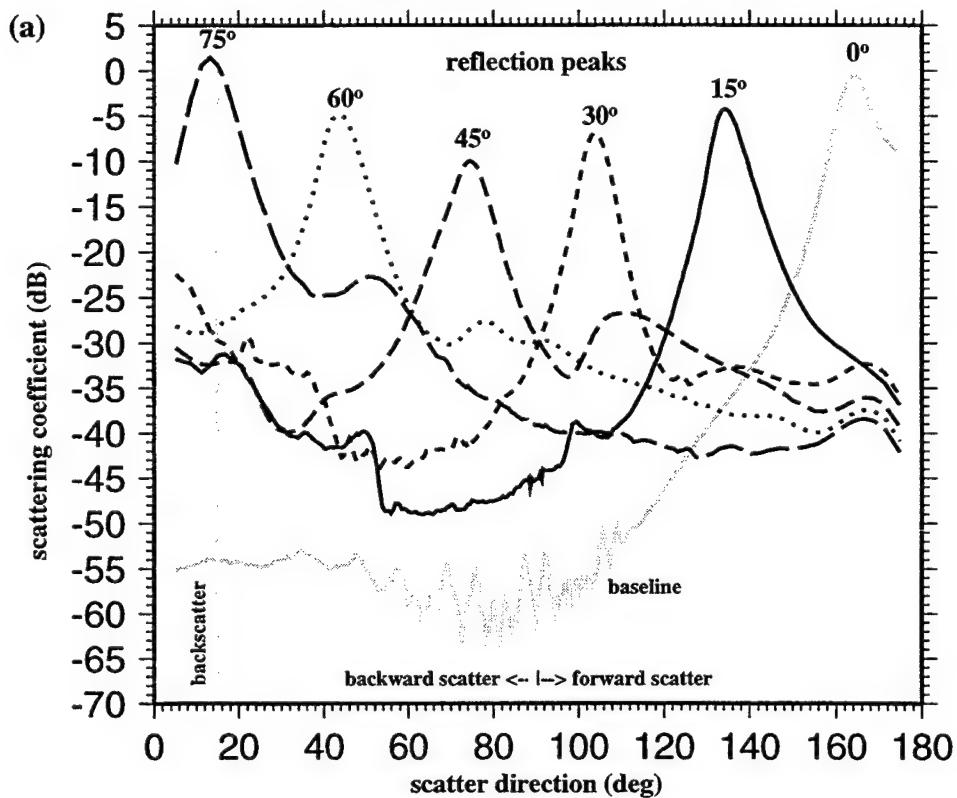


Figure 4-17: The scattering coefficient functions for sloping smooth seafloor, (a), are dominated by the reflected signal. The angles labeling each function refer to the slope of each surface modeled. The variation in the amplitude of the reflection peaks is due to dependence of the reflection coefficient on the angle of incidence. The microroughness produces a signal that in the backscatter direction is about 20 dB above the background noise level (baseline model).

(b) At 15° the scattering coefficients are primarily just a measure of scattering due to grid microroughness which is considered to be a realistic level of scattering from small-scale seafloor roughness.

Varying Smooth Seafloor Slope



15 ° Backscatter vs Slope

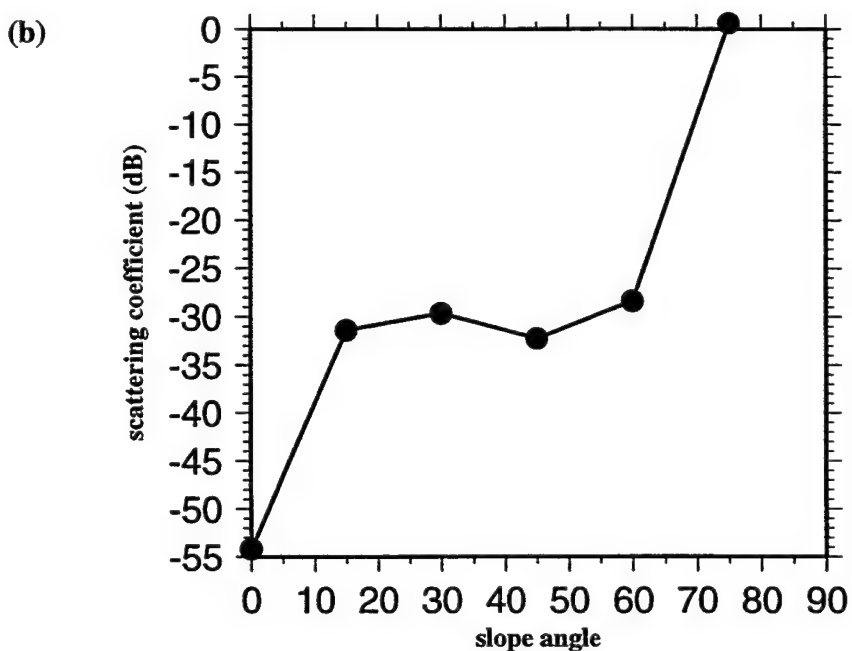


Figure 4-18: A series of models with sloping rough seafloor were generated by rotating the $ka = 6$, $k\sigma = 4$ (Fig. 4-3) Gaussian model to different large-scale slopes. The figure (a) shows the sloping rough surfaces at (i) 15° , (ii) 45° and (iii) 75° . Making a comparison of sloping seafloors with added stochastic roughness is difficult in a limited model chamber. Because the seafloor is truncated differently depending on angle, it is necessary to present different surfaces to the incident wavefield. To some extent this is minimized as the central portion of the rough model is always used. The actual ka and $k\sigma$ computed for the portion of the interface used in each case are shown above each model.

Models with Sloping Rough Seafloor

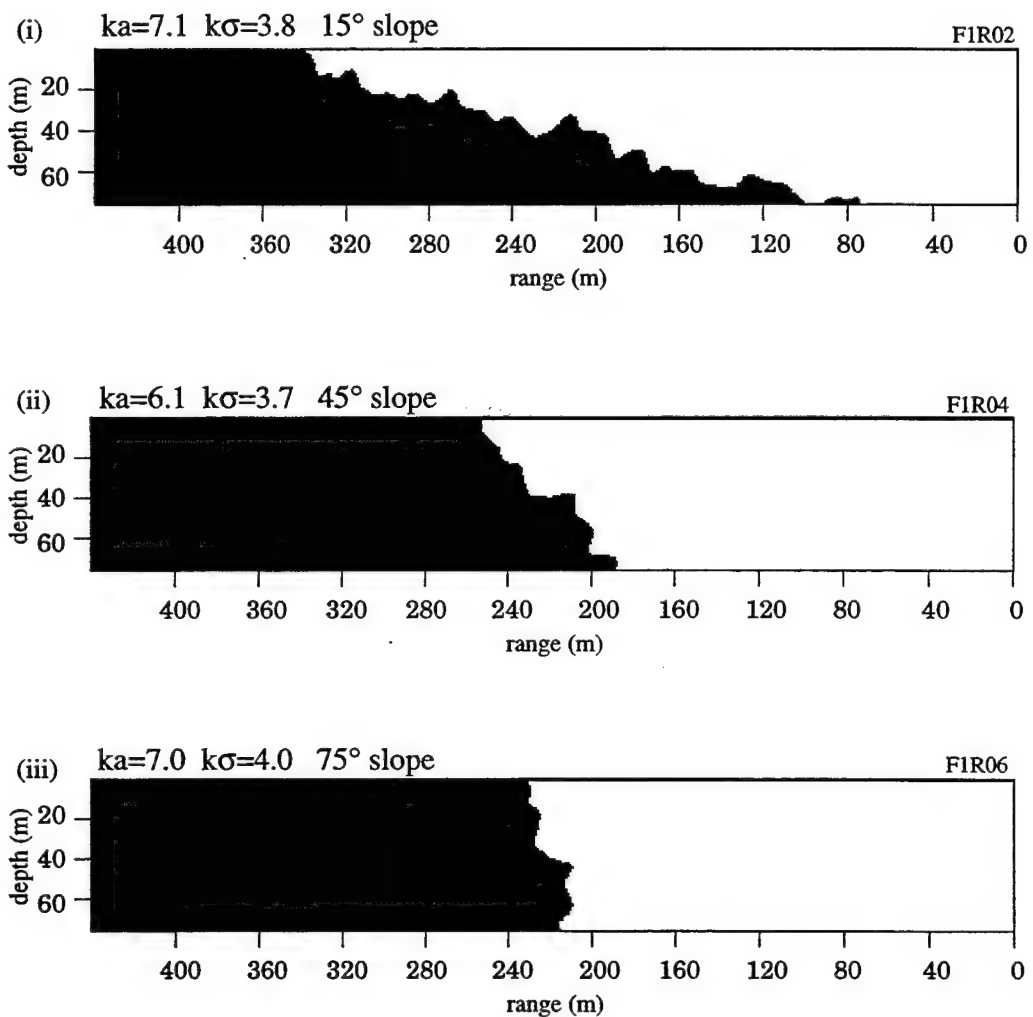


Figure 4-18: (b) The statistical parameters of the original rough surface (Fig. 4-3(b)) are $ka = 6$ and $k\sigma = 4$. The portions remaining in the model after rotation have (i) $ka = 7.1$ and $k\sigma = 3.8$, (ii) $ka = 6.1$ and $k\sigma = 3.7$ and (iii) $ka = 7.0$ and $k\sigma = 4.0$, corresponding to the rotated surfaces at 15° , 45° and 75° , respectively.

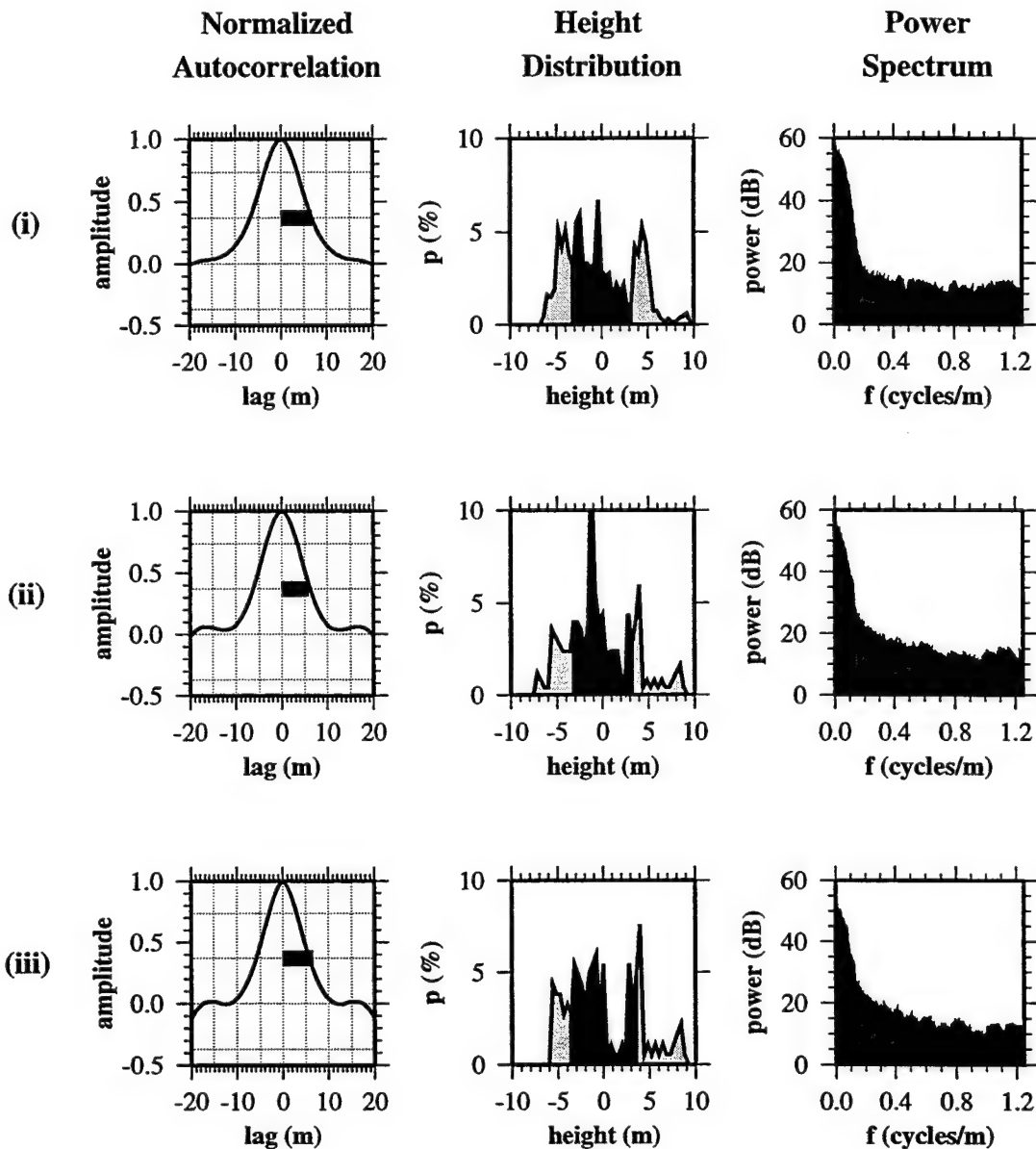


Figure 4-18: (c) As the slope of the rough surface increases, the true grazing angle of the incident wavefield increases. Over the range of large-scale slope shown in these schlieren diagrams, it is not clear that the scattering increases with increasing slope. If scattering could be predicted by Lambert's Rule, a substantial difference in scattering would be expected. These figures should be compared to the same seafloor without slope (Fig. 4-12(a)).

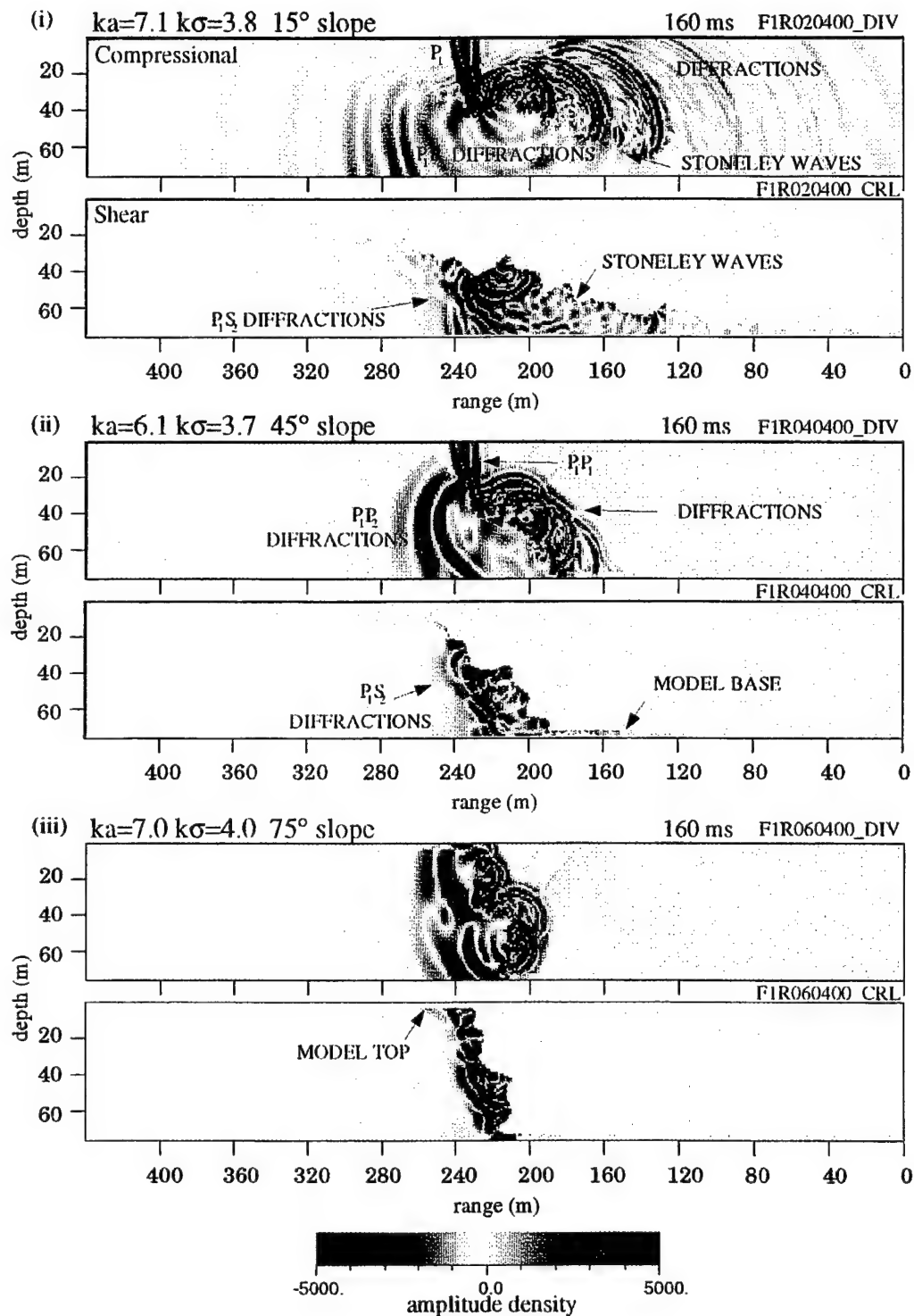
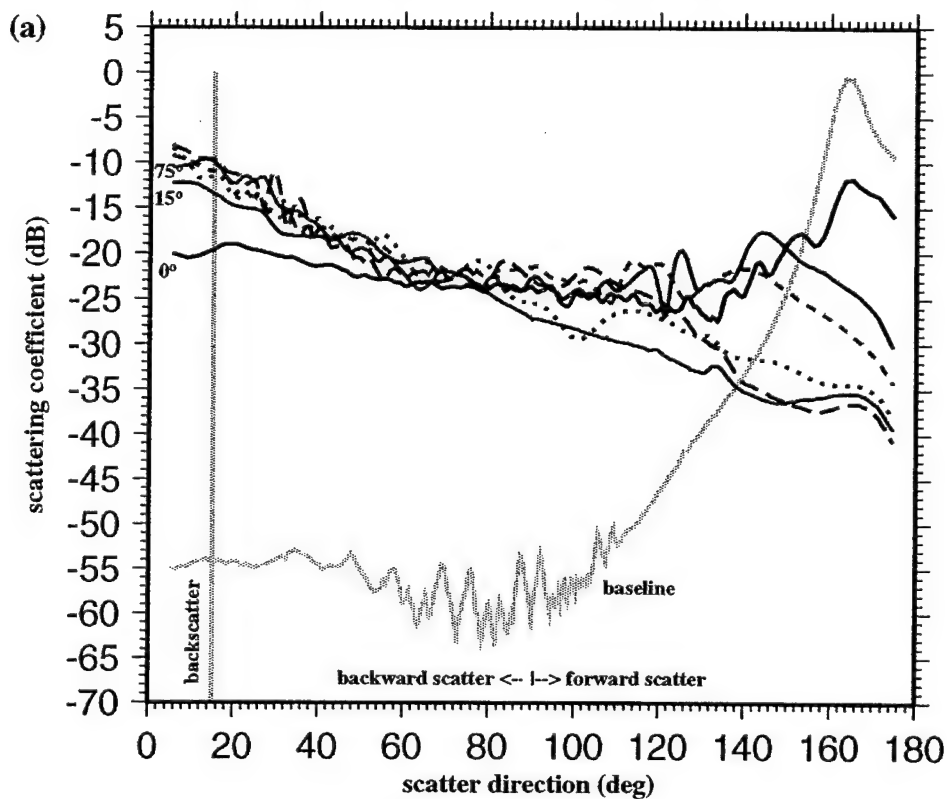


Figure 4-19: (a) Scattering coefficients for sloping rough seafloor all have about the same response in the backscatter direction. This suggests that the scattering is not very sensitive to changes in average seafloor slope, at least above 15° . Only a single realization for each model has been plotted for each slope: 0° (solid black), 15° (solid red), 30° (green short dash), 45° (blue long dash), 60° (black dots), and 75° (solid pink).

(b) This is clearly seen when the scattering coefficients in the 15° backscatter direction are plotted as a function of slope angle from 0° to 90° . The net increase in backscatter is about 10 dB, but almost half of this increase occurs in the change from 0° to 15° slope. The points plotted represent the average response from three realizations of each model. In general, the roughness of $ka = 6$ and $k\sigma = 4$ adds about 20 dB to the backscattered signal relative to the corresponding smooth sloping surfaces (grey circles), which only have microroughness scattering, and about 40-45 dB relative to the baseline model noise floor.

Varying Rough Seafloor Slope ($ka = 6$ $k\sigma = 4$)



15 ° Backscatter vs Slope

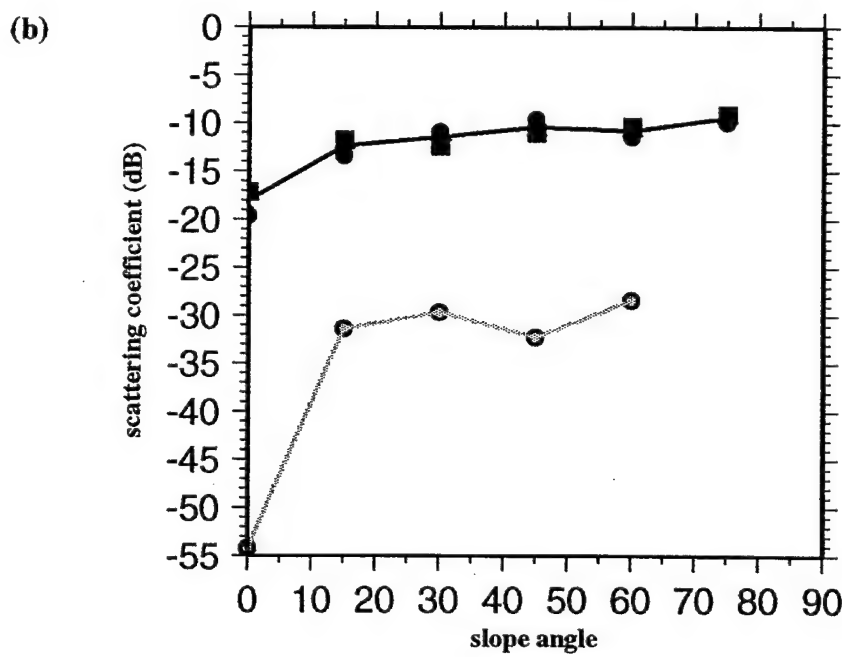


Figure 4-20: An 'effective grazing angle', θ_g^{eff} , incorporates all seafloor structural parameters and is defined (see text) as $\theta_g^{eff} \approx \theta_b + \theta_s + \theta_{rms}^s$. The rms slope of a Gaussian rough surface, θ_{rms}^s , is defined as $\theta_{rms}^s = \tan^{-1}(\sqrt{2} \frac{\sigma}{a})$.

- (a) For a horizontal, rough-seafloor model, where $ka = 6$ and $k\sigma = 4$, $\theta_{rms}^s = 43^\circ$. The actual rms grazing angle in the sloping, rough-seafloor models differs somewhat from this because of their variation in ka . The actual θ_{rms}^s calculated for each model is plotted in this figure. The solid line is the average value calculated at each large-scale slope angle, θ_s .
- (b) When θ_g^{eff} is computed for each of the sloping, rough-seafloor models, the scattering coefficients are more widely distributed. This plot shows that the sensitivity to increasing slope is reduced above $\theta_g^{eff} \approx 73^\circ$, which corresponds to models with seafloor slope of 15° . This suggests that changes in average seafloor slope in the range of 0° to 15° will produce a larger change in backscattered signals than the same slope variation above 15° . This plot suggests that seafloor slope can account for a maximum of about 10 dB variation in backscatter signals if roughness is held constant.

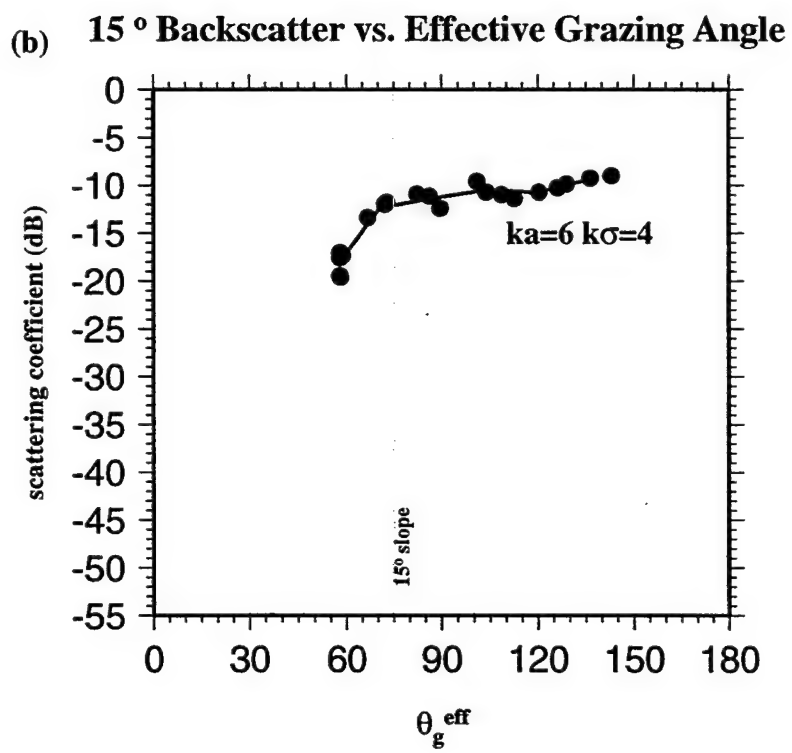
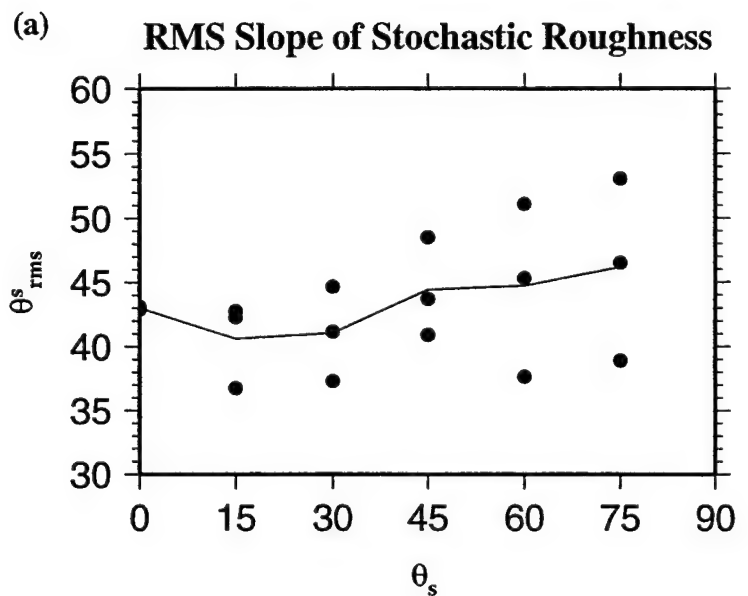
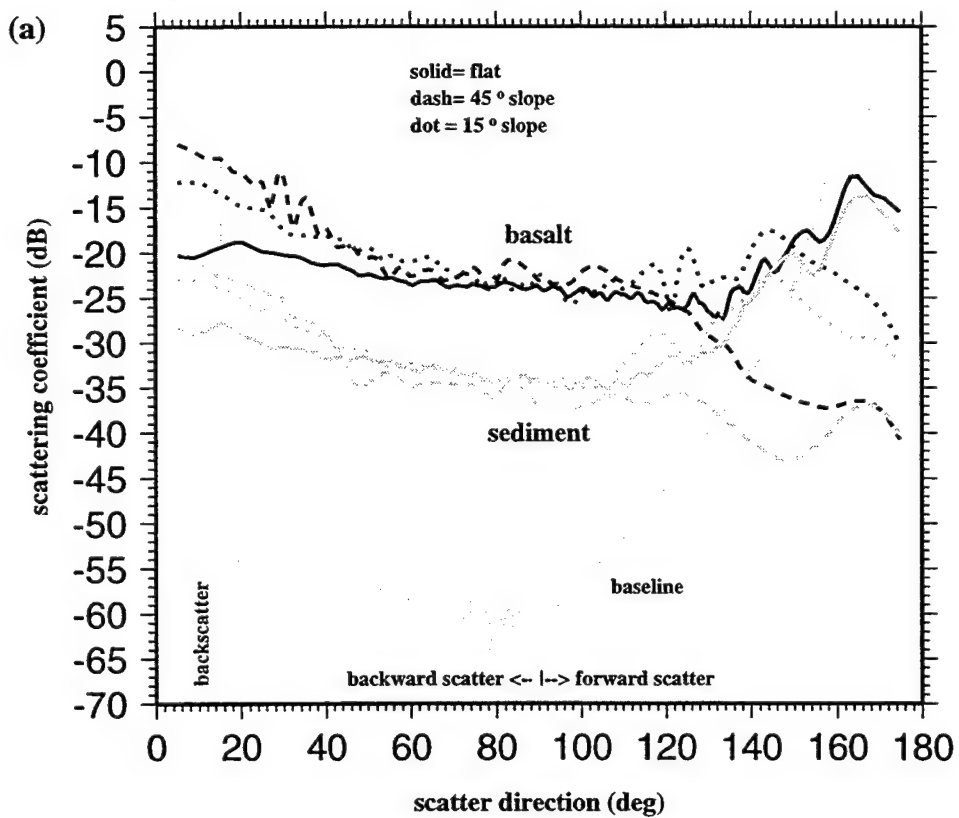


Figure 4-21: Comparing scattering coefficients of hard and soft rough sloping seafloor, (a), shows that there is a strong reduction in the scattered signal when the subsurface is defined with soft-bottom (sediment) properties, as compared to the signal from a hard-bottom material such as basalt. This figure compares hard and soft-bottom, rough ($ka = 6$ and $k\sigma = 4$) seafloor models with and without seafloor slope. Black (solid and dashed) lines correspond to basalt models and the grey (solid and dashed) lines correspond to the sediment-bottom models. Solid lines are for horizontal models, long dashed lines for 15° slope, and short dashed lines for 45° slope.

(b) When the 15° backscatter coefficients are plotted as functions of slope, it is seen that the sensitivity is about the same for both basalt- and sediment-bottom models. Although 15° slope could, realistically, be sediment covered, it is not expected for 45° slope. The higher-slope sediment models are included as an example of a soft-bottom model response. Talus might be expected to have a similar, but higher intensity response.

Hard vs. Soft Seafloor



15 ° Backscatter vs Slope

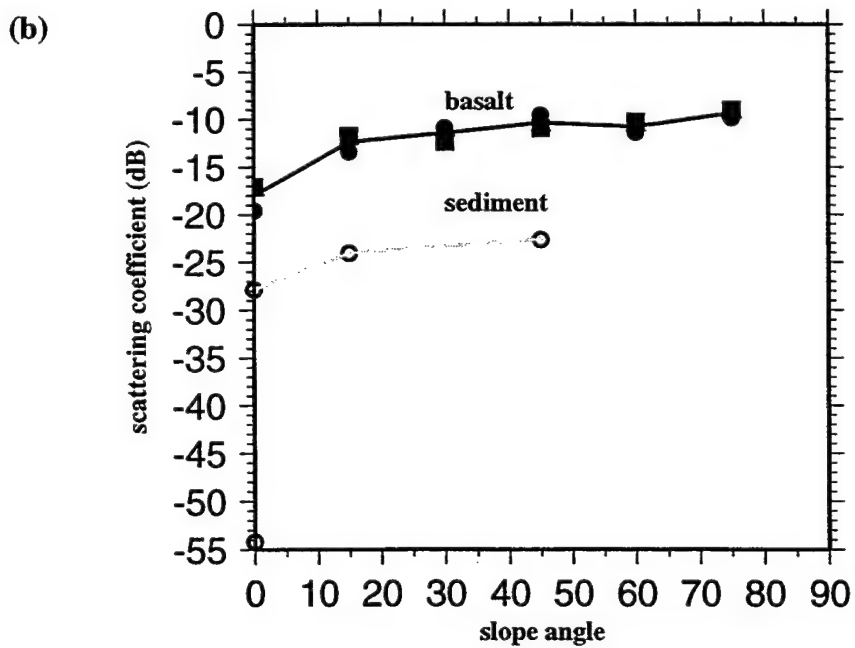


Figure 4-22: The Rayleigh roughness parameter is re-defined as a function of the 'effective grazing angle' parameters. The Rayleigh roughness parameter is defined as $R_a = k\sigma \sin \theta_g$; however, by substituting the 'effective grazing angle', θ_g^{eff} for θ_g , it becomes a function of large-scale slope and wavelength-scale roughness parameter (ka and $k\sigma$) as well as the incident beam grazing angle. In (a) this 'effective Rayleigh roughness parameter' (R_{eff}) is plotted as a function of ka for different fixed values of $k\sigma$. The box labelled 'Site A' indicates the range in ka and $k\sigma$ expected in this region. For large values of $k\sigma$ (> 5), the variation in R_{eff} , being sinusoidal with respect to ka , shows a peak as ka decreases. However, within the range of parameters at Site A, this peak is not reached, nor is it sharply defined.

Similarly, in (b) the effective Rayleigh roughness parameter is plotted as a function of $k\sigma$ for different fixed values of ka . Variation in R_{eff} with $k\sigma$ is almost linear in the range of ka at Site A. The fact that effective Rayleigh roughness is a much stronger function of $k\sigma$ than ka fits the rough-seafloor modeling results.

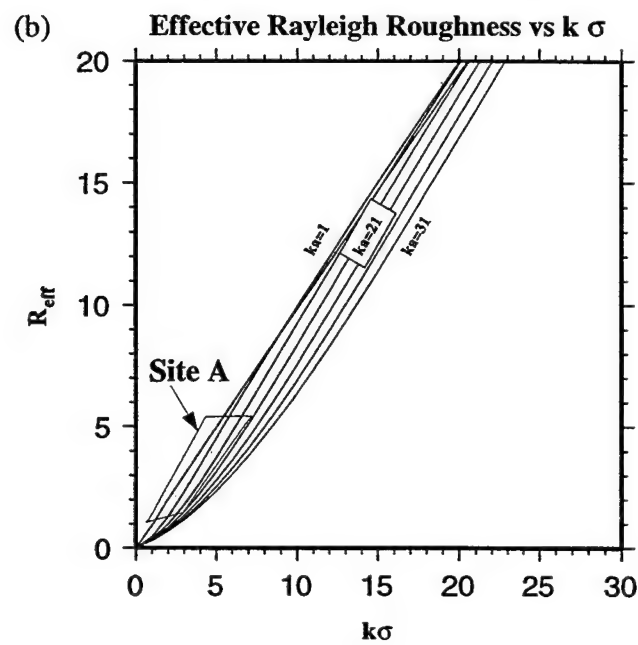
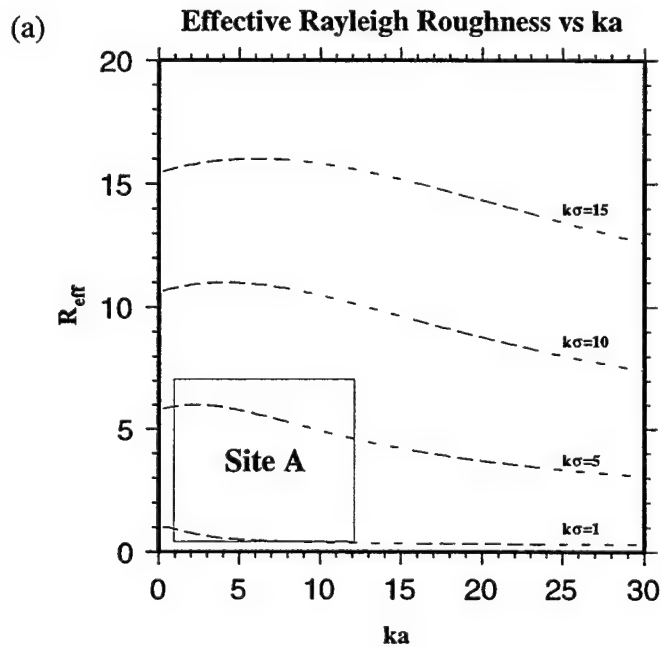


Figure 4-23: (a) A 'wire diagram' of scattering coefficients vs. effective Rayleigh roughness for horizontal, rough-seafloor models with basalt-bottom properties is shown. Effective Rayleigh roughness has been calculated for each model using the 'effective grazing angle'. The solid black lines join the average values for $ka = 1$ and $ka = 6$, as indicated, and the solid grey lines join the average values for constant $k\sigma = 0.5, 1, 2$ and 4 . There may be enough regularity in this relationship to interpret seafloor parameters from the scattering coefficients. For example, if the seafloor is believed to have a correlation length in the range $1 < ka < 6$ then a scattering coefficient of -25 dB would indicate a surface with rms height of $1 < k\sigma < 2$. Alternatively, an rms surface height of $k\sigma = 2$ indicates a correlation length of $ka = 6$.

(a)

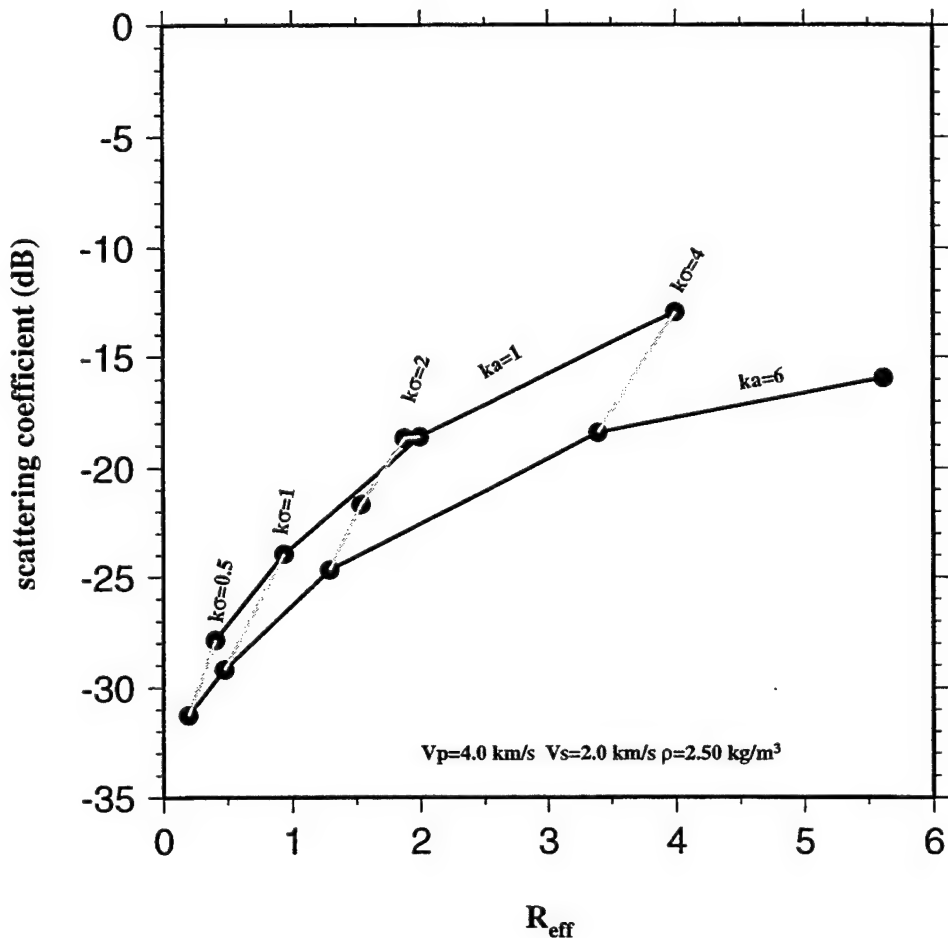
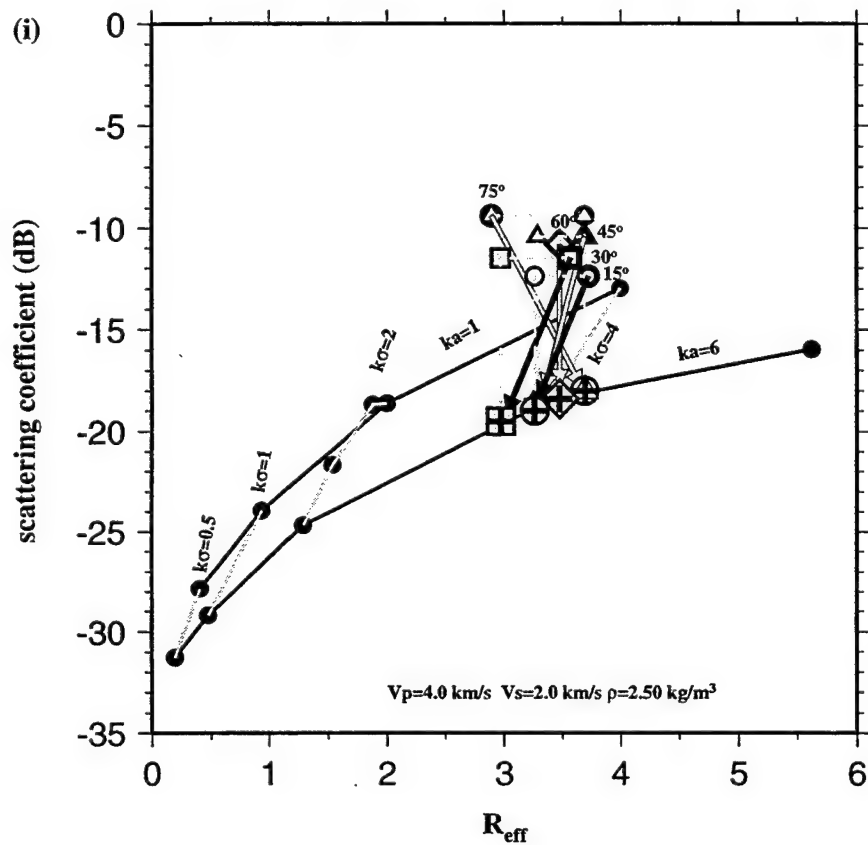
15 ° Backscatter vs. R_{eff} 

Figure 4-23: (b) This figure shows a system for estimating the effect of large-scale seafloor slope on scattering coefficient from modeling results. In (i) the scattering coefficient of each basalt model with sloping seafloor is plotted as a function of its calculated effective Rayleigh roughness (black symbols with grey symbols inside). Using the actual values of ka and $k\sigma$ for each sloping model, the effective Rayleigh roughness of horizontal models with these same roughness parameters is calculated. To remove the effect of slope on effective Rayleigh roughness, each scattering coefficient location is shifted horizontally to its calculated effective Rayleigh roughness for a horizontal seafloor (symbols with solid grey interiors). The scattering coefficient is then shifted vertically to the value that would be expected (based on the wire diagram) for a horizontal rough basaltic seafloor with these values of ka and $k\sigma$ (symbols with grey interior and black cross). Figure (ii) summarizes the shifts necessary in scattering coefficient and R_{eff} to remove the effect of large-scale slope for a rough basaltic seafloor. These shifts are presumed to be useful for other subseafloor velocity models (assuming uniform subseafloor velocity) but may not be appropriate for seafloor with much smaller effective Rayleigh roughness.

(b) **15 ° Backscatter vs. R_{eff} : Sloping Seafloor**



Slope Effect Removal

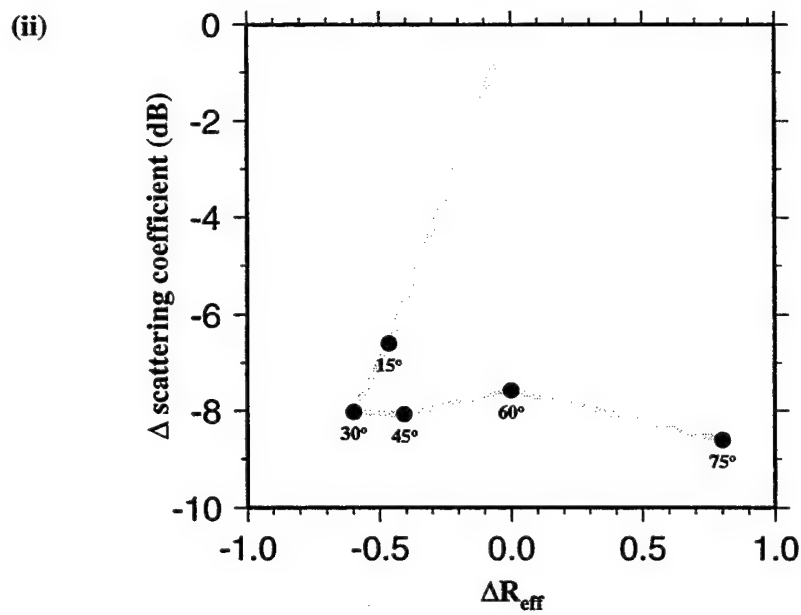


Figure 4-24: Wire diagrams of scattering coefficients vs. effective Rayleigh roughness for different velocities suggest a possible interpretation of scattering coefficients in areas where no information about seafloor properties is available. Scattering coefficients below -30 dB would be considered due to sediment covered areas. Seafloor sediment has low shear modulus (corresponding to low shear velocity) and therefore cannot be formed into very rough surfaces. Very hard rock, such as basalt, can be formed into very steep and rough seafloor features, and is therefore most likely to be the source of very high scattering coefficients (> -22 dB). The region between the sediment and basaltic seafloor zones would be interpreted as seafloor with higher velocity than sediment but similar roughness. Such seafloor could be formed by basaltic sheet flows, or the relatively smooth surface (compared to a basalt scarp, etc.) of a talus slope.

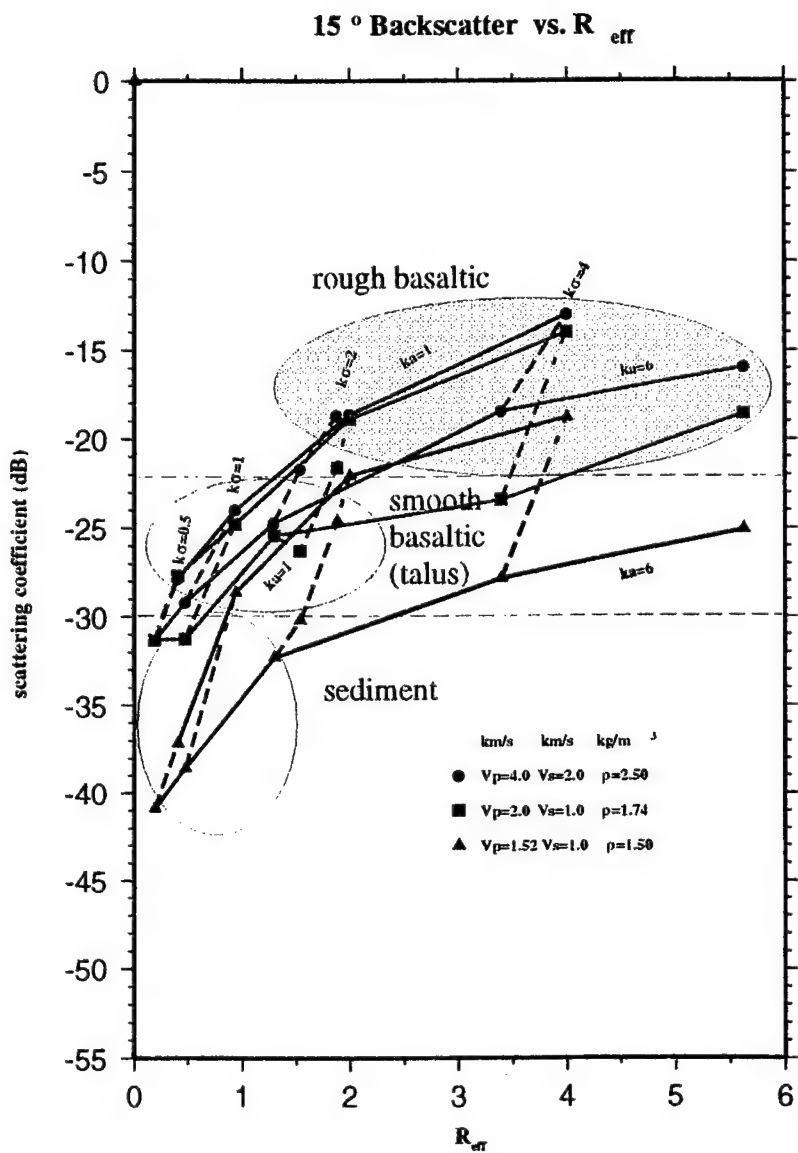


Figure 4-25: (a) The four realistic seafloor models extracted from the original seafloor profile in Fig. 4-4(a) have average large-scale seafloor slopes (dashed lines) that vary from 6° to 45° . These slopes are calculated as the best-fit line (least-square) for the bathymetry in each model. The stochastic parameters for each model are:

Model 1 - $ka = 9.42, k\sigma = 1.56$

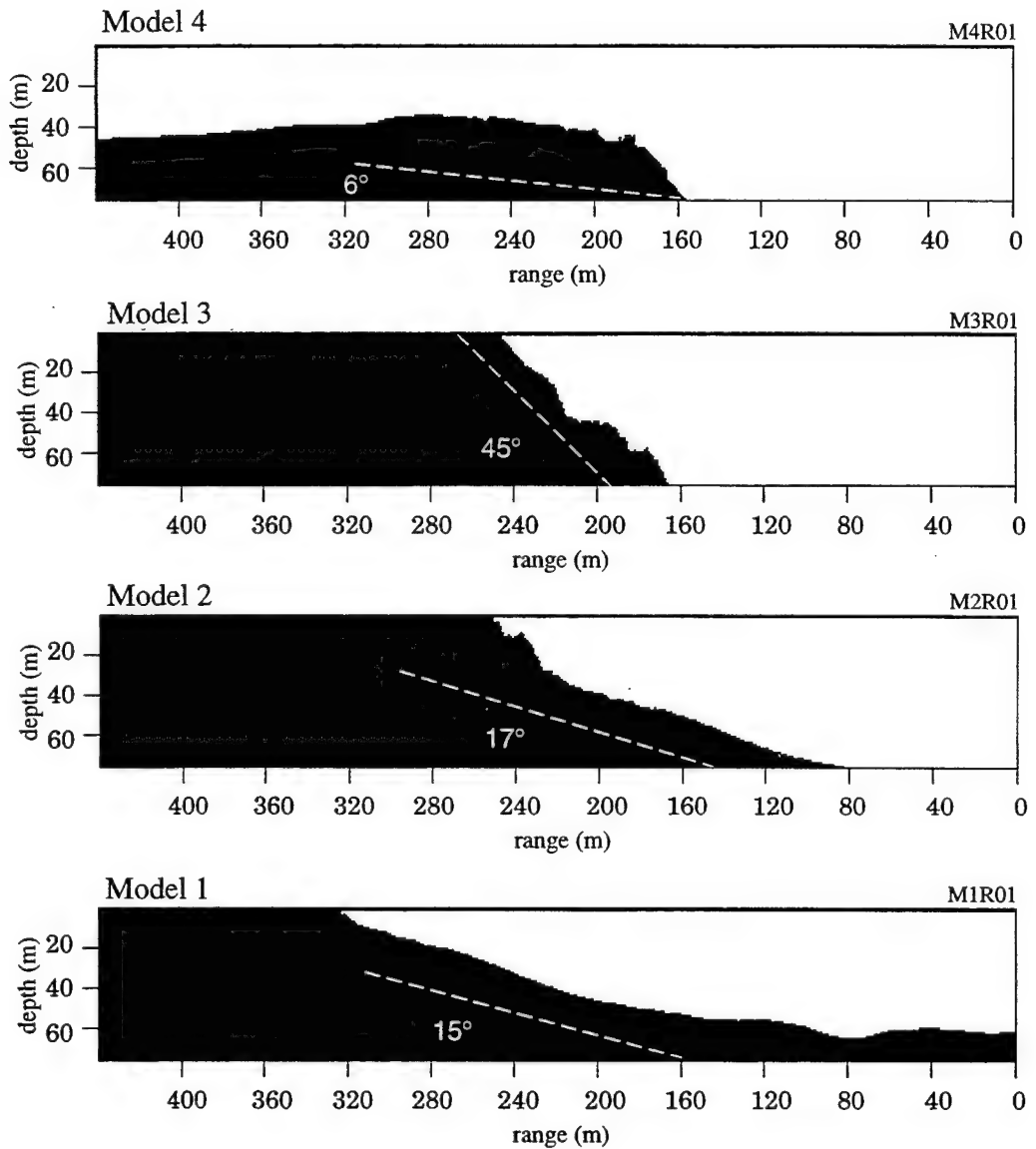
Model 2 - $ka = 7.33, k\sigma = 1.99$

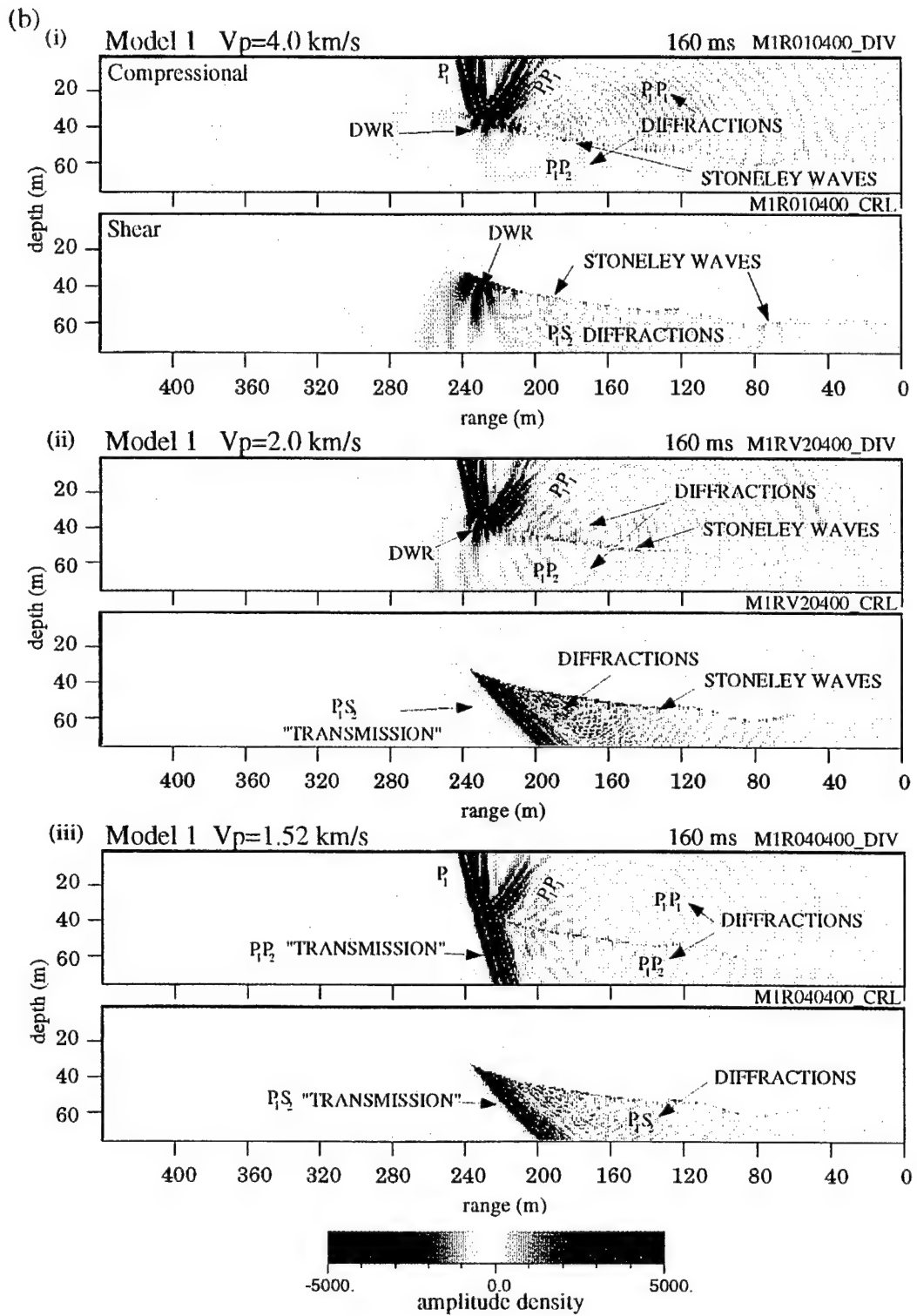
Model 3 - $ka = 6.28, k\sigma = 3.37$

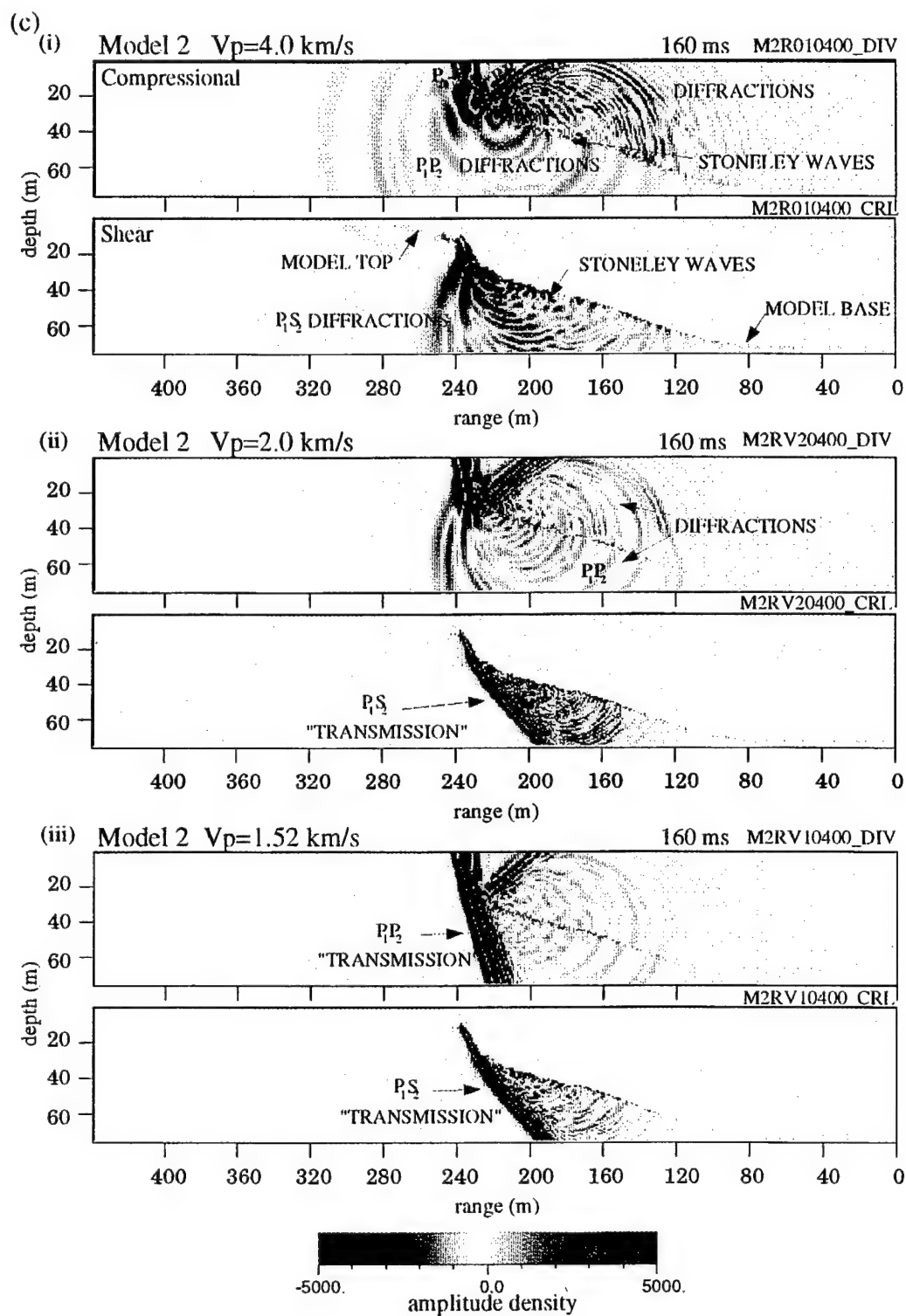
Model 4 - $ka = 5.24, k\sigma = 2.66$.

Schlieren diagrams at 160 ms for Models 1 to 4 in each model in (b)-(e) show that as subseafloor velocity and density decrease, the backscattered wavefield decreases and the amount of energy transmitted into the subseafloor increases. Model 1 consistently produces the minimum scattered field due to its relatively smooth seafloor.

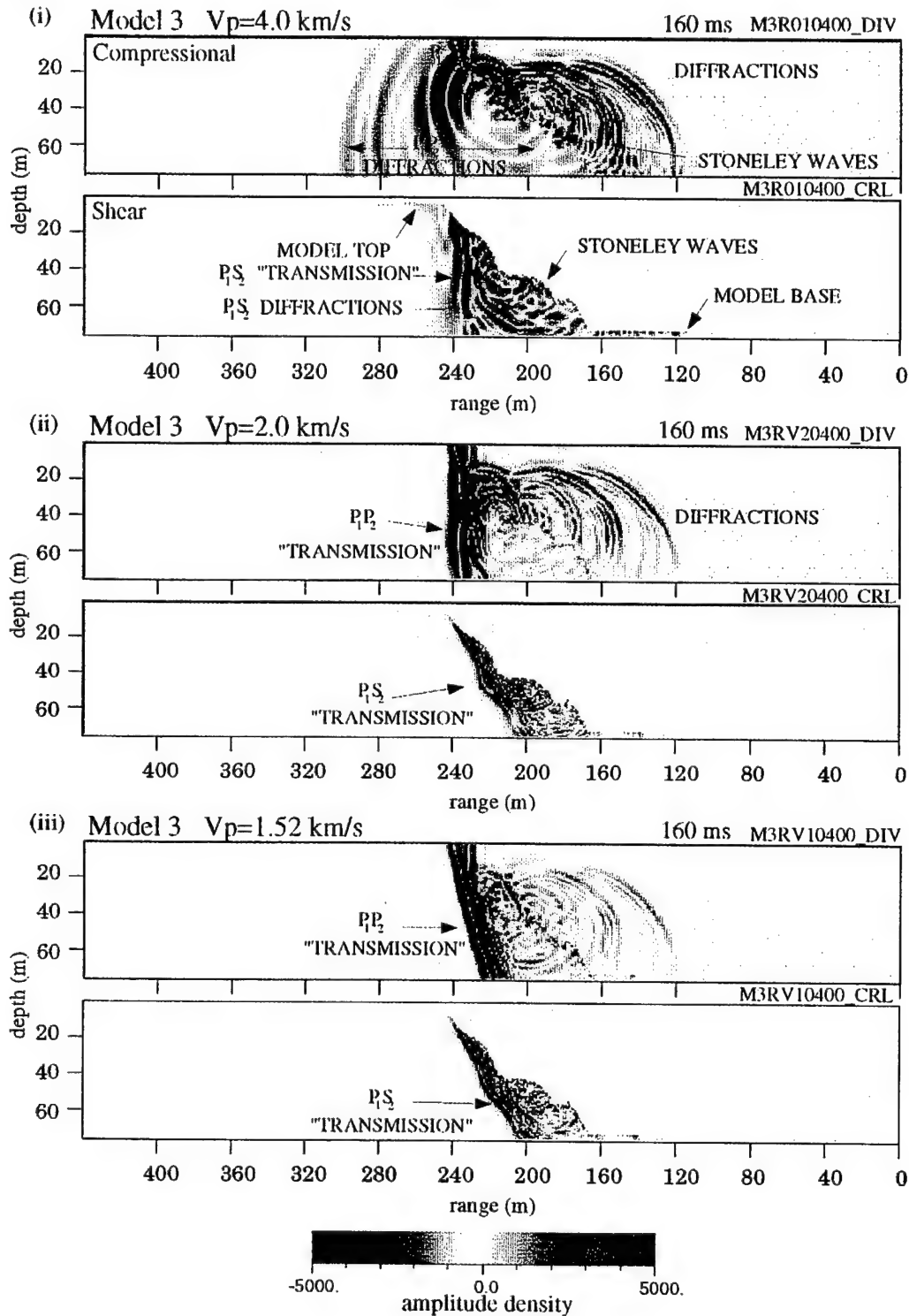
(a) Realistic Seafloor Models with Homogeneous Subseafloor







(d)



(e)

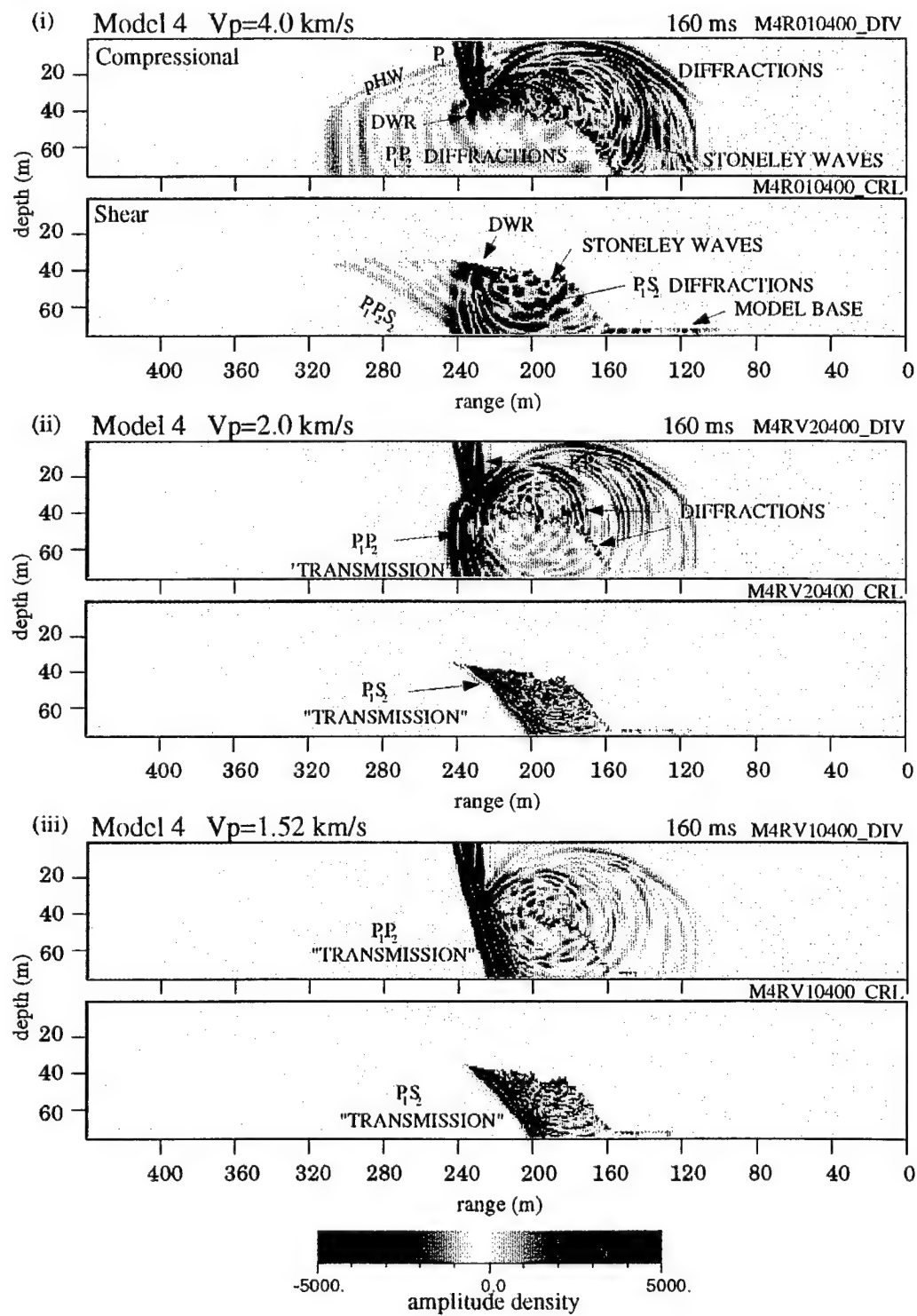
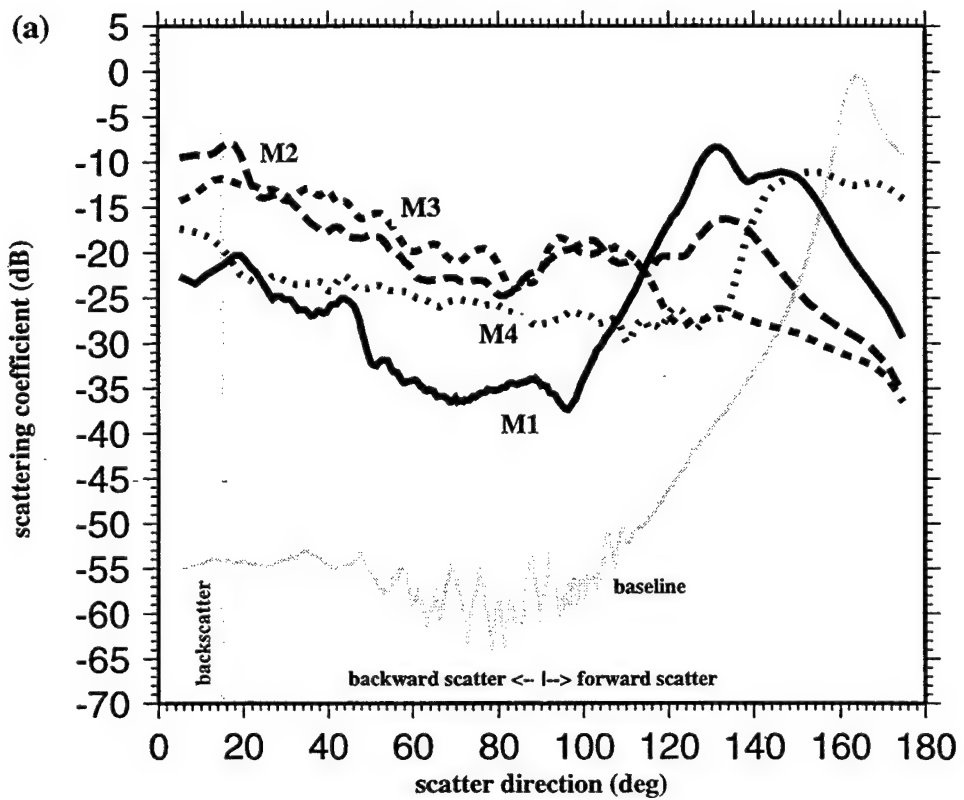
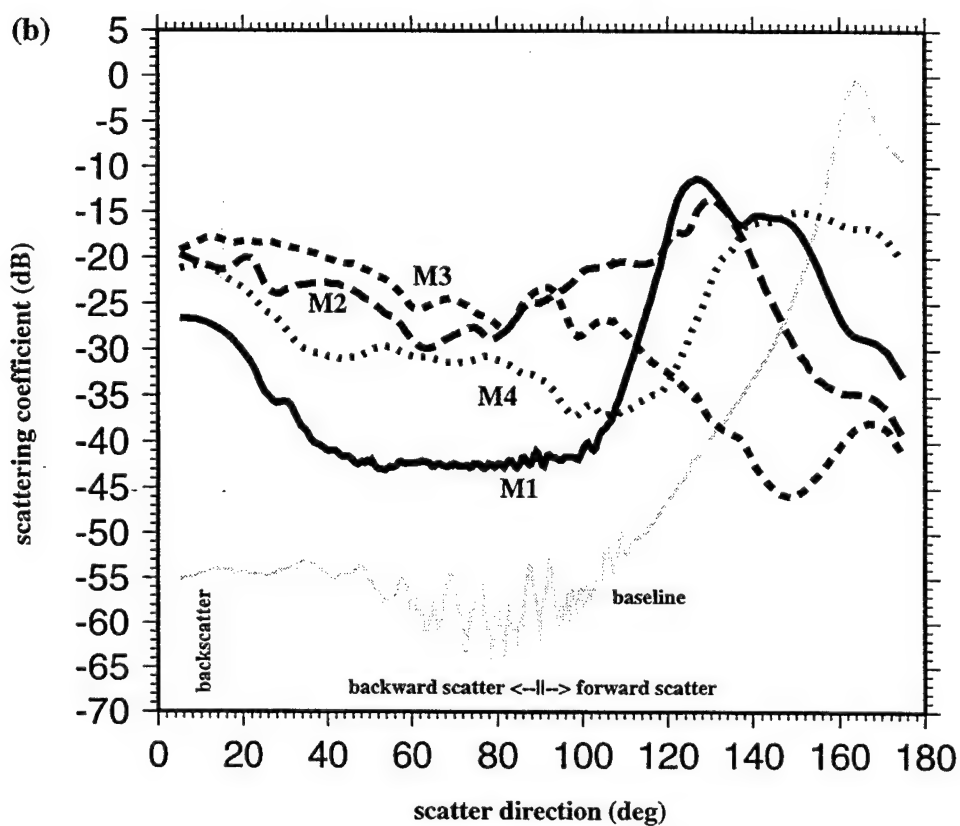


Figure 4-26: Scattering coefficients plotted for Models 1 to 4 with homogeneous sediment, talus, and basalt bottoms. The comparison in each case (a-c) shows that Model 1 always produces the lowest scattering coefficient in the backscatter direction. In (a) where $v_p = 4$ km/sec, the scattering coefficient for Model 2 is at least 5 dB higher than expected based on its stochastic roughness and average slope.

Models 1-4 with Basalt Seafloor



Models 1-4 with Talus Seafloor



Models 1-4 with Sediment Seafloor

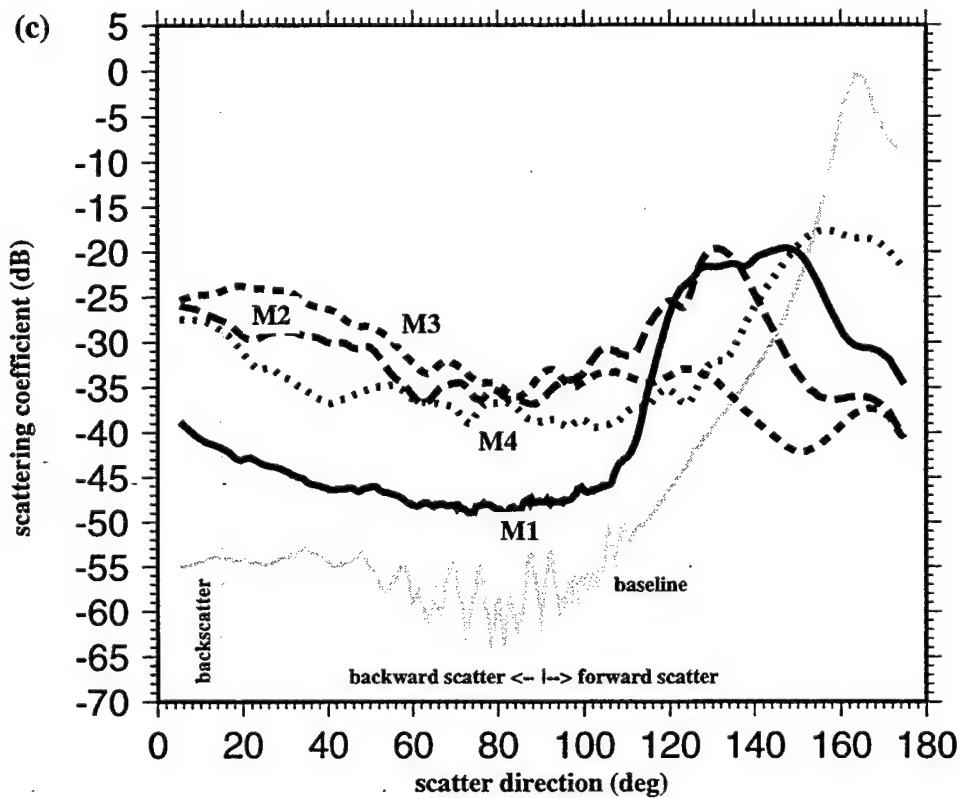


Figure 4-26: (d) The sensitivity of these models to velocity is similar to that of a rough-seafloor model with $ka = 6$ and $k\sigma = 4$ (grey line through crosses).

15° Scattering vs. P-wave Velocity

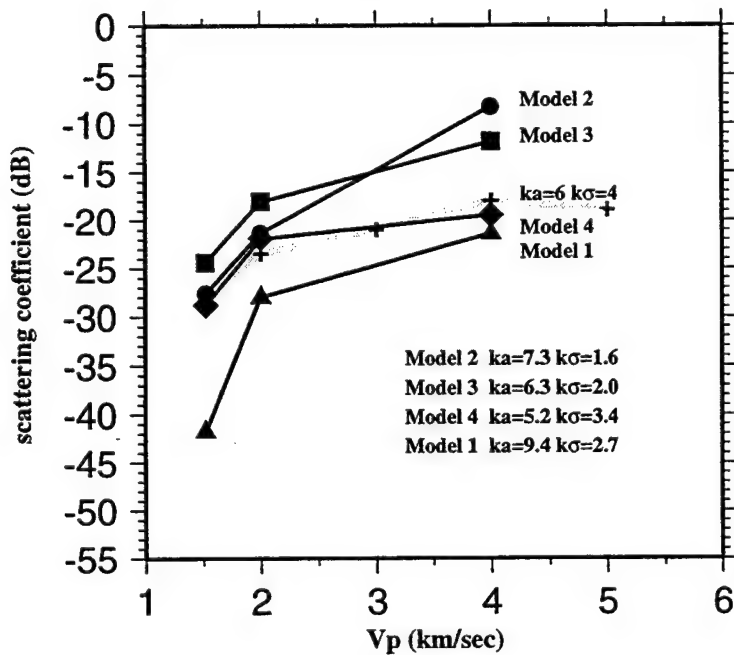
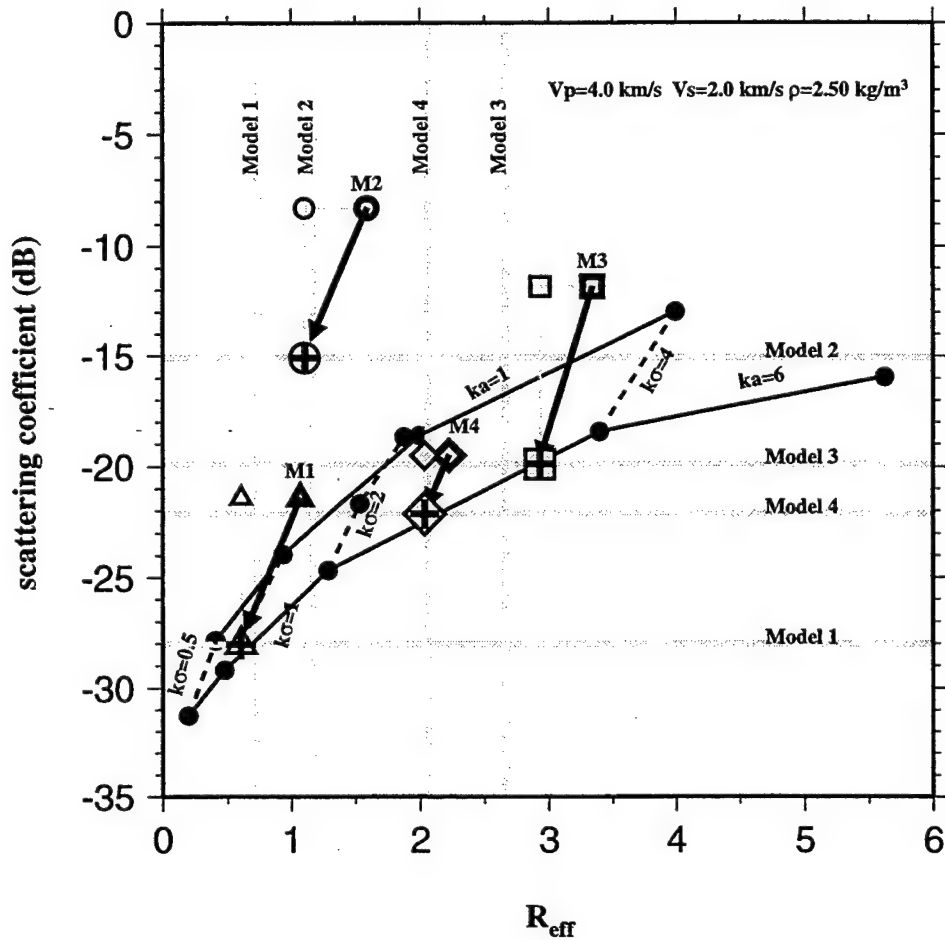


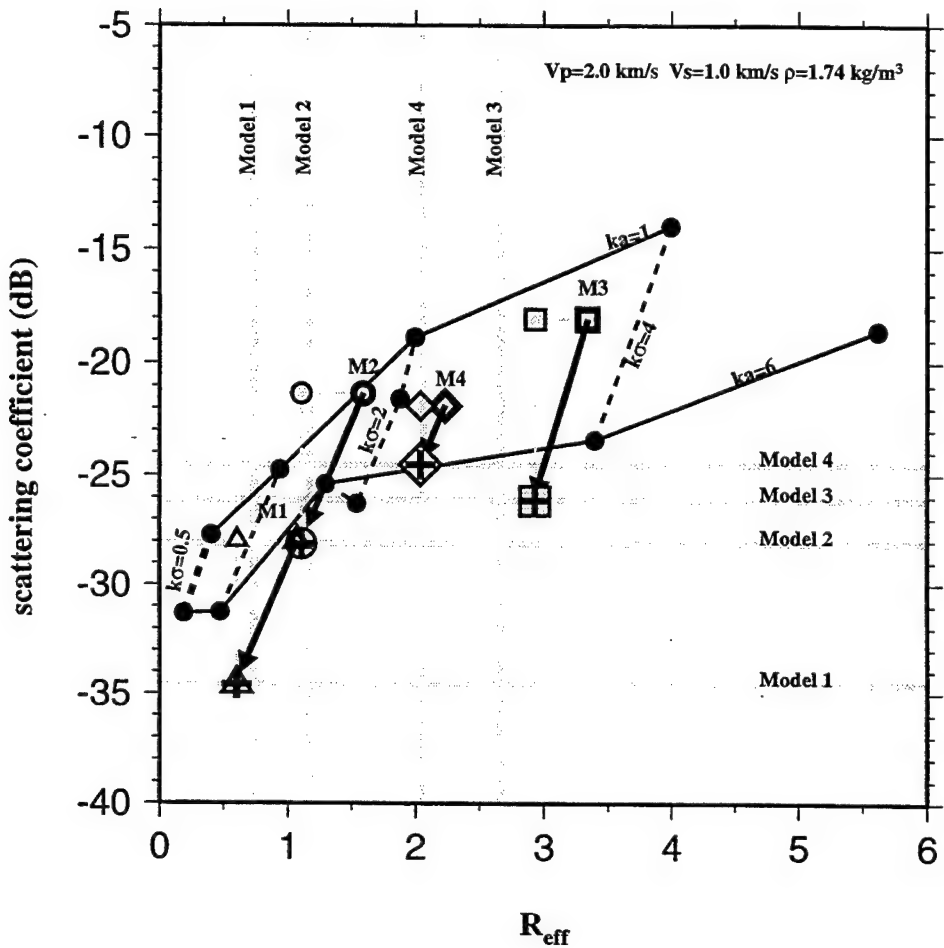
Figure 4-27: In these figures estimates are made of roughness parameters (ka and $k\sigma$) from scattering coefficients of realistic seafloor models. Scattering coefficients are calculated for each model (Models 1-4) when the subseafloor is defined as either homogeneous basalt, talus or sediment (a-c). Table 4-1 lists the velocity and density used in these models. The effective Rayleigh roughness (R_{eff}) is calculated using the values of ka and $k\sigma$ estimated from the bathymetry data and the large-scale slope (Fig. 4-25(a)) of each model. In (a-c) the calculated scattering coefficients are plotted as a function of the effective Rayleigh roughness (heavy lined open symbols with grey interior). From the large-scale slope, appropriate shifts in R_{eff} and scattering coefficients, estimated from Fig. 4-19(b), are applied to each scattering coefficient. The arrows point from the original scattering coefficient locations to the position after shifting to remove the effects of this large-scale slope. The shift in R_{eff} is shown as the horizontal displacement to light lined symbols with grey interiors. The shift in scattering coefficients is shown as the vertical displacement to heavy lined symbols with interior crosses. The vertical grey lines correspond to the effective Rayleigh roughness calculated using the ka and $k\sigma$ values (listed in Fig. 4-26) that were estimated from the stochastic part of each segment (Models 1-4) of the realistic seafloor model (Fig. 4-4). The horizontal grey lines correspond to the scattering coefficients of horizontal models with these same values of ka and $k\sigma$. If the shifts to correct for large-scale slope are correct, the shifted location should correspond to the intersection of the two grey lines for each model. The wire diagrams for each velocity model (from Fig. 4-24) are shown in each figure and used to estimate the values of ka and $k\sigma$ corresponding to the shifted locations of the scattering coefficients. The results are compared in Table 4-2.

If only large-scale seafloor slope is known, then after making the slope corrections the seafloor roughness must be chosen somewhere along the horizontal grey lines. In order to do so, some estimate of either ka or $k\sigma$ must be made. Table 4-3 shows an estimate of $k\sigma$ when it is assumed that $ka = 7$ in all cases.

(a) **15 ° Backscatter vs. R_{eff} : Models 1-4 as Basalt**



(b) **15 ° Backscatter vs. R_{eff} : Models 1-4 as Talus**



(c) **15 ° Backscatter vs. R_{eff} : Models 1-4 as Sediment**

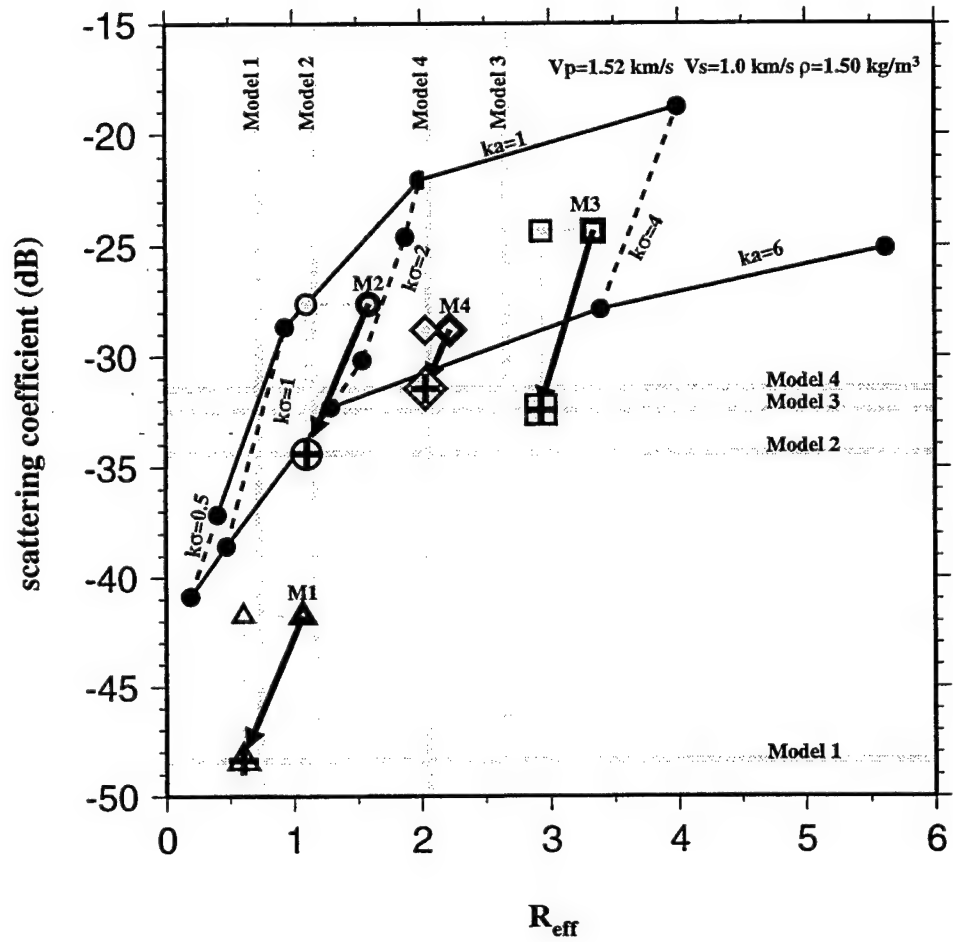


Figure 4-28: (a) Flat-seafloor models are shown with subseafloor volume heterogeneity. All of the models have volume heterogeneity with rms perturbation amplitude of 10% but have correlation lengths (i) $a_v = 11.8$ m , (ii) $a_v = 6.3$ m, and (iii) $a_v = 1.7$ m. Average velocity and density of the subseafloor corresponds to the basalt (hard-bottom) model.

Models with $\sigma_v = 10\%$ Volume Heterogeneity in Basalt

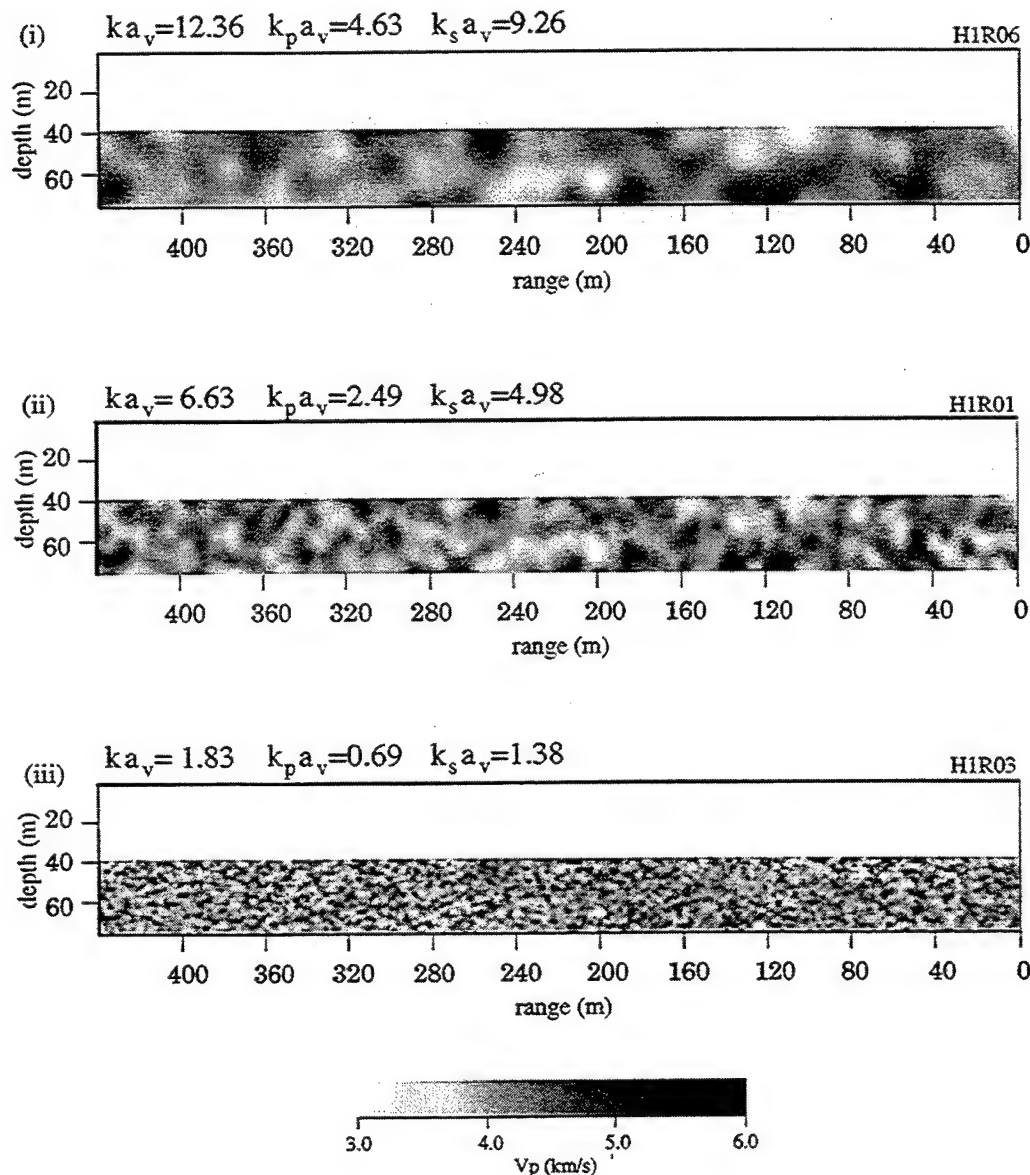


Figure 4-28: (b) For the flat basalt model, the source wavefield is incident on the seafloor at a subcritical grazing angle so that the only source of energy in the subseafloor is the direct wave root (DWR). As the DWR interacts with the subseafloor heterogeneity, body waves are created which are then scattered multiple times in the subseafloor. As these schlieren diagrams show, both the subseafloor scattering and the scattering into the water column increase as the correlation length decreases.

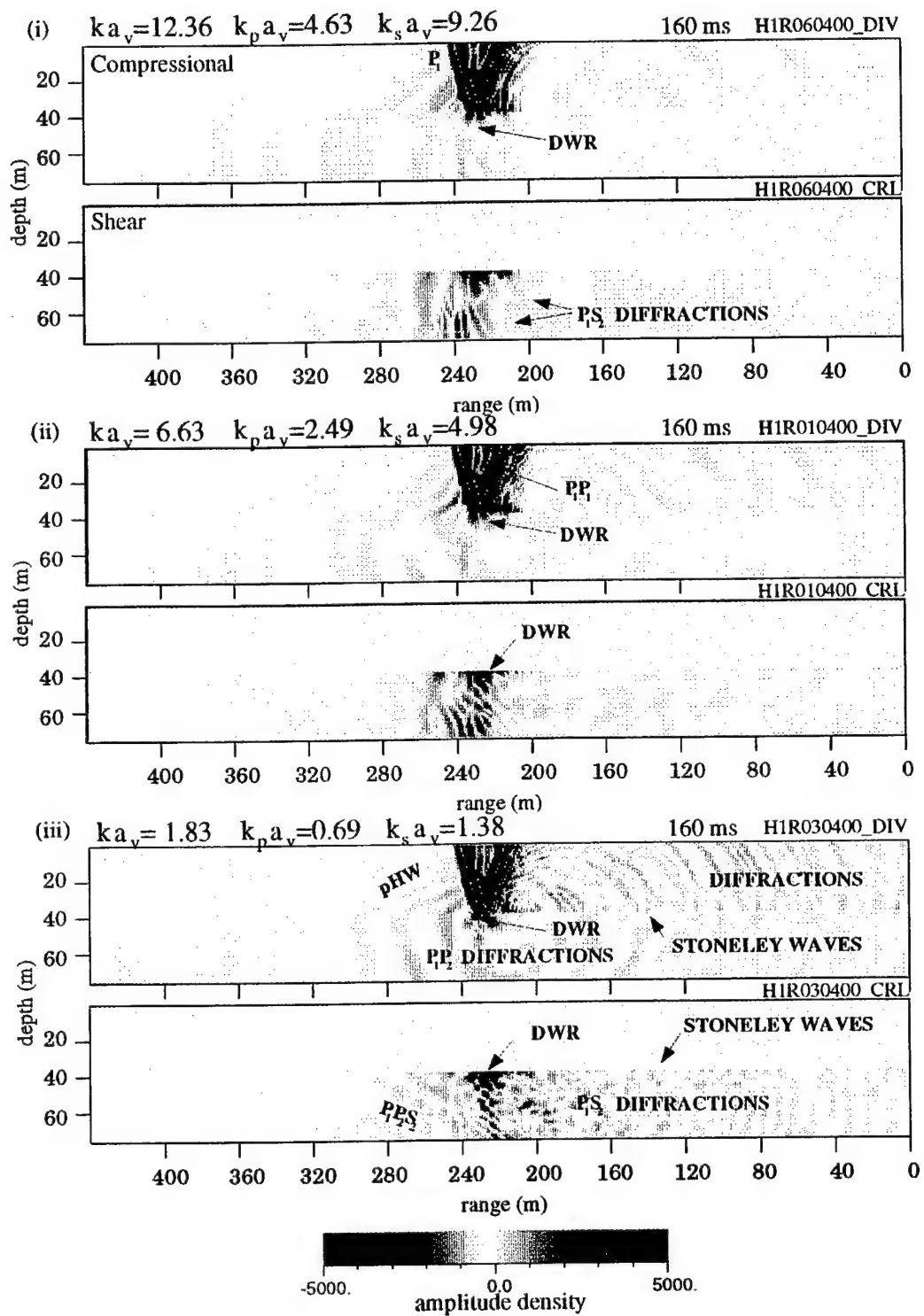


Figure 4-29: (a) Multiple realizations of a flat basalt seafloor with volume heterogeneity defined such that in each case the rms perturbation amplitude is 10% and the correlation length is about $a_v = 4$ m.

Model Realizations with $\sigma_v = 10\%$ Volume Heterogeneity in Basalt

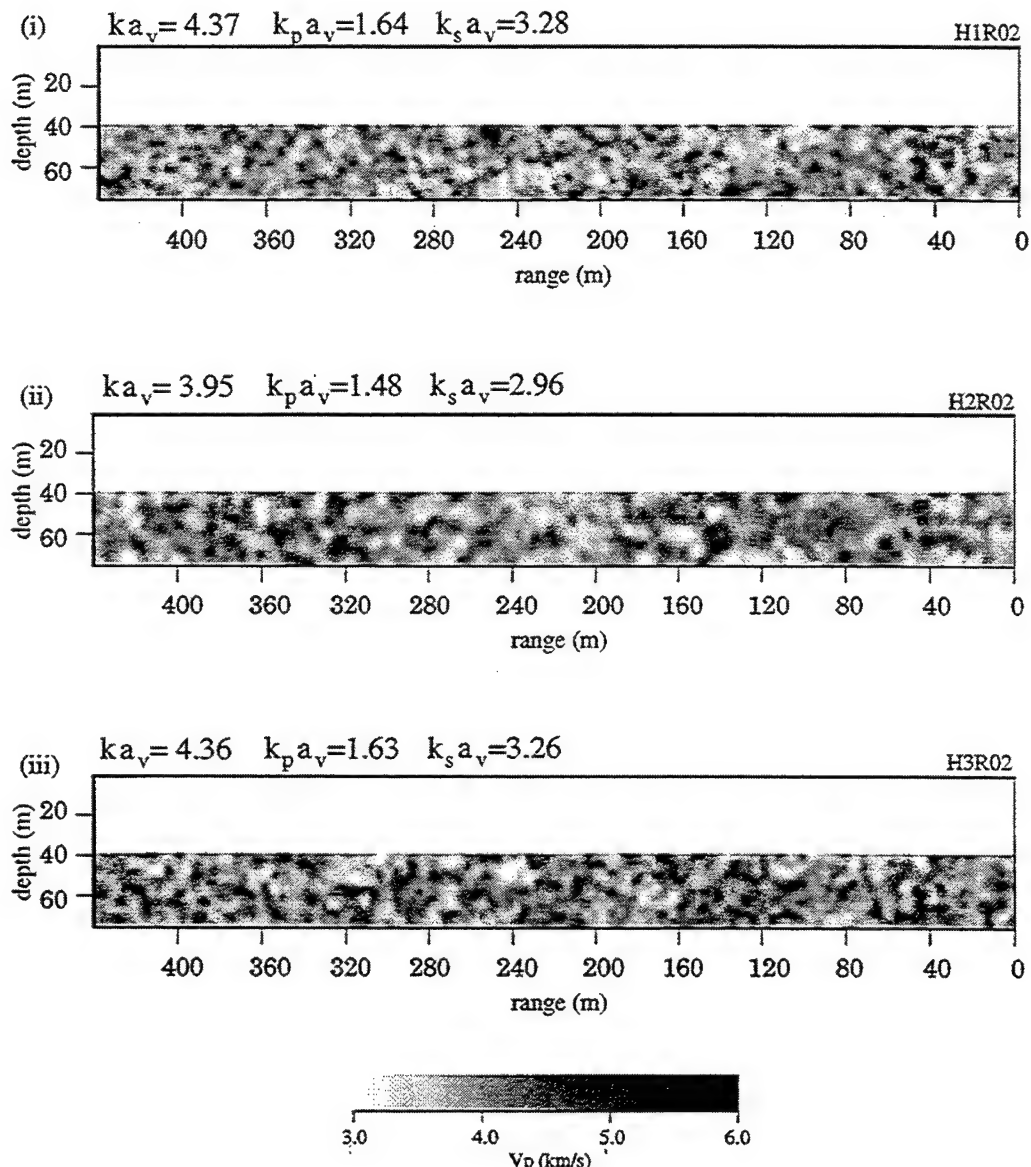


Figure 4-29: (b) At 160 ms the amplitude density distribution for these three realizations differs somewhat in detail but has no distinguishing characteristics.

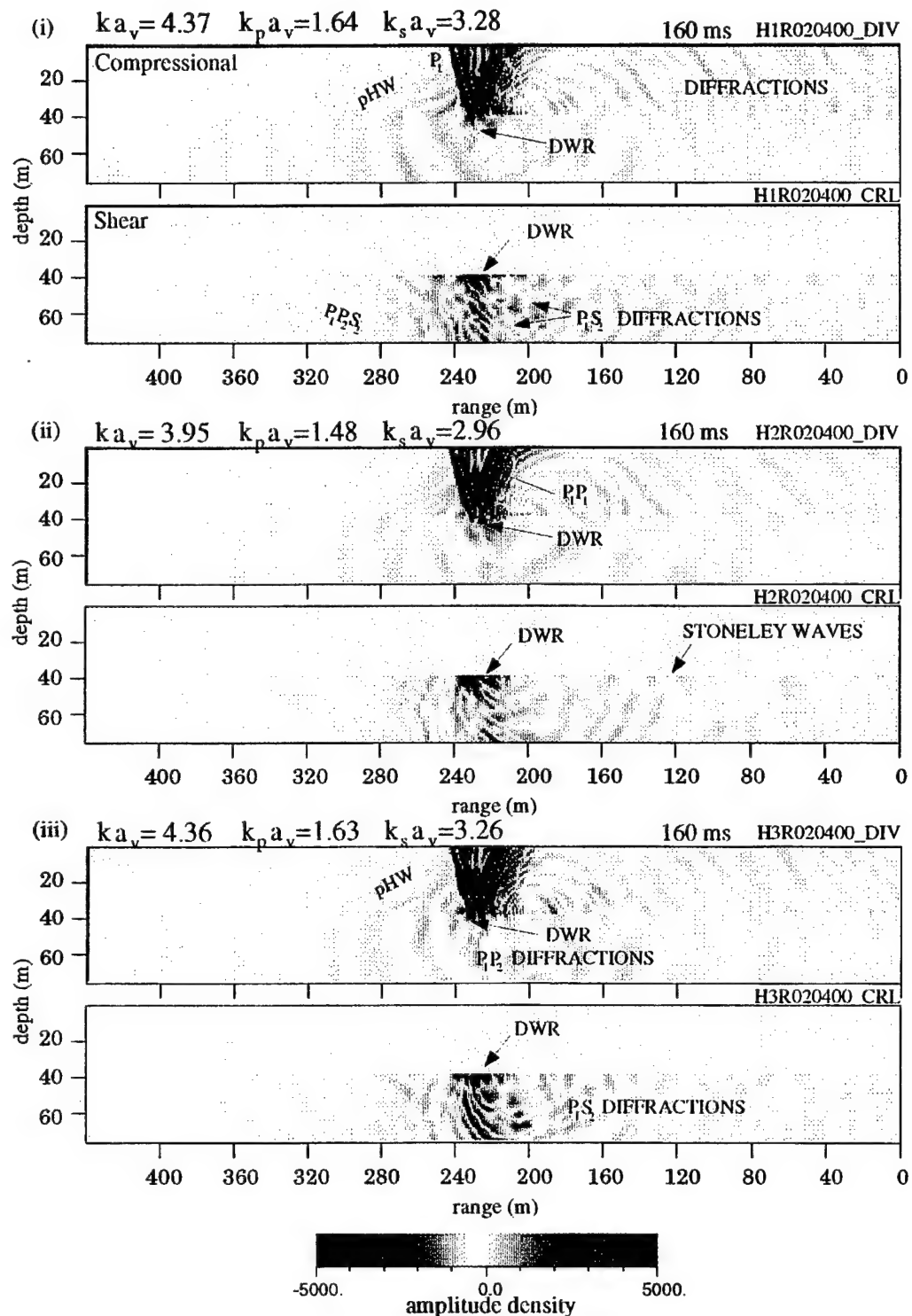
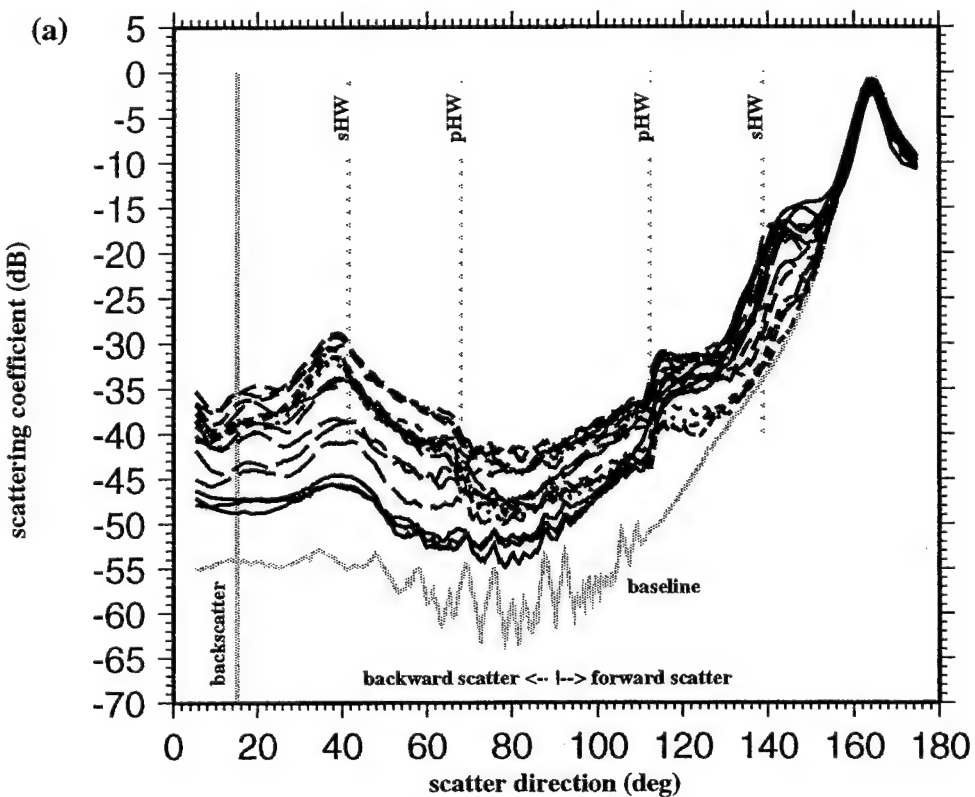


Figure 4-30: (a) Scattering functions are shown for flat-seafloor models with 10% rms perturbation amplitude in velocity and density and different correlation lengths. Three realizations are plotted for each model and realization error is about ± 1 dB. Volume heterogeneity produces relatively strong head waves, similar to the case of seafloor scattering from rough seafloor with small rms heights. The coefficients in the backscatter directions are generally much smaller than the scattering coefficients observed in seafloor scattering (compare with Fig. 4-9(a)). In the plot, solid black is $k_p a_v = 4.63$; long dash green, $k_p a_v = 2.49$; long dash red, $k_p a_v = 1.64$; medium dash black, $k_p a_v = 0.69$; short blue dash, $k_p a_v = 0.31$.

(b) The scattering coefficient in the 15° backscatter direction has a maximum as predicted when $k_p a \approx 1$. The sensitivity to correlation length is very similar to that of rough seafloor scattering (compare with Fig. 4-9(b)).

10% Volume Heterogeneity: Vary a_v (volume)



Scattering at 15°

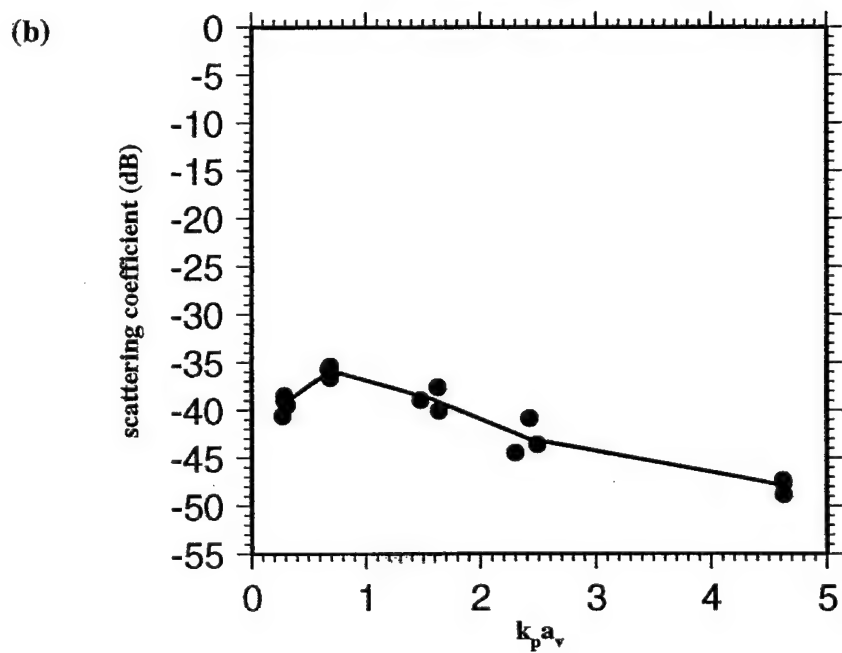


Figure 4-31: (a) Flat-seafloor models with subseafloor volume heterogeneity having rms perturbation amplitude of 50% and correlation lengths (i) $a_v = 11.8$ m, (ii) $a_v = 6.3$ m, and (iii) $a_v = 1.7$ m. Average velocity and density of the subseafloor are that of the basalt-bottom model. A 50% rms perturbation amplitude can be considered an upper limit to realistic geological variation. In this display of the models it is very clear that the original flat seafloor is transformed by the velocity variation into what is effectively a rough seafloor as the lower velocities in the basement approach the water velocity.

Models with $\sigma_v = 50\%$ Volume Heterogeneity in Basalt

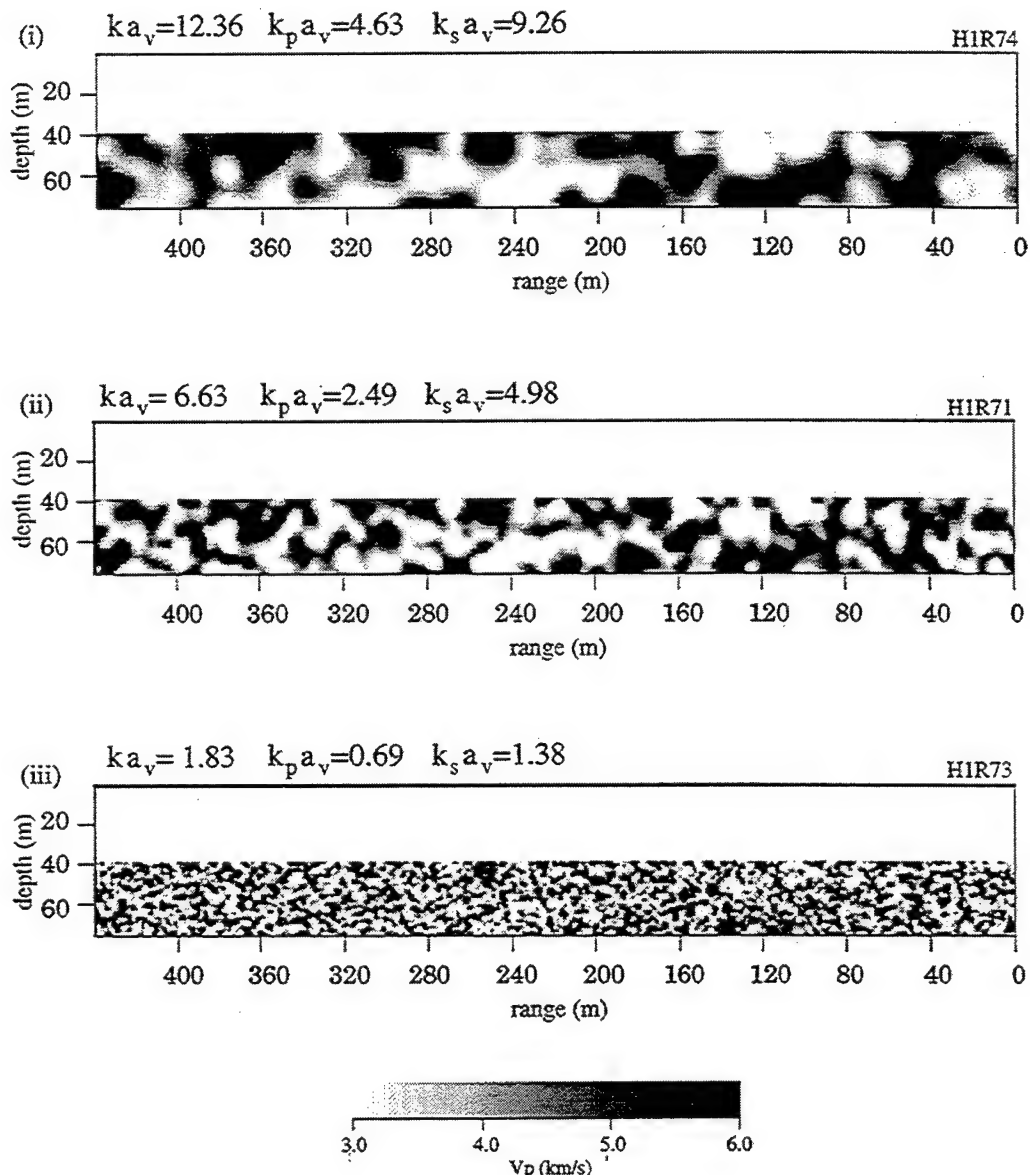


Figure 4-31: (b) Models with high perturbation amplitude show strong diffraction into the water column at levels comparable to seafloor scattering. The discrete diffraction events observed in the water column suggest that most of the scattering is, in fact, originating at the seafloor. This leads to the conclusion that the heterogeneity is interacting with the wavefield as would a rough surface. In spite of the high intensity levels of volume scattering in the deeper subseafloor, very little of this energy is returning to the seafloor above.

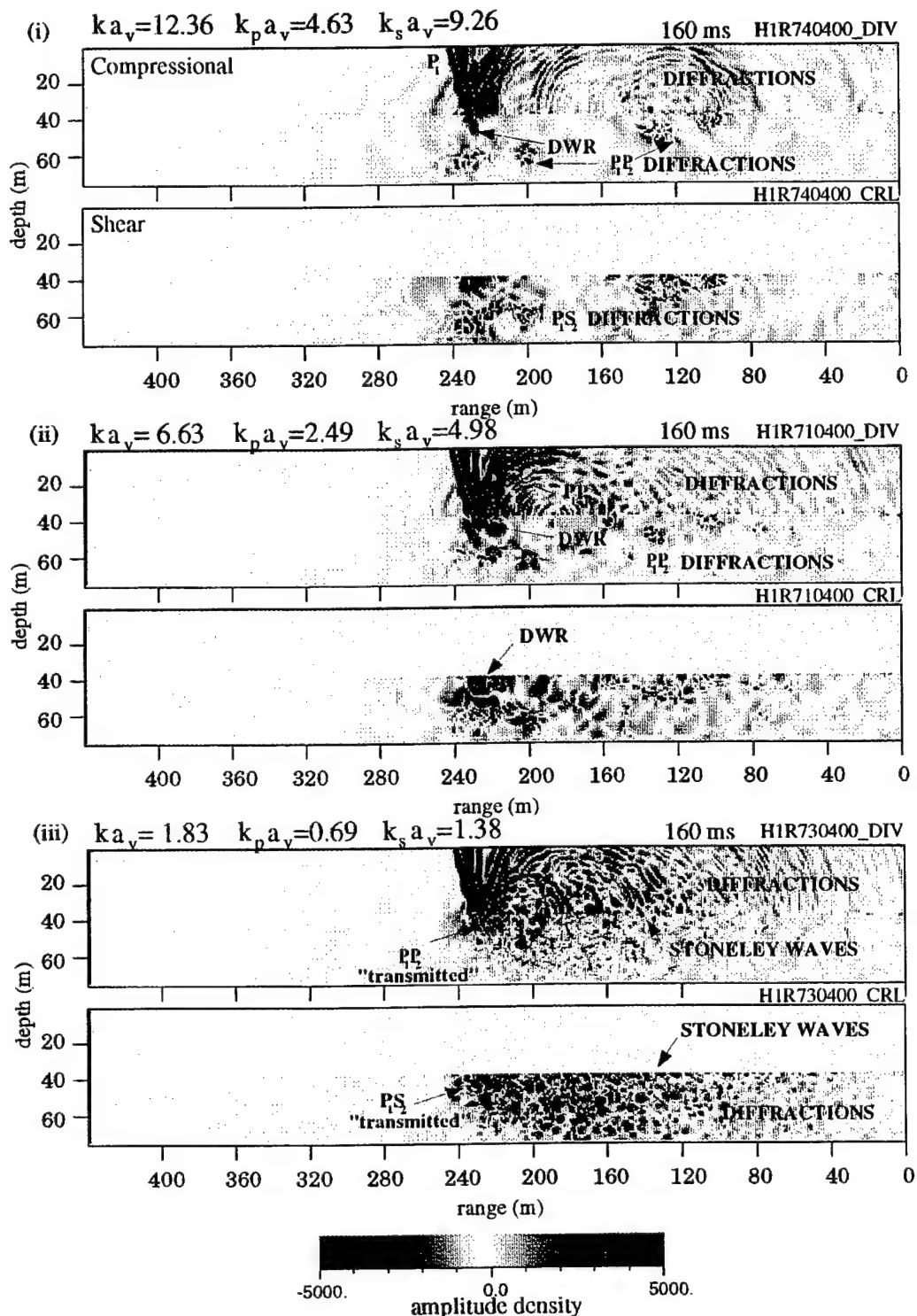
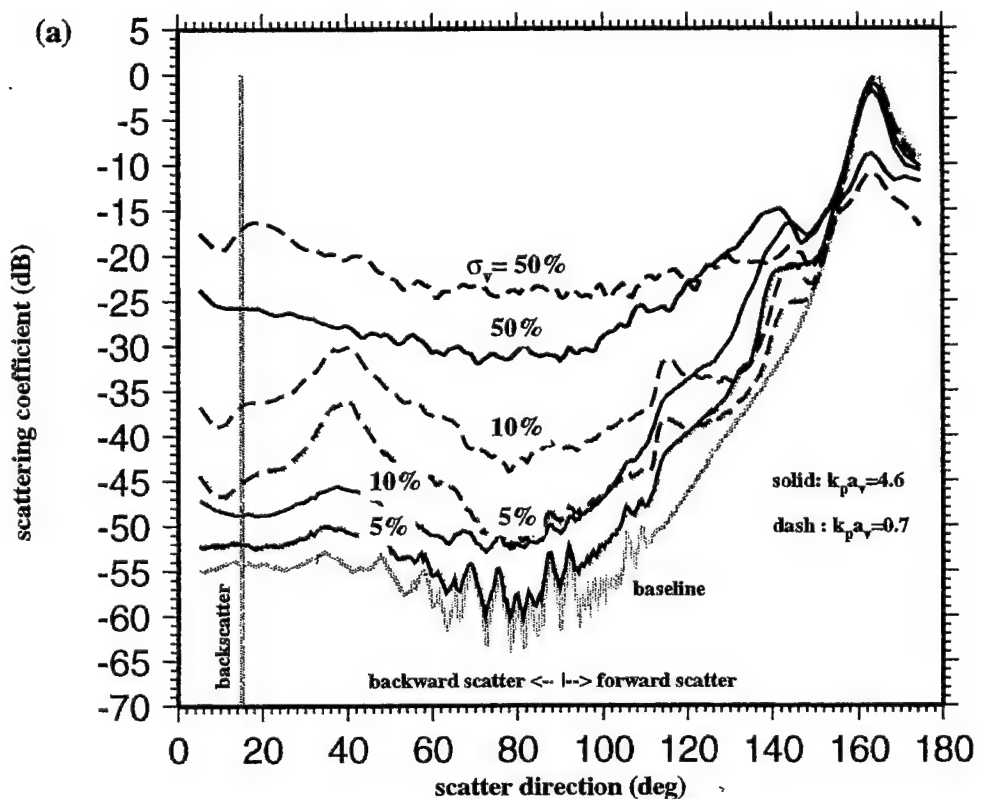


Figure 4-32: Scattering functions for flat-seafloor models with different perturbation amplitude in velocity and density. (a) The amplitude of the scattering function increases as the rms perturbation amplitude increases. This figure compares the scattering coefficients for the flat-seafloor models with volume heterogeneity having $\sigma_v = 5\%$ (green), 10% (red), and 50% (blue) for two different volume correlation lengths.

(b) The sensitivity to correlation length of the volume heterogeneity remains about the same as the rms perturbation amplitude varies. The sensitivity to variation in the perturbation amplitude is quite strong, but only very high rms perturbation produces signal levels in the -10 to -20 dB range that is typical of seafloor scattering in the previous modeling.

Vary Volume Heterogeneity: σ_v



Scattering at 15°

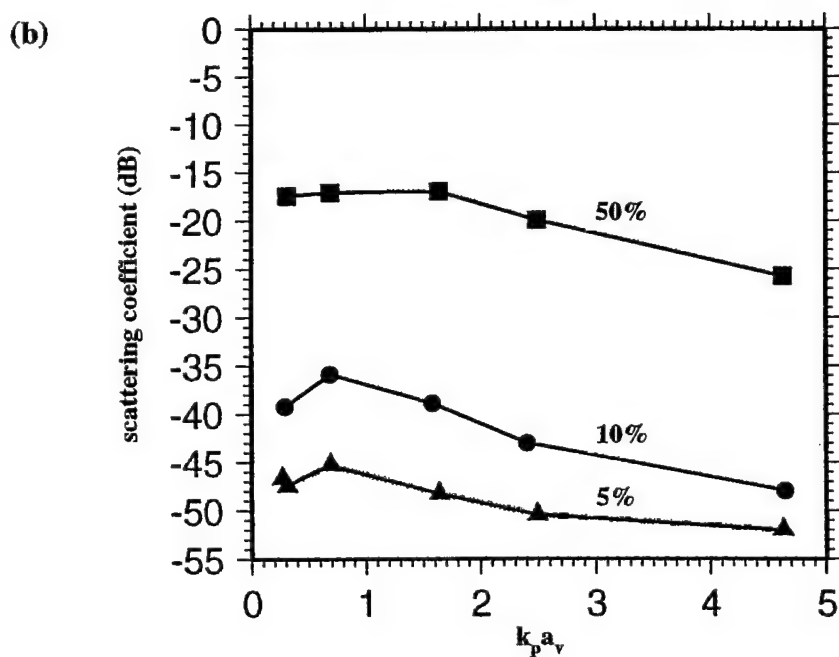


Figure 4-33: (a) These models combine seafloor roughness with volume heterogeneity. They differ only in the rms perturbation amplitude of the volume heterogeneity. The seafloor is the same as the Gaussian seafloor model in Fig. 4-3(a). Both models have average subseafloor properties equal to the basalt-bottom model.

Rough Seafloor with Volume Heterogeneity in Basalt

Seafloor $ka = 6$ $k\sigma = 4$

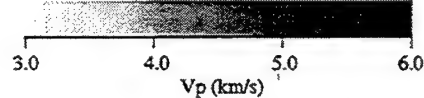
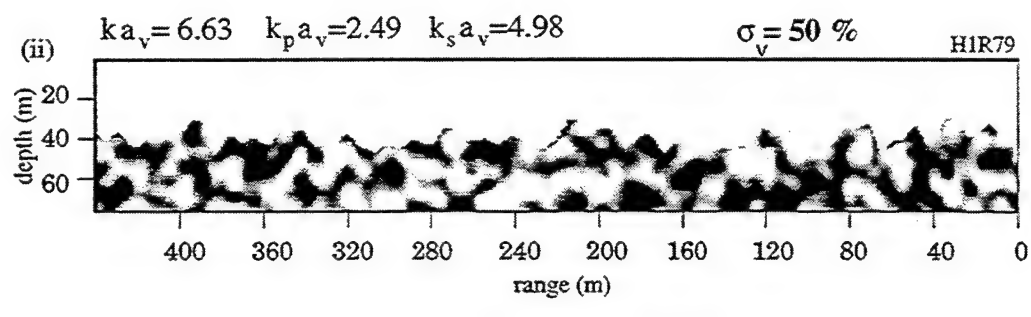
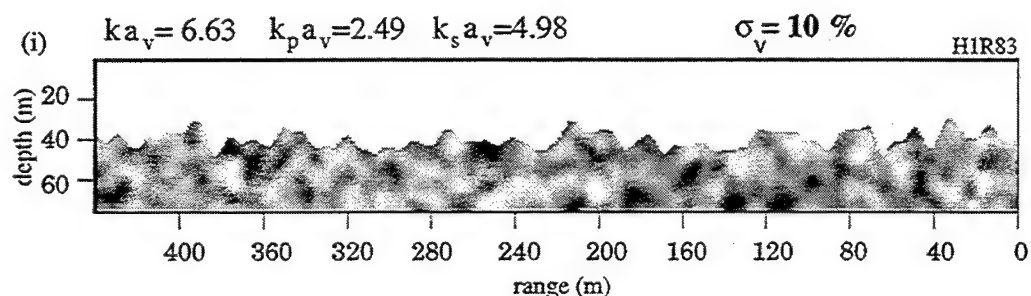


Figure 4-33: (b) Even though the models in Fig. 4-33(a) produce very different subseafloor scattering, the scattering observed in the water column is very similar in both cases. These schlieren diagrams should be compared to the scattering from the same seafloor with a homogeneous subseafloor shown in Fig. 4-12(a). Both homogeneous and heterogeneous models produce very similar scattered fields in the water column.

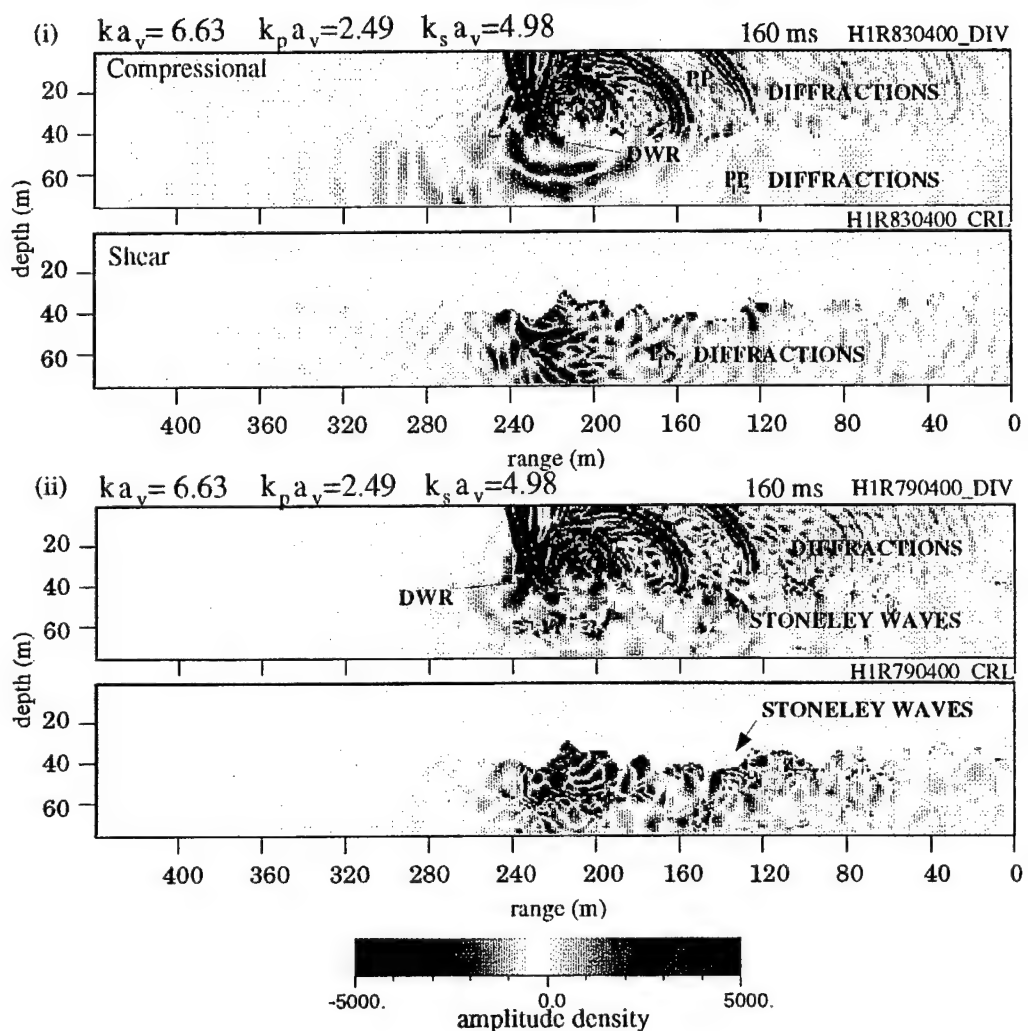


Figure 4-34: The scattering functions calculated for rough, basaltic seafloor with heterogeneous subseafloor differ very little from the same seafloor with homogeneous subseafloor. This is true even in the case of very high rms perturbation amplitude. The solid line is the scattering function of rough seafloor with a homogeneous subseafloor. The upper long-dash line is the same rough seafloor with volume heterogeneity having 10% rms perturbation amplitude. The short-dash line is the same rough seafloor with volume heterogeneity having 50% rms perturbation amplitude.

Volume Heterogeneity and Surface Roughness

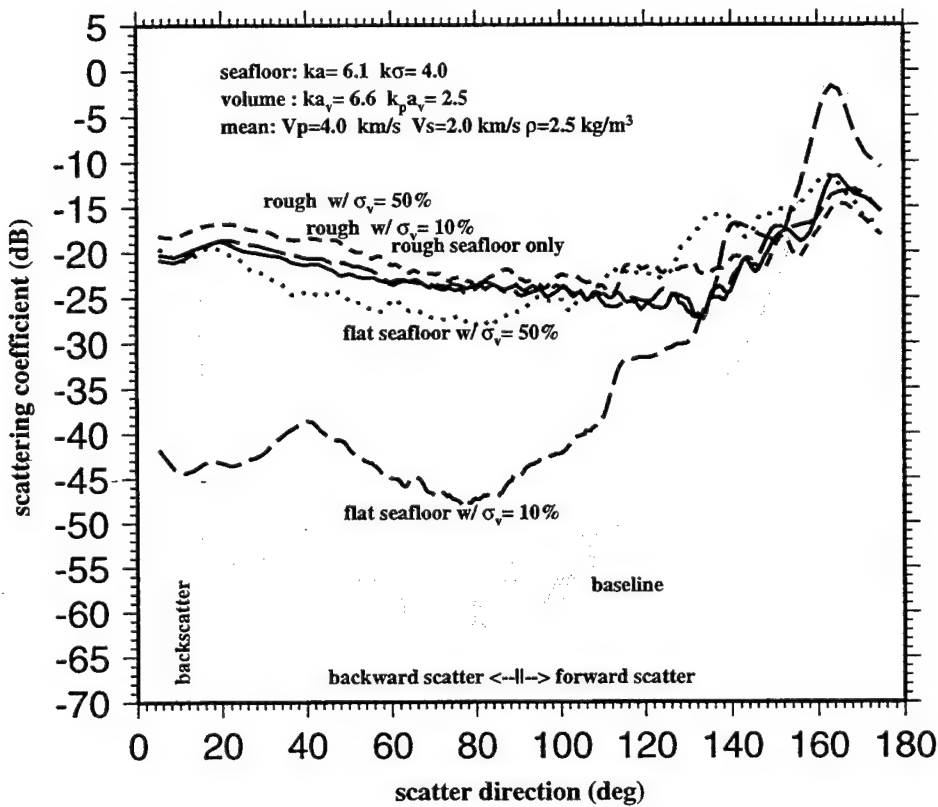


Figure 4-35: (a) Seafloor models computed with 45° large-scale slope, volume heterogeneity and with and without wavelength-scale roughness. Both of the models have 10% rms perturbation amplitude and average velocity and density of a basalt bottom. The seafloor roughness in (ii) has correlation length of $ka = 6.1$ and $k\sigma = 3.7$.

Sloping Seafloor with $\sigma_v = 10\%$ Volume Heterogeneity in Basalt

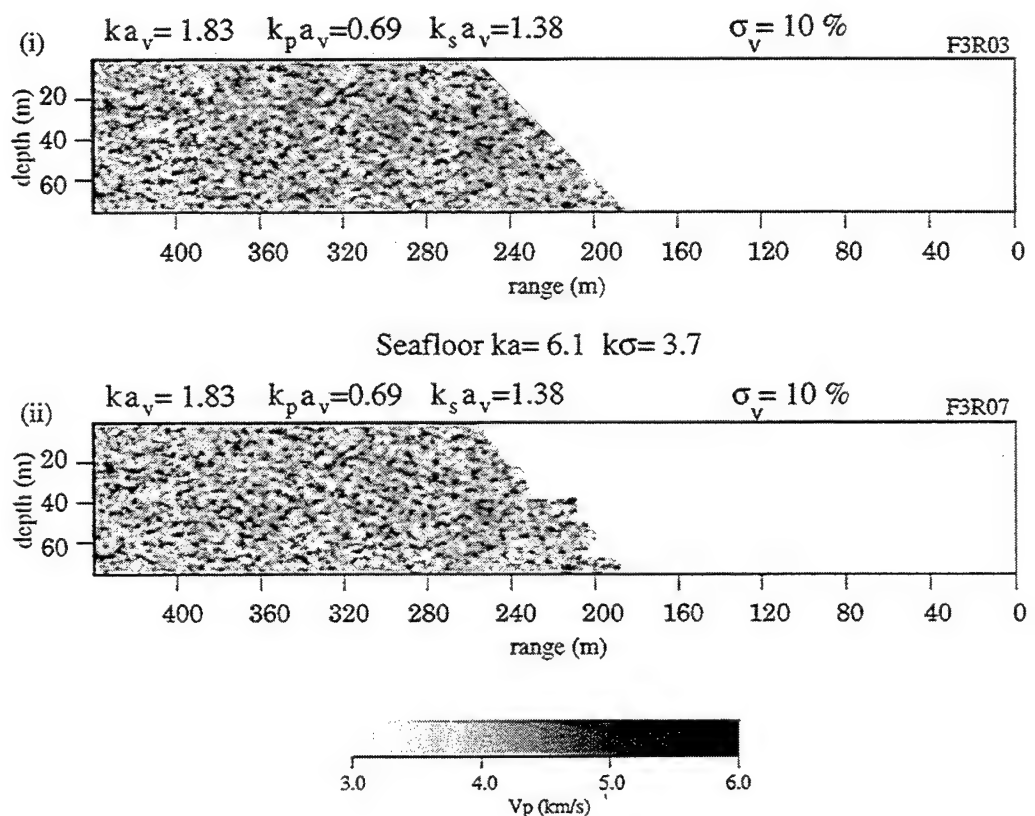


Figure 4-35: (b) The scattering from the heterogeneous subseafloor models in Fig. 4-35(a) should be compared to the scattering from the smooth sloping seafloor (Fig. 4-16b(ii)) and the rough sloping seafloor (Fig. 4-18c(ii)) with homogeneous subseafloor. Scattering in the water column is clearly stronger for a smooth, sloping seafloor with heterogeneous subseafloor (i) than for the homogeneous case (Fig. 4-16b(ii)). Scattering from the rough, sloping seafloor with subseafloor heterogeneity appears to be comparable to scattering from the same seafloor with a homogeneous subseafloor (Fig. 4-18c(ii)).

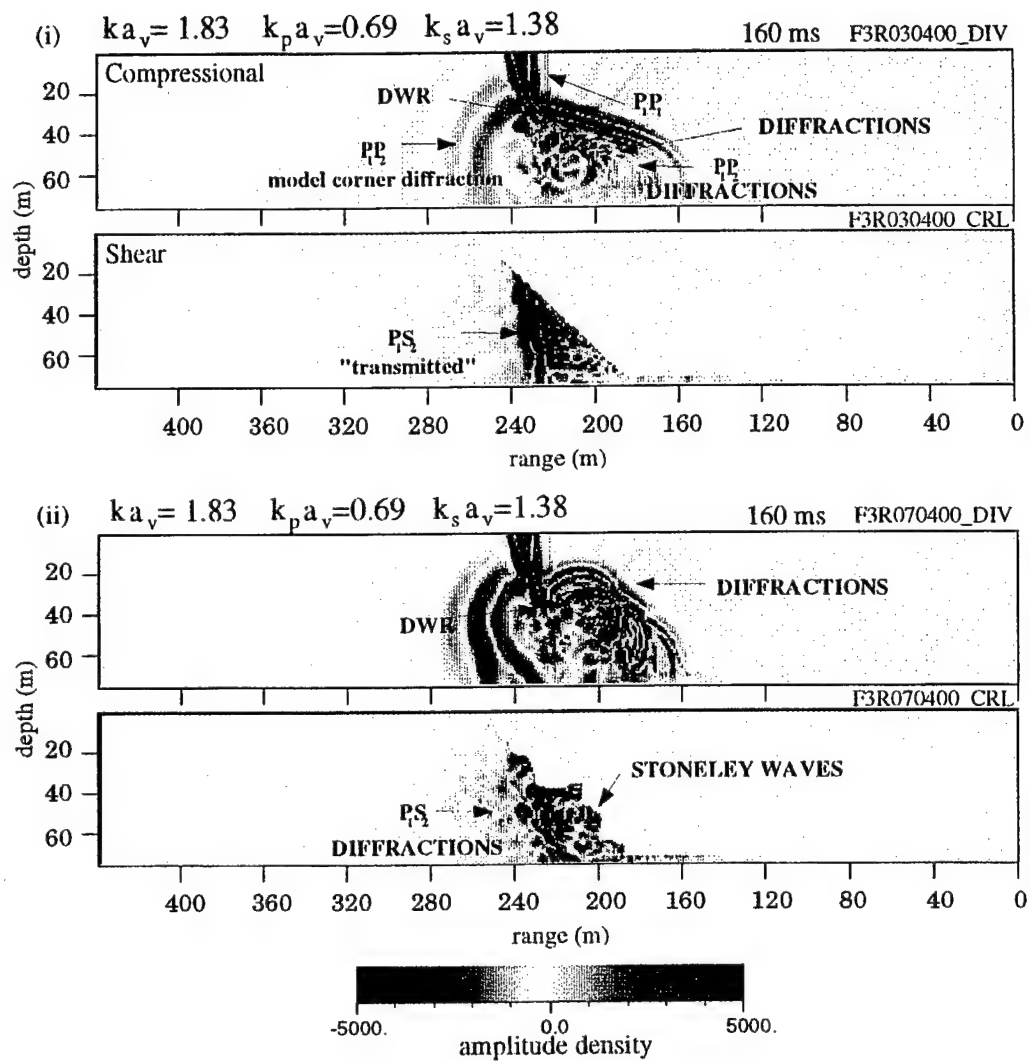


Figure 4-36: Scattering functions of smooth, sloping (45°) basaltic seafloor with volume heterogeneity having different correlation lengths show in (a) that as correlation length decreases the scattering coefficients increase, and in (b), when seafloor roughness (seafloor $ka = 6$ and $k\sigma = 4$) is added to heterogeneous sloping models ($\sigma_v = 10\%$ and $\sigma_v = 50\%$), there is almost no difference between the scattering from a homogeneous (grey line) subseafloor model compared to heterogeneous models.

Volume Heterogeneity and Sloping Seafloor

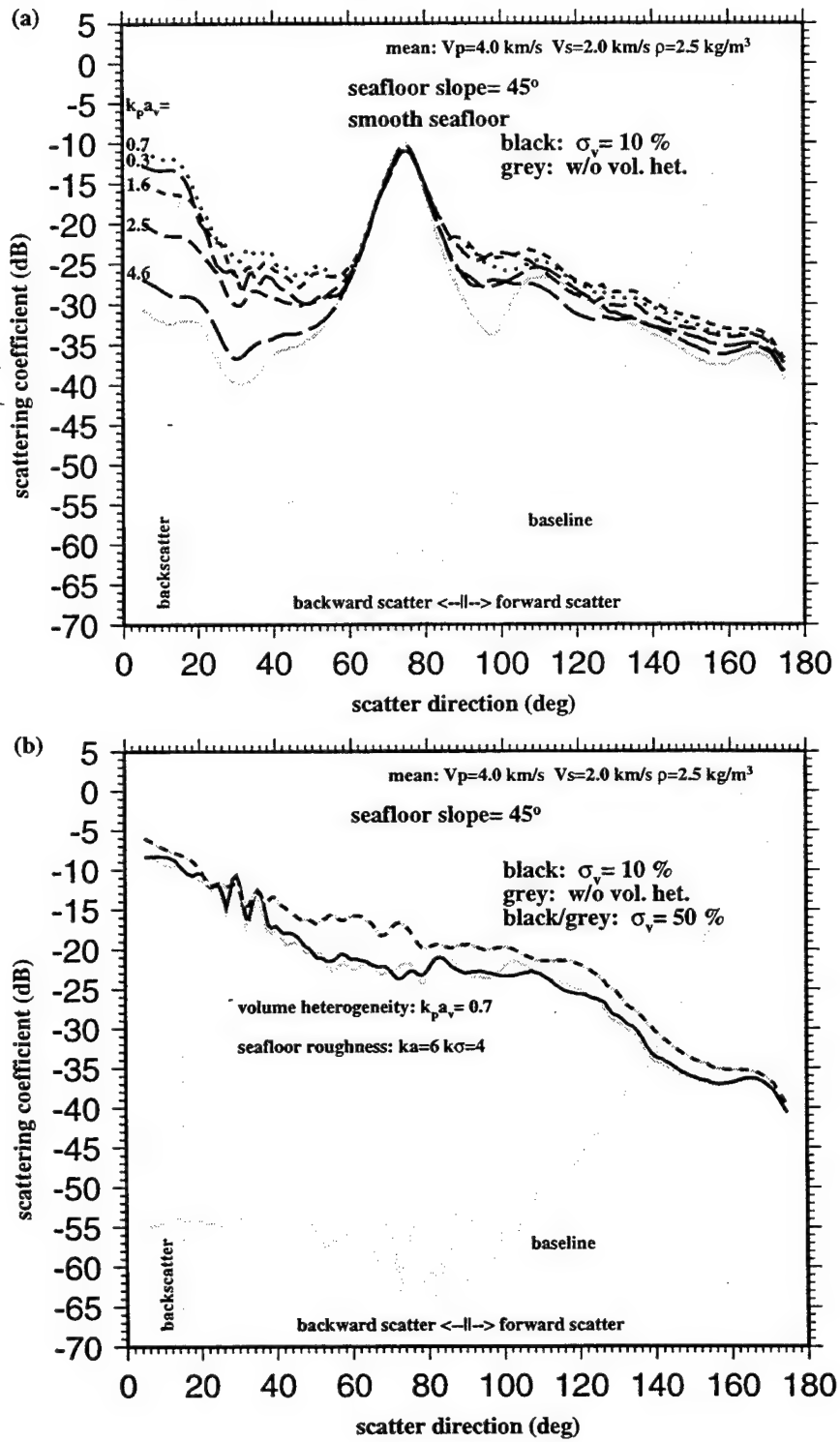


Figure 4-37: Comparisons showing scattering functions for hard (basalt) and soft (sediment) seafloor for different values of σ_v .

- (a) Flat heterogeneous models with either hard (solid lines) or soft (dashed lines) bottom subseafloor mean velocity and density generate comparable scattering functions when the volume heterogeneity is the same. Note that for the hard bottom with $\sigma_v = 10\%$, results from three realizations have been plotted to show that differences between scattering from flat seafloor due to changes in σ_v are within the range of the realization error.
- (b) When seafloor roughness ($ka = 6$ and $k\sigma = 4$) is added to the heterogeneous subseafloor, the difference between homogeneous (dotted lines) and heterogeneous (solid and dashed lines) scattering functions increases as average velocity of the subseafloor model decreases. These scattering functions are for the case of $\sigma_v = 10\%$.

Hard vs. Soft Seabed and Volume Heterogeneity

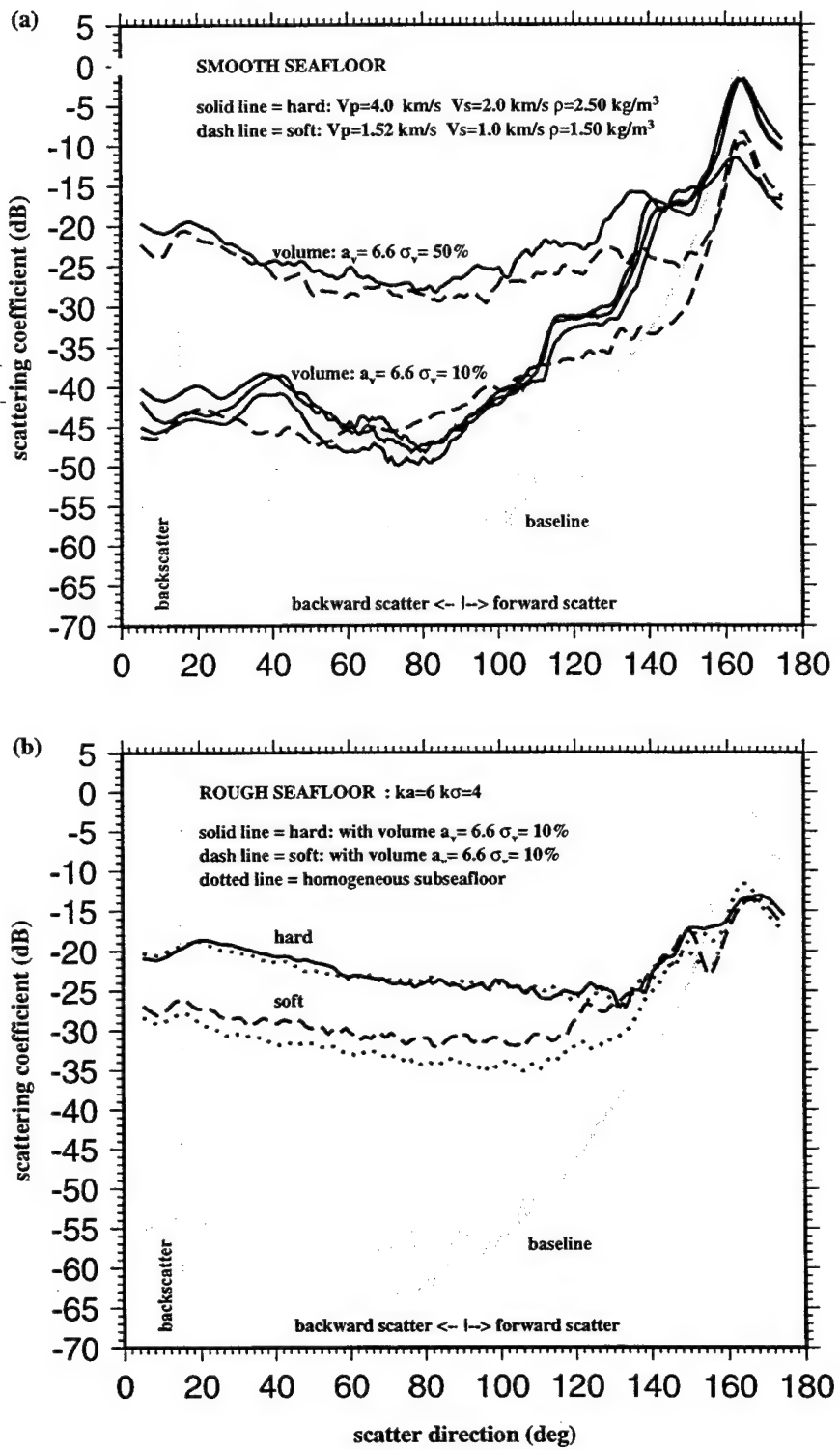


Figure 4-37: (c) The same as Fig. 4-37(b), except that $\sigma_v = 50\%$. Models with talus subseafloor properties are included in this plot for comparison (grey dash line). At this high level of perturbation amplitude in the heterogeneity, both talus and sediment bottoms produce substantially different scattering coefficients than the same rough seafloor with a homogeneous bottom.

(d) If seafloor slope is also added, the difference increases further. However, it may not be realistic to have a soft bottom (sediment) with such high slope.

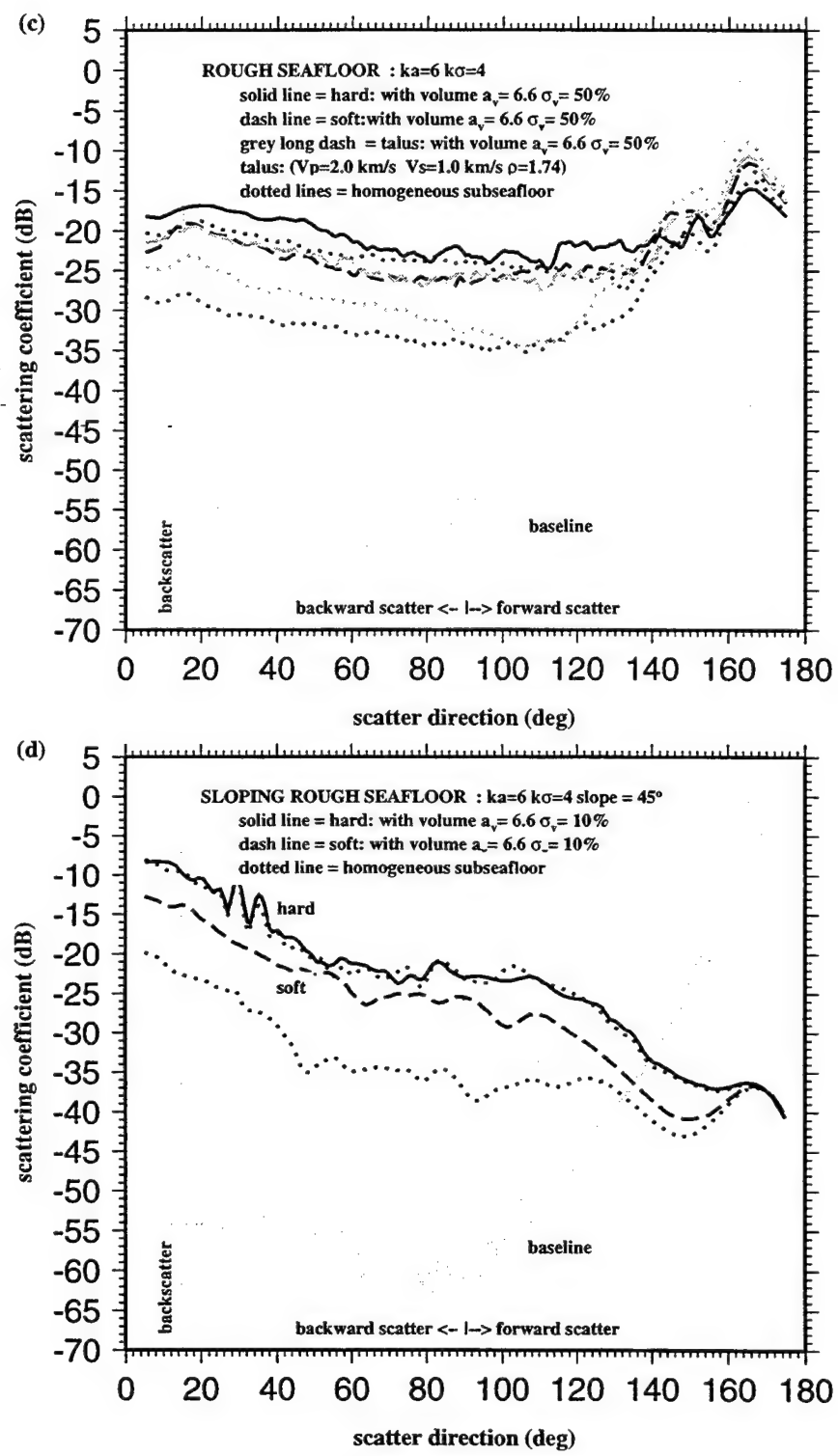


Figure 4-37: (e) For the horizontal, rough-seafloor models, where $ka = 6$ and $k\sigma = 4$, there is little sensitivity of the backscatter signal to variation in mean subseafloor velocity (and density). At $\sigma_v = 10\%$, the sensitivity is the same as that of the homogeneous model. When $\sigma_v = 50\%$, there is almost no sensitivity to velocity.

(f) The backscatter signal is most sensitive to the rms perturbation amplitude of the heterogeneity for rough surface models when the subseafloor velocity is very low. However, for a flat seafloor model with heterogeneity, the sensitivity to perturbation amplitude for the hard-bottom model (Fig. 4-32) was shown to be quite strong. The lack of sensitivity to volume heterogeneity, once seafloor roughness is added to the model, suggests that scattering effects of volume heterogeneity cannot be distinguished from surface scattering.

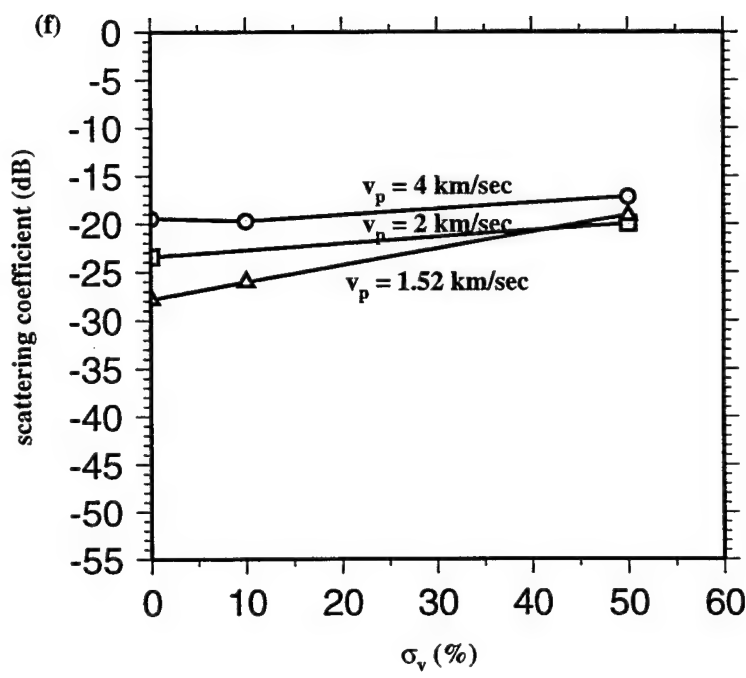
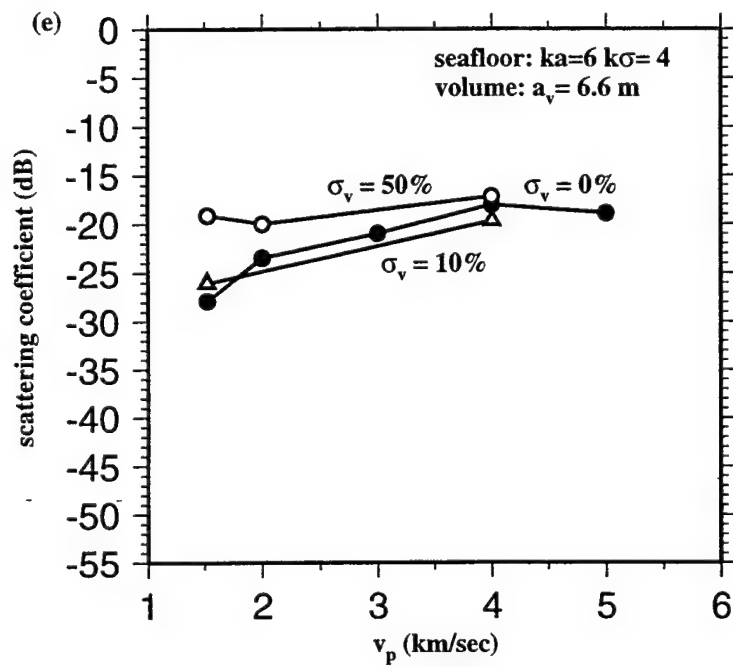
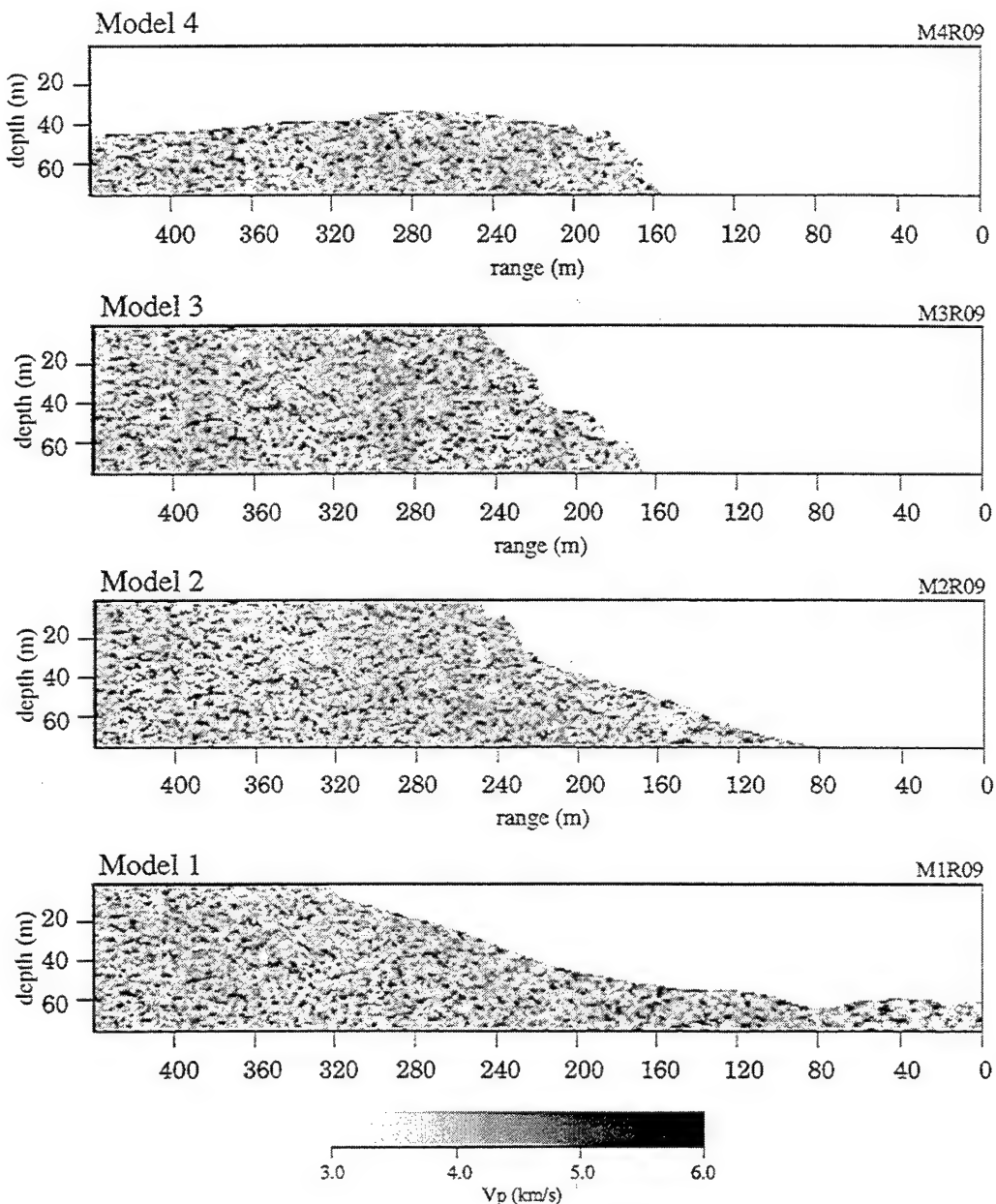


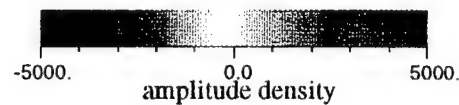
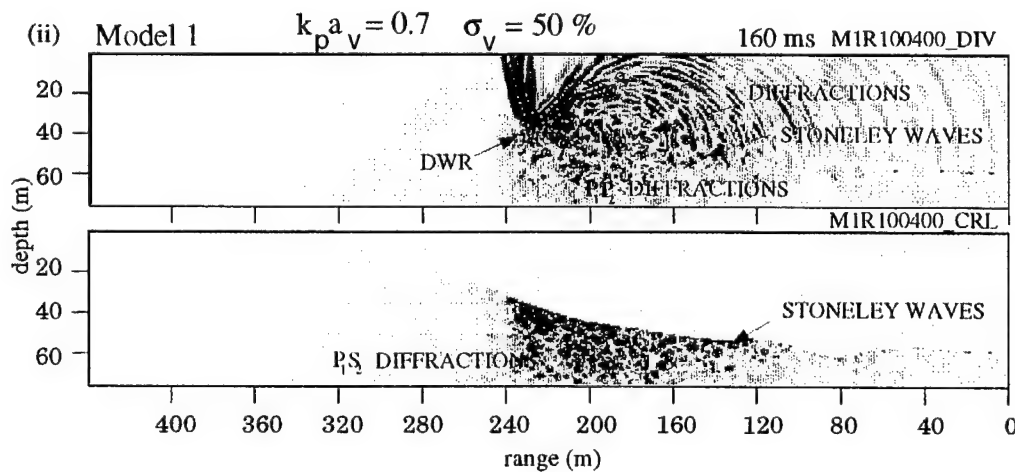
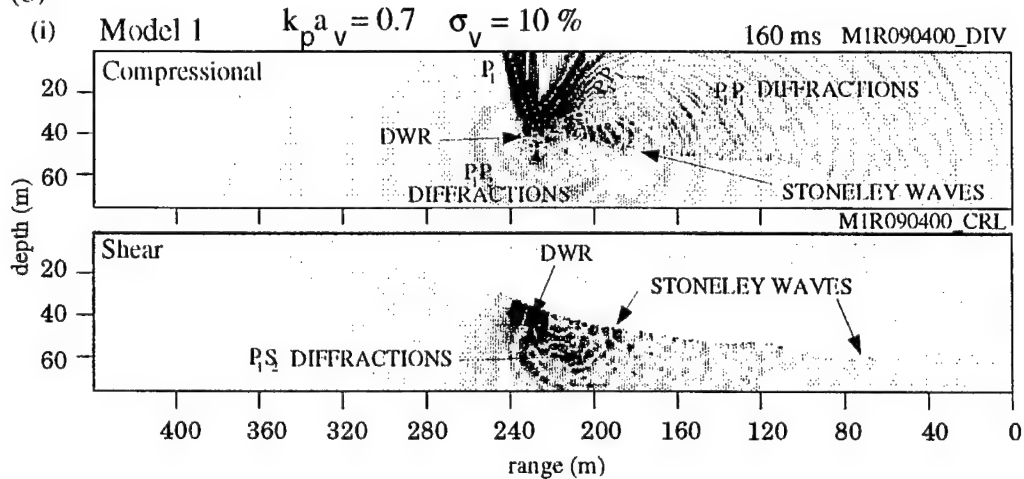
Figure 4-38: (a) The realistic seafloor models with volume heterogeneity having $\sigma_v = 10\%$ and correlation length $a_v = 1.7$ m. Average subseafloor velocity and density are that of the basalt-bottom seafloor.

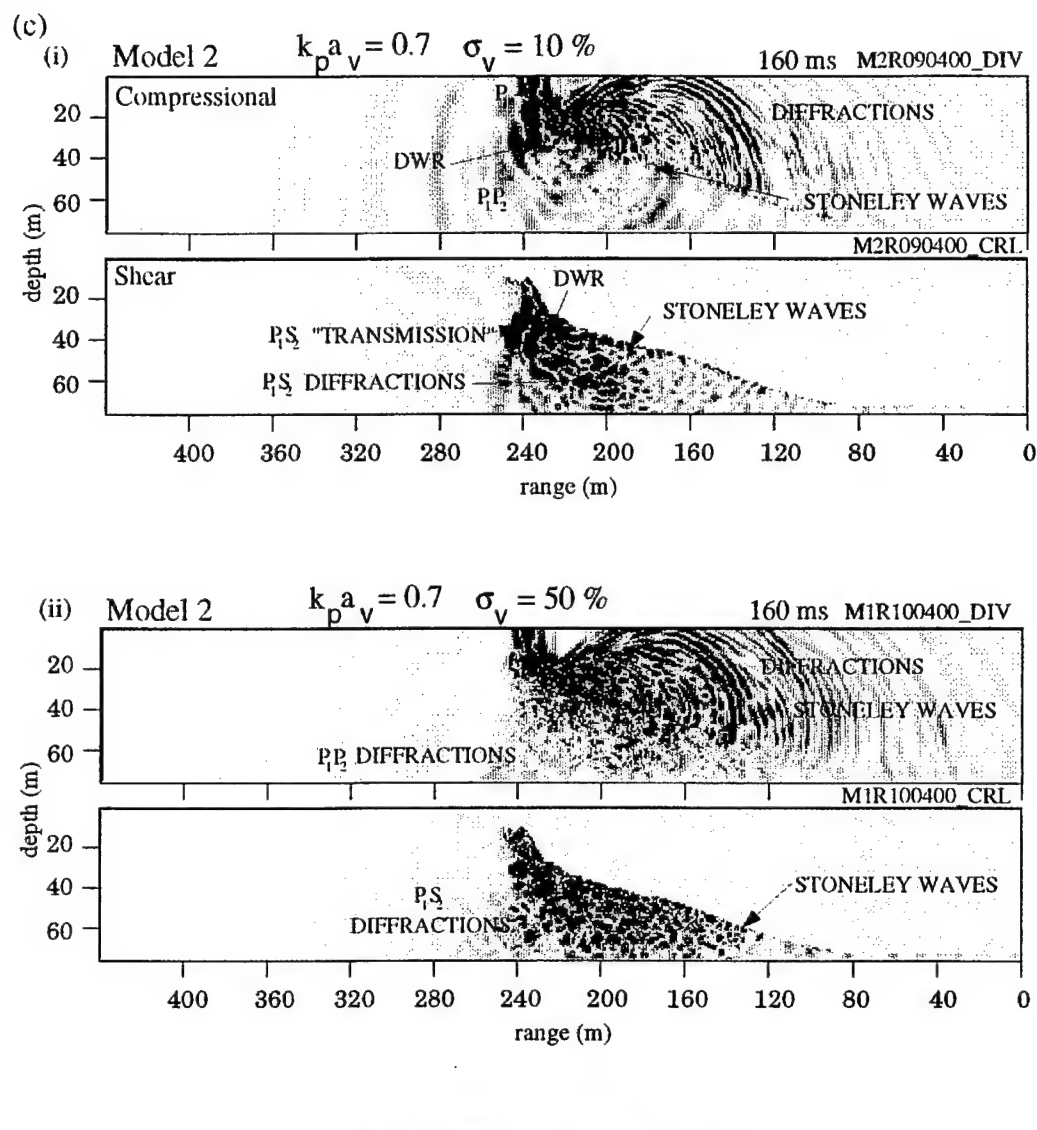
(b-e) Scattering from the models in (a) with $\sigma_v = 10\%$ and also for models with $\sigma_v = 50\%$. The schlieren diagrams shown here should also be compared to the corresponding schlieren diagrams for homogeneous hard-bottom models in Fig. 4-25. The scattering from Model 1, in (b), is the most significantly affected by the addition of volume heterogeneity to the model, in particular when $\sigma_v = 50\%$. In all of the models the continuity of subseafloor body waves is disrupted by volume scattering, but the scattered field in the water column differs primarily in the increase in the number of low-amplitude events.

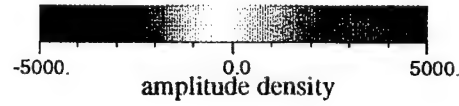
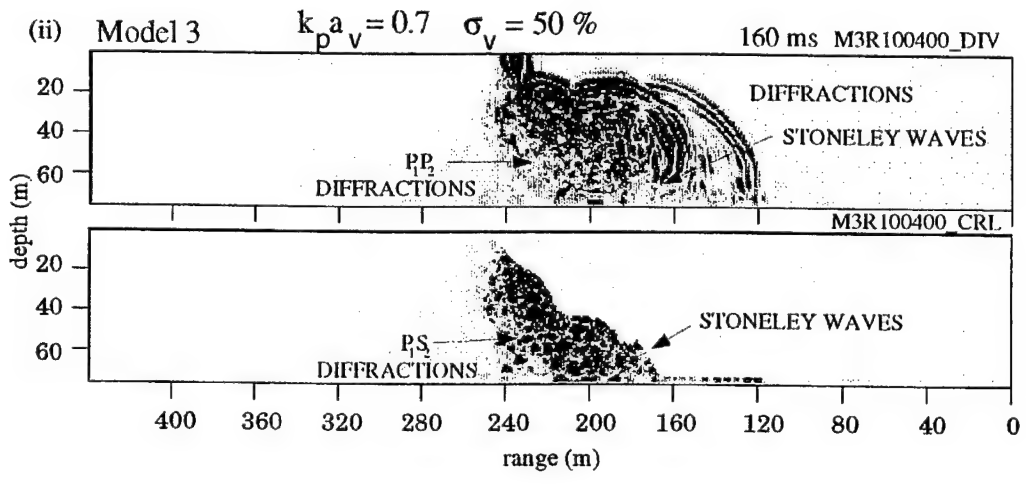
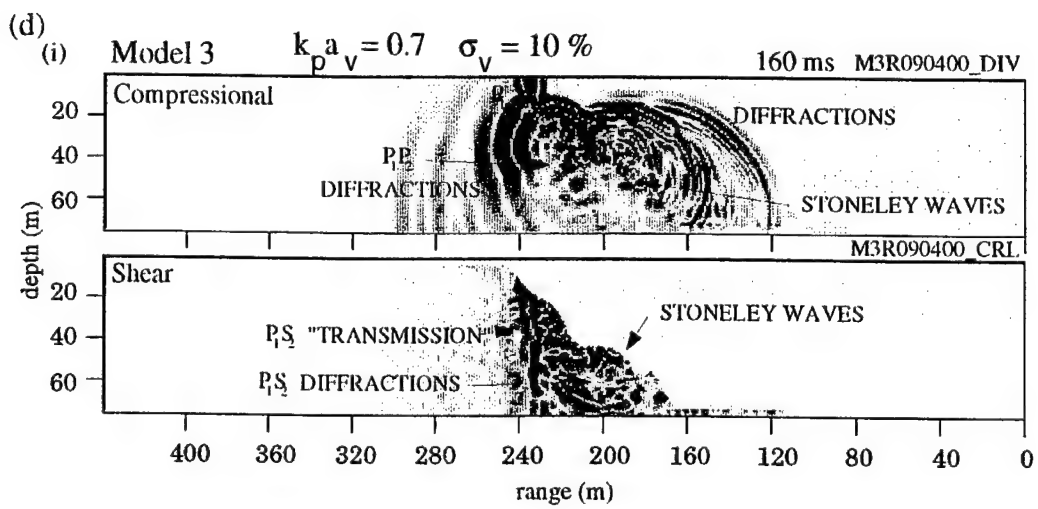
(a) Realistic Seafloor Models with $\sigma_v = 10\%$ Volume Heterogeneity in Basalt



(b)







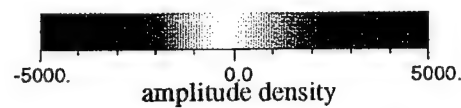
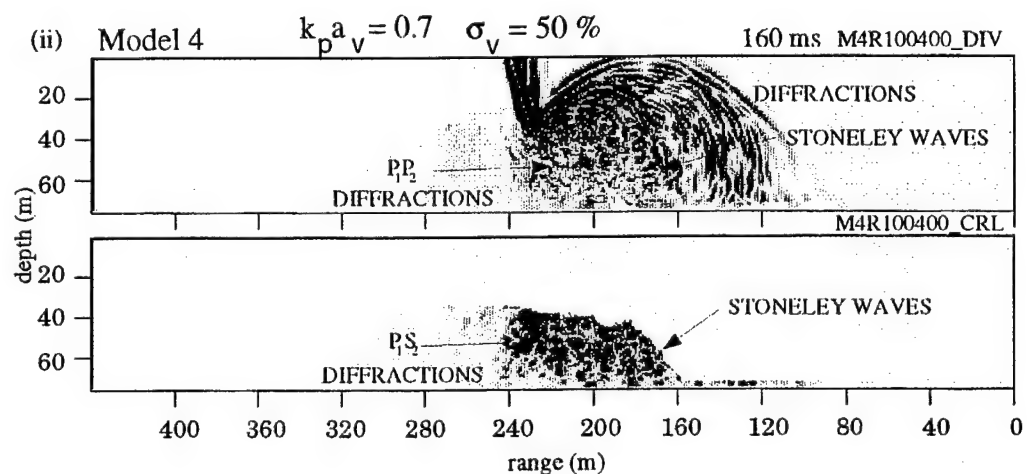
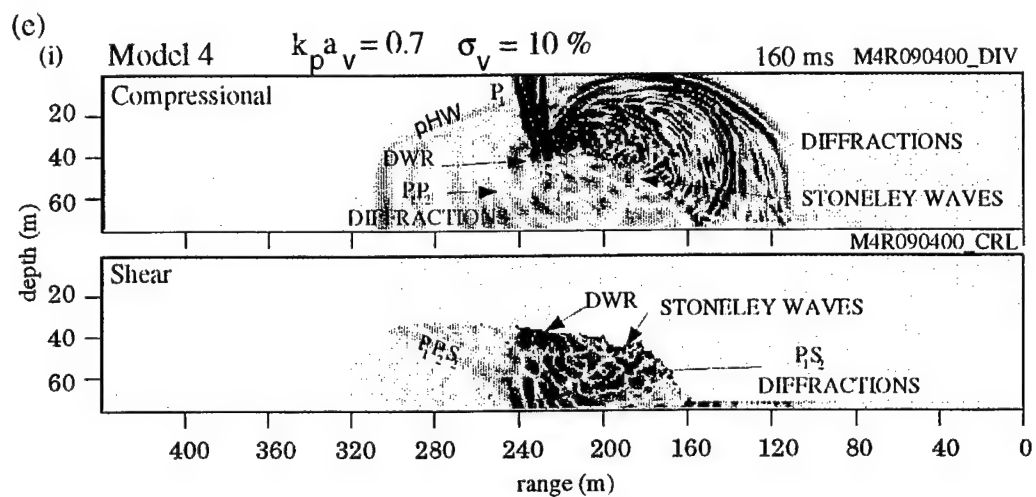


Figure 4-39: These plots show the comparison of scattering functions for Models 1-4 with homogeneous vs. 10% and 50% rms perturbation in velocity and density volume heterogeneity. In both figures the scattering functions of Model 1 are plotted as solid lines, Model 2 as long-dashed lines, Model 3 as short-dashed lines and Model 4 as dotted lines. The black lines correspond to each model computed with volume heterogeneity and the grey lines correspond to the models computed with homogeneous subseafloor. (a) When $\sigma_v = 10\%$, the scattering functions are comparable (within a few dB) to the corresponding functions for homogeneous models. Model 1 shows the largest difference which, in the backscattering direction, is 4 dB.

(b) When $\sigma_v = 50\%$, Models 2 and 3 still have approximately the same backscatter response for both homogeneous and heterogeneous subseafloor. However, Models 1 and 4 show more substantial differences. In the backscatter direction for Model 1, the scattering coefficient is about 14 dB greater than its corresponding homogeneous model. For Model 4 it has increased by about 6 dB. Both of these changes in response are within the range of variation that could be explained by variation in seafloor roughness. For the relatively smooth seafloors of Models 1 and 4, the effect of the volume heterogeneity is to produce a (velocity and density) surface that is much rougher than the actual seafloor. The same roughness in velocity and density occurs in Models 2 and 3; however, the effect on the scattered field in the water column cannot be distinguished from the effect of the actual seafloor roughness of these two models.

Models 1-4

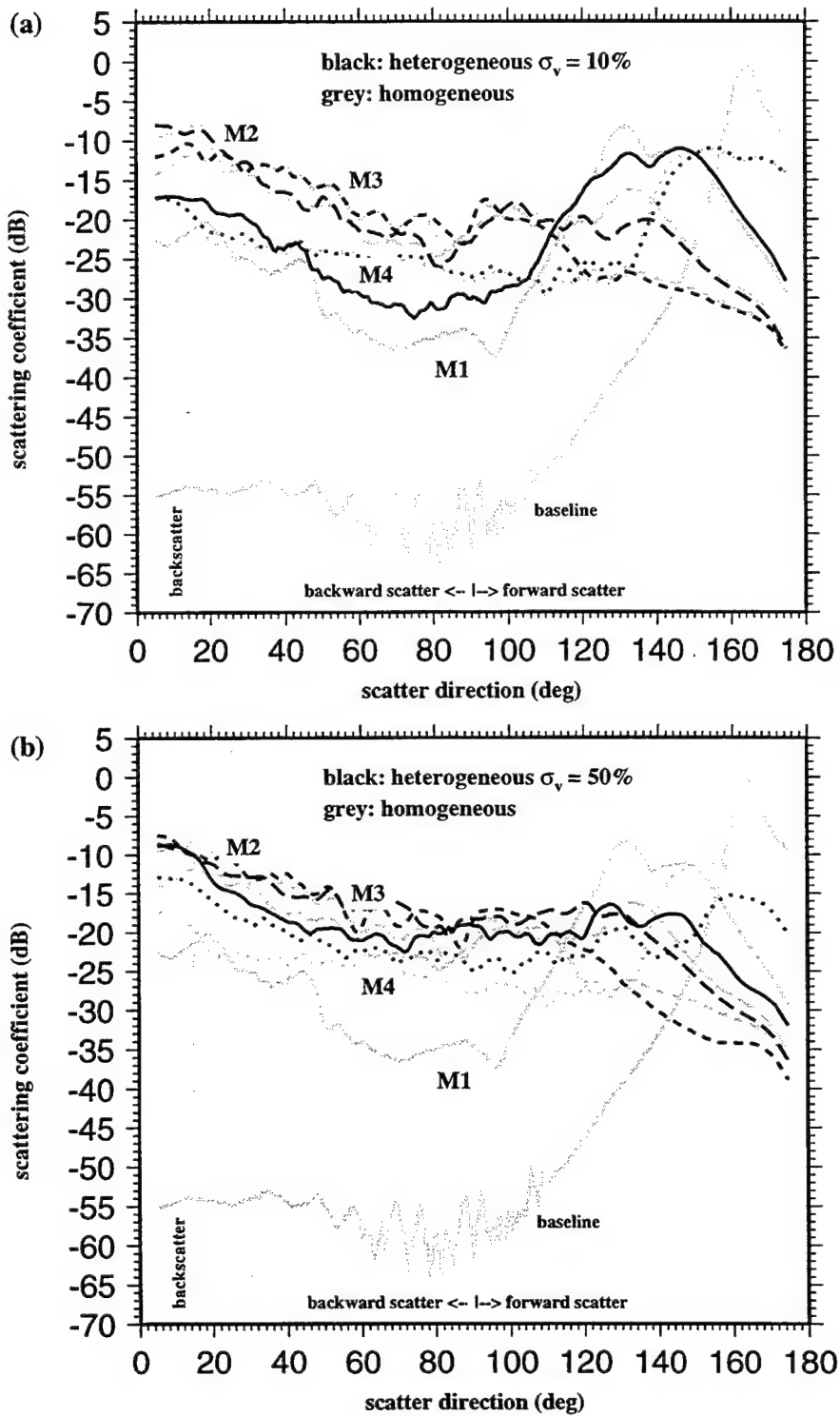
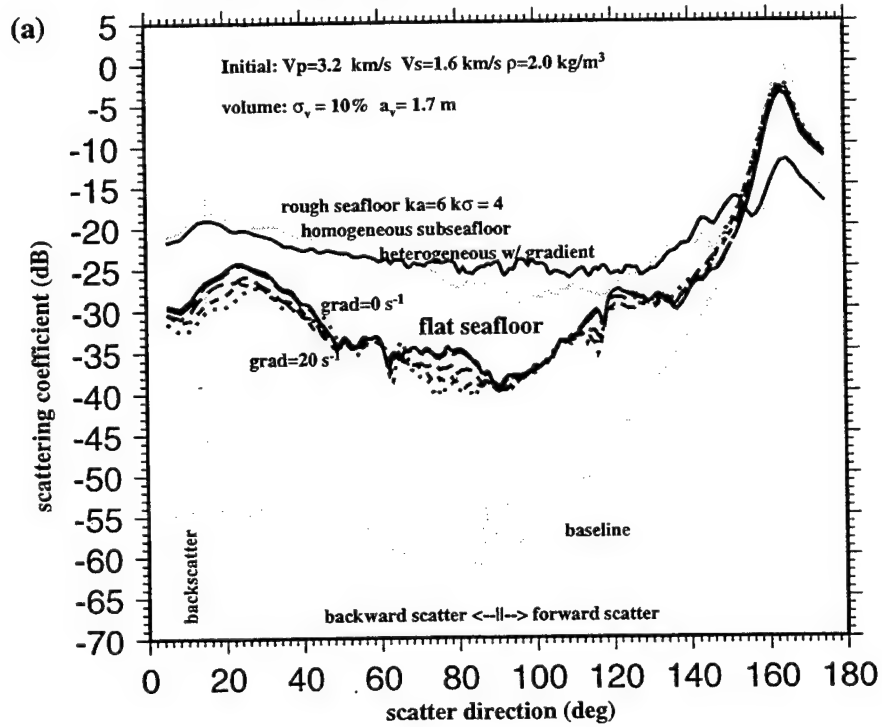


Figure 4-40: Basaltic seafloor models with volume heterogeneity and gradients in the average velocity and density show very little sensitivity to the magnitude or the presence of these gradients. In this figure, the scattering functions for models with gradients of $0\text{--}20 \text{ sec}^{-1}$ for flat heterogeneous models are almost identical (a). The monostatic backscatter coefficients show weak sensitivity to sub-bottom velocity gradients (b). Also shown in (a) is a comparison of a rough-surface heterogeneous model with (upper solid black line) and without (upper solid grey line) a gradient which confirms that the gradient is not significantly affecting the scattering.

Volume Heterogeneity with Vertical Gradients



Scattering at 15°

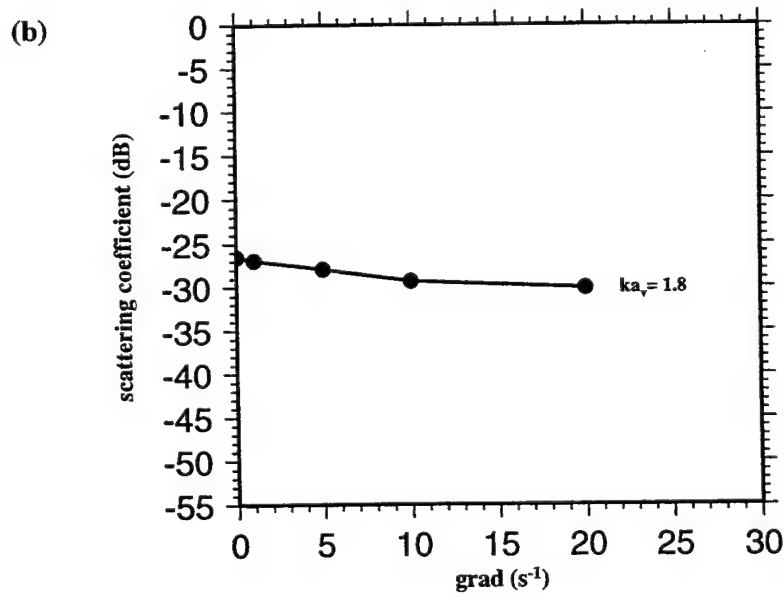
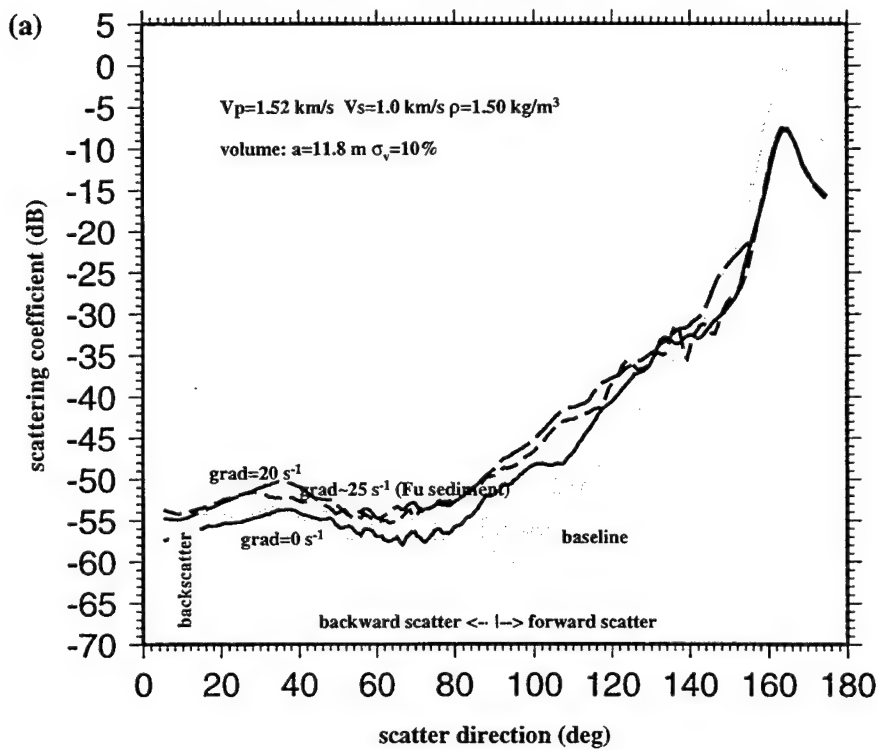


Figure 4-41: Scattering functions are shown for sediment models with gradients in subseafloor velocity and density computed for models with flat and rough heterogeneous seafloor. (a) The scattering functions calculated for flat heterogeneous seabed models with the low velocity and density of such soft-bottom models is also unresponsive to inclusion of gradients in the subseafloor. Included in this comparison is a gradient model with a velocity inversion in v_p (the sediment model defined in Chapter 3 and based on the Fu et al. (1996) data), but it too does not show any significant difference in the response (b). The sensitivity to gradients in these models is minimal.

Volume Heterogeneity with Vertical Gradients



Scattering at 15°

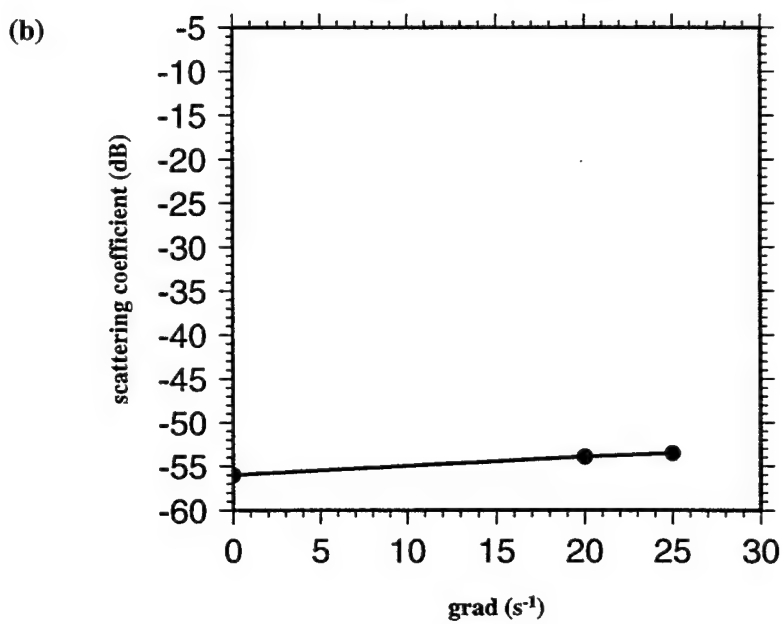
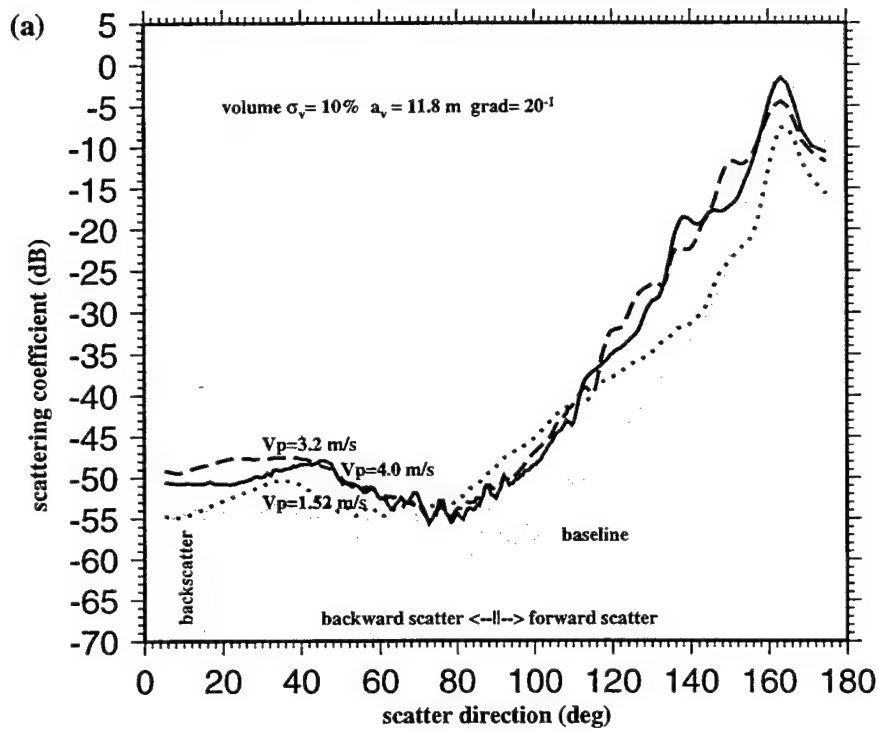


Figure 4-42: (a) Scattering functions for models with gradients in subseafloor velocity and density for different starting velocities and densities at the seafloor. (b) Variation in the initial subseafloor velocity in models with gradients shows only low sensitivity to the velocity. Note that the volume heterogeneity used in these models has a longer correlation length of $a = 11.8$ m. The models all have a gradient of 20 sec^{-1} and $\sigma_v = 10\%$.

Vary Initial Velocity of Heterogeneity with Vertical Gradients



Scattering at 15°

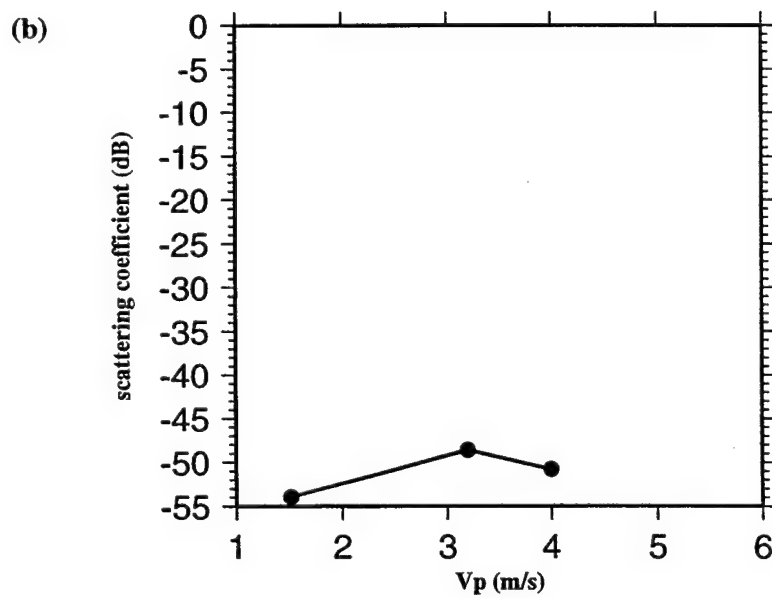


Figure 4-43: Scattering functions of sloping, rough, talus/basalt seafloor models with homogeneous subseafloor are compared to the same models with a heterogeneous subseafloor and a gradient. The plot also compares these scattering functions to similar heterogeneous models without seafloor roughness. Models with 15° large-scale slope are plotted as dashed lines and models with 30° large-scale slope are plotted as solid lines. In all heterogeneous models (black) a gradient of 20 sec^{-1} is included and $\sigma_v = 10\%$. Homogeneous models are plotted as grey lines. Initial velocity and density are representative of either talus or a slower basalt ($v_p = 3.2 \text{ km/s}$) than in previous models. Smooth sloping heterogeneous seafloors have scattering functions that differ little in the backscatter direction but have average intensity levels more than 15 dB down compared to all of the sloping models with rough surfaces. Both the 15° and 30° rough, sloping-seafloor models with homogeneous subseafloor generate backscatter that is almost identical to the backscatter calculated for the same models with heterogeneous subseafloors.

Heterogeneity, Gradients and Sloping Seafloor

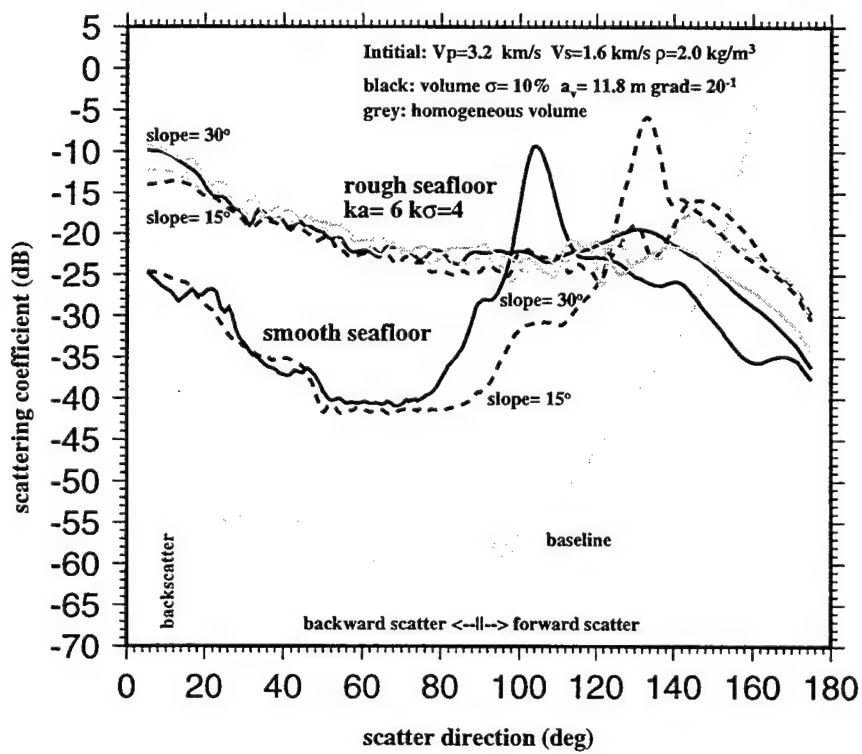


Figure 4-44: (a) Models can also be defined with heterogeneity as fault zones. Fault zones are very common in basaltic seafloors. Single (i) and multiple (ii) fault zones are added to Model 3 with an otherwise homogeneous subseafloor. The fault zones are defined as lower velocity and density zones ($v_p = 2.0$ km/sec, $v_s = 1.0$ km/sec and $\rho = 1.74$ kg/m³) than the surrounding rock.

Realistic Seafloor Models with Fault Zones

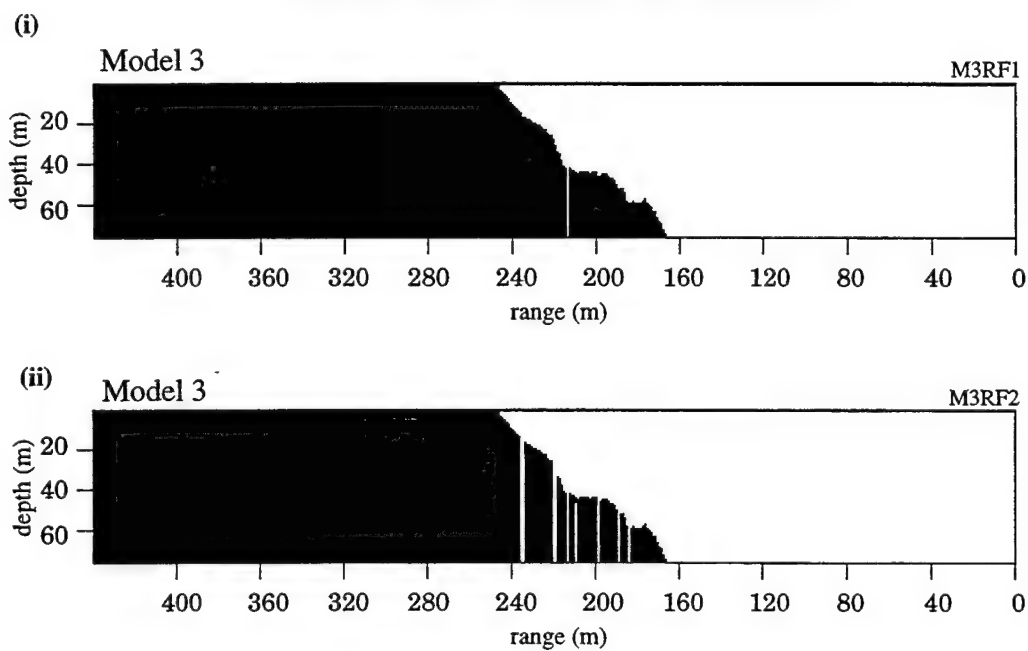


Figure 4-44: (b) Schlieren diagrams for the models in Fig. 4-44(a) show that the fault zones disrupt the body wave propagation in the subseafloor, but in comparison to the homogeneous model (Fig. 4-25d(i)), the scattered field in the water column is not significantly affected.

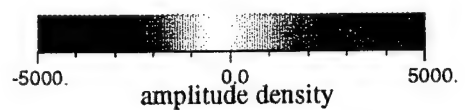
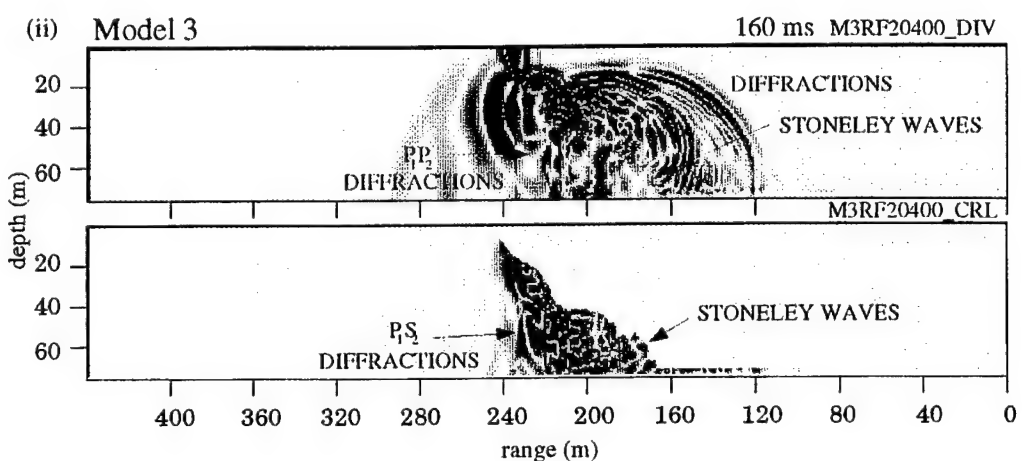
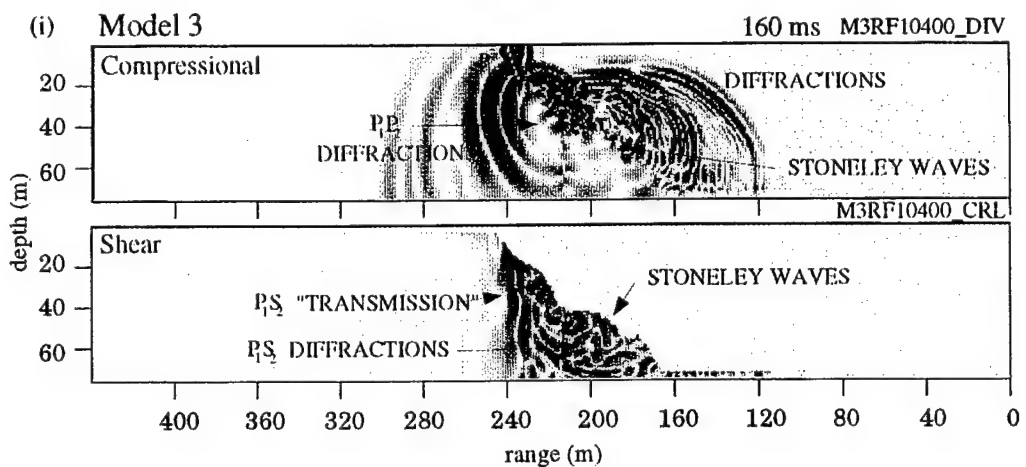


Figure 4-45: The scattering functions for Model 3 with and without fault zones are almost identical. The short-dash line corresponds to the model with one fault and the long-dash line corresponds to the model with multiple faults. The grey solid line corresponds to the same model without any faults.

Model 3 with Fault Zones in Basalt

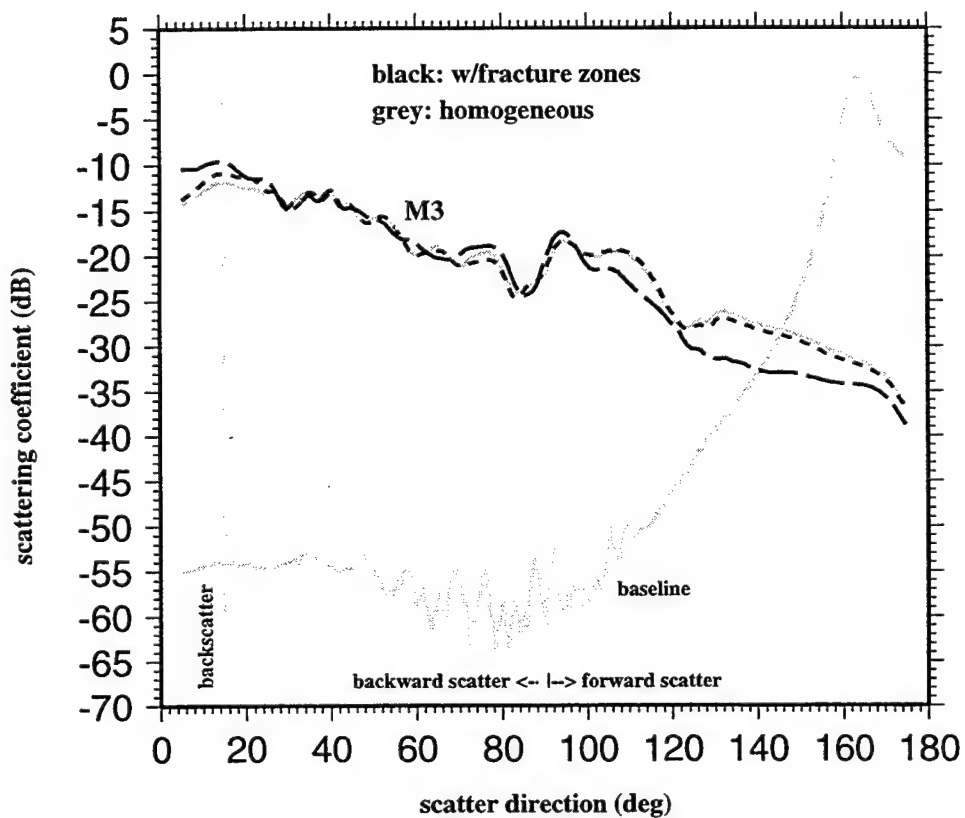
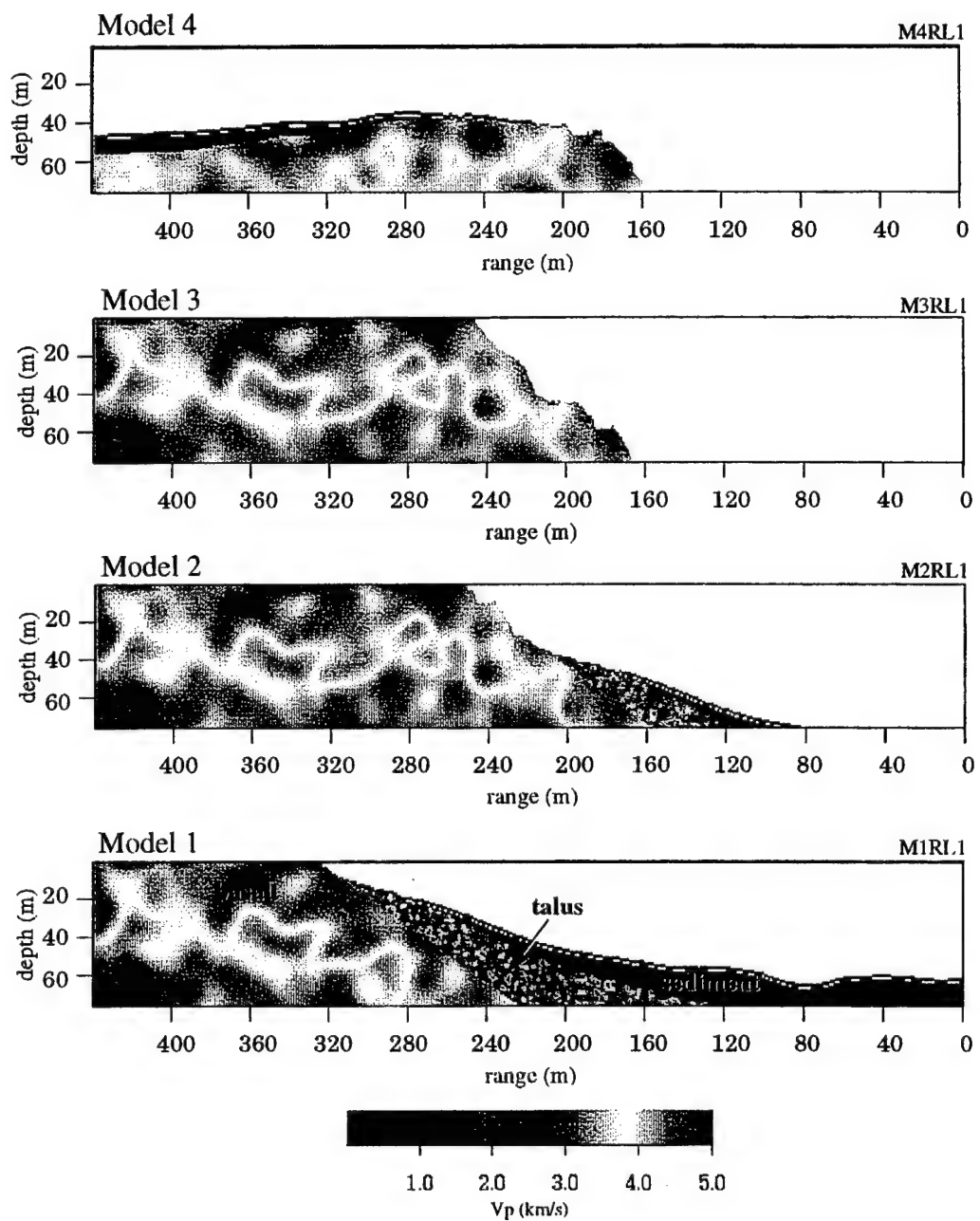
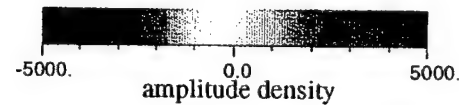
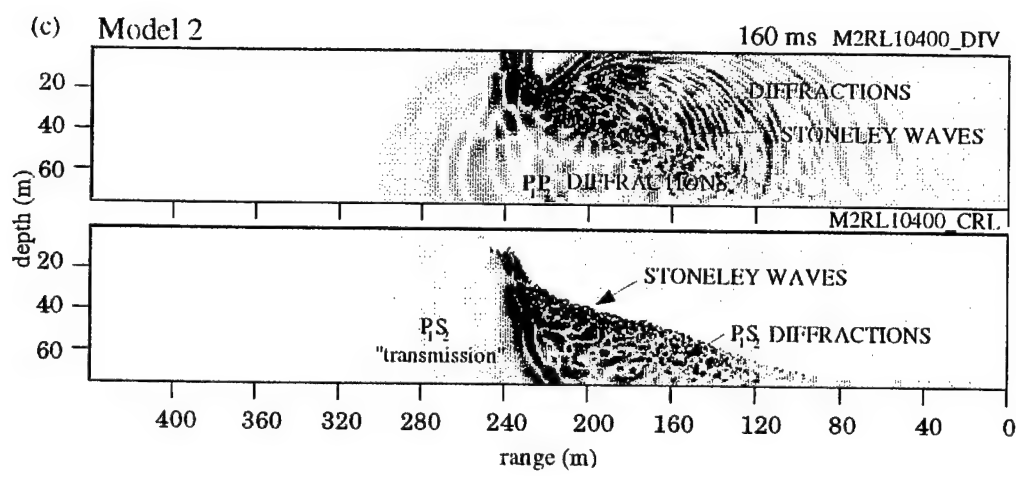
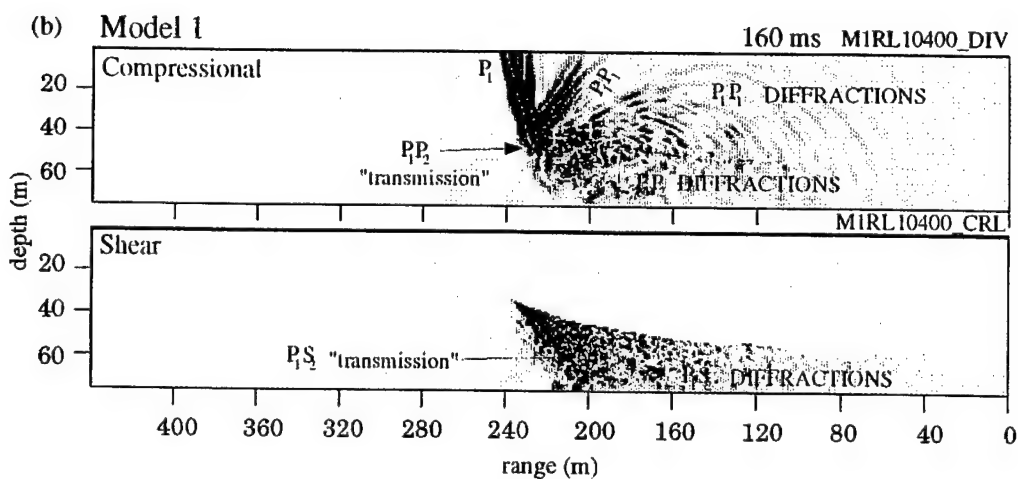


Figure 4-46: (a) Models 1-4 are provided with realistic sediment, talus and basalt layers, volume heterogeneity and gradients. Sediment (blue) is defined with the sediment model based on data from Fu et al. (1996) (defined in Chapter 3), so it has variable gradients and soft-bottom velocity and density, but it is not defined with volume heterogeneity. Talus and basalt have vertical gradients in velocity of 20 sec^{-1} . Because density is defined as a linear function of compressional velocity, it also has a gradient. Volume heterogeneity for talus is defined with a correlation length, $a = 1.7 \text{ m}$ and an rms perturbation of $\sigma_v = 50\%$. Initial velocity at the top of the talus layer is defined as $v_p = 2.0 \text{ km/sec}$, $v_s = 1.0 \text{ km/sec}$ and $\rho = 1.73 \text{ kg/m}^3$. Volume heterogeneity of the basalt is defined with $a = 11.8 \text{ m}$ and $\sigma_v = 10\%$. Initial velocity at the top of the basalt layer is defined as $v_p = 3.2 \text{ km/sec}$, $v_s = 1.6 \text{ km/sec}$ and $\rho = 2.0 \text{ kg/m}^3$.

(b-e) Schlieren diagrams of Models 1 to 4 in (a) show that the subseafloor wavefield is very complicated. The wavefield scattered into the water column is similar to that observed for the same models with homogeneous subseafloor (Fig. 4-25), with the exception of Model 1. In Model 1, scattering from the talus slope region is much greater than observed in homogeneous models.

(a) Realistic Layered Seafloor Models with Heterogeneity and Gradients





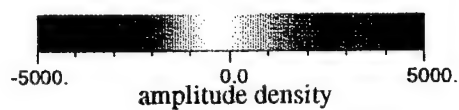
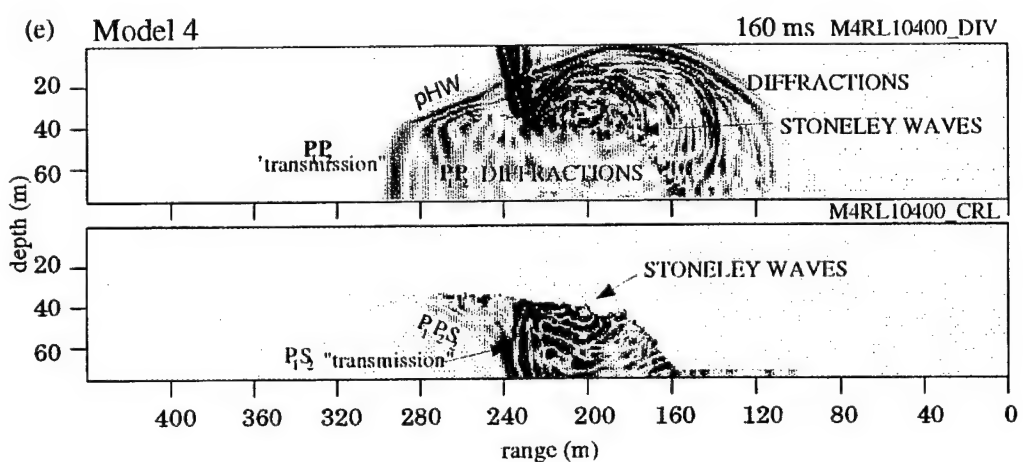
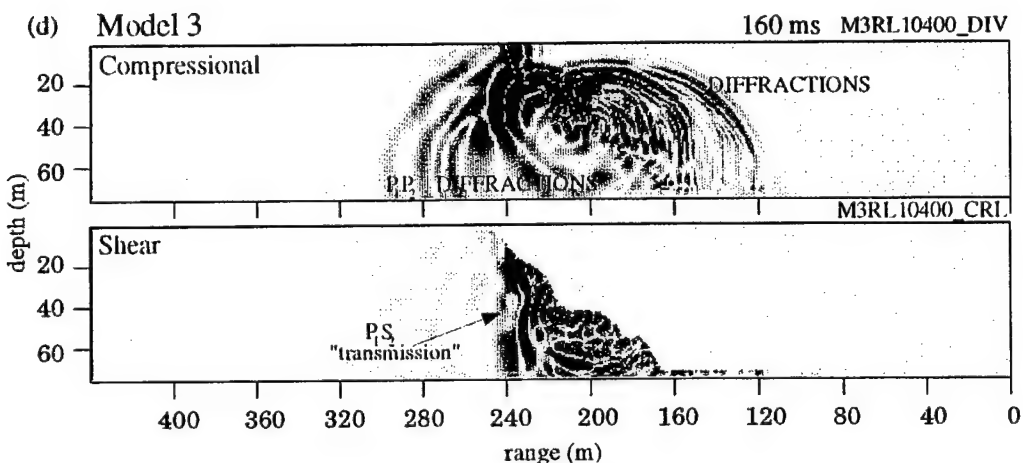
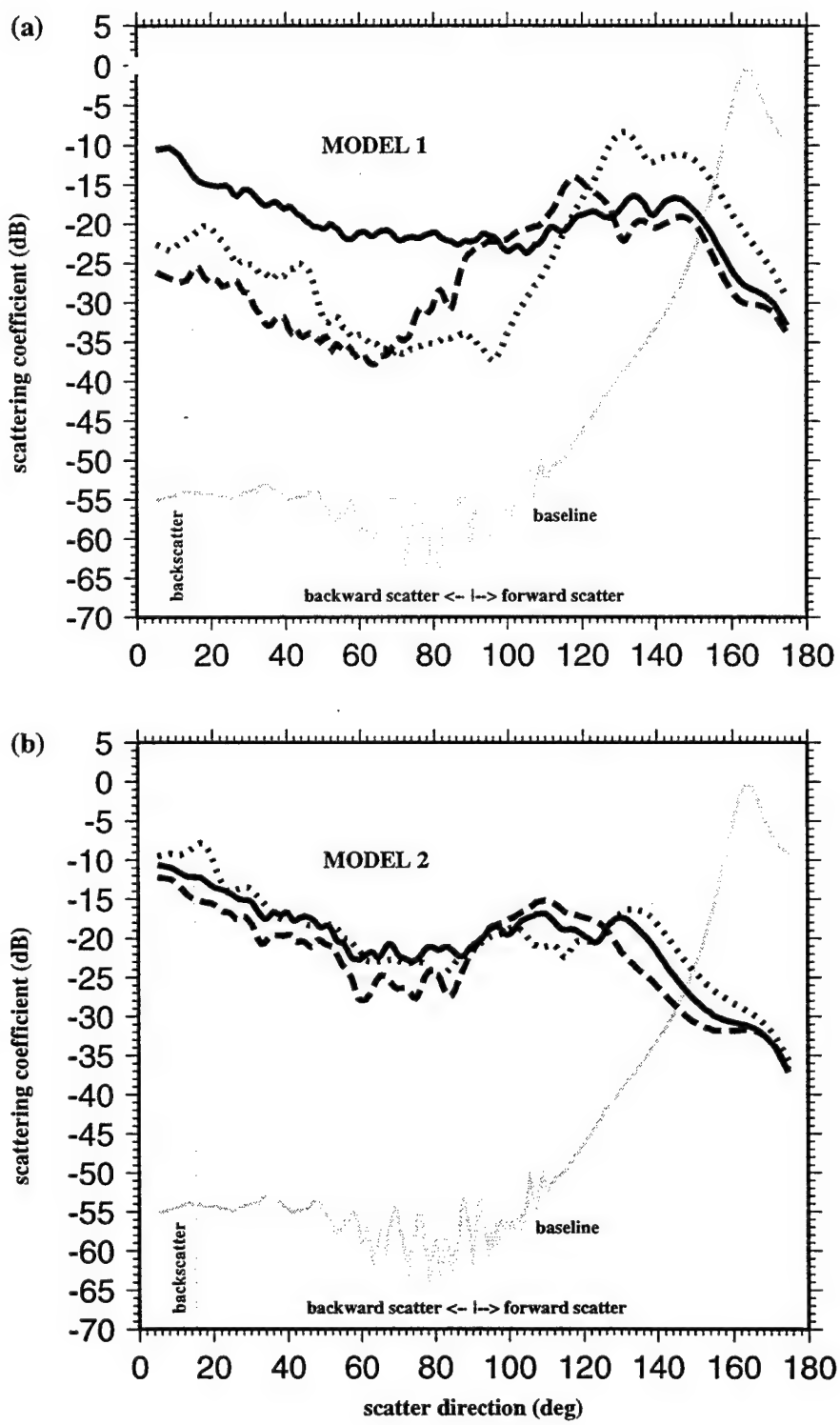
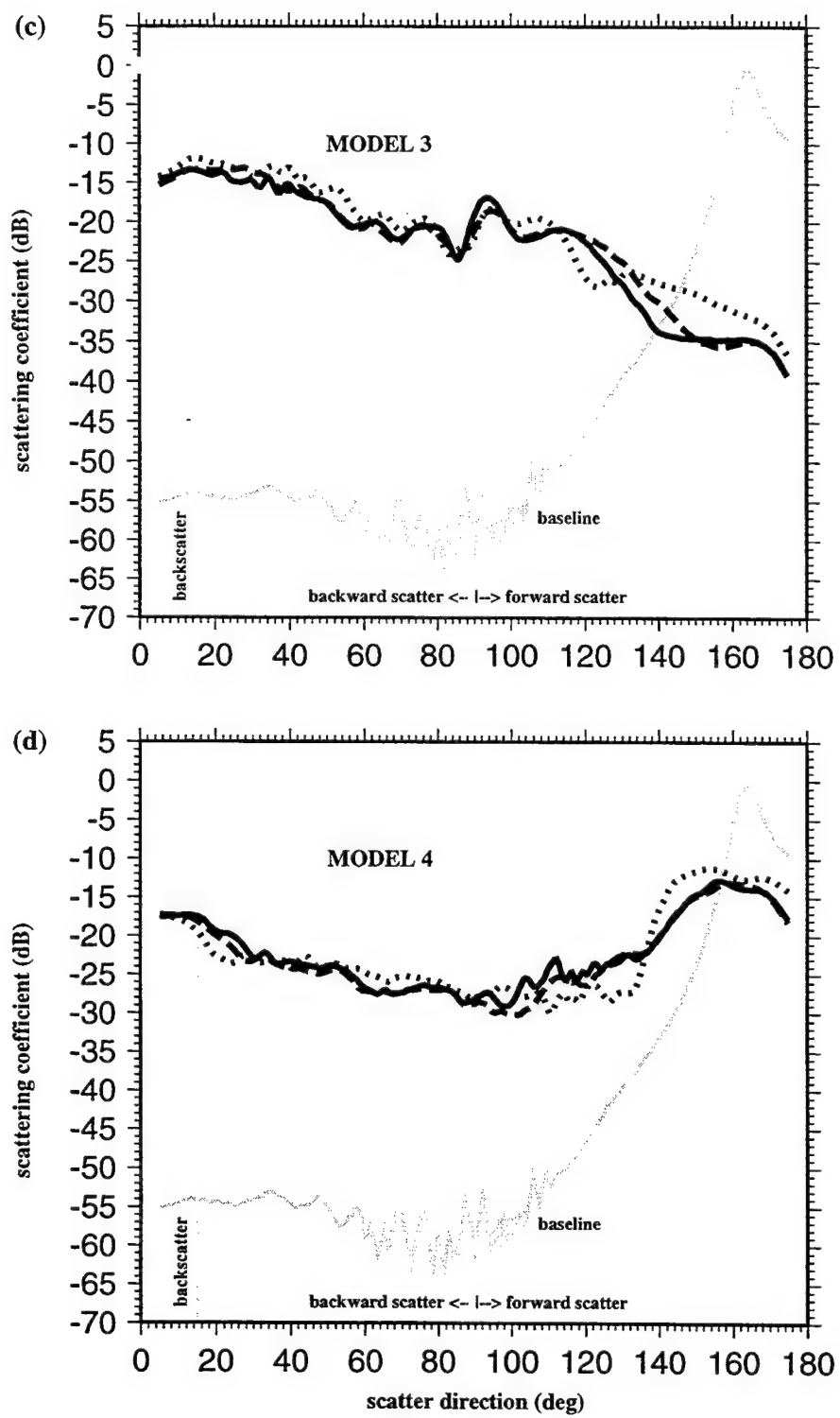


Figure 4-47: Scattering functions of Models 1-4 (a-d). The scattering functions computed for the very complicated layered models (solid lines) in Fig. 4-46a do not differ significantly from the simple homogeneous models (dotted lines). The only strong exception is in Model 1 which, because of its relatively smooth seafloor seems to be more sensitive to the apparent surface roughness produced by the volume heterogeneity, particularly in the region of the talus slope. Models with uniform layers have scattering functions (dashed lines) that are slightly lower or comparable to the homogeneous hard-bottom models.





Chapter 5

Summary and Conclusions

5.1 Introduction

This thesis has been an investigation into the scattering of low-grazing-angle acoustic wavefields from the seabed. The primary objective has been to find quantitative relationships between seabed geological characteristics and backscattered acoustic reverberation signals. Another objective has been to determine the usefulness of monostatic acoustic reverberation survey data for mapping seafloor structure and subseafloor geological properties. The basic tool used to study seabed scattering has been finite-difference elastic wavefield modeling. Because the acoustic reverberation data available for analysis is in the form of time-averaged scattering intensities corresponding to the acoustic beam footprint, a unique interpretation of these data is possible only if the intensity can be shown to depend on a single seabed characteristic. The results of this study have shown that this is not the case. In fact, it has been shown that the range of variation in scattering intensity observed in reverberation data can be explained by geologically reasonable variations in surface roughness parameters, or by the influence of changes in elastic properties at the seafloor boundary or the average seafloor slope. It has also been shown that scattering from subseafloor heterogeneity is primarily from the subseafloor very close to the interface. This simplifies the analysis of the reverberation signals, but it also removes the possibility of interpreting subseafloor variations from the data. The results of this research sug-

gest that an interpretation of monostatic reverberation intensity in terms of seabed stochastic structure can be accomplished if some prior knowledge of average slope and average subseafloor elastic parameters is available.

One of the most important considerations in any study of scattering from the seabed is the physical scale of the variations in seabed characteristics. Only when these variations occur over distances that are at the same order of magnitude as the wavelength of the sound field is a significant scattered field produced. Variations in geological characteristics that occur over very large distances or very small distances, compared to the wavelength, do not produce significant scattering. From the standpoint of interpreting acoustic reverberation data, it is very important to understand that large-scale seabed characteristics do influence the level of scattering but that they are not the sources of the observed signals. All of the signal observed in the acoustic reverberation data is the result of scattering from features that are defined by variations in seabed characteristics that occur over distances within an order of magnitude of the insonifying wavelength (6 m for the ARSRP monostatic reverberation data). The idea that the backscattered signal contains any reflected signal is unrealistic, because it would require large seafloor features with smooth surfaces (i.e., surfaces with small-scale structure that is much smaller than the wavelength) facing normal to the insonifying wavefield. For the wavefields considered in this study, this would require numerous seafloor structures with slopes of about 75° that extended laterally and vertically by at least 100 m with no small scale structures larger than about 0.1 m. Such features rarely, if ever, exist on the seafloor, and they are nothing like the seafloor observed in many hundreds of seafloor photographs at Site A analyzed for this thesis.

In the remainder of this chapter, the results of this research are discussed and general conclusions are drawn about the possible interpretation of acoustic reverberation data. As part of this discussion, some monostatic acoustic reverberation data from the Site A monostatic experiment is considered.

5.2 Summary

The results of the research described in Chapter 2 led to the conclusion that the correspondence of high-intensity backscattering to seafloor ridge areas could not be shown to be a quantitative function of the large-scale slope, as measured at ~ 200 m lateral scales in Hydrosweep bathymetry data. In view of the modeling done in Chapter 4, it seems likely that the real cause of high scattering from ridge areas is twofold: they tend to have more exposed (i.e. not sediment covered) wavelength-scale seafloor roughness, and; the relatively steep large-scale slope ($> 15^\circ$) enhances the scattering from such areas by increasing the grazing angle, locally, of the insonifying acoustic wavefield.

When the ridges are insonified from directions more oblique to their strike direction (i.e., sources north of Site A), it was observed that the backscattering was significantly reduced. Part of an explanation for this, based on the modeling results in Chapter 4, is that at oblique angles the ridges appear to be much less steep and therefore the slope enhancement of scattering from surface roughness is reduced. Another part of the explanation may be that many of the small scale roughness features along the ridge examined in Chapter 3 have a general trend or strike parallel to the ridge strike. At oblique angles such features would appear to the insonifying field as having longer correlation lengths so that the scattered field would have a significantly lower intensity than when the ridges are insonified from directions more perpendicular to the ridge strike. However, these arguments are based on 2-D modeling and insonification of these ridges at oblique angles to the ridge strike is a truly 3-D problem. This is an issue that will be addressed in future work.

It was also concluded in Chapter 2 that the spatial distribution of backscattered intensity can be used to determine the shape and orientation of large-scale seafloor features. Because some of these feature shapes are characteristic of specific crustal regions, e.g., the long linear ridges associated with outside-corner crust, the acoustic reverberation data could be useful in mapping regional crustal types. Similar analyses can be done with side-scan sonar systems. However, if the analysis of the acoustic

reverberation data is carried out over multiple 1/2 CZ's (convergence zones), very large regions of the seafloor can be mapped from a small number of source/receiver locations.

The results of Chapter 3 led to a realistic seabed model, considered typical for areas on the flank of the Mid-Atlantic Ridge. The seafloor profile was constructed from high-resolution bathymetry data and is centered on what is considered a typical ridge-facing fault scarp. These ridges are quite linear on outside-corner crust, such that the seafloor can be considered approximately 2-D at large scale. Seafloor type was categorized as either sediment, talus, or basalt based on analysis of seafloor photographs. In the process of developing this model it was found that very little data is available for defining subseafloor properties for high-resolution seabed models, i.e., models with variations that occur over the scale of the acoustic wavelength ($\lambda = 6$ m) used in the reverberation experiments. The range of realistic subseafloor velocity and density could not be narrowed down below regional average values, because no site-specific data were available. For modeling, shear-wave velocity and density are defined as linear functions of compressional-wave velocity. These relationships maintain the velocity and density values within the ranges defined for each seabed material type. Fortunately, some high-resolution bathymetry data and seafloor photographs were available within the study area. Notably lacking in deep-ocean studies are data on the scales of lateral variation in subseafloor velocity and density.

Chapter 4 focussed on determining the sensitivity of backscattered acoustic reverberation to variations in seafloor wavelength-scale roughness and subseafloor volume heterogeneity. Wavelength-scale heterogeneity was defined in terms of Gaussian stochastic functions so that geological variation at this scale could be parameterized in terms of rms amplitude and correlation length of the distributions. Backscattering was found to be much more sensitive to variation in rms height than to variation in correlation length. For rough seafloors, scattering from subseafloor volume heterogeneity was shown to be a less significant factor in scattering than the scattering produced by the rough seafloor itself.

The influence of deterministic seafloor parameters (seafloor slope and average

subseafloor velocity and density) on scattering was also quantified. Both large-scale seafloor slope and subseafloor velocity and density influence the scattered intensity levels, but primarily within a narrow range of variation. That is, scattering intensity varies most rapidly in the range of seafloor slope from 0° to 15° , and the strongest variation due to a change in average subseafloor velocity occurs in the transition from low (sediment) velocity ($v_p \sim 1.5$) km/sec to higher (talus and basalt) velocity seafloor ($v_p \geq 2.$ km/sec). In order to incorporate all seafloor structure in a single parameterization of seafloor scattering, the large-scale slope and wavelength-scale seafloor spatial features characterized by rms height and correlation length were included, along with the acoustic beam grazing-angle relative to a horizontal seafloor, in the definition of an 'effective grazing angle'. This definition of grazing angle was found useful as a phenomenological description of scattering when combined with the Rayleigh roughness parameter. Scattering coefficients from a variety of seafloor models plotted versus the 'effective Rayleigh roughness' parameter are a potentially useful interpretation scheme if the bottom types (sediment, talus, and basalt) are known.

The modeling in Chapter 4 shows that seafloor scattering is caused by wavelength-scale variations in geological properties, whether they are seafloor or subseafloor variations. Large-scale features influence the intensity level of the scattering but do not generate scattering. The sensitivity of the backscattered intensity to variations in both large-scale and wavelength-scale characteristics can produce variations in backscattered signals comparable to those observed in monostatic reverberation experiments. Because so many parameters can be the source of observed signal variations, it may not be possible to interpret acoustic backscatter data rigorously in terms of seafloor characteristics. An exception to this would be a situation where the seafloor is very well characterized from other data, such that only one or a very few seafloor parameters are to be solved for; for example, if large-scale seafloor slope and subseafloor velocity and density are well known it is possible to determine seafloor roughness from the backscatter intensity. However, this is not usually the case, and therefore the crude interpretation based on the distribution shown in Figure 4-24

seems to be the best that can be expected at the moment. Unfortunately, this is not a particularly satisfying result. One possible, more rigorous approach would be to search for an inversion scheme that would relate backscatter intensity to a linearized model of seafloor parameters. The relationship of the effective Rayleigh roughness parameter, defined with the effective grazing angle, is a step in this direction. However, as seen in Figure 4-24, this relationship is significantly non-linear. It might be possible to develop an inversion scheme assuming that the effective Rayleigh roughness parameter versus intensity is linear over limited ranges, but this is left for future work. Such an interpretation scheme would inevitably require either prior knowledge or assumption of the seafloor characteristics, and it would yield a statistical interpretation.

5.3 Site A Monostatic Acoustic Reverberation Data

Acoustic reverberation from two receiver locations in the Site A (Run 1) monostatic experiment were chosen for comparison to the modeling results and analysis. Figure 5-1 shows the receiver locations (Segments 44 and 76) and the projections of the beams that pass closest to the location of the seafloor model used in the previous chapter. Also plotted are the projections of the opposite-side beams. Although the central beams from the two segments are co-linear in the direction of Site A, their opposite-side beam directions are not co-linear. The directional ambiguity in the acoustic reverberation data must be considered in any analysis. Site A is within the first 1/2 CZ of the signal propagation from all source locations in the monostatic experiment. If the water depth at the 1/2 CZ range in the opposite side direction is much deeper than the maximum turning depth of the source radiation, then it could be assumed that none of the observed acoustic signals came from that direction; however, this is not the case at Site A. If multiple source directions are used in the analysis, it is possible to combine the beam data corresponding to reduce each location and reduce the ambiguity problem (as in Chapter 2). At multiple 1/2 CZ's the ambiguity can be reduced by eliminating directions that have blocking seafloor topography (Makris

et al., 1995) and by combining beam data from different source directions (Makris, 1993). None of these techniques can be applied to the reverberation data at Site A, and therefore the left-right ambiguity must be considered in the analysis of the data.

Figure 5-2 shows the DSL-120 bathymetry corresponding to the left and right central-beam directions in the monostatic reverberations data at the range of Site A for both segments. The bathymetry corresponding to the directions not crossing Site A is referred to as 'opposite side' in all plots. Also, note that the range in all plots is relative to the receiver location of Segment 76. In other words, the true range across Site A for Segment 44 acoustic data and bathymetry data has been adjusted to plot within the same range as Segment 76 data. Also plotted in the figure is the region of the detailed geological surveys (the seafloor model profile from the previous chapter). In both opposite-side bathymetry plots, the large-scale structure within the range of Site A is of the same magnitude as that observed at Site A. The most obvious difference is that the opposite sides differ in depth by about 200 m in both cases. The opposite-side bathymetry for Segment 44 is about 200 m deeper than at Site A and for Segment 76, is about 200 m shallower. However, in both cases the scattering from the opposite sides cannot be assumed to be negligible based on differences in depth or large-scale structure.

5.4 Acoustics Data

After beamforming, each segment in the acoustics experiment has 126 beams. Each beam is a time-series with amplitude in units of squared pressure which are converted to intensity values and corrected for transmission loss (for details of acoustics data and processing see Chapter 2). To find the correspondence of seafloor location and the time series data within Site A, the two-way traveltime was calculated using a ray-tracing method. At the range of Site A from the source/receiver locations for these segments, these beams have footprints on the seafloor of approximately 13 m x 200 m. As has been previously discussed, the beam footprint in the Site A data is a topic of debate. The resolution of the traveltime-to-seafloor location calculation is

estimated to be on the order of 20-30 m.

Figure 5-2 shows plots of the acoustic time-series data corresponding to the range within Site A from Segment 76 and Segment 44 respectively. For Segment 76, the central beam that intersects the area of the seafloor profile is Beam 29. The central beam for Segment 44 is Beam 40. Three adjacent beams on either side of these central beams are also plotted. The order of the beams is from north to south relative to the central beam and in the direction of Site A. The time-series data have been corrected for transmission loss and converted from time to their corresponding range, as in Chapter 2. These data have also been smoothed over a range window of 10 m.

It is notable that there is not as much correspondence from segment to segment as would be expected for co-linear beams. Some features in the reverberation are repeated from segment to segment and are circled in Figure 5-2. At this point the only possible explanation for this is that scattering from the opposite-side directions is significantly contributing to the total signal. In spite of this problem, it is possible to make a very crude interpretation of seafloor geological type from these data. The basic correspondence between sediment, talus, basalt and intensity that is shown in Figure 4-24 was used to show an example of interpretation. The actual relationship between modeling intensity and reverberation measurements is not known, so it was necessary to decide on an arbitrary shift of the interpretation model. The shift was chosen so that the most steeply dipping and bare basalt region observed within the modeled area at Site A would be interpreted as basalt. The original breakdown in Figure 4-24 is that all signals below -30 dB are considered sediment and all signals above -22 dB were considered basalt, with talus or a smooth basalt filling the intermediate range. For the following interpretation this was shifted up such that any signal below -15 dB is labelled as sediment and any signal above -7 dB is labelled as basalt. Figure 5-3 shows the beam data, color-coded according to this interpretation. There is a general correspondence of areas interpreted as basalt to the known basalt exposure in the region of the seafloor model. There is also a strong suggestion, particularly from the Segment 44 beams, that the scattering from the region at the toe of the seafloor model and extending for several hundred meters is from a sediment bottom.

Other areas with a strong suggestion of basalt bottom correspond in most cases to a high-slope portion of either the Site A or one of the opposite bathymetry profiles. If the color coded average beams are indicative of seafloor geology, they would lead to the conclusion that much of the seafloor is covered by talus or relatively smooth basaltic material. These results are interesting, but without analysis of much more beam data it is not clear how this interpretation would fit into the general picture of regional geology.

5.5 Thesis Conclusion

This thesis has shown that the backscattered signals observed in monostatic reverberation experiments are caused by scattering from wavelength-scale seafloor and subseafloor variations in the propagation parameters, velocity and density. This is an important result, because much of the previous interpretation of acoustic reverberation data has been in terms of large-scale seafloor characteristics, i.e. much larger than wavelength scales of the insonifying wavefield. It has been shown in this thesis that large-scale features, in particular high-standing ridges with steep slope, will generate the expected high backscatter intensities. However, the source of this scattering is not the slope but the exposed basaltic rough seafloor that is found on these ridge flanks. The large-scale slope acts to enhance the scattering intensity by increasing the local grazing angle, but is not the actual source of the scattered wavefield. It is also clear from the results of this study that similar strong scattering can be generated in relatively low-slope areas if the seafloor is an exposed and is very rough basaltic bottom. Such seafloor is expected in regions of young oceanic crust where sediment accumulation is negligible.

It has been shown that scattering intensity is clearly a function of most of the seafloor characteristics included in this study, namely, average subseafloor velocity and density, large-scale slope, wavelength-scale rms amplitude, and correlation of seafloor and subseafloor heterogeneity. Some parameters, such as subseafloor gradients and individual faults have no discernible effects on scattering. In general, the sensitivity

of backscattering to the former parameters is such that they can each account for much of the signal variation in reverberation data. However, the apparent functional relationships between these parameters and the backscattered signals is non-linear in each case. This leads to the conclusion that a unique interpretation of monostatic reverberation data may not be possible.

Another important conclusion is that although subseafloor volume heterogeneity at wavelength scales can produce a strong backscatter signal (comparable to scattering from rough seafloor) if the seafloor is very smooth and the perturbation is large, when the seafloor is rough the effect of volume heterogeneity on the backscattering cannot be distinguished from the seafloor scattering. In general, volume-scattering effects, observed in the water column, are primarily the result of scattering from heterogeneity that occurs at or just below the seafloor. The volume heterogeneity adds an apparent roughness to the seafloor as the density and velocity vary, particularly when they vary strongly. It is estimated that most of this volume-scattering effect occurs within one wavelength of the seafloor. In future work this depth limitation will be quantified more precisely by comparing the scattering from seafloor with different thicknesses of heterogeneous subseafloor.

This study has yielded a greater understanding of the true complexity of the scattered signal that is observed in monostatic reverberation experiments. Finite-difference modeling has proved to be a very effective technique for determining the sensitivity of scattering to variations in morphology and geological properties. It is important to keep in mind that sound scattered from the earth does, in fact, carry information about the geological properties of the earth, even though interpreting such signals is a very complex process. The study of scattering has been a very interesting and consuming experience, however it can certainly be said that there is always more to learn.

Figure 5-1: Projections of beams from Segments 44 and 76 of the Site A (Run 1) monostatic reverberation experiment that intersect the location of the realistic model defined in Chapter 3. Each beam has an equivalent opposite-side orientation (dashed lines) that does not cross the model location. The central beams for Segments 44 and 76 are co-located in the direction of Site A but not in their opposite-side directions. Three beams on either side of the central beam are also included in the analysis.

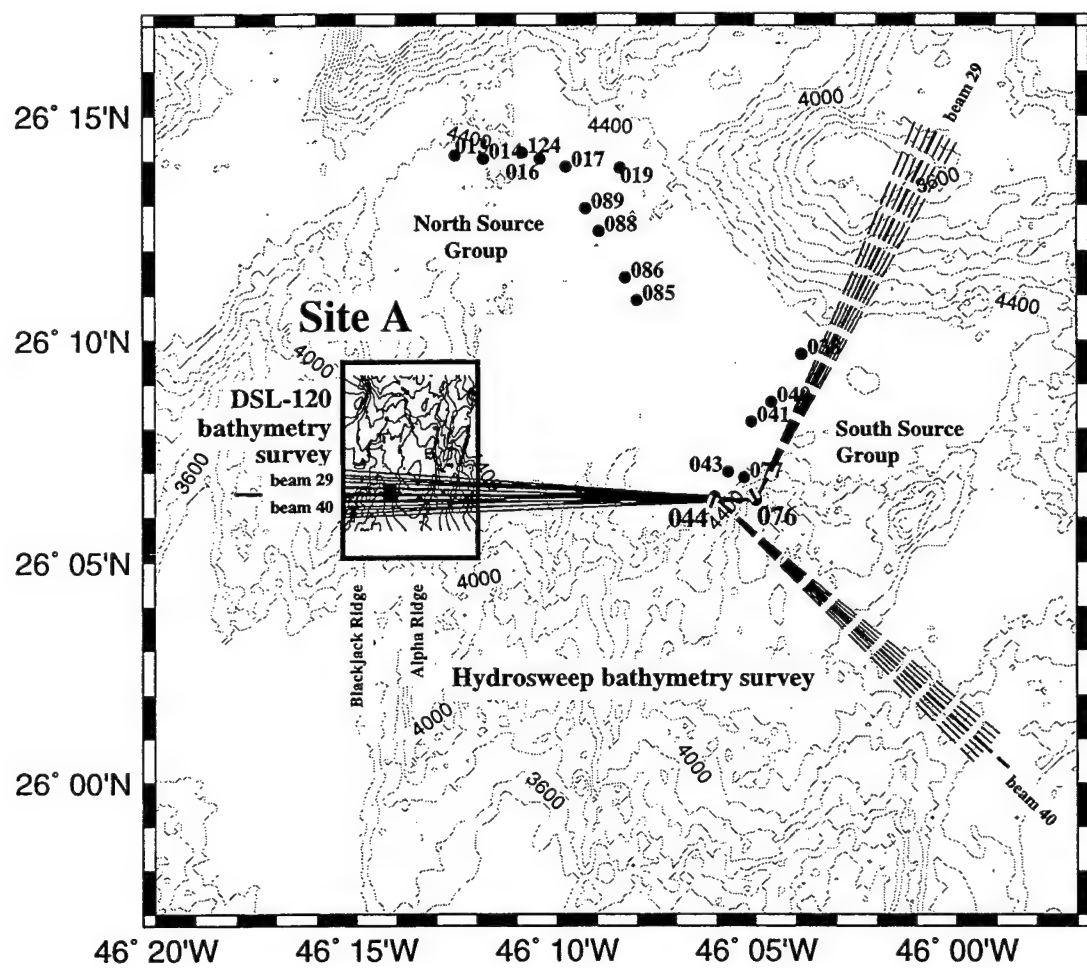


Figure 5-2: Some of the acoustic reverberation beam data, Segments 44 and 76, intersects the seafloor model location. Only the central beams (76/29 and 44/40) are truly co-linear. A few examples of comparable signals are circled in the plot but overall the correspondence is not as good as might be expected. This may in fact be due to the inclusion of scattering from the opposite-side seafloor areas. Bathymetry profiles corresponding to the central beam direction across Site A are plotted as well as the opposite-side bathymetry profile for each case. Clearly, the structure on the opposite side for both of the central beams could be the source of at least as much scattering as Site A. The location of the detailed geological survey and finite-difference model is also plotted in its correct location as a reference.

Site A: Segment 44 and 76 Beam Data

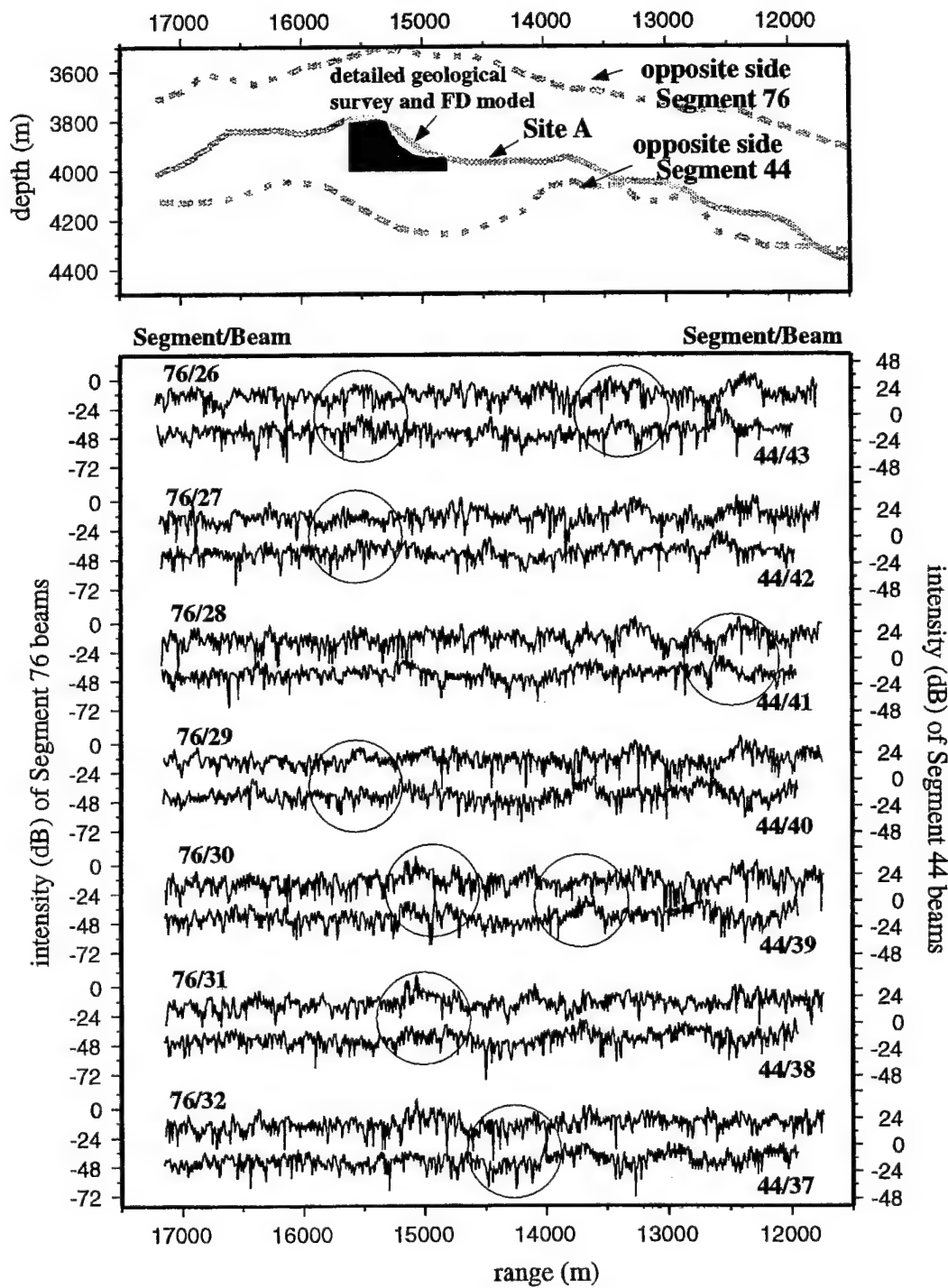
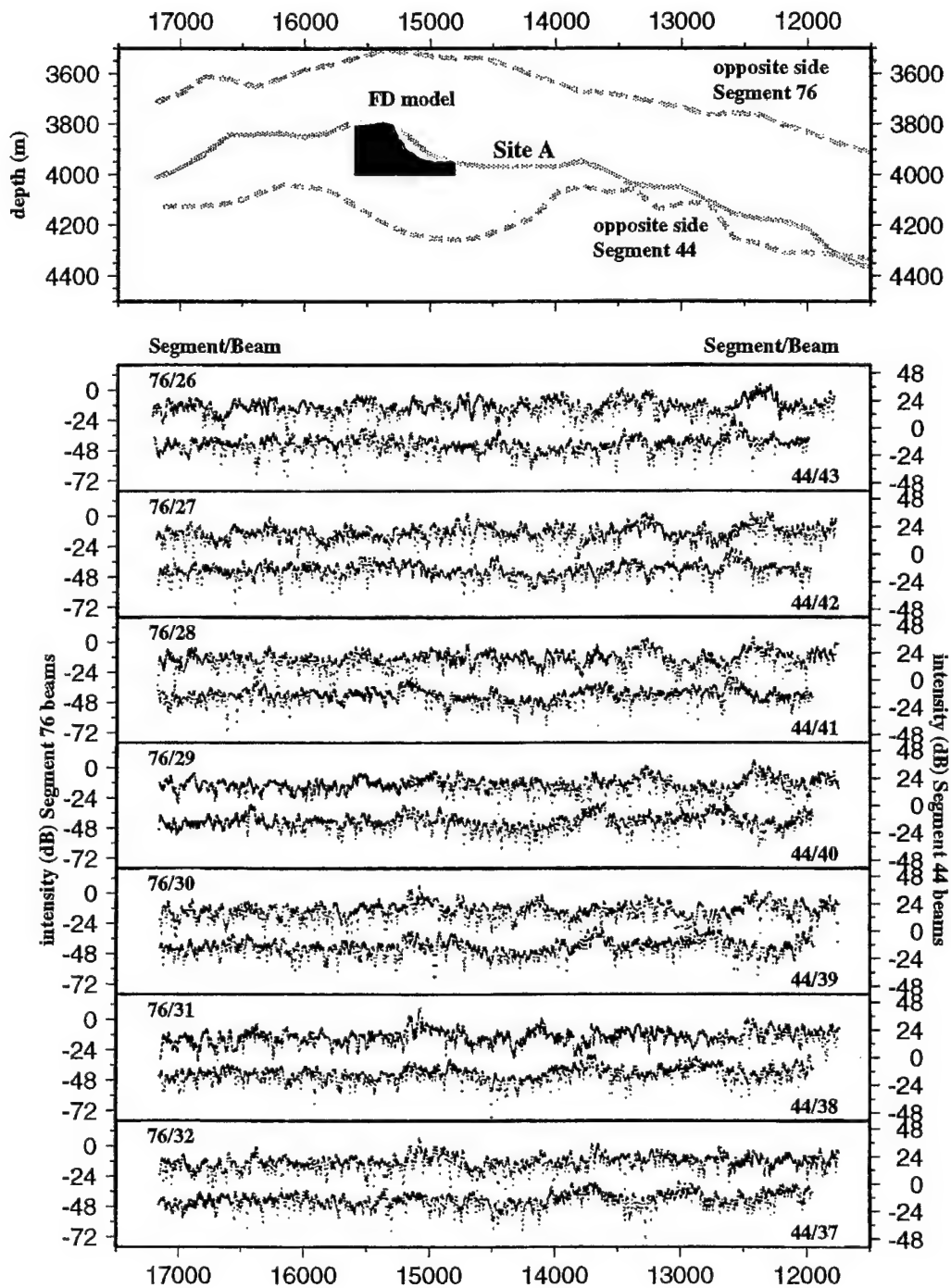


Figure 5-3: Site A acoustic reverberation beam data, Segments 44 and 76, interpreted as sediment, talus, and basalt. This interpretation is based on the simple breakdown suggested by Figure 4-24. Red is indicative of intensities corresponding to scattering from basalt. Blue is indicative of intensities corresponding to talus or a relatively smooth high-velocity (higher than sediment velocity) seafloor. Green is indicative of intensities corresponding to scattering from sediment bottoms.

Site A: Segment 44 and 76 'Interpreted' Beams



Appendix A

Transmission Loss Approximation

In this section we show that the transmission loss associated with geometric spreading and source spatial beam (radiation) pattern can be approximated by a shifted cylindrical spreading loss function.

The VLA farfield beam pattern is estimated by the response function of a vertical line source in the vicinity of a free surface (ARSRP Initial Report, 1993, p. 220). The equation for the farfield spatial beam pattern, $S(\theta)$, in terms of pressure for a harmonic (CW) source, is given by

$$S(\theta) = \frac{\sin(2\pi(v - V)\frac{L}{2})}{2\pi(v - V)\frac{L}{2}} \exp(i2\pi(v - V)x_o) - \frac{\sin(2\pi(v + V)\frac{L}{2})}{2\pi(v + V)\frac{L}{2}} \exp(-i2\pi(v + V)x_o) \quad (\text{A.1})$$

where x_o is the depth from the free surface to the center of the line source which has length L and

$$v = f \frac{\sin\theta}{c} \quad (\text{A.2})$$

$$V = f \frac{\sin\theta_s}{c} \quad (\text{A.3})$$

where f is the source frequency, θ is the observation angle (grazing angle), θ_s is the source array downward steering angle and c is the propagation velocity. For simplicity, uniform velocity across the array is assumed so that c is a constant. For the Site A experiment $\theta_s = 9^\circ$, $L = 20.6$ m, $x_o = 184$ m, $c = 1522$ m/s at source depth, and the frequency ranges from 200-255 Hz.

Unless the acoustic propagation environment is known very accurately, it is best to represent the source beam pattern by the 'incoherent' pressure field, in which the phase information is neglected (Jensen et al, 1994). The discrete expression for the incoherent broadband source beam signal level ($BL(\theta)$) at a particular observation angle is

$$BL(\theta) = 10 \log_{10} (\Delta f \sum_f |S(\theta)|^2) \quad (A.4)$$

where Δf is the frequency interval. For our calculation f ranged from 200 to 255 Hz and $\Delta f = 1$ Hz. We normalize $S(\theta)$, prior to the summation over frequency, such that the total power output is equivalent to a point source that produces a pressure of $1 \mu\text{Pa}$ on the surface of a sphere 1 meter in radius. This approach is consistent with defining the source level relative to the total energy emitted from a sphere, one meter in radius, located at the center of the array. After the calculation for the total incoherent pressure field, we again normalize the broad-band beam level so that its peak level (at $\theta_s = 9^\circ$) is 0 dB. This is consistent with the idea that the actual peak source level (SL= 230 dB) is measured on the central beam axis and that all other beam levels are measured relative to this.

The theoretical geometric spreading loss as a function of energy density is determined from ray divergence and combined with $BL(\theta)$ to find a net transmission loss correction term. Ray tracing through an ocean acoustic velocity model (Figure A-1) was used to estimate the true geometric energy decay due to wavefield divergence. The energy density, or intensity, in a multi-layered (velocity) ocean can be described in terms of horizontal range from the source, r , at a fixed depth, z , and the variation of the ray parameter, p , with range; that is, $\frac{dp}{dr}$. The ray parameter, for horizontally layered media, is defined by (Aki and Richards, 1980, p. 92)

$$p = \frac{\sin \phi}{v} \quad (A.5)$$

where v is the velocity in any particular layer and ϕ is the propagation incidence angle relative to the vertical. We calculate $\frac{dp}{dr}$ as a function of depth and range in the

ray tracing. The decay in energy density can be shown to be given by (Urick, 1983, p. 127),

$$\frac{I}{I_0} = \frac{1}{r} \frac{v_o^2 p}{\sqrt{1 - (v_o p)^2} \sqrt{1 - (vp)^2}} \frac{dp}{dr} \quad (\text{A.6})$$

where I_0 is an initial source intensity, v_o is the velocity at the source, and v is the velocity at the depth for which we are calculating the loss. Transmission loss, based on ray divergence, expressed in dB, is then

$$TL_{rd} = -10 \log_{10} \frac{I}{I_0} \quad (\text{A.7})$$

To account for two-way propagation we multiply the decay expressed in Equation (A-7) by a factor of two.

In Figure A-2 we show the net observed intensity, $TL = -(BL - 2TL_{rd})$, predicted for signals returned from the range of depths used in our analysis. This is energy intensity, for two-way propagation, as a function of range for a reference source and is in absolute units (i.e. dB down from an axial level of $1 \mu\text{Pa}$ at 1 m from the center of the array). Actual geometric propagation loss in the ocean is described by spherical spreading loss close to the source and cylindrical spreading loss in the far field (Jensen et al., 1994). For simplicity in processing the data, we fit the net intensity curves with transmission loss curves based solely on cylindrical spreading. The loss predicted by cylindrical spreading is

$$TL_{cyl} = 2 \times (10 \log_{10} \sqrt{r^2 + d^2}) + TL_o \quad (\text{A.8})$$

where d is the seafloor depth and TL_o is a reference level used to match transmission loss within the offset range used in our analysis. From 10 km to 25 km, the cylindrical spreading curve has similar slope to the envelope of the sum of the beam pattern and ray divergence curve but is offset in absolute units. In Figure A-2 we plot $-TL_{cyl}$ for three depths, with

$$TL_o = 0.00243d + 71.15dB \quad (\text{A.9})$$

which fits $-TL_{cyl}$ to $BL - 2TL_{rd}$ in this depth range. The cylindrical spreading curves predict the energy loss between 12 km and 22 km within +/- 0.5 dB. Between 10 km and 12 km the error is larger but only for deep seafloor areas. In the worst case, 4500 m at a range of 10 km, the error is about -4 dB. At far ranges, the prediction error is larger for the most shallow scatterers; for example at the 25 km range and 3200 m depth, the error is as much as 4 dB. However, very little data used in our analysis have ranges greater than 20 km (see Figure 2-7) or depths greater than 4000 m.

We conclude that the correction needed to account for source beam pattern and geometric transmission loss can be approximated by a cylindrical spreading loss as:

$$TL = -(BL - 2 \times TL_{rd}) \approx TL_{cyl}^{src} + TL_{cyl}^{rec} + TL_o \quad (\text{A.10})$$

where

$$TL_{cyl}^{src} = 10 \log_{10} r_{src} \quad (\text{A.11})$$

and

$$TL_{cyl}^{rec} = 10 \log_{10} r_{rec} \quad (\text{A.12})$$

taking r_{src} as the propagation distance (slant range) from the source to a seafloor grid cell and r_{rec} as the propagation distance from the receiver to the grid cell. The net approximation to the equivalent target scattering strength is

$$TS \approx RL_s - SL + TL_{cyl}^{src} + TL_{cyl}^{rec} + TL_o \quad (\text{A.13})$$

The surface scattering strength

$$S_s = TS - 10 \log_{10} A \quad (\text{A.14})$$

is then approximated by

$$S_s \approx RL_s - SL + TL_{cyl}^{src} + TL_{cyl}^{rec} + TL_o - 10 \log_{10} A \quad (\text{A.15})$$

Figure A-1: Velocity-depth profile used in ray tracing. The data are from a CTD profile collected at $26^{\circ}14.18' N$, $46^{\circ}13.51' W$, on Dec. 7, 1993. Values below 4000 m (thin line) are extrapolated from the measured profile.

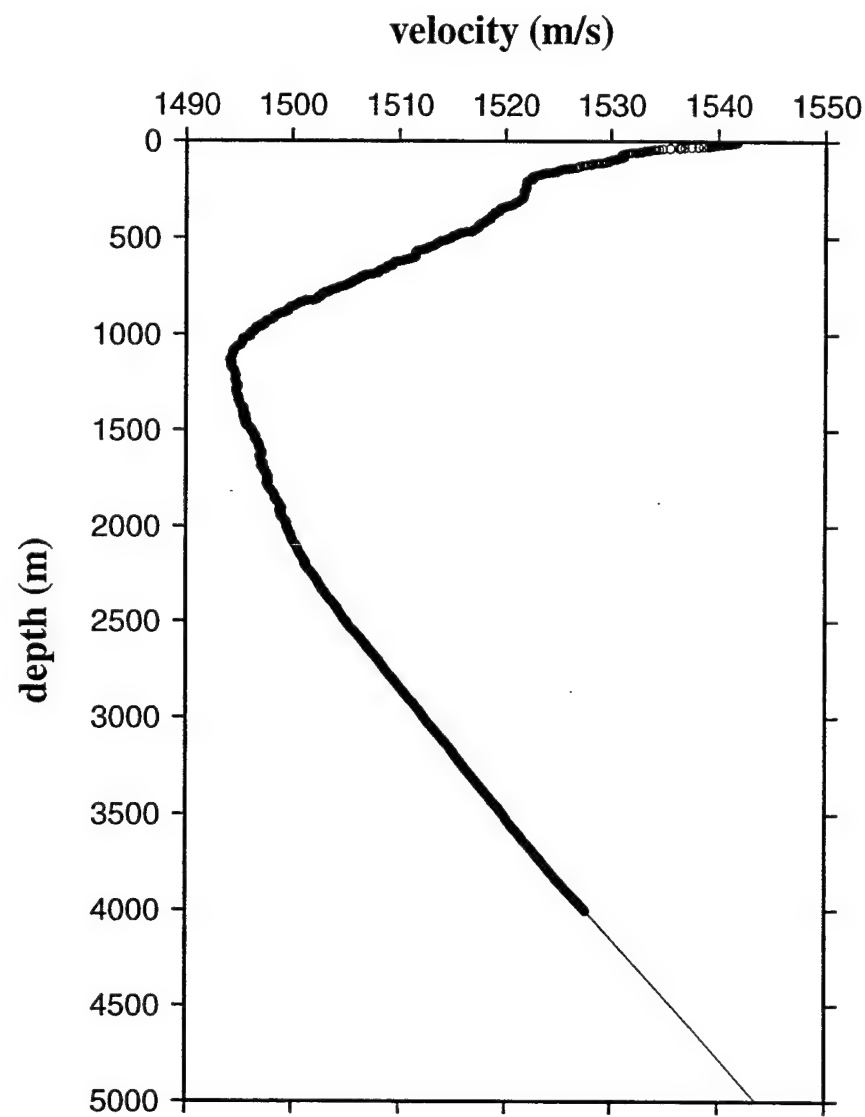
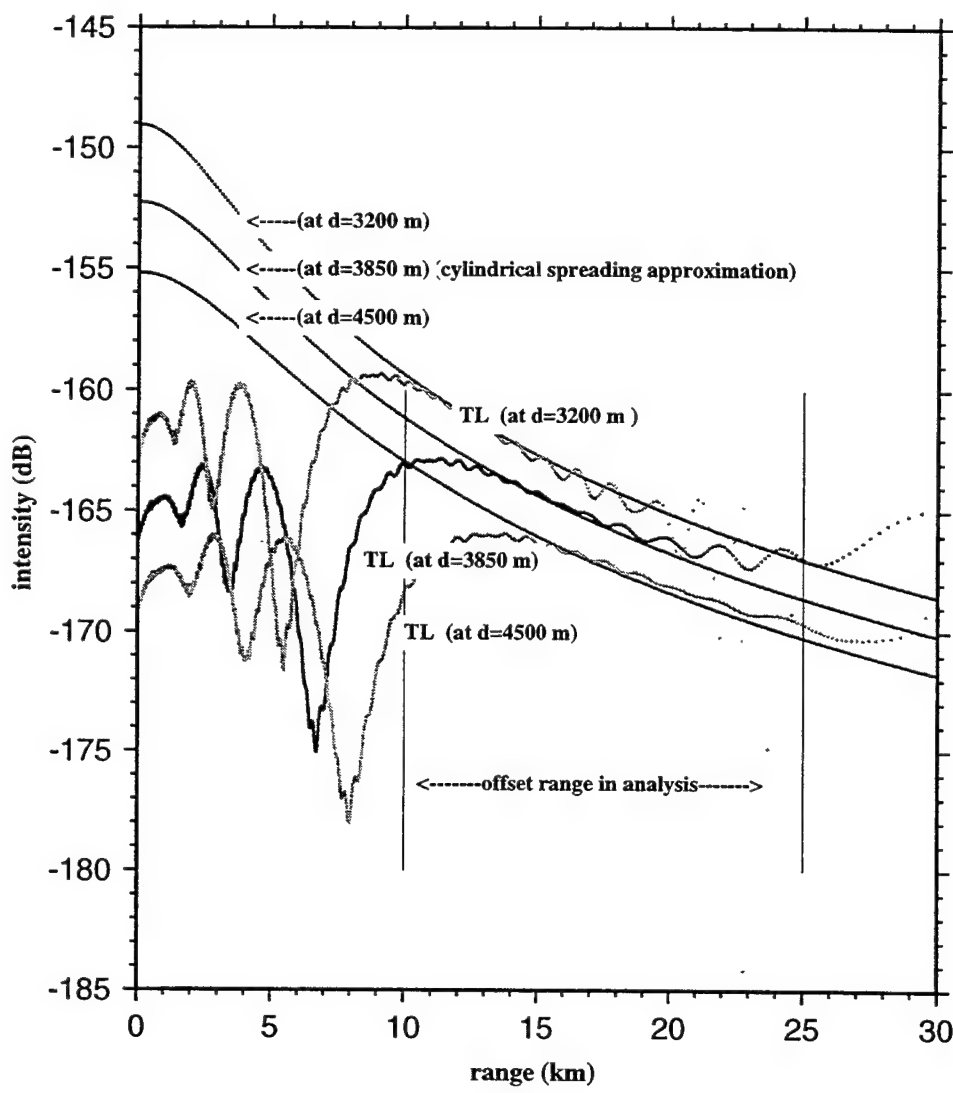


Figure A-2: Transmission loss predicted by two-way cylindrical spreading decay (shifted by $TL_o = 0.00243d + 71.15$ dB where d is the depth) compared to the transmission loss predicted by total energy decay (TL), calculated as the combination of ray divergence and the incoherent spatial beam pattern, for the depth range used in our analysis. The cylindrical spreading curves predict the energy loss between 12 km and 22 km within +/- 0.5 dB. Between 10 km and 12 km the error is larger but only for deep seafloor areas. In the worst case, 4500 m at a range of 10 km, the error is about -4 dB. In the far ranges, the error is larger for the most shallow depths. In the worst case, (3200 m at 25 km), the error is about 4 dB, however little data was observed in this range (see Figure 7).



Appendix B

Seafloor Photograph Interpretations

Interpretations of photographs taken from JASON in Site A.

ESC Photos SITE A							
SITE	LOWERING	TAPE	IMAGES	DATE	TIME	FEATURES	SFLR CLASS
A	153	14	3-5	5/31/93	11:09:34- 11:10:13	mottled sediment (mottled=sed covered volcanic cobbles ?)	mottled sediment (MS)
A	153	14	6	5/31/93	11:10:33	3/4 smooth sediment 1/4 mottled	smooth sediment (SS)
A	153	14	7	5/31/93	11:10:53	1/2 smooth sediment 1/2 mottled	SS
A	153	14	8	5/31/93	11:11:13	1/2 smooth sediment 1/2 mottled	SS
A	153	14	9	5/31/93	11:11:33	1/3 smooth sediment 2/3 mottled	MS
A	153	14	10	5/31/93	11:11:53	smooth sediment	SS
A	153	14	11-22	5/31/93	11:12:13	smooth sediment	SS
A	153	14	23	5/31/93	11:16:13	sediment with some worm burrows	bioturbated sediment (TS)
A	153	14	24	5/31/93	11:16:33	worm burrow in (cobbled?) sediment	TS
A	153	14	25	5/31/93	11:16:53	sediment with burrows	TS

	A	153	14	123	5/31/93	12:16:01	sediment (rippled sediment (RS))	rippled sediment (RS)
A	153	14	124	5/31/93	12:16:21	" " "		RS
A	153	14	125	5/31/93	12:16:41	1/3 smooth sediment ; hummocky sediment or sediment covered cobbles ; some linear	2/3	MS
A	153	14	126	5/31/93	12:17:01	sediment pond, smooth sediment	SS	
A	153	14	127	5/31/93	12:17:21	2/3 smooth sediment ; slightly lineated hummocky sediment or sediment covered	1/3	SS
A	153	14	128	5/31/93	12:17:41	1/3 smooth sediment ; hummocky sediment or sediment covered cobbles ; some linear streaks	2/3	MS
A	153	14	129	5/31/93	12:18:01	hummocky sediment or sediment covered cobbles	MS	
A	153	14	130	5/31/93	12:18:21	sediment with burrows	TS	
A	153	14	131-132	5/31/93	12:18:41	1/4 smooth sediment ; 3/4 - mottled sediment with burrows	TS	
A	153	14	133	5/31/93	12:19:21	mottled sediment	MS	
A	153	14	134	5/31/93	12:19:41	smooth sediment	SS	
A	153	14	135	5/31/93	12:20:01	smooth sediment	SS	

A	153	14	136	5/31/93	12:20:21	?	
A	153	14	137	5/31/93	12:20:41	smooth sediment	SS
A	153	14	138	5/31/93	12:21:01	top 1/3 mottled sediment; bottom 2/3 smooth sediment with sparse exposures of jagged basalt	jagged cobbles w/ sediment fill (JC)
A	153	14	139-140	5/31/93	12:21:21	1/2 smooth sediment;	
A	153	14	141	5/31/93	12:22:01	- mottled sediment	MS
A	153	14	142	5/31/93	12:22:21	mottled sediment (covered cobbles?) with some worm burrow	TS
A	153	14	143	5/31/93	12:22:41	" " "	
A	153	14	144	5/31/93	12:23:01	S-shaped burrows	TS
A	153	14	145	5/31/93	12:23:21	mottled sediment	MS
A	153	14	146	5/31/93	12:23:41	lower left corner smooth sediment; rest mottled sediment	MS
A	153	14	147	5/31/93	12:24:01	4/5 smooth sediment; right side streaked mottled sediment	SS
A	153	14	148-149	5/31/93	12:24:21- 12:24:41	mottled sediment	MS
A	153	14	150	5/31/93	12:25:01	lower left 1/3 smooth sediment; rest mottled sediment	MS

A	153	14	151-154	5/31/93	12:25:29	mottled sediment w/ large S-shaped burrow trail	TS
A	153	14	155-165	5/31/93	12:26:29	mottled sediment	MS
A	153	14	166	5/31/93	12:30:29	low left 1/4 smooth sediment; rest is mottled w/ burrow trails	TS
A	153	14	167	5/31/93	12:30:49	1/2 smooth 1/2 mottled sediment	MS
A	153	14	168-170	5/31/93	12:31:09	mottled sediment	MS
A	153	14	171	5/31/93	12:32:09	slightly mottled sediment w/ burrows	TS
A	153	14	172	5/31/93	12:32:29	left 1/2 smooth sediment; 1/2 mottled	MS
A	153	14	173-174	5/31/93	12:32:49	left 1/2 smooth 1/2 mottled sediment	MS
A	153	14	175	5/31/93	12:33:29	mottled sediment	MS
A	153	14	176	5/31/93	12:33:49	mottled sediment w/ some linear streaks	MS
A	153	14	177	5/31/93	12:34:09	mottled sediment	MS
A	153	14	178	5/31/93	12:34:29	left 1/2 smooth sediment; 1/2 mottled sediment	MS
A	153	14	179	5/31/93	12:34:49	mottled sediment w/ linear streaks	MS
A	153	14	180	5/31/93	12:35:09	mottled sediment w/ linear streaks	MS

A	153	14	181	5/31/93	12:35:29	lower left and upper right smooth sediment; rest mottled	SS
A	153	14	182	5/31/93	12:35:49	mottled sediment	MS
A	153	14	183	5/31/93	12:36:09	lower left 1/6 smooth; rest is mottled sediment with lineations normal to smooth sediment contours and burrows	MS
A	153	14	184	5/31/93	12:36:29	lower left 1/2 smooth sediment; 1/2 mottled w/ same lineations	MS
A	153	14	185-187	5/31/93	12:36:49	lower left 1/3 smooth sediment; - 2/3 mottled with same	MS
A	153	14	188	5/31/93	12:37:49	sediment	MS
A	153	14	189 -190	5/31/93	12:38:09	sediment (or water column?)	MS
A	153	14	191	5/31/93	12:38:49	lower left 1/3 smooth sediment; rest mottled w/ lineations	MS
A	153	14	192	5/31/93	12:39:09	top of basalt scarp; pillows or talus at bottom ;lineations down slope direction (from rocks rolling down?); burrow on slope; feathery lineation at what appears to be the slope break is normal to dip direction may be a sediment slump feature	BB (exposed basalt basement)

A	153	14	193	5/31/93	12:39:29	sets of pillow basalts and talus at bottom of slope in stairstep orientation; sediment between pillow groups is smooth; linear streak downslope	BB
A	153	14	194	5/31/93	12:39:49	basalt ledges; thinly sedimented basalt at top of scarp; pillow basalts w/ sediment fill	BB
A	153	14	195	5/31/93	12:40:09	basalt scarp; upper right corner pillows; some smooth sediment	BB
A	153	14	196	5/31/93	12:40:29	basalt scarp with mottled sediment	BB
A	153	14	197	5/31/93	12:40:49	scarp; linear grouping of fractured pillow basalts ; may be overlying flows; very rough	FF (fractured basalt
A	153	14	198	5/31/93	12:41:09	fractured basalt pillows with sediment in between	FF
A	153	14	199	5/31/93	12:41:29	fractured basalt pillows with some filling sediment; partial view of very rough and steep	FF
A	153	14	200 - 201	5/31/93	12:41:49	pillows and talus w/ filling sediment	TT
A	153	14	202	5/31/93	12:42:29	overhang of scarp or top of steep scarp	unfractured basalt scarp (UF)d
A	153	14	203 - 205	5/31/93	12:42:49	steep (90 deg ?) scarp of pillow basalts and talus; scarp is down to right in image and orientated	FF
					12:43:29		

A	153	14	206	5/31/93	12:43:49	base of this portion of scarp	FF
A	153	14	207	5/31/93	12:44:13	sloping basalt ledges	FF
A	153	14	208 - 217	5/31/93	12:44:33	looking down another steep slope; pillows and talus; down -	FF
A	153	14	218 - 220	5/31/93	12:47:53	pillows on top of another steep scarp edge; scarp azimuth is about 60 deg from bottom of	FF
A	153	14	221	5/31/93	12:48:33	-	
A	153	14	222	5/31/93	12:48:53	pillows on top of 90 deg scarp or even overhang	FF
A	153	14	223-224	5/31/93	12:49:13	top of scarp, may overhang; also see streaks leading toward edge (perp. to scarp azimuth); some other lineations parallel to	FF
A	153	14	225	5/31/93	12:49:33	scarp edge w/ cracks parallel to scarp ; may be looking down on edge below scarp	FF
A	153	14	226-239	5/31/93	12:50:13	still see cracks parallel to scarp and possible ledge below	FF
A	153	14	240-246	5/31/93	12:50:33	Jason seems to be hovering over scarp and looking down at ledge	UF
A	153	14	247-280	5/31/93	12:57:33	floating particle only, no bottom image	
A	153	14	281-289	5/31/93	13:08:56-	poor image; scarp	FF
A	153	14	290-293	5/31/93	13:11:36	no bottom image	

A	153	14	294-296	5/31/93	13:13:16	top left corner of image shows scarp with pillow basalts on top	FF
A	153	14	297	5/31/93	13:13:56	which is to top left corner	
A	153	14	298-302	5/31/93	13:14:16	scarp, down to right; break through pillows on top	FF
A	153	14	303-307	5/31/93	13:14:36	scarp with possible mass wasting of about 1/3 of scarp edge seen in image	FF
A	153	14	308-312	5/31/93	13:16:16	scarp on left side of image	FF
A	153	14	313 - 314	5/31/93	13:17:56	similar to image 298	FF
A	153	14	315-317	5/31/93	13:19:41	broken pillow basalts; some possibly from mass wasting of scars above	FF
A	153	14	319-336	5/31/93	13:20:21-	no bottom image	
A	153	14			13:21:01	moderate slope mostly sediment covered	FF
A	153	14			13:21:21	poor image; some outcropping basalt cobbles in sediment	
A	153	14			13:27:41	top left 2/3 of image looks like a scarp edge	BB
A	153	14				top of scarp; top half of image looks like mottled sediment; bottom half looks like boulders	BB

A	153	14	339	5/31/93	13:28:21	top of scarp	
A	153	14	340-341	5/31/93	13:28:41	looks like may be a cobbley or pillow covered floor in the	rounded cobbles
		14	347	5/31/93	13:31:01	rippled sediment	rippled sediment (RS)
A	153	15	0-209	5/31/93		black except fish and shadow on image 190	
A	153	15	210-216	5/31/93	15:01:41- 15:03:41	left 1/2 mottled; right half pillow flow	BB
A	153	15	217-227	5/31/93	15:04:01- 15:07:21	right 1/2 is rough blocks of basalt pillows surrounded by sediment; left 1/2 mottled sediment; probably sediment over talus pile (TT)	
A	153	15	228-231	5/31/93	15:07:41- 15:08:41	right bottom 1/4 and bit of top right is basalt blocks; rest is	TT
A	153	15	232-234	5/31/93	15:09:01	top right 1/4 looks like pillow flow but blocks are jagged with	TT
A	153	15	235-239	5/31/93	15:10:01 - 15:11:21	pillow flow	BB

A	153	15	240	5/31/93	15:11:41	scarp or edge of pillow flow cuts image down from left to right at about 20 deg below horizontal	TT
A	153	15	241-242	5/31/93	15:12:01	rough pillows or broken pillows with sediment fill and some	TT
A	153	15	243-250	5/31/93	15:12:41	down to left; mottled look probably top of pillow flow with	BB
A	153	15	251-257	5/31/93	15:15:21	right half looks like 243-250; left half too deep to see	BB
A	153	15	258-260	5/31/93	15:17:44	bottom right 1/4 edge of basalt flow or cone	BB
A	153	15	261	5/31/93	15:18:44	top right 1/2 pillows w/ sediment, may be base of slope; bottom too deep in rest of image	RC
A	153	15	262-270	5/31/93	15:19:04	left 1/2 seds with some pillows; right 1/2 is edge of	RC
A	153	15	271-274	5/31/93	15:22:04	right 1/2 scarp at about 60 deg above horiz down to left; upper side pillow flow; lower side may be sediment covered ledge; jointing in outcrops	BB
A	153	15	275-282	5/31/93	15:23:24	left 1/3 too deep to see; middle 1/3 is continuation of lower	BB
A	153	15	283-294	5/31/93	15:26:04	right 7/8 sparse covering of pillow boulders in sediment;	BB
A	153	15	295-405	5/31/93	15:30:04	black	

A	153	16	0-1	5/31/93	16:09:15- 16:10:04	mottled sediment
A	153	16	2-9	5/31/93	16:10:24	mottled with some burrows
A	153	16	10-15	5/31/93	16:13:04 -	left 1/2 smooth sed. pond; right half mottled sed.
A	153	16	16-21	5/31/93	16:15:04 -	left side smooth sed. pond increasing from 2/3 image to 1/8
A	153	16	22-23	5/31/93	16:17:04 -	mottled sediment w/ Jason pickup
A	153	16	24	5/31/93	16:17:44	no usable image/ Jason pickup
A	153	16	25-51	5/31/93	16:18:04 -	mottled sediment
A	153	16	52-53	5/31/93	16:27:06 -	mottled sediment w/ single pillow basalt boulder at top of
A	153	16	54	5/31/93	16:27:46 -	mottled sediment w/ single pillow basalt boulder at bottom
A	153	16	55-58	5/31/93	16:28:06 -	mottled sed. w/ burrow tracks
						and striation across image at about 60 -70 deg clockwise relative to Jason direction; sediment covered talus slope?
A	153	16	59-69	5/31/93	16:29:26 -	mottled sed. w/ occasional burrow track; talus slope?
A	153	16	70-71	5/31/93	16:33:06 -	mottled sed w/ a set of wiggly but parallel tracks (burrows?); sediment covered talus?
						TT

A	153	16	72	5/31/93	16:33:46	mottled sediment over talus at base of scarp	TT
A	153	16	73	5/31/93	16:34:06	mottled sediment over talus at base of scarp	TT
A	153	16	74	5/31/93	16:34:26	mottled sed w/ a very nice S-shaped burrow track	TT
A	153	16	75-81	5/31/93	16:34:46	mottled sediment w/ burrow tracks	TS
A	153	16	82-84	5/31/93	16:37:06	upper left corner pillows; upper right corner bowl shaped bare	FF
A	153	16	85-90	5/31/93	16:38:06	base of scarp; top left corner large pillows rising above mottled sediment, looks like edge of flow; rest is mottled sed	FF
A	153	16	91-92	5/31/93	16:40:06	upper left 1/2 pillow pile or flow edge; rest looks now like	FF
A	153	16	93	5/31/93	16:40:46	top 1/8 of image looks like flow overriding a lower flow in left	FF
A	153	16	94-95	5/31/93	16:41:06-	upper 1/3 is pillow flow ; scarp edge about 90 deg	FF
A	153	16	96-97	5/31/93	16:41:46	upper 1/2 pillow flow; scarp down toward bottom of image; 90	FF

A	153	16	98	5/31/93	16:42:26	large round pillows w/ sed between; looks like flow with dropoff on either side; drops off in upper right and lower left corners	FF
A	153	16	99	5/31/93	16:42:46	upper right corner pillow pile; lower 1/2 also pillows but in between these pillows looks like an open joint or fissure filled sediments and a few pillow fragments	FF
A	153	16	100	5/31/93	16:43:06	pillows in upper 2/3; low 1/3 is the fissure; there appear to be lineations of pillows which step down to the right in both pillow flow and the channel	FF
A	153	16	101	5/31/93	16:43:26	upper 1/3 pillows that appear higher than bottom half of image which is also pillows with steps dropping off to the right; fissure in between running left	FF
A	153	16	102-105	5/31/93	16:43:51	top 1/2 high side of scarp; scarp down toward bottom of	FF
A	153	16	106-111	5/31/93	16:45:11	top of scarp or edge of flow; down to lower left corner	UF
A	153	16	112-113	5/31/93	16:47:11	pillow field interfilled w/ seds; talus fill	TT
					16:47:31		

A	153	16	114	5/31/93	16:47:51	lower left 1/2 of image is pillows w/scarp diagonal across	TT
A	153	16	115	5/31/93	16:48:11	upper 1/2 half smooth sed w/ linear tracks that look like traces of boulders rolling; lower 1/2 is pillows probably	TT
A	153	16	116	5/31/93	16:48:31	upper 1/3 pillows; left 1/2 seds with tracks; boulder step on right with steep slope down to right past step; talus pile	TT
A	153	16	117	5/31/93	16:48:51	left 1/2 pillows and channel; scarp diagonally across image	FF
A	153	16	118-119	5/31/93	16:49:11	top 1/2 pillows; scarp almost 90 deg degraded in spots and down	FF
A	153	16	120-122	5/31/93	16:49:51	tall cliff cut image diagonally from top right corner to middle	FF
A	153	16	123-128	5/31/93	16:50:51	scarp corner up to top left down to right	FF
A	153	16	129-138	5/31/93	16:52:51	looking down the scarp at possible ledge covering middle diagonal 1/3 of image with another scarp down to right from	FF
A	153	16	139-144	5/31/93	16:56:11	left 2/3 pillows w/ seds; right 1/3 down steeply to right	UF
A	153	16	145-147	5/31/93	16:58:11	top left diagonal 1/2 pillows; steep (90deg) scarp with breaks for ledges down to right; substantial scarp but can't tell	UF

A	153	16	148-150	5/31/93	16:59:11	down slope to lower right; leaving boulder (pillows) strewn	UF
A	153	16	151	5/31/93	17:00:11	boulder field view with sed fill	FF
A	153	16	152-160	5/31/93	17:00:31	boulder field down to right; Jason descending?	FF
A	153	16	161-164	5/31/93	17:03:37	either large pillow or close-up of pillows; near top of ridge	BB
A	153	16	165-167	5/31/93	17:04:57	pillows with slightly higher crag of pillows in upper left	BB
A	153	16	168	5/31/93	17:05:57	mostly the crag of pillows with edge in lower left corner	BB
A	153	16	169-175	5/31/93	17:06:17	pillows	BB
A	153	16	176-179	5/31/93	17:08:37	top left and bottom left corners	MS
A	153	16	180-181	5/31/93	17:09:57	pillows: rest is sediment image no good	
A	153	16	182	5/31/93	17:11:22	top left 1/2 smooth sediment, sediment pond; lower right 1/2	MS
A	153	16	183	5/31/93	17:11:42	left 2/3 smooth sed (pond?); rest mottled sed	SS
A	153	16	184-185	5/31/93	17:12:02	image no good?	
A	153	16	186-187	5/31/93	17:12:42	mottled sed w/ a few pillow fragments	MS
A	153	16	188-196	5/31/93	17:13:22	mottled sed w/burrow tracks and some lineations	TS
A	153	16	197	5/31/93	17:16:22	mottled sed w/ some tracks and occasional pillow fragment	TS

A	153	16	198-199	5/31/93	17:16:42	mottled sed w/ nice S-shaped burrow tracks	TS
A	153	16	200-220	5/31/93	17:17:22	mottled sed w/ occasional burrow track	TS
A	153	16	221	5/31/93	17:24:02	sed pond in left 1/2 of image; rest is mottled sed	MS
A	153	16	222	5/31/93	17:24:22	mottled sed w/ Jason kickup	MS
A	153	16	223	5/31/93	17:24:42	lower 1/2 sed pond; rest mottled sed	MS
A	153	16	224-235	5/31/93	17:25:02	rippled mottled seds	RS
A	153	16	236-239	5/31/93	17:28:48	mottled sed w/ burrow (or creature itself?); furry, wiggly	TS
A	153	16	240-250	5/31/93	17:30:08	mottled sediment	MS
A	153	16	251	5/31/93	17:33:48	left 3/4 smooth sed pond; right 1/4 streaked mottled sed.	SS
A	153	16	252	5/31/93	17:34:08	left 1/2 smooth sed pond; right 1/2 mottled sed	MS
A	153	16	253	5/31/93	17:34:28	mottled sed	MS
A	153	16	254	5/31/93	17:34:48	mottled sed w/ burrow track	TS
A	153	16	255-256	5/31/93	17:35:08	mottled sed	MS
A	153	16	257	5/31/93	17:35:48	lower left 1/3 smooth sed pond; rest mottled sed	MS

A	153	16	258-260	5/31/93	17:36:08	mottled sed w/ burrow tracks	TS
A	153	16	261-290	5/31/93	-	no images	
A	153	17	0-5	5/31/93		blank	
A	153	17	6-11	5/31/93		blank	
A	153	17	12-122	5/31/93	0:00:00	black	
A	153	17	123-137	5/31/93		flat pillow field	

JASON VIDEO IMAGES: ARSRP SITE A
(JULY 31, 1993)

TIME	Hi 8 tape	Beta tape	DESCRIPTION
11:11:41	34	1	mottled sediment, gentle slope : JASON stationary
11:15:00		1	image dark but still mottled sediment
11:17:00- 11:17:19		1	no image
12:16:15		1	no image
12:16:25		1	image dark; mottled sediment
12:17:00		1	camera panning around
12:17:11		1	no image
12:17:21- 12:17:54		1	mottled sediment, flat seafloor, poor lighting
12:18:43- 12:19:27		nr	no image; not copied on beta tape
12:19:27- 12:22:00		1	still mottled sediment; JASON stationary; camera panning
12:22:00- 12:23:00		1	water column
12:23:04- 12:23:52		nr	no image; not copied
12:23:52		1	mottled sediment; gently sloping seafloor
12:24:11- 12:27:54		1	linear track in sediment; JASON moving up and down
12:28:00- 12:29:15		1	water column
12:29:15- 12:30:14		nr	no image; not copied
12:30:14		1	dark
12:30:18		1	can see mottled sediment bottom only when strobe light flashes
12:30:29- 12:33:38		1	mottled sediment in strobe
12:35:01- 12:36:11		nr	no image; not copied
12:36:11- 12:37:58		1	mottled sediment in strobe; gentle slope
12:38:00- 12:39:00		nr	no image; not copied
12:39:01		1	mottled sediment
12:39:18		1	basalt fragments w/ sediment fill; slope down to top right of image; image only visible in strobe
12:39:58		1	in strobe; steep basalt scarp with pillows and pillow fragments
12:40:18		1	very dark; sediment at top of slope break
12:40:18- 12:40:38		1	steep scarp; bare rock; pillows and fragments
12:40:58		1	linear fissure through pillows; scarp down to top right of image
12:41:18		1	rough basalt slope; very steep
12:41:58		1	more cracks through pillows
12:42:08		1	70-90 degree basalt scarp; essentially a cliff

TIME	Hi 8 tape	Beta tape	DESCRIPTION	
12:42:34	34	1	pillow at top of scarp; clearly sheared off at scarp break; very steep slope below	
12:43:42		1	lineations due to joints and cracks parallel to slope strike	
12:43:57		1	base of ledge on scarp	
12:44:02		1	side view of corner in scarp; may be edge of pillow flow	
12:44:22		1	scarp with joints parallel to slope strike; bare basalt	
12:44:36		1	improved lighting; steep slope with exposed basalt; sediment on small ledges; small sediment chutes	
12:45:20		1	jointing in two directions; parallel to slope strike and some oblique to strike	
12:48:25- 12:48:34		1	shear planes?; basalt fractured such that seafloor looks like end of stack of plates	
12:52:33		1	scarp	
12:54:22		1	bare basalt scarp; pillows and some sheet flow	
12:55:22		1	decrease in slope; more sediment cover; may be 10's of cm thick here	
12:57:42		1	in strobe can still see bottom is basalt scarp with collected sediment on small ledges	
12:57:59	34	1	End of Hi 8 tape 1	
***	***	***	START WIDE ANGLE CAMERA IMAGES	
11:11:41- 12:38:00	35	2	no visible images until 12:39 in following most images only visible when the ESC strobe light flashes	
12:39:18		2	in ESC strobe can see mottled sediment on crest of scarp; co-linear ledges on scarp stepping down to right in image	
12:39:58		2	very sharply delineated joints and ledge edges creating stairway down slope	
12:40:18		2	sediment on large ledge or edge of plateau with bare basalt on right followed by drop off to scarp	
12:40:38		2	in strobe can see some slump lines in sediment parallel to scarp edge, probably indicating sediment on fairly steep slope	
12:40:58		2	fractures or fissures in basalt parallel to scarp strike	
12:41:18- 12:41:38		2	scarp	
12:42:22		2	large pillow basalt clearly sheared off at the scarp dropoff. May also be sheared off on backside where there is a lineation that is a joint or crack in the pillow	
12:43:22			steep rough scarp face with sediment collected in small ledges; mostly bare basalt	

TIME	Hi 8 tape	Beta tape	DESCRIPTION	
12:44:22	35	2	pile of basalt pillows or a pillow flow	
12:45:42- 12:46:26		2	steep slope of basalt fragments	
12:48:02- 12:51:02		2	looking down on very steep basalt slope with linear sediment covered ledges	
12:52:22- 12:55:02		2	steep slope with vertical drop at base	
12:55:22		2	more sediment on slope	
12:56:42- 12:57:22		2	same steep scarp	
12:57:42		2	End of Tape	
13:13:01- 13:13:25	36	3	black	
13:13:25		3	dim image of basalt scarp	
13:13:45		3	scarp with dropoff to deep on right side of image	
13:14:05		3	scarp	
13:14:25		3	lineations in scarp due to fissures or cracks	
13:14:45- 13:16:30		3	scarp with wide ledge at foot of it	
13:16:50- 13:18:50		3	scarp with sediment on ledges	
13:19:10- 13:20:30		3	poor image but looks like increasing amount of sediment and decreasing slope; probably talus ramp	
13:20:50- 13:21:50		3	blank; EOT	
13:12:58	37	3	pipe on frame of JASON	
13:13:25- 13:14:25		3	dim bottom image of sediment scarp	
13:14:45- 13:15:05		3	fractures on scarp face and parallel to ridge strike	
13:15:25		3	rough scarp face	
13:15:50- 21:50:11		3	nothing visible ; EOT	
	39	3	camera on MEDEA but nothing useful and no times	
	38	4	camera on MEDEA but nothing useful and not timed	
*	*	*	CLOSE UP CAMERA ON JASON most images only showing up when ESC strobe flashes	
16:07:11	40	5	black	
16:09:04- 16:10:15		5	mottled sediment with bottom dweller tracks	
16:10:53- 16:11:13		5	mottled sediment with single boulder in small crater	
16:11:33- 16:11:53		5	mottled sediment with bioturbation	
16:12:13- 16:12:33		5	mottled sediment with what may be ripples	
16:12:53		5	mottled sediment; gently sloping up toward top left corner of image	

TIME	Hi 8 tape	Beta tape	DESCRIPTION	
16:15:12	40	5	mottled sediment with shallow drainage channels or chutes meandering down a gentle slope; occasional basalt cobble	
16:18:14		5	mottled sediments	
16:19:34- 16:24:52		5	mottled sediment with more cobbles	
16:26:12		5	isolated pillow or pillow fragment on sediment; note that it is held up by the sediment	
16:27:15		5	mottled sediment with some streaks probably due to rocks rolling or slipping down the gentle slope	
16:29:25		5	another jagged boulder resting on sediment in small crater	
16:31:35		5	mottled sediment with ripples or bioturbation that seems to be perpendicular to the local gentle slope	
16:32:30		5	basalt fragment and large zigzag bottom track	
16:32:55		5	may be cucumber shaped creature on bottom	
16:34:23		5	lots of tracks and bioturbation in mottled sediments	
16:35:21- 16:35:41		5	mottled sediment with what appears to be small slumping but is probably just creature tracks	
16:35:44		5	beginning of bare basalt and clearly transition from sediment to bare basalt of scarp	
16:36:32- 16:36:40		5	fractures and joints in solid basalt with some fractured pillows; sediment filled chutes	
*	*	*	SWITCHED TO WIDE ANGLE CAMERA ON JASON	
15:39:01	41	5	pipe on frame of JASON sled	
16:09:04- 16:22:32		5	mottled sediment with occasional basalt cobble	
16:32:35		5	large zigzag tracks leading up to base of basalt scarp	
16:36:00		5	start of bare basalt scarp; sediment on small ledges; pillows and fragments	
16:39:04		5	scarp	
*	*	*	CAMERA ON MEDEA	
15:07:00	42	6	pile of basalt pillows surrounded by sediment; JASON seems stationary; copied to EOT but not much of use in images	
*	*	*	CLOSE UP CAMERA ON JASON	
16:37:45- 16:39:45	43	7	fractured basalt scarp with light dusting of sediment; jointing and fractures clear; sediment on ledges and in chutes;	
16:41:35		7	pillow basats	
16:42:00		7	top of first large scarp section; can see corner of scarp with wider ledge at top	
16:42:12		7	starting up next section of scarp; very steep with more sediment but still more than 50% bare basalt, pillows and fragments	

TIME	Hi 8 tape	Beta tape	DESCRIPTION
16:46:48- 16:48:00	43	7	large sediment and talus filled chute
16:52:20		7	back to steep basalt scarp
16:56:20		7	can see scarp is very steep > 45 degrees; whole slope covered by basalt rubble and pillows
17:00:10		7	scarp slope is less steep ; less fragments seen and more sediment between fragments and pillows
17:03:27- 17:04:46		7	vertical or overhanging cliff; cobbled bottom at base of cliff
17:06:12		7	near ridge crest; still steep but sediment cover increasing and covering much of basalt
17:07:06		7	mottled sediment
17:09:26		7	a few exposures of basalt in low ridges but mostly sediment with bioturbation
17:10:01		7	some sediment slump lines sub-parallel to slope strike
17:10:40		7	basalt exposed on two sides of what may be large sediment chute
17:11:37		7	mottled sediment with bioturbation
17:15:48		7	can only see bottom in strobe; mottled sediment
17:16:09		7	sediment with some possible ripples
17:20:24		7	very dark
17:21:12		7	mottled sediments visible in strobe
17:23:25- 17:25:06		7	mottled sediments; looks very flat; bioturbated
17:26:12- 17:33:37		7	mottled sediment with clear bioturbation and bottom dweller tracks
17:37:17		7	EOT
*	*	*	WIDE ANGLE CAMERA ON JASON
16:39:29	44	8	dark but can see basaltic slope
16:39:35		8	cliff with talus at foot and talus slope
16:39:55		8	ragged, fractured basalt scarp
16:40:15		8	very steep ~90 degrees; fractured basalt
16:40:15- 16:40:35		8	very steep with small pools of sediment on ledges
16:41:55		8	steep scarp covered with pillows; fissure or large open fracture parallel to slope strike
16:43:41		8	slope with more sediment chutes and jointing of basalt
16:45:08		8	sheared pillow tube with fractures and surrounded by basalt debris
16:47:01- 16:56:03		8	large ledge with increased sediment cover
16:56:21		8	camera direction changed and can see scarp
16:58:00		8	basalt scarp

Bibliography

- K. Aki. Scattering and attenuation. *Bulletin of the Seismological Society of America*, 72(6):S319–S330, 1982.
- K. Aki and P.G. Richards. *Quantitative Seismology, Theory and Methods, V. 1*. W.H. Freeman and Co., New York, 1980.
- ARSRP, 1992. 15-kHz Hydrosweep bathymetry data, Mesotech bathymetry and electronic photographic images were collected during the 1992 R/V Ewing Cruise 9208. The Principal Investigator B.E. Tucholke and Co-Principal Investigators, M.C. Kleinrock and J. Lin, were from Woods Hole Oceanographic Institution.
- A. Baggeroer, December 1994. personal communication.
- A. B. Baggeroer and I. Dyer. Long range, low frequency acoustic backscattering: a review. In T. Akal and J.M. Berkson, editors, *Ocean Seismo-Acoustics, Low-frequency Underwater Acoustics*, pages 313–326. Plenum Press, New York, 1986.
- A.B. Baggeroer, W.A. Kuperman, and Henrik Schmidt. Matched field processing: Source localization in correlated noise as an optimum parameter estimation problem. *Journal of the Acoustical Society of America*, 82(2):571–587, 1988.
- A.B. Baggeroer and J.A. Orcutt. An overview of the 1991 Reconnaissance Cruise of the Acoustic Reverberation Special Research Program. In D.D. Ellis, J.R. Preston, and H.G. Urban, editors, *Ocean Reverberation*, pages 183–188. Kluwer Academic Publishers, The Netherlands, 1993.

- F.A. Bowles. A geoacoustic model for fine-grained unconsolidated calcareous sediments (ARSRP Natural Laboratory). NRL/MR/7432-93-7082, Naval Research Lab, Stennis Space Center, MS, 1994.
- R.N. Bracewell. *The Fourier Transform and Its Applications*. McGraw-Hill Book Co., New York, 1978.
- C.R. Bradley. *Very low frequency seismo-acoustic noise below the sea floor (0.2-10 Hz)*. PhD thesis, Massachusetts Institute of Technology/Woods Hole Oceanographic Institution, 1994.
- L.M. Brekhovskikh. *Waves in Layered Media*. Academic Press, New York, 1960.
- S.L. Broschat and E.I. Thorsos. An investigation of the small slope approximation for scattering from rough surface. Part II. Numerical studies. *Journal of the Acoustical Society of America*, 101(5):2615–2625, 1997.
- Jerald W. Caruthers, E.J. Yoerger, and J.C. Novarini. Modeling low-frequency reverberation near the Mid-Atlantic Ridge and comparison with ARSRP data. *Journal of the Acoustical Society of America*, 101(5):2555–2565, 1997.
- N.I. Christensen, R.D. Hyndman, J.M. Hull, and M.H. Salisbury. Seismic velocities, electrical resistivities, densities, and porosities of basalts from DSDP Leg 46. In L. Dmitriev, J. Heirtzler, and *et al*, editors, *Initial Reports of the Deep Sea Drilling Project, Volume 46*, pages 383–388. U.S. Government Printing Office, Washington, 1978.
- G.L. Christeson. *Seismic constraints on shallow crustal processes at the East Pacific Rise*. PhD thesis, Massachusetts Institute of Technology/Woods Hole Oceanographic Institution, 1994.
- L. Dmitriev, J. Heirtzler, and *et al*. Introduction and explanatory notes. In L. Dmitriev, J. Heirtzler, and *et al*, editors, *Initial Reports of the Deep Sea Drilling Project, Volume 46*, pages 3–13. U.S. Government Printing Office, Washington, 1978.

- M.E. Dougherty and R.A. Stephen. Geoacoustic scattering from seafloor features in the ROSE area. *Journal of the Acoustical Society of America*, 82(1):238–256, 1987.
- M.E. Dougherty and R.A. Stephen. Seismic energy partitioning and scattering in laterally heterogeneous ocean crust. *Pure and Applied Geophysics*, 128(1/2):195–229, 1988.
- M.E. Dougherty and R.A. Stephen. Seismo/acoustic propagation through rough seafloors. *Journal of the Acoustical Society of America*, 90(5):2637–2651, 1991.
- I. Dyer, A.B. Baggeroer, H. Schmidt, and J.R. Fricke. Discrete backscatter can be dominant in rough bottom reverberation. In D.D. Ellis, J.R. Preston, and H.G. Urban, editors, *Ocean Reverberation*, pages 51–57. Kluwer Academic Publishers, 1993.
- P. Elisseff. ARSRP 93: Acoustic shape estimation of a linear towed array. Internal report, Dept. of Ocean Engineering, MIT, 1995.
- D.D. Ellis, J.R. Preston, and H.G. Urban. *Ocean Reverberation*. Kluwer Academic Publishers, Netherlands, 1993.
- C.M.R. Fowler. *The Solid Earth*. Cambridge University Press, Cambridge, 1990.
- A. Frankel and R.W. Clayton. Finite difference simulations of seismic scattering: Implications for the propagation of short-period seismic waves in the crust and models of crustal heterogeneity. *Journal of Geophysical Research*, 91(B6):6465–6489, 1986.
- G.V. Frisk, J.A. Doutt, and E.E. Hays. Bottom interaction of low-frequency acoustic signals at small grazing angles in the deep ocean. *Journal of the Acoustical Society of America*, 69(1):84–94, 1981.
- S.S. Fu, R.H. Wilkens, and L.N. Frazer. Acoustic lance: New *in situ* seafloor velocity profiles. *Journal of the Acoustical Society of America*, 99(1):234–242, 1996.

- M. Gensane. Sea-bottom reverberation: The role of volume inhomogeneities of the sediment. In D.D. Ellis, J.R. Preston, and H.G. Urban, editors, *Ocean Reverberation*, pages 59–64. Kluwer Academic Publishers, 1993.
- J.A. Goff and T.H. Jordan. Stochastic modeling of seafloor morphology: Inversion of Sea Beam data for second-order statistics. *Journal of Geophysical Research*, 93(B11):13,589–13,608, 1988.
- D. Goldberg and Y.F. Sun. Seismic structure of the upper oceanic crust revealed by *in situ* Q logs. *Geophysical Research Letters*, 24(3):333–336, 1997.
- R.J. Greaves and R.A. Stephen. Seafloor acoustic backscattering from different geological provinces in the Atlantic Natural Laboratory. *Journal of the Acoustical Society of America*, 101(1):193–208, 1997.
- N.R. Grindlay, P.J. Fox, and P.R. Vogt. Morphology and tectonics of the Mid-Atlantic Ridge (25° - $27^{\circ}30'$ s) from Sea Beam and magnetic data. *Journal of Geophysical Research*, 97(B5):6983–7010, 1992.
- E.L. Hamilton. Compressional-wave attenuation in marine sediments. *Geophysics*, 37(4):620–646, 1972.
- E.L. Hamilton. Shear-wave velocity versus depth in marine sediments: a review. *Geophysics*, 41(5):985–996, 1976.
- E.L. Hamilton. Sound velocity gradients in marine sediments. *Journal of the Acoustical Society of America*, 65(4):909–922, 1979.
- E.L. Hamilton. Geoacoustic modeling of the sea floor. *Journal of the Acoustical Society of America*, 68(5):1313–1340, 1980.
- E.L. Hamilton, R.T. Bachman, W.H. Berger, T.C Johnson, and L.A. Mayer. Acoustic and related properties of calcareous deep-sea sediments. *Journal of Sedimentary Petrology*, 52(3):733–753, 1982.

- R. Houtz and J. Ewing. Upper crustal structure as a function of plate age. *Journal of Geophysical Research*, 81:2490–2499, 1976.
- R. Houtz, J. Ewing, and X. Le Pichon. Velocity of deep-sea sediments from sonobuoy data. *Journal of Geophysical Research*, 73:2615–2641, 1968.
- R.D. Hyndman and M.J. Drury. The physical properties of oceanic basement rocks from deep drilling on the Mid-Atlantic Ridge. *Journal of Geophysical Research*, 81(23):4042–4052, 1976.
- R.S. Jacobson and B.T.R. Lewis. The first direct measurements of upper oceanic crustal compressional wave attenuation. *Journal of Geophysical Research*, 95(B11):17,417–17,429, 1990.
- G.E. Jaroslow. *The geological record of oceanic crustal accretion and tectonism at slow-spreading ridges*. PhD thesis, Massachusetts Institute of Technology/Woods Hole Oceanographic Institution, 1997.
- F.B. Jensen, W.A. Kuperman, M.B. Porter, and H. Schmidt. *Computational Ocean Acoustics*. American Institute of Physics, New York, 1994.
- J.A. Karson and H.J.B. Dick. Tectonics of ridge-transform intersections at the Kane Fracture Zone. *Marine Geophysical Researches*, 6:51–98, 1983.
- K.R. Kelly, R.W. Ward, S. Treitel, and R.M. Alford. Synthetic seismograms: A finite-difference approach. *Geophysics*, 41(1):2–27, 1976.
- A.C. Kibblewhite. Attenuation of sound in marine sediments: A review with emphasis on new low-frequency data. *Journal of the Acoustical Society of America*, 86(2):716–738, 1989.
- R.J. Kirkpatrick. Results of downhole geophysical logging Hole 396B, DSDP Leg 46. In L. Dmitriev, J. Heirtzler, and *et al*, editors, *Initial Reports of the Deep Sea Drilling Project, Volume 46*, pages 401–407. U.S. Government Printing Office, Washington, 1978.

- M.C. Kleinrock. Capabilities of some systems used to survey the deep-sea floor.
In Richard A. Geyer, editor, *CRC Handbook of Geophysical Exploration at Sea, Hard Mineral*, pages 35–85. CRC Press Inc., second edition, 1992.
- N.C. Makris. Imaging ocean-basin reverberation via inversion. *Journal of the Acoustical Society of America*, 94(2):983–993, 1993.
- N.C. Makris, L.Z. Avelino, and R. Menis. Deterministic reverberation from ocean ridges. *Journal of the Acoustical Society of America*, 97(6):3547–3574, 1995.
- N.C. Makris and J. M. Berkson. Long-range backscatter from the Mid-Atlantic Ridge. *Journal of the Acoustical Society of America*, 95(4):1865–1881, 1994.
- L.A. Mayer. Deep-sea carbonates: acoustic, physical and stratigraphic properties. *Journal of Sedimentary Petrology*, 49(3):819–836, 1979.
- P. Milholland, M.H. Manghnani, S.O. Schlanger, and G.H. Sutton. Geoacoustic modeling of deep-sea carbonate sediments. *Journal of the Acoustical Society of America*, 68(5):1351–1360, 1980.
- S.K. Mitchell and K.C. Focke. New measurements of compressional wave attenuation in deep ocean sediments. *Journal of the Acoustical Society of America*, 67(5):1582–1589, 1980.
- D. Moos. Petrophysical results from logging in DSDP Hole 395A, ODP Leg 109.
In R. Detrick, J. Honnorez, W.B. Bryan, T. Juteau, and *et al*, editors, *Proceedings of the Ocean Drilling Program, Scientific Results, Vol. 106/109*, pages 237–253, College Station, TX, 1990.
- D. Moos and D. Marion. Morphology of extrusive basalts and its relationship to seismic velocities in the shallow oceanic crust. *Journal of Geophysical Research*, 99(B2):2985–2994, 1994.
- P.M. Morse and H. Feshbach. *Methods of Theoretical Physics*. McGraw-Hill, 1953.

J.E. Nafe and C.L. Drake. Variation with depth in shallow and deep water marine sediments of porosity, density and the velocities of compressional and shear waves. *Geophysics*, 22(3):523–552, 1957.

J.E. Nafe and C.L. Drake. Physical properties of marine sediments. In M.N. Hill, editor, *The Sea*, volume 3, pages 794–815. Wiley, New York, 1963.

Office of Naval Research. *Acoustic Reverberation Special Research Program, Initial Report, Acoustics Experiment, R/V Cory Chouest 5-26 July, 1993*.

J.A. Ogilvy. *Theory of Wave Scattering from Random Rough Surfaces*. Institute of Physics Publishing, Great Britain, 1991.

W.G. Oldham and S.E. Schwarz. *An Introduction to Electronics*. Holt, Rinehart and Winston, Inc., New York, 1972.

K.B. Olsen, R.J. Archuleta, and J.R. Matarese. Three-dimensional simulation of a magnitude 7.75 earthquake on the San Andreas Fault. *Science*, 270:1628–1632, 1995.

V.V. Ol'shevskii. *Characteristics of Sea Reverberation*. Consultants Bureau, New York, 1967.

A.D. Pierce. *Acoustics*. Acoustic Society of America, New York, 1991.

J.R. Preston, T. Akal, and J. Berkson. Analysis of backscattering data in the Tyrrhenian Sea. *Journal of the Acoustical Society of America*, 87(1):119–134, 1990.

G.M. Purdy. New observations of the shallow seismic structure of young oceanic crust. *Journal of Geophysical Research*, 92(B9):9351–9362, 1987.

M.D. Richardson, E. Muzi, B. Miaschi, and F. Turgutcan. Shear wave velocity gradients in near-surface marine sediment. In J.M. Hoven, M.D. Richardson, and R.D. Stoll, editors, *Shear Waves in Marine Sediments*, pages 295–304. Kluwer Academic Publishers, the Netherlands, 1991.

- J.O.A. Robertsson and A. Levander. A numerical study of seafloor scattering.
Journal of the Acoustical Society of America, 97(6):3532–3546, 1995.
- H. Schouten and R.S. White. Zero-offset fracture zones. *Geology*, 8:175–179, 1980.
- E. Schreiber and P.J. Fox. Compressional wave velocities and mineralogy of fresh basalts from the FAMOUS area and Oceanographer Fracture Zone and the texture of Layer 2A of the oceanic crust. *Journal of Geophysical Research*, 81(23):4071–4076, 1976.
- E. Schreiber and P.J. Fox. Density and p-wave velocity of rocks from the FAMOUS region and their implication to the structure of the oceanic crust. *Geological Society of America Bulletin*, 88:600–608, 1977.
- J.P. Severinghaus and K.C. MacDonald. High inside corners at ridge-transform intersections. *Marine Geophysical Researches*, 9:353–367, 1988.
- P.R. Shaw, D.K. Smith, R.A. Stephen, and J.W. Caruthers. Multiscale, multi-sensor analysis of seafloor topography in the ONR Atlantic Natural Laboratory. In *Acoustic Reverberation Special Research Program Symposium*. Scripps Institution of Oceanography, December 1993.
- P.M. Shearer. Cracked media, Poisson's ratio and the structure of the upper oceanic crust. *Geophysical Journal*, 92:357–362, 1988.
- R.E. Sheriff. *Encyclopedic Dictionary of Exploration Geophysics, Third Edition*. Society of Exploration Geophysicists., New York, 1978.
- K.B. Smith, W.S. Hodgkiss, and F.D. Tappert. Propagation and analysis issues in the prediction of long-range reverberation. *Journal of the Acoustical Society of America*, 99(3):1387–1404, 1996.
- R.A. Stephen. Lateral heterogeneity in the upper ocean crust at Deep Sea Drilling Project Site 504. *Journal of Geophysical Research*, 93(B6):6571–6584, 1988.

R.A. Stephen. Solutions to range-dependent benchmark problems by the finite-difference method. *Journal of the Acoustical Society of America*, 87(4):1527–1534, 1990.

R.A. Stephen and S.T. Bolmer. The direct wave root in marine seismology. *Bulletin of the Seismological Society of America*, 75(1):57–67, 1985.

R.A. Stephen and M.E. Dougherty. Canonical seafloor models and the finite difference method for low-angle acoustic backscatter. In R.L. Lau and A.R. Robinson, editors, *Computational Acoustics - Volume 1*, pages 227–246. Elsevier Science Publishers B.V., 1993.

R.A. Stephen, P.R. Shaw, and J.W. Caruthers. Modeling deterministic features in the ARSRP acoustic data. In *Acoustic Reverberation Special Research Program Symposium*. Scripps Institution of Oceanography, December 1993.

R.A. Stephen and S.A. Swift. Modeling seafloor geoacoustic interaction with a numerical scattering chamber. *Journal of the Acoustical Society of America*, 96(2):973–990, 1994.

S.A. Swift and R.A. Stephen. The scattering of a low-angle pulse beam from seafloor volume heterogeneities. *Journal of the Acoustical Society of America*, 96(2):991–1001, 1994.

M. Talwani, C.C. Windisch, and Jr. M.G. Landseth. Reykjanes Ridge Crest: A detailed geophysical study. *Journal of Geophysical Research*, 76(2):473–517, 1971.

D. Tang, G. Frisk, C.J. Sellers, and D. Li. Low-frequency acoustic backscattering by volumetric inhomogeneities in deep-ocean sediments. *Journal of the Acoustical Society of America*, 98(1):508–516, 1995.

E.I. Thorsos. The validity of the Kirchhoff approximation for rough surface scattering using a gaussian roughness spectrum. *Journal of the Acoustical Society of America*, 83(1):78–92, 1988.

- B.E. Tucholke. Acoustic environment of the Hatteras and Nares Abyssal Plains, western North Atlantic Ocean, determined from velocities and physical properties of sediment cores. *Journal of the Acoustical Society of America*, 68(5):1376–1390, 1980.
- B.E. Tucholke. Geological and geophysical survey of the Acoustic Reverberation Corridor, Mid-Atlantic Ridge. In *Acoustic Reverberation Special Research Program Symposium*. Scripps Institution of Oceanography, March 1991.
- B.E. Tucholke, M.C. Kleinrock, and W.K. Stewart. Fine-scale geological and geophysical surveys at sites B', C', A and D in the Acoustic Reverberation Corridor. In *Acoustic Reverberation Special Research Program Symposium*. Scripps Institution of Oceanography, December 1993.
- B.E. Tucholke and J. Lin. A geological model for the structure of ridge segments in slow spreading ocean crust. *Journal of Geophysical Research*, 99(B6):11,937–11,958, 1994.
- B.E. Tucholke, W.K. Stewart, and M.C. Kleinrock. Long-term denudation of ocean crust in the central North Atlantic ocean. *Geology*, 25(2):171–174, 1996.
- R.J. Urick. *Principle of Underwater Sound*. McGraw-Hill, Inc., New York, third edition, 1983.
- J. Urmos and R.H. Wilkens. In situ velocities in pelagic carbonates: new insights from Ocean Drilling Program Leg 130, Ontong Java Plateau. *Journal of Geophysical Research*, 98(B5):7903–7920, 1993.
- J. Virieux. P-SV wave propagation in heterogeneous media: Velocity-stress finite-difference method. *Geophysics*, 51(4):889–901, 1986.
- H.F. Webb and T.H. Jordan. Sedimentation and morphology in the ONR Acoustic Reverberation Corridor. *EOS, Trans. AM. Geophys. Union*, 76:553, 1995.

W.W. Wepfer and N.I. Christensen. Compressional wave attenuation in ocean basalts. *Journal of Geophysical Research*, 95(B11):17,431–17,439, 1990.

DOCUMENT LIBRARY

Distribution List for Technical Report Exchange – July 1998

University of California, San Diego
SIO Library 0175C
9500 Gilman Drive
La Jolla, CA 92093-0175

Hancock Library of Biology & Oceanography
Alan Hancock Laboratory
University of Southern California
University Park
Los Angeles, CA 90089-0371

Gifts & Exchanges
Library
Bedford Institute of Oceanography
P.O. Box 1006
Dartmouth, NS, B2Y 4A2, CANADA

NOAA/EDIS Miami Library Center
4301 Rickenbacker Causeway
Miami, FL 33149

Research Library
U.S. Army Corps of Engineers
Waterways Experiment Station
3909 Halls Ferry Road
Vicksburg, MS 39180-6199

Marine Resources Information Center
Building E38-320
MIT
Cambridge, MA 02139

Library
Lamont-Doherty Geological Observatory
Columbia University
Palisades, NY 10964

Library
Serials Department
Oregon State University
Corvallis, OR 97331

Pell Marine Science Library
University of Rhode Island
Narragansett Bay Campus
Narragansett, RI 02882

Working Collection
Texas A&M University
Dept. of Oceanography
College Station, TX 77843

Fisheries-Oceanography Library
151 Oceanography Teaching Bldg.
University of Washington
Seattle, WA 98195

Library
R.S.M.A.S.
University of Miami
4600 Rickenbacker Causeway
Miami, FL 33149

Maury Oceanographic Library
Naval Oceanographic Office
Building 1003 South
1002 Balch Blvd.
Stennis Space Center, MS, 39522-5001

Library
Institute of Ocean Sciences
P.O. Box 6000
Sidney, B.C. V8L 4B2
CANADA

National Oceanographic Library
Southampton Oceanography Centre
European Way
Southampton SO14 3ZH
UK

The Librarian
CSIRO Marine Laboratories
G.P.O. Box 1538
Hobart, Tasmania
AUSTRALIA 7001

Library
Proudman Oceanographic Laboratory
Bidston Observatory
Birkenhead
Merseyside L43 7 RA
UNITED KINGDOM

IFREMER
Centre de Brest
Service Documentation - Publications
BP 70 29280 PLOUZANE
FRANCE

REPORT DOCUMENTATION PAGE	1. REPORT NO. MIT/WHOI 98-15	2.	3. Recipient's Accession No.
4. Title and Subtitle Seismic Scattering of Low-Grazing-Angle Acoustic Waves Incident on the Seafloor		5. Report Date June 1998	6.
7. Author(s) Robert J. Greaves		8. Performing Organization Rept. No.	
9. Performing Organization Name and Address MIT/WHOI Joint Program in Oceanography/Applied Ocean Science & Engineering		10. Project/Task/Work Unit No. MIT/WHOI 98-15	11. Contract(C) or Grant(G) No. (C) N00014-93-1-1352 (G) N00014-90-J-1493 (G) N00014-95-1-0506
12. Sponsoring Organization Name and Address Office of Naval Research		13. Type of Report & Period Covered Ph.D. Thesis	14.
15. Supplementary Notes This thesis should be cited as: Robert J. Greaves, 1998. Seismic Scattering of Low-Grazing-Angle Acoustic Waves Incident on the Seafloor. Ph.D. Thesis. MIT/WHOI, 98-15.			
16. Abstract (Limit: 200 words) The goal of this thesis is to develop a methodology to interpret sound scattered from the seafloor in terms of seafloor structure and subseafloor geological properties. Specifically, this work has been directed towards the interpretation of matched-filtered, beamformed monostatic acoustic reverberation data acquired on the west flank of the Mid-Atlantic Ridge when the seafloor is insonified by a band-limited, low-grazing-angle acoustic pulse. Analysis of monostatic reverberation data acquired at Site A on the ARSRP 1993 Acoustics Cruise suggests that the scattered signals cannot be quantitatively explained in terms of large-scale slope alone, even though a strong correspondence between high intensity backscatter and seafloor ridges is observed. Numerical modeling using a finite-difference solution to the elastic wave equation shows that large-scale seafloor slope and subseafloor average velocity influence the backscattered intensity levels but that the source of scattering is wavelength-scale heterogeneity. Modeling results show that scattering from rough, basaltic bottoms is dominated by interface scattering. Subseafloor volume heterogeneity is shown to be capable of producing scattered signals comparable to rough seafloor scattering when the bottom is smooth and/or has a low velocity. An 'effective Rayleigh roughness parameter' is defined that incorporates all seafloor structure parameters, including large-scale slope, the correlation length and rms height of wavelength-scale structure, and the acoustic beam grazing-angle. This leads to an interpretation scheme for backscatter intensity in terms of seafloor roughness.			
17. Document Analysis a. Descriptors scattering reverberation bottom-interaction			
b. Identifiers/Open-Ended Terms			
c. COSATI Field/Group			
18. Availability Statement Approved for publication; distribution unlimited.		19. Security Class (This Report) UNCLASSIFIED	21. No. of Pages 433
		20. Security Class (This Page)	22. Price